TEMPLATE-ASSISTED SYNTHESIS AND CHARACTERIZATION OF HIGH ASPECT RATIO METALLIC NANOSTRUCTURES

A THESIS SUBMITTED TO THE

UNIVERSITY OF PUNE

FOR THE DEGREE OF

DOCTOR OF PHILOSOPHY

IN

CHEMISTRY

By

MAHIMA S.

Dr. K. VIJAYAMOHANAN
(Research Guide)

PHYSICAL AND MATERIALS CHEMISTRY DIVISION

NATIONAL CHEMICAL LABORATORY

PUNE – 411 008

INDIA

JUNE 2008

Dedicated to My Late
Grandmother...

DECLARATION

I, hereby declare that all the experiments embodied in this thesis entitled, **"TEMPLATE-ASSISTED SYNTHESIS AND CHARACTERIZATION OF HIGH ASPECT RATIO METALLIC NANOSTRUCTURES"**, submitted for the degree of Doctor of Philosophy in Chemistry, to the University of Pune have been carried out by me at the Physical and Materials Chemistry Division, National Chemical Laboratory, Pune, 411 008, India, under the supervision of Dr. K. Vijayamohanan. The work is original and has not been submitted in part or full by me, for any degree or diploma to this or to any other University.

Date: **Mahima S.**

Physical and Materials Chemistry Division
National Chemical Laboratory
Pune – 411 008.

Dr. K. Vijayamohanan
Scientist

Physical and Materials
Chemistry Division
National Chemical Laboratory
Pune – 411 008
INDIA

Tel: 91-020-2590 2588
Res: 91-020-2587 0307
Fax: 91-020-2590 2636
Email: vk.pillai@ncl.res.in

CERTIFICATE

This is to certify that the work incorporated in the thesis entitled, **"TEMPLATE-ASSISTED SYNTHESIS AND CHARACTERIZATION OF HIGH ASPECT RATIO METALLIC NANOSTRUCTURES"** submitted by **Ms. Mahima S.,** has been carried out by her under my supervision at the Physical and Materials Chemistry Division, National Chemical Laboratory, Pune, 411 008, India. All the materials from other sources have been duly acknowledged in the thesis.

Date:
Place: Pune

Research Guide
(K. Vijayamohanan)

ACKNOWLEDGEMENTS

This is perhaps the most difficult thing I intend to do, i.e., to sincerely thank and express my heartfelt gratitude to everybody who has, in one way or the other, contributed in the successful completion of my thesis. I wouldn't be doing justice by merely naming everybody who helped me but at the same time it will be too difficult for me to express my sincere thanks in the form of words, I will nonetheless try to make a sincere effort …

Firstly, my heartfelt gratitude to Dr. K. Vijayamohanan, my research advisor, for his guidance, fruitful discussions, trenchant critiques, valuable advice, constant support and encouragement throughout the course of this work. I must also mention that he is also a very good teacher & a wonderful research guide with vast knowledge and insight, which are often quite rare. His constant effort to instill us with several, most essential habits, like weekly seminars & group meetings, monthly reports & daily planning, makes me confident to start an independent scientific carrier. He has also trained us to write manuscripts independently and guide the undergraduate students. He is also instrumental in teaching us to effectively communicate with people, to give a better presentation, to efficiently handle multitasking simultaneously and so on. My sincere regards and reverence are for him, forever.

I am grateful to Dr. S. Sivaram, Director, NCL, who gave me an opportunity to work in this prestigious research institute and also to CSIR for financial support. I wish to thank Dr. S. Pal, head of Physical Chemistry Division for allowing me to use all the available facilities in the division.

I would like to offer my sincere thanks to Dr. I. S. Mulla and Dr. K. Sreekumar for their help, support and advice during the course of this study. I also extend my admiration to Dr. P. A. Joy for his valuable suggestions and discussions.

My sincere thanks to Drs. Anil Kumar, P. C. Ghosh, Pankaj Podhar, B. L. V Prasad, V. Ravi, Gohkhale and Manjusha for their valuable advice and help. I am highly indebted to Mr. Gholap, Mr. A.B. Gaikwad, Dr. K. R. Patil, Mrs. Suguna, Mrs. Renu, Mrs. Anuya, Mrs. Arti and Mrs. Dhoble who were helpful for characterising various samples. I extend my gratitude to Mr. Dipak, Mr. Punekar and other office staffs for their timely help. My sincere thanks to the library staff, members of glassblowing, stores and purchase, workshop, security and GJ Hostel mess workers for their help during my stay in NCL.

I am forever indebted to all my former teachers from School of Chemical Sciences (Mahatma Gandhi University), CMS College, Baselius College and St. Joseph's School, as they built the foundation for this achievement.

My sincere thanks to our collaborators Prof. C.V. Dharmadhikari and Mrs. Minakshi, Dept. of Physics, University of Pune, Dr. A. M. Rao, Clemson University for their valuable discussions.

My special gratitude to my seniors, Drs. Aslam, Nirmal, Jadab, Trupti, Niranjan, Murugan and Deepali for their mentoring & care during my initial days in NCL. I should thank Aslambai especially, for his efforts in getting good electron micrographs from Northwestern University.

I owe deeply to my ever-trustful friends in lab; Bhalchand, Meera, Kannan, Bhasku, Shindu, Beena, Dr. Meenu, Kuttan, Ramanujan, Vivek, Girish, Abbay, Mrudula, Sanjay, Dhanu, Pravin, Praveen, Neelesh, Ranjith, Bhudha dev, Mandar, Mukta, Heloise, Subhash, Roopali, Sonali, Shalaka for all their affection, help and support. I must thank Bhalchand especially, for the constant support and help he has provided. Also, my heartfelt thanks to MSc. Project students Annu, Ashwini, Indu and Beena for their love, help and support. My sincere thanks to Beena, Bhasku and Shindu for their love, support and timely help.

Also it gives me immense pleasure to express my sincere thanks to my colleagues of Physical Chemistry Division Shreeja, Vijay, Mangesh, Pankaj, Anita, Selvakannan, Suvarna, Sanjay, Sivaram, Shraedha, Khupse, Gitanjali, Sarita, Shabana, Sumit, Pratap, Manasi, Deepti, Maggie, Tushar, Remya, Umesh, Imran and Tuhina for providing me with an excellent working ambience during the course of this work.

My special thanks to other friends in NCL Kala Chechi, Surendran Chettan, Prakash, Rohit, Pranju, Sandeep, Mahesh, Potrekar, Nazrul, Manasi (my roommate), Atul, Ramakant, Ankur, Suman, Amol, Suchita, Ankush, Bhange, Sachin, Rajish, Mitra, Lakshi, Maitri, Trupti, Selva, Kaaja, Dharma, Pradeep and Rosy. I also extend my gratitude to all my Mallu friends in NCL for their help. I would also thank all GJ hostelites for their help and support.

My special admiration to Manju Chechi for her motherly care, constant support and love.

I wholeheartedly thank my friends Sony Chechi, Smitha Chechi, Panchu, Manoj Chettan, Shyla, Veena, Nabanitha bhabhi, Mikku and Elsu for their love, support and constant encouragement. Their friendship shall always be remembered.

I acknowledge an appreciation that extends beyond any words for the support and encouragement of my friend Prashant. Also I express my deep sense of gratitude to his parents for their continuing encouragement and affection.

I find no words to express my feelings for my Amma, Achan, Manju and Manoj. Their love, support, blessings has always been my strength. Their patience and sacrifice will remain my inspiration throughout my life. I also express my heartfelt gratitude to Uchamma, Geema, Uncle, Ramdas Uncle, Mohan Uncle, Chettan (brother-in-law), Manu whose moral support, love and constant encouragement are instrumental to achieve this feet of goal.

Above all, I thank God; the almighty for guiding me in my life.

Though, many have not been mentioned, none is forgotten.

Mahima S.

List of Abbreviations

Expansion	Abbreviation
Anodization Voltage	V_A
Atomic Force Microscope	AFM
Binding Energy	BE
Brunauer Emmett Teller	BET
Barrett-Joyner-Halenda	BJH
Contact Angle	CA
Carbon Nanotube	CNT
Complex Nonlinear Least Square	CNLS
Charge Transfer Resistance	R_{CT}
Chemical Vapor Deposition	CVD
Critical Surface Tension	γ_{crit}
Cyclic Voltammetry	CV
Current Density	j
Density of States	DOS
Direct Current	DC
Dimethyl formamide	DMF
Dimethyl sulfoxide	DMSO
Diffused Reflectance Infrared Fourier Transform	DRIFT
Electroactive Area	A
Energy Dispersive X-ray Analysis	EDX
Enhancement Factor	R
Exchange Current Density	j_o

Faced Centered Cubic	fcc
Fast Fourier Transform	FFT
Field Emission Scanning Electron Microscope	FESEM
Frequency Response Analyzer	FRA
Full Width at Half Maximum	FWHM
Fourier Transform Infrared	FTIR
High-Resolution Transmission Electron Microscopy	HRTEM
Inter-pore Distance	D_{int}
Micro/Nano-Electromechanical Systems	MEMS/NEMS
Monolayer Protected Nanocluster	MPC
Nanocrystals	NCs
Ohmic Resistance	R_{Ω}
One-Dimensional	1-D
Porous Alumina Membrane	PAM
Pore Diameter	D_P
Porosity	P
Pore Density	ρ
Polyvinylpyrrolidone	PVP
Polymer Electrolyte Membrane Fuel Cell	PEMFC
Quantum Dots	Q-dots
Selected Area Electron Diffraction	SAED
Scanning Electrochemical Microscope	SECM
Saturated Calomel Electrode	SCE
Surface Plasmon Resonance	SPR
Scanning Tunnelling Microscope	STM
Scanning Electron Microscope	SEM
Tetrahexahedra	THH
Transmission Electron Microscope	TEM

Thermogravimetric Analysis	TGA
Two-Dimensional	2-D
Three-Dimensional	3-D
Ultra-Violet-Visible	UV-vis
X-ray Photoelectron Spectroscopy	XPS
X-ray Diffraction	XRD
Zero-Dimensional	0-D

Table of Contents

Chapter 1

Chapter 2

CHAPTER 1

High Aspect Ratio Metallic Nanostructures: An Overview

This chapter provides a comprehensive review of the current research activities on high aspect ratio metallic nanostructures which include wires, rods and tubes. The crucial role of these structures in nanotechnology is illustrated by considering some of their unique aspect ratio dependent properties. A brief account of recent endeavours on the synthesis of these nanostructures through different routes is provided, simultaneously discussing some of the fundamental issues related to controlling their dimensionality, stability and surface passivation. Potential applications of these structures in various fields are also discussed with special emphasis on the impact of these nanomaterials on fuel cell electrocatalysis. Finally after illustrating some of the major advantages and limitations of these materials, the objectives of the present investigation are explained in an attempt to fill the existing gaps in literature for this class of low dimensional nanostructures.

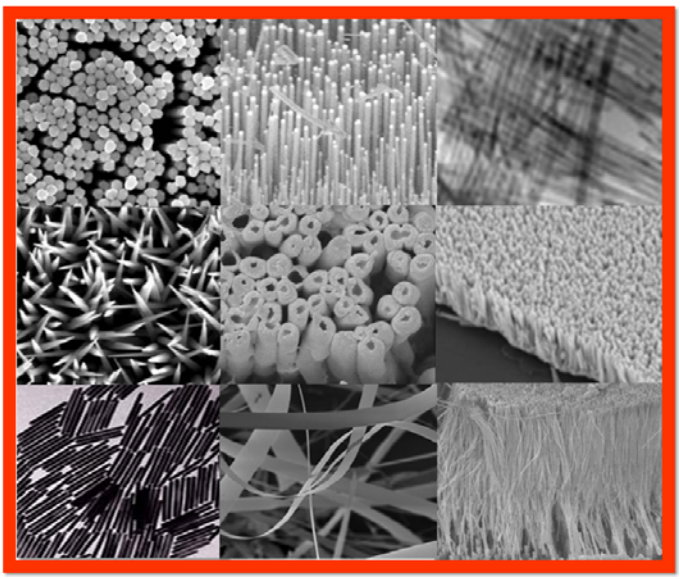

1.1. Introduction

In recent years, ‘‘nanotechnology’’ has emerged as a new direction of research with enormous societal importance representing an exciting, intellectually challenging and rapidly expanding area that crosses the seamless borders between many branches of physical/biological sciences and engineering.[1] It has shown outstanding promise for providing many breakthroughs that will change the direction of technological advances in a wide range of applications in the near future. Often, it is defined as the technology to fabricate, characterize, and manipulate structures whose features are controlled at the nanometer (1-100 nm) level.[2] Research in this direction has been triggered by the recent availability of revolutionary instruments and approaches that allow the investigation of material properties with subatomic resolution. Strongly connected to such technological advances are the pioneering efforts that have recently revealed new physical and chemical insights of materials at a level intermediate between atomic/molecular and bulk, which are expected to make a significant impact on many applications with direct societal benefits.

Amazing attention has been captured by these nanostructured materials (even from general public) and as a result, their growth has actually been at an unprecedented rate, principally due to their unique and outstanding physical and chemical properties which could be controlled remarkably by tuning their morphology (i.e., size, shape, and dimensionality).[3] A large number of prospective applications spanning wide areas such as optoelectronics, sensors, catalysis, energy and photochemistry could be realized due to the development of many innovative hybrid materials using these advances.[4] One of the most successful examples is provided by micro/nanoelectronics, where “smaller” has meant enhanced performance ever since the invention of integrated circuits: more components per chip, faster operation, lower cost, and less power consumption pointing out eventually to use molecules as both passive and active electronic components.[5] Moreover, a wealth of interesting and new phenomena are also associated with these

nanostructures, with unprecedented examples including quantized or ballistic conductance, coulomb blockade or single electron tunnelling, and metal-insulator transition all depending on some critical length scale.[6]

1.2. Classification of Nanostructures

It is interesting to classify these nanostructures in terms of their dimensionality since this has a profound effect on the behavior of all classes of materials. The classification scheme is essentially a macroscopic approach, based on the size dependence of some physical behavior of the system.[7] This could involve, for example, transport, usually of electrons/phonons, in which case an important length scale is the mean free path, Λ. Thus, a system is of reduced dimensionality if the size, L_i of a macroscopic material is reduced sufficiently in one or more orthogonal directions, i = {x, y, or z}, so that in those directions the mean free path is determined by the boundary scattering and not by some other intrinsic mechanisms for electrons/phonons. Thus reduced dimensionality occurs in this picture if $\Lambda_{int} > L_i$, so that $\Lambda_{tot} \simeq L_i$ for transport in the i^{th} direction, since the total mean free path is given by a reciprocal sum of intrinsic and extrinsic (boundary scattering) mechanisms, $\Lambda^{-1}_{tot} = \Lambda^{-1}_{int} + \Lambda^{-1}_{ext}$.

Alternatively, the important length scale can be correlated to the size 'L_o' of electron wave function, such as the Fermi wavelength, $\lambda_F = 2\pi/k$, the effective Bohr radius, a_o or the electron phase coherence length, L_φ given as, $L_\varphi = (D\tau_\varphi)^{1/2}$, where D is the diffusion coefficient of electron and τ_φ is the time between elastic collisions. In this case, size quantization sets in if $L_i < L_o$. Hence, a zero dimensional system (strictly speaking quasi-zero dimensional) is one in which all three orthogonal lengths of a sample are less than Λ_{int} and a quantum dot results when the length is such that $L_{x,y,z} < L_o$. Similarly, one-dimensional system is one in which two spatial dimensions are smaller than Λ_{int}; transport is then allowed along the remaining one dimension, unencumbered by boundary scattering. For example, a quantum wire is an one-dimensional sample with size quantization in two dimensions ($L_{y,z} < L_o$). They constitute an ideal and interesting

system to study the dependence of electrical and thermal transport or mechanical properties on dimensionality and size confinement. Finally, a two-dimensional system is that in which only one spatial dimension is less than Λ_{int} and hence transport is allowed in two dimensions, limited only by intrinsic scattering mechanisms. A quantum well is a two-dimensional sample with size quantization in the third dimension ($L_z < L_o$). Different dimensional nanostructures and their associated type of confinement are summarized in Table 1.1.

Table 1.1. Examples of reduced-dimensional material geometries, and definitions of their dimensionality and of the associated type of confinement. [Adopted from ref. 7b]

$L_{X,Y,Z} > L_0$	No nanostructures	No confinement	Bulk material	
$L_{X,Y} > L_0 > L_Z$	Two-dimensional (2-D) nanostructures	One-dimensional (1-D) confinement	Wells	
$L_X > L_0 > L_{Y,Z}$	One-dimensional (1-D) nanostructures	Two-dimensional (2-D) confinement	Wires	
$L_0 > L_{X,Y,Z}$	Zero-dimensional (0-D) nanostructures	Three-dimensional (3-D) confinement	Dots	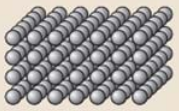

An alternate simple way of visualizing nanomaterials is by looking at their sizes. They are characterized by at least one dimension in the nanometer range, (1-100 nm) and can be considered to constitute a bridge between single molecules and infinite bulk systems. The density of states (DOS) in nanostructures is strongly dependent on the dimensionality.[2a,8] The DOS for these nanostructures of different dimensionality is compared with that of bulk solid as shown in figure 1.1, where it is clear that as the dimensionality is reduced from three to zero, DOS evolve from continuous levels into

discrete states. Hence, it is obvious that DOS is strongly affected by the dimensionality reduction because of the corresponding reduction of degrees of freedom in wavevector space.

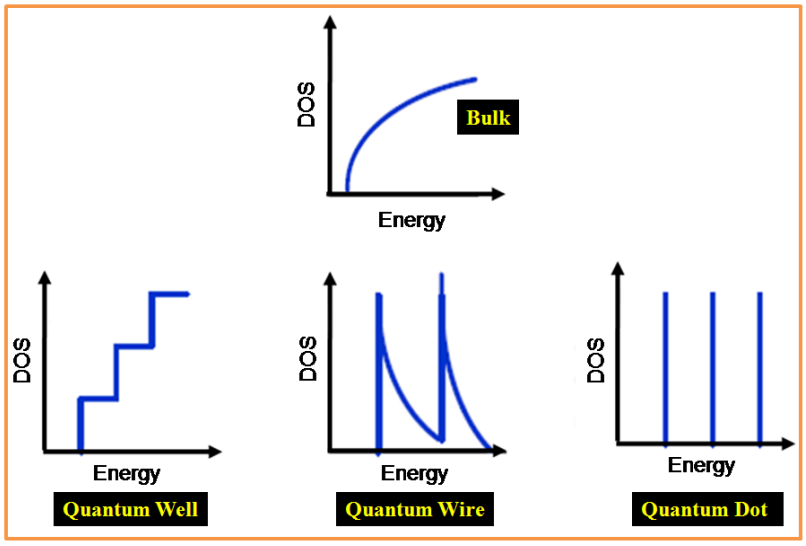

Figure 1.1. The electronic density of states of bulk material (3-D), quantum well (2-D), quantum wire (1-D) and quantum dot (0-D). [Adopted from ref. 2a]

Are these nanostructures in various dimensionalities interesting and worth pursuing? We believe that the answer to this question is an unqualified yes from the standpoints of both fundamental science and technology. One needs to look no further than the past studies of the 2-D electron gas in semiconductor heterostructures, which have produced remarkably rich and often unexpected results, electron tunnelling through quantum dots, have facilitated concepts of the artificial atom and the creation of single electron transistors.[1b,d,9] Recently, 1-D nanostructures such as nanowires and nanotubes have also become the focus of intensive research owing to their unique applications in the fabrication of nanoscale devices.[10] 1-D systems are the smallest dimensional structures that can be used for efficient transport of electrons/phonons and optical excitations, and are thus expected to be critical to the function and integration of nanoscale devices. However, little is known about the nature of, for example, localization that could

preclude transport through 1-D system. Moreover, these systems should exhibit density of states singularities, can have energetically discrete molecule like states extending over large linear distances, which might show more exotic phenomena, such as the spin-charge separation predicted for a Luttinger liquid.[11] There are also many other applications where 1-D nanostructures could be exploited, including nanoelectronics, superstrong and tough composites, functional nanostructured composites, and novel probe microscope tips.[3b,12]

In this context, another important question that arises is how can nanostructures that have controlled dimensionality and size be rationally synthesized or fabricated? How can atoms or other building blocks be assembled logically into structures with nanometer size and desired (low) dimensionality? A better insight and understanding of major factors which control the growth of the nanostructures is indispensable for assembling these nanobuilding blocks. It has been quite clear in recent years that conventional "top-down" approaches are beset with many insurmountable experimental difficulties owing to various physical effects that are not easily scalable, and also because of the cost issues associated with nanoscale fabrication.[13] This state of affairs has led to a great interest in the development of new methodologies based on bottom-up approaches. The following section briefly discusses some of the recent developments in the synthesis of nanostructures with a closer look at one-dimensional nanostructures.

1.3. Synthesis of Nanostructures: A brief Review

Two-dimensional nanostructures have been conveniently synthesized using techniques such as molecular beam epitaxy (MBE) and atomic layer deposition (ALD).[14] These techniques offer precise control of deposition parameters possibly at the single atom level, along with the best film quality. Similarly significant progress has also been made with regard to the preparation and characterization of zero-dimensional nanostructures in the past two decades. For example, several chemical methods have already been developed for these nanostructures with well-controlled dimensions to prepare a broad range of materials.[15]

However, in comparison with 0-D and 2-D nanostructures, the advancement of 1-D nanostructures (high aspect ratio nanostructures) has been slow until very recently, perhaps, due to difficulties associated with the synthesis of these nanostructures with well-controlled dimensions, morphology, phase purity, and chemical composition. Although high aspect ratio nanostructures can now be fabricated using a number of advanced nano-lithographic techniques, such as electron-beam or focused-ion-beam writing, proximal-probe patterning, and X-ray or extreme-UV lithography, further development of these techniques into practical routes for large quantities of structures, rapidly, and at reasonably low costs, still requires great ingenuity.[16] In contrast, chemical as well as electrochemical routes might provide an alternate strategy for generating high aspect ratio structures in terms of material diversity, cost, and the potential for high-volume production.[17] The following section briefly reviews different strategies for the formation of high-aspect ratio metallic nanostructures with special emphasis on nanorods and nanowires of noble metals (platinum and palladium). Platinum and palladium have been specially selected because of their outstanding role as multifunctional catalysts in many industrial applications, and also due to its important use as electrocatalysts in fuel cells.[18] However, the high cost of these remains a challenge that demands its full or partial replacement without affecting the performance. The manipulation of the size and shape at the nanoscale can contribute to lowering of the metal usage concomitantly achieving the necessary cost reduction. Moreover, since the catalytic reactivity of nanostructures depends on their morphology, it is important to design and prepare well-controlled shapes and sizes of these nanostructures for effective applications, especially in the field of catalysis and electrocatalysis.[19] Although an exhaustive description of all available reports is difficult, an attempt is carried out to summarise the central contributions in this area.

1.3.1. Synthesis of Platinum and Palladium

Because of the highly symmetric face centered cubic (fcc) crystal structure of platinum, it is not easy for the system to acquire a non-spherical shape, which involves a

competition against the desire to minimize the surface energy through the formation of thermodynamically stable spherical particles.[20] In this context, it would be of interest to examine, how atoms (and other building blocks) could be rationally assembled into linear nanostructures but with much longer length scales. Thus there is great interest in the development of new methodologies based on bottom-up approaches for the selective synthesis of anisotropic shapes. One of the commonly adopted strategies for achieving shape control is based on the manipulation of growth kinetics with the help of a capping molecule that preferentially binds to crystal faces of the growing particle, thus introducing anisotropy into the particle geometry along with preferred growth direction.[21]

Another interesting strategy is the addition of foreign species in the reaction mixture which could significantly alter the growth kinetics of different crystallographic facets thus inducing anisotropy.[22] For the polyol synthesis, these foreign ions are expected to have a pronounced influence on the nucleation of nanocrystallites than surfactants or polymers because of their relatively smaller size and increased ability to form complexes with reactive species in the solution. A slightly different strategy for the growth of anisotropic structures is through the introduction of defects in the seed crystals, which could reduce the symmetry of the cubic lattice.[23] Apart from these strategies, anisotropic structures are also realized through physical constrictions imposed by structure directing materials which include both hard and soft templates.[24] Some of the key issues and shortcomings involved in these approaches along with the utility of these nanostructures for various applications are discussed below.

1.3.1.1. Platinum Nanowires/Nanorods

For the synthesis of platinum nanowires with well-controlled aspect ratio, several routes have been demonstrated including template-assisted approach and reduction in presence of surfactants/capping molecule. In the case of former, both soft (e.g., micelles) as well as hard templates (e.g., carbon nanotubes, mesoporous silica and porous alumina membrane) have been successfully used for preparing platinum nanowires and nanorods.[25] This route provides several distinct advantages over the latter approach,

offering a convenient way for structurally uniform nanostructures often, periodically aligned in template matrices. For example, Kim et al. have demonstrated the preparation of ordered Platinum nanowire arrays through an electrochemical route using porous alumina membrane templates.[25e] The field-emission scanning electron microscopic (SEM) image of platinum nanowire arrays in figure 1.2a, suggests individual Pt nanowires to be dense and continuous with a uniform diameter and length of ca. 60 nm and 2.6 μm respectively.

Thus linear structures with significantly higher aspect ratio are formed without any external agent, which is indeed beneficial for their catalytic activity due to better purity. However, these structures are often polycrystalline.[26] In the light of this drawback, a different approach based on polyol route (but with the mediation of foreign metal ions such as Fe^{2+} or Fe^{3+}), has been adopted for the synthesis of Pt nanowires.[27] Even though, single crystalline and high aspect ratio nanowires as shown in figure 1.2b are achieved through this route, these foreign metal ions could have deleterious effect on the catalytic activity. For example, due to the presence of Ag in platinum nanostructures, the kinetics of ethylene hydrogenation undergoes a dramatic decrease.[28] Moreover, the presence of capping agents such as polyvinylpyrrolidone (PVP) interacts strongly with the metal surface through the carbonyl moiety to block significant number of active sites, which again retard the catalytic activity.[29] Therefore, shape-control without the aid of foreign metal ions is highly desirable for many of these applications.

A slightly different approach without any external metal ions has been developed for the synthesis of platinum nanowires using K_2PtCl_4 and $K_2C_2O_4$ as the metal precursor and stabilizing agent respectively.[30] The reaction has been carried out in the presence of pre-formed Pt seeds under H_2 atmosphere. Even though, the "as obtained" nanowires are very thin (diameter 1.5-3 nm) as in figure 1.2c, they are neither perfectly linear nor smooth appearing more or less like a branched or network structures.

Through a fundamentally different approach, Gurlu et al. have demonstrated the formation of one-atom-thick (0.4 nm) and 380 nm long metallic nanowires by the self-organization of Pt atoms on a Ge(001) surface after a high-temperature annealing.[31]

Scanning tunnelling microscopic (STM) image of this is shown in figure 1.2d revealing the formation of one-dimensional Pt in a defect-free manner with a very high aspect ratio. The advantage of this approach over the above procedure is that the nanowires are synthesized without any capping agent or foreign species.

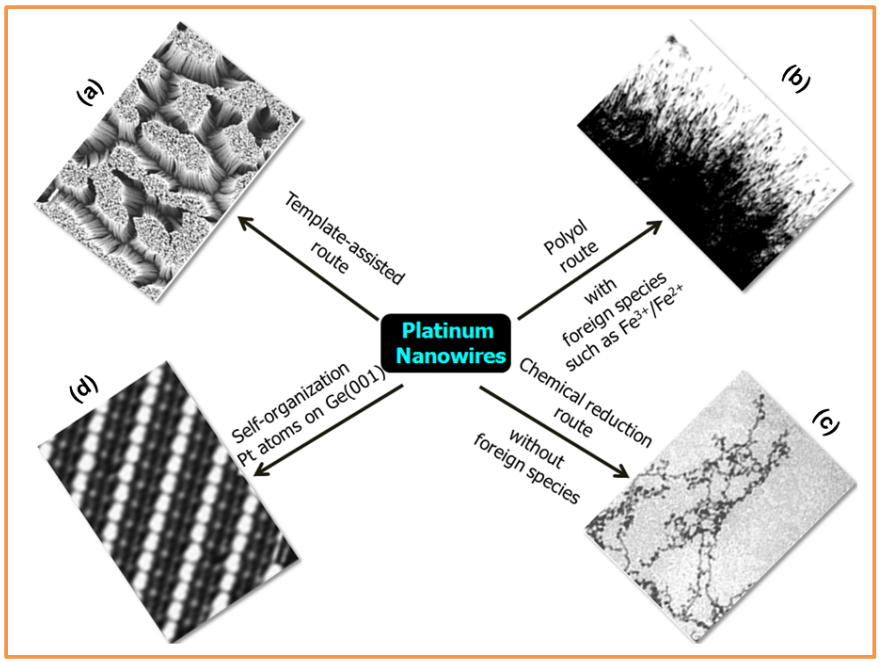

Figure 1.2. Comparison of different routes adopted for the synthesis of platinum nanowires; electron micrographs of the nanowires obtained through each routes are also given. [Adopted from ref. 25e, 27, 30 and 31]

1.3.1.2 Platinum nanotubes

The synthesis of platinum nanotubes has been realized mainly through two approaches, either galvanic displacement or using selected templates.[32] For example, through the former approach, excellent platinum nanotubes have been synthesized using silver nanowire as the substrate.[32a] Although, these nanotubes are formed with a relatively high yield (figure 1.3a), the major drawback of this route is that the dimension and wall thickness of the resultant hollow structures cannot be independently varied. Template-assisted approach, on the other hand, seems to be more beneficial in forming nanotubes with controllable wall thickness as illustrated by the formation of highly ordered Pt

nanotubule using porous alumina membrane (PAM) through electrodeposition.[32d] For example, a typical SEM image after template removal (Figure 1.3b) reveals the formation of highly ordered, defect-free Pt nanotubule arrays having an outer diameter of ca. 300 nm, inner variable diameter and a length of about 25 µm. In this case, the pre-deposited Ag plays a key role for Pt nanotubule growth and consequently the length and thickness of the tube walls could be tuned by controlling the electrodeposition parameters.

In another illuminating example, trigonal selenium (t-Se) nanowires have been used for the synthesis of Pt nanotubes after treating with platinum (II) chloride to form a desired thickness of Pt coating on the surface and subsequent removal of Se cores by hydrazine.[32b] These Pt nanotubes have a uniform wall thickness of 9 ± 2 nm as shown in figure 1.3c, where triangular cross-section of the t-Se template is clearly duplicated by the Pt nanotubes. The wall thickness of Pt nanotubes could be readily controlled by varying the concentration of $PtCl_2$ solution and/or the coating time.[32b]

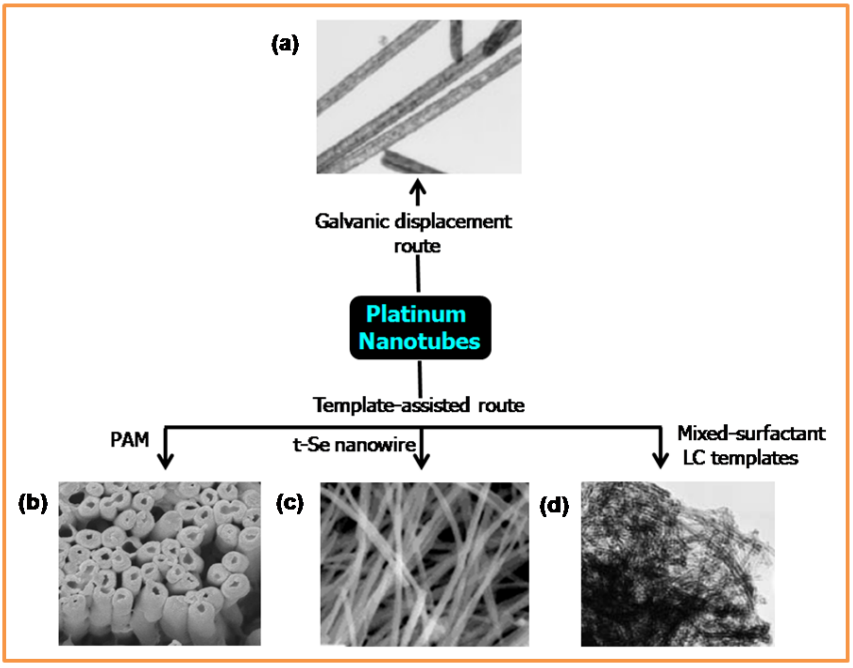

Figure 1.3. Different routes adopted for the synthesis of Platinum nanotubes along with the respective electron micrographs. [Adopted from ref. 32a,b,d,e]

Although above templating approach yields uniformly aligned nanotubes with controllable thickness and length, the inner and outer diameter of the nanotubes are relatively large. As a result, an improved technique has been recently illustrated using Lyotropic Mixed-Surfactant Liquid-Crystal Templates.[32e] In this platinum nanotubes are formed by a mixed surfactant templating mechanism using equimolar amounts of nonaethylene glycol monododecyl ether and polyoxyethylene (20) sorbitan monostearate molecules to form a hexagonal array of cylindrical rod-like micelles and the aqueous outer shell of these micelles facilitates the growth. Interestingly, the transmission electron microscopic (TEM) image as shown in figure 1.3d reveals that the nanotubes are formed with inner and outer diameters of 3 nm and 6 nm respectively, which are significantly smaller compared to that of other methods despite poor alignment and random aggregation.

Apart for these high aspect ratio nanostructures, much effort is also devoted on the synthesis of various interesting shapes of platinum such as cubes, multipods, tertrahexahedra and flowers considering their unique size and shape dependent properties.

1.3.1.3. Platinum Nanocubes

The synthesis of platinum nanocube involves the reduction of a Pt salt using sodium borohydride, alcohol or hydrogen in the presence of a surfactant. However, the resultant structures are often non-uniform faceted.[33] As a result, a different strategy based on polyol method has been reported for the formation of regular nanocubes. In this route, PVP is used as the capping agent, in addition to foreign species such as $AgNO_3$ for controlling the shape and surface structure.[34] A similar strategy has also been followed by other groups for the synthesis of nanocubes.[35] A summary of diverse routes for preparing Pt nanocubes is given in figure 1.4 in order to understand the relative role of various key parameters. Although monodispersed Pt nanocubes are formed by this procedure (Figure 1.4a), many a times the assistance of Ag for nanocube growth and the use of capping agents such as PVP could have deleterious effects on their catalytic activity. Therefore,

shape-controlled synthesis of uniform Pt nanocubes without the aid of external nucleating agents or capping molecules is highly desirable for exploiting the unique electrocatalytic behaviour of various shapes.

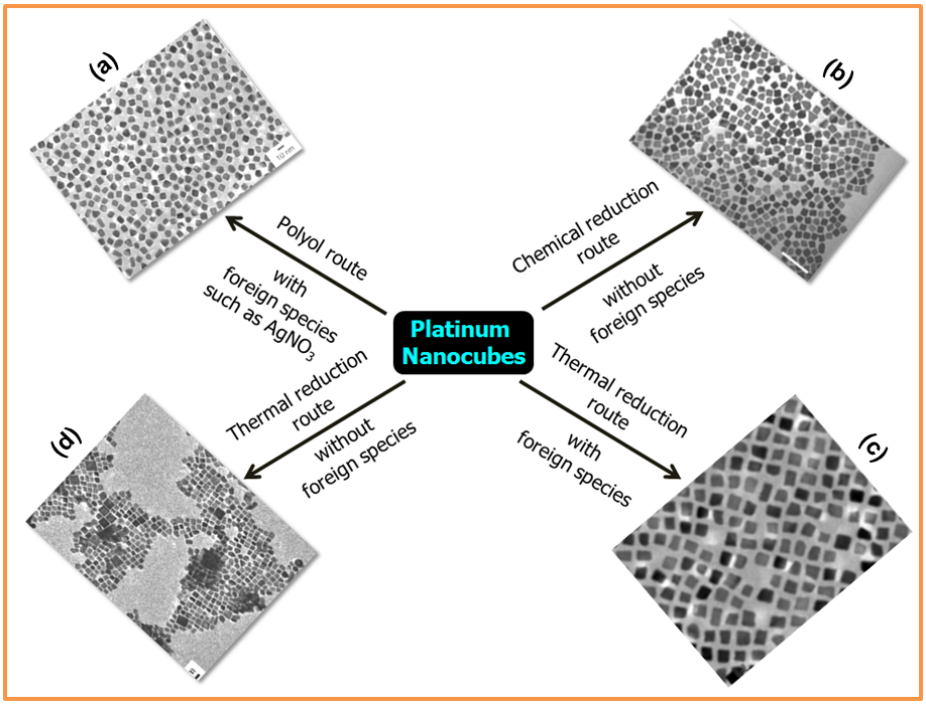

Figure 1.4. Different routes adopted for the synthesis of Platinum nanocubes along with their respective electron micrographs. [Adopted from 34,36-38]

Considering the drawbacks of the aforementioned procedures, another route has been known recently using an interesting organometallic complex ($(C_{14}TA)_2PtBr_4$) as the Pt precursor and excess $NaBH_4$ as the reducing agent.[36] Transmission electron micrographs of the nanocubes with diameter ca. 13.4 ± 1.8 nm are shown in figure 1.4b, where the formation of cubic structure with 73 % yield is clear. Interestingly, the nanocubes are capped by tetradecyltrimethylammonium, where the interaction of these alkylammonium ions with Pt surfaces is considerably weaker than that of the carbonyl group of PVP. However, in addition to nanocubes, irregular particles are also obtained despite the simplicity and elegance of the method.

A fundamentally different approach based on thermal reduction has been reported, where the nanocubes are formed in the presence of $Fe(CO)_5$, which plays a key role in achieving shape control.[37] Additionally, along with the platinum acetylacetonate ($Pt(acac)_2$) precursor, oleic acid and oleylamine are also used both for nanostructure stabilization and shape control. TEM image of the resulting nanocubes are also shown in figure 1.4c, where interestingly, monodispersed nanocubes are formed with an average size of 8 nm with nearly 100 % yield. Moreover, the energy disperse analysis reveals no evidence for Fe in the nanocubes in contrast to the nanocubes obtained by the earlier case. Similarly, thermal reduction has also been employed by other groups without the assistance of shape control agents, where the synthesis has been carried out using ($Pt(acac)_2$), and oleylamine.[38] However, the "as prepared" nanocubes are poly-dispersed with size ranging from 10 to 100 nm as shown in figure 1.4d.

Table 1.2 summarizes a comparative study of different routes employed for the formation of nanocubes to reflect the importance of key parameters controlling both the size and selectivity. Although nanocubes are also formed in the absence of foreign species, those formed with the help of shape controlling agents comparatively reveal higher selectivity and better size distribution. However, with respect to their application in catalysis, synthesis without the aid of any external ions and strong surface passivating agents are always more important.

Table 1.2. Different synthetic routes employed for the formation of Pt nanocubes along with key parameters involved in controlling the shape; both the size and selectivity of nanocubes estimated from the electron micrographs are also mentioned.

Synthetic Approach	Metal Precursor	Capping/ Stabilizing Agent	Reducing Agent	Foreign Species	Size and Selectivity	Ref.
Chemical reduction route	$(C_{14}TA)_2PtBr_4$	$C_{14}TABr$	Excess $NaBH_4$	-	13.4 ± 1.8 nm ~ 73 %	36
Polyol route	$H_2PtCl_6.6H_2O$	PVP	Ethylene glycol	$AgNO_3$	9.4 ± 0.6 nm ~ 80 %	34
Thermal reduction route	$Pt(acac)_2$	Oleylamine	H_2	-	10-100 nm ~ 80 %	38
Thermal reduction route	$Pt(acac)_2$	Oleic acid and Oleylamine	-	$Fe(CO)_5$	8 nm ~ 100 %	37

1.3.1.4. Platinum Multipods

Although well-defined multipods of semiconducting materials have been developed for several years, metallic multipods and hyper-branched nanostructures have been explored only recently. Moreover, in most of these approaches multipods are synthesized with the aid of foreign metal ions which control the nucleation and growth direction.[39] However, multipods formed in this route have branches which are rather short and not well defined, although they appear like a cone rather than straight rod.

As a result, a completely different approach is needed as reported more recently by introducing defects in the seed crystals since this is a very effective way to reduce the symmetry of the cubic lattice common for most of the metals leading to the formation of anisotropic structures like multipods. [40] For example, Yang et al. have demonstrated the synthesis of Pt multipods by generating a twinned crystal.[40] For this, $Pt(acac)_2$ is used as

the platinum precursor and 1,2-hexadecanediol as the reducing agent while adamantanecarboxylic acid and hexadecylamine act as capping agents. Typical TEM image of this platinum tripods is shown in figure 1.5, where a large quantity of tripods with ca. 8.0 nm width and length of around 140 nm is evident.

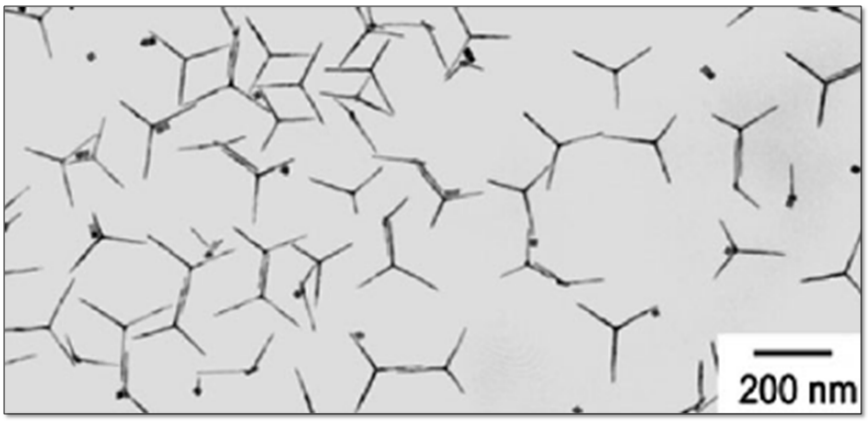

Figure 1.5. TEM image of Pt tripods synthesized in the presence of a twinned crystal, where the tripods are formed with ca. 8.0 nm width and length of around 140 nm. [Adopted from ref. 40]

Even though, multipods with comparatively good aspect ratio arms are formed through this route by means of defects, this strategy is limited owing to the fact that defects are generally difficult to control. However, by knowing the number and type of defects it is possible to control the shape of nanostructures. One of the major limitations is that the synthesis has been carried out in the presence of capping agent with carbonyl moiety, which as discussed earlier could passivate the metal surface. As a result, blocking of some of the active sites is possible along with a concomitant inhibition in their catalytic activity.

1.3.1.5. Platinum tertrahexahedra

Another important faceted nanostructure is tetrahexahedra (THH) bound by 24 facets. These THH nanostructures of Pt are synthesized through an electrochemical treatment of Pt nanospheres supported on glassy carbon by a square-wave potential.[41] A typical SEM image of THH Pt nanocrystals produced with a growth time of 60 min with

a yield of > 90 %, and average size of 200 nm is shown in figure 1.6a. Selected-area electron diffraction (SAED) and high-resolution (TEM), show the formation of a single-crystal THH enclosed by 24 high index facets with the dominant facets as (730). Although most of the facets are bounded by the (730), some are bounded by (210), (310), or (510) facets also.

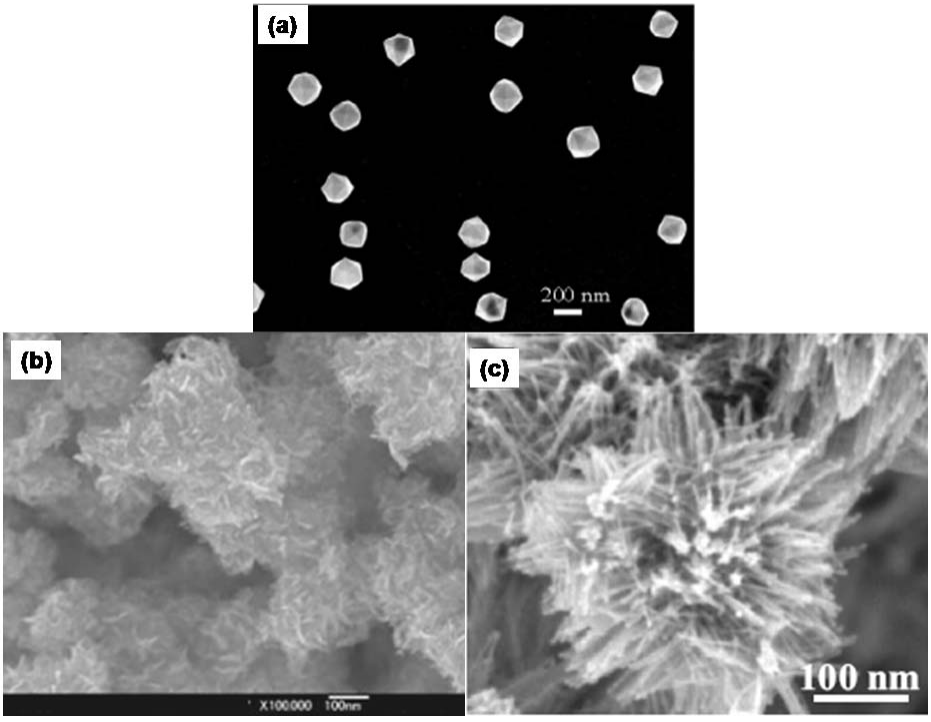

Figure 1.6. SEM image of (a) THH Pt NCs synthesized through an electrochemical treatment of Pt nanospheres; Platinum nanoflower synthesized through a chemical reduction route using (b) $NaBH_4$ and (c) HCOOH as the reducing agent. [Adopted from ref.41-43]

1.3.1.6. Platinum Nanoflowers

Platinum nanoflower is yet another interesting variant, prepared through a fast reduction using $NaBH_4$ and more importantly without the assistance of any stabilizing agent or templates.[42] High resolution SEM images of the samples shown in figure 1.6b, reveal the formation of non-spherical structures with numerous thin irregular projections on the surface, resembling petals which give a flower-like appearance. Fast addition of

excess $NaBH_4$ plays a very important role in generating these thin projections (petals) on the surface. Interestingly, when $NaBH_4$ is replaced by HCOOH, nanoflowers comprised of large quantities of nanowires in the form of petals are obtained.[43] SEM image as shown in figure 1.6c reveals flower-like structures with diameter in the range of 150-400 nm and nanowires with length 100-200 nm. Further, high resolution TEM images of the single Pt nanowires reveal a diameter of about 4 nm indicating its single crystal nature with a growth direction along the (111) axis. In contrast to the earlier case where fast reduction favours the formation of flower-like shape, slow rate of reduction holds here the key.

1.3.1.7. Palladium Nanowires/Nanorods

As in the case of platinum, Pd nanowires/nanorods could also be synthesized by various approaches although template-based route generates uniform and well isolated Pd nanowire arrays which are parallel to one another.[44] For example, formation of Pd nanowire arrays with ca. 3 μm length (figure 1.7a) has been demonstrated using PAM through a potentiostatic route.[44b] Similarly, Pd nanowires have also been prepared on a highly ordered pyrolytic graphite (HOPG) substrate selectively, using a three-step electrochemical decoration procedure of the step edges.[45] The merit of this method is its capability to form nanowires without the formation of nanoparticles although compared to template-based route, one gets poor uniformity in size distribution with diameter ranges from 40-50 nm, as shown by the AFM (Atomic Force Microscope) image in figure 1.7b. In a slightly different approach, Pd nanorods have been synthesized through a polyol route using PVP as the capping agent.[46] In contrast to the incorporation of iron species for the synthesis of Pt nanowires, KBr is used for the selective growth of Pd nanorods. However, as revealed by the TEM image (figure 1.7c), both the aspect ratio and selectivity of nanorods are significantly very poor and a larger percentage of spherical particles is also formed.

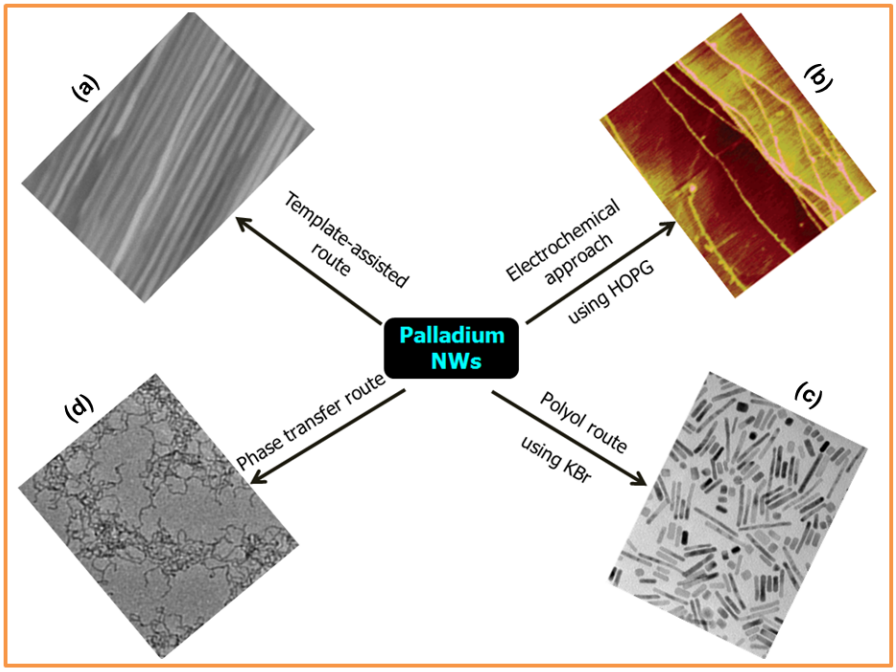

Figure 1.7. Different routes (both chemical and electrochemical) adopted for the synthesis of palladium nanowires; micrographs of the respective nanowires are also shown. [Adopted from ref. 44b,45-47]

Another route is based on phase-transfer approach for the formation of ultrathin Pd nanowires, where the Pd precursor is transferred into a non-aqueous phase containing capping agent octadecylamine using the phase transfer agent such as n-dodecyltrimethylammonium bromide (DTAB) followed by reduction using $NaBH_4$.[47] Even though, ultrathin nanowires are formed (ca. 2.5 nm), the length of the wires (ca. 25 nm) is sufficiently small and most of them seem to be interconnected at various angles (figure 1.7d).

1.3.1.8. Palladium Nanotubes

Synthesis of Palladium nanotubes is possible through either a galvanic displacement or template-assisted route. For example, in the case of galvanic displacement, a similar procedure as mentioned for Pt is carried out using Ag nanowires as the substrate and $Pd(NO_3)_2$ as the precursor.[32a] Although, Pd nanotubes are obtained in

high yield as revealed by the TEM image (figure 1.8a), the wall thickness could not be controlled by this. Palladium nanotubes have also been synthesized using templates. For example, ordered porous alumina membranes first wetted with a solution containing polylactide and palladium acetate up on subsequent annealing forms Pd.[48] However, this method often causes Pd nanoparticles (in cavities) instead of continuous nanotubes on the pore walls as shown by the SEM image (figure 1.8b) especially after the removal of polylactide and in order to overcome this limitation, Wang et al. have recently demonstrated a one-step direct electroless plating procedure to obtain continuous and granular Pd nanotubes.[49] Activated polycarbonate membrane template has been immersed in a solution containing $PdCl_2$ (metal precursor), disodium EDTA (complexing agent) and hydrazine (reducing agent) and nanotubes of Pd are formed with a fairly uniform wall thickness (50 nm) as revealed by the SEM image, figure 1.8c.

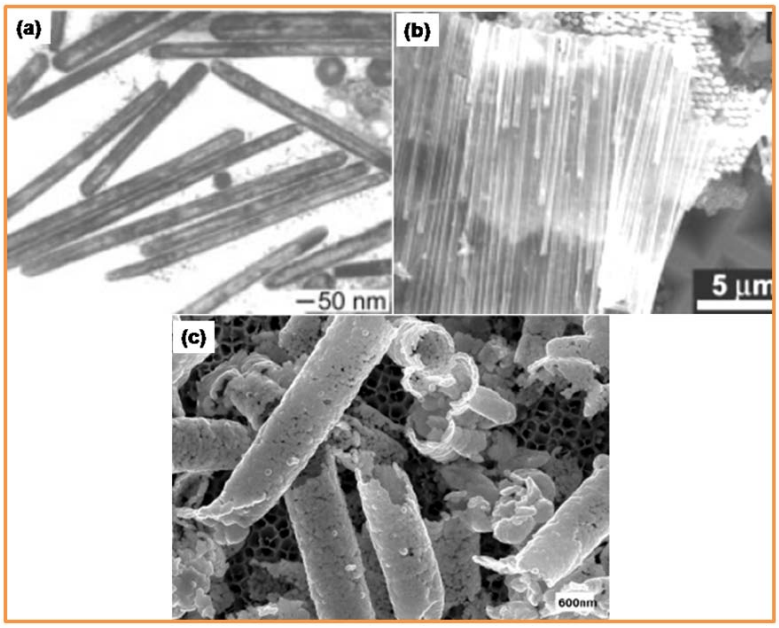

Figure 1.8. Palladium nanotubes synthesized through different routes (a) galvanic; (b and c) templated-approach; electron micrographs are also shown for comparison. **[**Adopted from ref. 32a,48 and 49]

1.4. Applications of High Aspect Ratio Metallic Nanostructures

From the above discussion, we are now in a stage to rationally assemble atoms or other building blocks into structures with few nanometer diameters but with much longer lengths. Now it would be of interest to consider, in what way these structures including other anisotropic metallic nanostructures differ from their spherical and bulk counterparts. Even though the application of these structures spans wide areas including sensors, optoelectronics, catalysis etc, we concentrate more on the electrocatalytic activity, considering their profound importance for fuel cell technology. One reason is, perhaps that these structures of well controlled size and shape possess different surface area and crystallographic facets which could finely tune both the selectivity and reactivity of many major catalytic reactions.[19] As a result, the influence of size and shape of nanostructures on both catalytic and electrocatalytic processes has been extensively investigated by many groups.

Even though, this area has undergone an explosive growth during the past decade, most of the studies deal with size dependent catalytic activity of spherical nanoparticles.[50] For example, the seminal work by Haruta et al. has demonstrated that the activity of supported Au nanoparticles toward CO oxidation is significantly enhanced for diameters below 4 nm.[50a] Moreover, several Density functional calculations combined with molecular dynamics have been also used to investigate the origin of size effect on catalysis.[51] In contrast, there are only limited studies comparing the catalytic activity of anisotropic nanostructures mainly because these structures are not easily accessible.

Since a majority of electrocatalytic reactions are structure sensitive or site demanding, it is essential to correlate the structure/shape of nanomaterials with their electrocatalytic properties for both fundamental and technological reasons. Before examining their applications directly, it is important to have a general background on nanostructured electrocatalysts.

1.4.1. Nanostructured Electrocatalyst: A General Background

Electrocatalysis may be defined as the relative ability of different electrode materials, under the same conditions to accelerate the rate of a given electrochemical process. Unlike catalytic effects in the conventional sense, the relative electrocatalytic properties of a group of materials at a given temperature and concentration of reactant and product are not necessarily constant. They may vary owing to the different dependence of rates on electric field, although an equilibrium parameter like exchange current density could be useful for comparison.[52] A key process in an electrocatalytic reaction is the interaction of the reactants with surface sites of the catalyst in the presence of the electric field. This interaction as observed for normal catalytic reactions, strongly depends on the surface properties of the catalyst. To maximize this interaction, the use of nanomaterials as catalysts has a number of important attributes including, a large surface area to volume ratio, high surface concentrations of corner and edge atoms, low coordination numbers of surface atoms and unique electronic properties (quantum size effects).[19c,53] Moreover, in the case of structure sensitive reactions, these interactions of reactant species vary depending on different crystallographic planes exposed on the surface. All these factors could be fine-tuned by the size, shape, composition, crystallinity, and structure (solid versus hollow), which acquires great relevance from a fundamental point of view.[19c,50,54]

Besides the above factors, the presence of high-miller-index crystal faces also influences the electrocatalytic activity.[55] For example, in the case of oxygen reduction reaction (ORR), it has been observed that electrocatalytic performance is higher for flower-like structures of gold compared to other shapes such as pinecone- and nanosheets.[55b] This enhanced activity of gold flowers is ascribed to the presence of high-miller-index crystal faces such as (220) and (331), which expose surface irregularities, steps, and kinks.

In the following section, we will be highlighting some of the important structure/shape sensitive electrocatalytic reactions of platinum and palladium high aspect ratio nanostructures relevant for fuel cell applications.

1.4.2. Electrocatalytic Reactions of Platinum and Palladium Nanostructures

One of the distinguishing features of electrocatalytic reactions is that majority of them are structure sensitive since their rates will vary dramatically with shape and/or crystallographic facets. For example, in the case of CO electrooxidation on cubo-octahedral Pt nanostructure bound by (111) and (100) facets, where during the oxidation of CO to CO_2, the transfer of CO molecules from (100) to (111) site takes place, which is a thermodynamically favoured site for CO oxidation.[56]

Electrocatalytic performance of Pt and Pd nanowires has been investigated for several fuel cell reactions and observed enhanced activity. For example, Pt nanowire arrays have been used as the catalyst for methanol oxidation for better performance and long-term stability.[57] This is attributed to the high aspect ratio of the nanowires and the brush shapes of the Pt nanowires array electrode, which produces enough space between Pt nanowires for the efficient transport of reactant species. Moreover, these structures reveal long-term stability. Similar studies have also been carried out for Pd nanowires toward ethanol oxidation to reveal significantly higher activity compared to that of Pd films.[58] The electroactive area of these nanowires shows higher value compared to that of films mostly due to the well-defined and uniform arrays of high aspect ratio structures.

Besides these high aspect ratio nanostructures, several other non-spherical structures also reveal better electrocatalytic properties. For example, highly faceted structures such as tetrahexahedra (bounded by 24 high index facets) of platinum reveal significantly higher activity towards both ethanol and formic acid oxidation compared to that of Pt nanospheres.[41] This has been mainly attributed to the high density of stepped atoms on the surfaces of THH Pt nanocrystals (NCs), since these NCs are bounded by

high-index crystal facets having a higher density of atomic steps, edges, and kinks, which usually serve as active sites.

Interestingly, a comparison of the performance of nanocubes towards ORR with that of spherical particles reveals higher activity of the former.[37] This enhancement is mainly due to the dominant (100) facet in the Pt nanocubes assembly on the carbon paper. This is in agreement with the findings of earlier studies on ORR in acid electrolytes, where Pt(100) planes are more active than (111) planes.[50b,59]

Investigations of the electrocatalytic properties of different shaped platinum nanostructures (spherical clusters, clump-like crystal aggregations and elongated leaf-like flake clusters) for methanol oxidation and oxygen reduction suggest the following order: clump-like crystal aggregations > elongated leaf-like flake clusters > spherical clusters. This is mainly attributed to the higher electrochemically active specific surface area, for clump-like structure compared to that of elongated leaf-like and spherical clusters.[60]

1.5. Conclusions

High aspect ratio nanostructures constitute one of the most fascinating class of nanomaterials which has attracted immense recent interest. After understanding the significance of high aspect ratio nanostructures and also their different synthetic routes, it is important to ask how the properties unique to these nanostructures could be exploited for applications? This has been answered by considering their crucial role in the area of electrocatalytic reactions relevant for clean energy technologies like that of fuel cells. There are also a range of applications for high aspect ratio nanostructures outside electrocatalysis, including molecular electronics, ultrasensitive chemical and biosensors, micro/nano-electromechanical systems (MEMS/NEMS), optoelectronics, information storage, medical diagnostics etc. There are almost unlimited research opportunities in many of these applications of nanotechnology and the future potential seems to be surely bright.

However, there are a number of unsolved issues that remain to be addressed before these materials could reach industrial applications. For example, in

electrocatalysis, better performance of a catalyst requires the absence of surface passivating agents, or foreign species normally used during the synthesis, often via the soft route. More importantly, the nanostructures which are used as catalysts should have high uniformity in size and shape distribution. However, a majority of the cases have the presence of strong surface passivating agents (or foreign species added to trigger the growth) giving rise to difficulties of separations and impurity removal. Furthermore, there are several other barriers to cross during the research on nanomaterials including daunting tasks like addressing the environmental concern and societal impact of these materials since very little is known about these materials especially how they behave inside living organisms.

1.6. Objective of the Present Thesis

The aforementioned critical review of current research activities on high aspect ratio metallic nanostructures reveals the pivotal role of these structures in nano technology, different routes for their synthesis and their potential applications mainly in the field of electrocatalysis. Although, much attempts have been devoted for their synthesis, several lacunae still plague their wider utilization for various applications. For example, most of the synthesis of high aspect ratio nanostructures through reduction often employ shape controlling agents such as surfactants/capping molecules and in some cases these foreign inorganic species drastically hamper their potential benefits. Accordingly, selective (100%) synthesis of high aspect ratio nanostructures is a daunting challenge. A simple synthetic approach for these nanostructures with uniformity in both size and shape distribution and without destroying their surface properties is important for realizing their prospective applications in wider areas.

Since one of the important areas of interest of these metallic nanostructures is in electrocatalysis, it is necessary to understand the effect of morphology on their electrocatalytic performance. Although, many reports are available on the investigation of the electrocatalytic activity of several metallic nanostructures, most of them deal mainly

with spherical particles of various sizes. In contrast, investigation of the shape dependent electrocatalytic activity is sparse, and hence it is extremely important to investigate other non-spherical shapes. Hence, the objectives of the present investigation have been formulated to address some of these important challenges related to the synthesis, characterization and their applications especially in electrocatalysis. We have focused mainly on platinum, palladium and ruthenium oxide because of their outstanding role as multifunctional catalysts in many industrial applications, particularly for clean energy technology.

The specific objectives of the present work are:

- To fabricate templates of porous alumina membrane, both linear and hierarchically branched, having varying pore dimensions through an anodization route.
- To synthesize different shaped platinum mesostructures such as multipods, discs, and hexagons through a purely electrochemical route.
- To compare the electrocatalytic performance of different shaped platinum mesostructures for reactions relevant for fuel cell applications.
- To synthesize nanoneedles of RuO_2 through a suitable template-assisted electrodeposition route and to understand their temperature dependent electrical conductivity in comparison to bulk.
- To prepare Y-junction nanostructures of platinum through an electrodeposition route and to compare their electrocatalytic performance with respect to linear nanostructure of platinum.
- To synthesize Y-junction nanostructures of palladium through chemical vapour deposition route and to compare their electrocatalytic performance with respect to platinum Y-junction.
- Templated approach to synthesize Rh@Au core-shell nanorods.

1.7. Organization of the Present Thesis

In the light of the above objectives, the present thesis has been organized as seven chapters.

First chapter represents a general introduction on nanotechnology, which includes a classification of nanostructures based on dimensionality, followed by an elementary discussion of their exciting shape dependent physical and chemical properties. After this, a discussion on high aspect ratio nanomaterials, their impact on nanotechnology for diverse applications such as multifunctional catalysts, optical and electronic device fabrication and various methods for the preparation of these structures is given. Also, a few existing limitations with respect to the synthesis and processing of these high aspect ratio materials are also discussed, before concluding on the utility of these materials. In the end, specific objectives of the present study are discussed with special relevance on shape-dependent electrocatalytic activity.

Since, the whole thesis deals with the template- assisted synthesis of high aspect ratio nanostructures, the fabrication methodology of these templates is discussed in the **second chapter**. This chapter specifically comprises of the fabrication of hard templates such as porous alumina membrane (PAM) through a two-step anodization process. This also includes a discussion on plausible mechanism of pore formation during the anodization process depending on the detailed experimental conditions. Several techniques such as x-ray diffraction (XRD), x-ray photoelectron spectroscopy (XPS), fourier transform infrared spectroscopy (FTIR), scanning electron microscopy (SEM) and electrochemical impedance are used to characterize these templates. More importantly, contact angle studies are carried out to understand the interaction of various solvents with the alumina pores, which in turn facilitates to understand the role of solvent in filling the porous structure. In addition, the fabrication of Y-branched and multilevel Y- branched alumina nanochannels is also discussed in the end of this chapter.

In **third chapter**, we demonstrate a potential-dependent morphological evolution of platinum mesostructures in the form of multipods, discs and hexagons using linear PAM. In addition to these mesostructures, nanorods of platinum are also obtained as usually expected from linear PAM. These structures prepared potentiostatically at different potentials, reveal unique shape-dependent electrocatalytic activity towards the oxidation of formic acid, methanol and ethanol, three important reactions for micro-fuel cells. These structures are further characterized using SEM, XRD and XPS techniques.

Fourth chapter concerns with the formation of bundles of RuO_2 nanoneedles by a PAM-assisted electrodeposition from aqueous $RuCl_3$ solution under potentiostatic conditions at room temperature. In this chapter, we examine the specific capacitance of these nanoneedles in order to compare the performance with that of bulk commercial RuO_2. More importantly, electrical transport measurements reveal a transition from metallic to semiconducting behavior especially at low temperature, in contrast to that of bulk commercial RuO_2. These structures are further characterized using SEM, XRD, XPS, thermogravimetric analysis (TGA), and feed-back mode of scanning electrochemical microscope (SECM).

Subsequently, **fifth chapter** demonstrates the utility of Y-branched alumina nanochannels for the formation of platinum Y-junction nanostructures through electrodeposition. Further, these Y-junctions are characterized using different techniques such as SEM, transmission electron microscopy (TEM), selected area electron diffraction (SAED), field emission SEM (FESEM), XPS and XRD. These structures reveal enhanced electrocatalytic activity for the oxidation of formic acid, methanol and ethanol compared to that of commercial platinized carbon and Pt nanowires, which are of relevance to fuel cell technology. We also discuss the formation of Pd Y-junction nanostructures using the Y-branched alumina nanochannels through a chemical vapour deposition route followed by their characterization using all the above tools. In addition, we also compare their electrocatalytic performance in relation to that of Pt Y-junction nanostructures.

Our preliminary attempt to the formation of core-shell nanorods of Rh@Au is discussed in **chapter six**. These core-shell nanorods are synthesized using the functionalized PAM, followed by deposition of Rh inside the pore through a chemical vapour deposition route. Further, these core-shell structures are characterized using SEM, high resolution TEM (HRTEM), XRD and FTIR.

A summary of all the major conclusions of the present study with respect to preparation, characterization, properties and potential applications of these nanostructures is presented in **chapter seven**, clearly indicating the usefulness of template-assisted route in preparing shape-selective metallic nanostructures. One of the unique observations is the electrocatalytic activity of different morphology platinum structures. These nanostructures would be of interest for various applications because of their exquisite size and shape-dependent properties and also find technological relevance in diverse areas such as catalysis, photochemistry, chemical sensors and optoelectronics, mainly because of the absence of any surfactants/capping molecules on the surface of the nanostructures. This chapter also outlines some of the limitations of template-assisted route including poor yield, low mechanical stability and tendency to congregate upon release from the template. Since these disadvantages restrict the full potential of commercial applications of these structures, further work is desired to alleviate some of these problems. Despite these limitations, the results of present study are believed to be useful to understand several size and shape-dependent fundamental phenomena of these nanomaterials for fabricating nanoscale devices in future. Finally, the long term future prospects of these materials are outlined within the broad perspective of both fundamental and technological interest in different interdisciplinary areas like chemistry, physics, biology, and engineering.

1.8. References

1 (a) Alivisatos, A. P. *Science* **1996**, *271*, 933. (b) Dvoret, M. H.; Esteve, D.; Urbina, C. *Nature* **1992**, *360*, 547. (c) Ashoori, R.C. *Nature* **1996**, *379,* 413. (d) Reed, M. E.; Kirk, W. *Nanostructures and Mesoscopic Systems*; Academic: San Diego, 1992.

2 (a) Schmid, G. *Nanoparticles: From Theory to Application*; Wiley-VCH: Weinheim, Germany, 2004. (b) Kelsall, R.; Hamley, I.; Geoghegan, M. *Nanoscale Science and Technology*: John Wiley & Sons, Ltd.: England, 2005.

3 (a) Peng, X. G.; Manna, L.; Yang, W.; Wickham, J.; Scher, E.; Kadavanich, A.; Alivisatos, A. P. *Nature* **2000**, *404*, 59. (b) Lieber, C. M. *Solid State Commun*. **1998**, *107*, 607. (c) Smalley, R. E.; Yakobson, B. I. *Solid State Commun*. **1998**, *107*, 597. (d) Gudiksen, M. S.; Lauhon, L. J.; Wang, J. F.; Smith, D.C.; Lieber, C. M. *Nature* **2002**, *415*, 617. (d) Hu, M.; Chen, J.; Li, Z. –Y.; Au, L.; Hartland, G. V.; Li, X.; Marquez, M.; Xia, Y. *Chem. Soc. Rev*. **2006**, *35*, 1084. (e) Wong, E. W.; Sheehan, P. E.; Lieber, C. M. *Science* **1997**, *277*, 1971. (f) Kane, C. L.; Fisher, M. P. A. *Phys. Rev. Lett*. **1992**, *68*, 1220. (g) Watanabe, K.; Menzel, D.; Nilius, N. Freud, H. –J. *Chem. Rev*. **2006**, *106*, 4301. (h) Burda, C.; Chen, X.; Narayanan, R. El-Sayed, M. A. *Chem. Rev*. **2005**, *105*, 1025. (i) Morones, J. R.; Elechigeurra, J. L.; Camacho, A.; Holt, K.; Kouri, J. B.; Ramirez, J. T.; Yacaman, M. J. *Nanotechnology* **2005**, *16*, 2346. (j) Lee, H.; Habas, S. E.; Kweskin, S.; Butcher, D.; Somorjai, G. A.; Yang, P. D. *Angew. Chem. Int. Ed*. **2006**, *45*, 7824.

4 (a) Narayanan, R.; El-Sayed, M. A. *J. Am. Chem. Soc*. **2004**, *126*, 7194. (b) Morones, J. R.; Elechigeurra, J. L.; Camacho, A.; Holt, K.; Kouri, J. B.; Ramirez, J. T.; Yacaman, M. J. *Nanotechnology* **2005**, *16*, 2346. (c) Rosi, N. L.; Mirkin, C. A.; *Chem. Rev*. **2005**, *105*, 1547. (d) Rashid, M. H.; Mandal, T. K. *J. Phys. Chem. C* **2007**, *111*, 16750. (e) Lee, H.; Habas, S. E.; Kweskin, S.; Butcher, D.; Somorjai, G. A.; Yang, P. D. *Angew. Chem. Int. Ed*. **2006**, *45*, 7824. (f) Xu, R.; Wang, D.; Zhang, J.; Li, Y. *Chem. Asian J*. **2006**, *1*, 888. (g) Shipway, A. N.;

Katz, E.; Willner, I. *ChemPhysChem* **2000**, *1*, 18. (h) Walter, E. C.; Penner, R. M.; Liu, H.; Ng, K. H.; Zach, M. P.; Favier, F. *Surf. Interface Anal.* **2002**, *34*, 409. (i) Li, Y.; Lu, G.; Wu, X.; Shi, G. *J. Phys. Chem. B* **2006**, *110,* 24585. (j) Thomas, J. M. *Pure Appl. Chem*. **1988**, *60*, 1517. (k) Kolmakov, A.; Zhang, Y. X.; Cheng, G. S.; Moskovits, M. *Adv. Mater*. **2003**, *15*, 997. (l) Heins, E. A.; Siwy, Z. S.; Baker, L. A.; Martin, C. R. *Nano Lett*. **2005**, *5*, 1824. (m) Matsumiya, M.; Shin, W.; Izu, N.; Murayama, N. *Sens. Actuators B* **2003**, *93*, 309. (n) Stewart, M. E.; Anderton, C. R.; Thompson, L. B.; Maria, J.; Gray, S. K.; Rogers, J. A.; Nuzzo, R. G. *Chem. Rev*. **2008**, *108*, 494. (o) Miyazaki, A.; Asakawa, T.; Nakano, Y.; Balint, I. *Chem. Commun*. **2005**, 3730. (p) Oku, T.; Suganuma, K. *Chem. Commun*. **1999**, 2355. (q) Liz-Marzan, L. M.; Mulvaney, P. *New J. Chem*. **1998**, *22*, 1285. (r) Pileni, M. P. *New J. Chem*. **1998**, *22*, 693. (s) Kamat, P. V. *J. Phys. Chem. B* **2002**, *106*, 7729. (t) Brugger, P. A.; Cuendet, P.; Gratzel, M. *J. Am. Chem. Soc*. **1981**, *103*, 2923.

5 (a) Luryi, S.; Xu, J.; Zaslavsky, A. *Future Trends in Microelectronics: The Nano Millennium*; Wiley-Interscience: New York, 2002. (b) Special issue of *Nature* **2000**, *406*, 1021.

6 (a) Krans, J. M.; van Rutenbeek, J. M.; Fisun, V. V.; Yanson, I. K.; de Jongh, L. J. *Nature* **1995**, *375*, 767. (b) Al'tshuler, B. L.; Lee, P. A. Phys. Today **1988**, 36. (c) Likharev, K. K.; Claeson, T. *Sci. Am.* 1992, 80.(d) Likharev, K. K. *IBM J. Res. Dev*. **1988**, *32*, 144. (e) Markovich, G.; Collier, C. P.; Henrichs, S. E.; Remacle, F.; Levine, R. D.; Heath, J. R. *Acc. Chem. Res*. **1999**, *32*, 415.

7 (a) Elliot, S. R. *The Physics and Chemistry of solids*; Wiley-VCH, 2003. (b) Martienssen, W.; Warlimont, H. *Springer Handbook of Condensed Matter and Materials Data*, 2005.

8 Poole, C. P. Jr.; Owens, F. J. *Introduction to Nanotechnology*; John-Wiley and Sons, Inc.: New Jersey, 2003.

9 (a) Das-Sarma, S.; Pinczuk, A. Eds.; Wiley: New York, **1997**. (b) Stormer, H. L. *Solid State Commun*. **1998**, *107*, 617. (c) Grabert, H.; Devoret, M. H., Single Electron Tunneling, Plenum: New York, **1991**. (d) Dvoret, M. H.; Esteve, D.; Urbina, C. *Nature* **1992**, *360*, 547. (e) Klein, D. L.; Roth, R.; Lim, A. K. L.; Alivisatos, A. P.; McEuen, P. L. *Nature* **1997**, *389*, 699.

10 (a) Wang, Z. L. Adv. Mater. **2000**, *12*, 1295. (b) Hu, J.; Odom, T. W.; Lieber, C. M. *Acc. Chem. Res.* **1999**, *32*, 435. (c) A Special issue in *MRS Bull*. **1999**, *24*, 20.

11 (a) Voit, J. *Rep. Prog. Phys*. **1994**, *57*, 977. (b) Kane, C.; Balents, L.; Fisher, M. P. A. *Phys. Rev. Lett*. **1997**, *79*, 5086.

12 (a) Bockrath, M.; Cobden, D. H.; McEuen, P. L.; Chopra, N. G.; Zettl, A.; Thess, A.; Smalley, R. E. *Science* **1997**, *275*, 1922. (b) Tans, S. J.; Devoret, M. H.; Dai, H.; Thess, A.; Smalley, R. E.; Geerligs, L. J.; Dekker, C. *Nature* **1997**, *386*, 474. (b) Tans, S. J.; Verschueren, A. R. M.; Dekker, C. *Nature* **1998**, *393*, 49. (c) Yang, P.; Lieber, C. M. *Science* **1996**, *273*, 1836. (d) Yang, P.; Lieber, C. M. *Appl. Phys. Lett*. **1997**, *70*, 3158. (e) Yang, P.; Lieber, C. M. *J. Mater. Res*. **1997**, *12*, 2981. (e) Dai, H.; Hafner, J. H.; Rinzler, A. G.; Colbert, D. T.; Smalley, R. E. *Nature* **1996**, *384*, 147. (f) Wong, S. S.; Harper, J. D.; Lansbury, P. T.; Lieber, C. M. *J. Am. Chem. Soc.* **1998**, *120*, 603.

13 (a) Schmid, G. *Clusters and Colloids: From theory to applications*; Wiley-VCH: New York, 1994. (b) Mirkin, C. A.; Rogers, J. A. *MRS Bull*. **2001**, *26*, 506. (c) Odom, T. W.; Nehl, C. L. *ACS Nano* **2008**, *2*, 612. (d) Hawker, C. J.; Russel, T. P. *MRS Bull*. **2005**, *30*, 952. (e) Li, M.; Coenjarts, C. A.; Ober, C. K. *Adv. Polym. Sci*. **2005**, *190*, 183.

14 (a) Herman, M. A.; Sitter, H. *Molecular Beam Epitaxy-Fundamentals and Current Status*; Springer-Verlag: Berlin, 1989. (b) Parker, E. H. C. *The Technology and Physics of Molecular Beam Epitaxy*; Plenum Press: New York, 1985. (c) Ritala, M.; Leskela, M. *Nanotechnology* **1999**, *10*, 19.

15 (a) Berchmans, S.; Thomas, P. J.; Rao, C. N. R. *J. Phys. Chem. B* **2002**, *106*, 4647. (b) Lee, D.; Donkers, R. L.; DeSimone, J. M.; Murray, R. W. *J. Am. Chem. Soc*. **2003**, *125*, 1182. (c) Pillai, Z. S.; Kamat, P. V. *J. Phys. Chem. B* **2004,** *108,* 945. (d) Chaki, N. K. ; Singh, P. ; Dharmadhikari, C. V. ; Pillai, V. K. *Langmuir* **2004,** *20*, 10208. (e) Peng, X. *Adv. Mater.* **2003**, *15*, 459. (f) Schmid, G. *Nanoparticles: From Theory to Application*; Wiley-VCH: 2004. (g) G. Cao, *Nanostructures and Nanomaterials: Synthesis, Properties and Applications;* Imperial College London, 2004. (h) Peng, S.; Wang, C.; Xie, J.; Sun, S. *J. Am. Chem. Soc*. **2006**, *128*, 10676. (i) Ganesan, M.; Freemantle, R. G.; Obare, S. O. *Chem. Mater*. **2007**, *19*, 3464. (j) Kim, M. –K.; Jeon, Y. –M.; Jeon, W. S.; Kim, H. –J.; Hong, S. G.; Park, C. G.; Kim, K. *Chem. Commun*. **2001**, 667. (k) Brust, M.; Walker, M.; Bethell, D.; Schiffrin, D. J.; Whyman, R. *J. Chem. Soc., Chem. Commun*. **1994**, 801. (l) Egusa, S.; Redmond, P. L.; Scherer, N. F. *J. Phys. Chem. C* **2007**, *111*, 17993.

16 (a) Cerrina, F.; Marrian, C. *MRS Bull*. **1996**, *21*, 56. (b) Gibson, J. M. Phys. Today 1997, October, 56. (c) Matsui, S.; Ochiai, Y. *Nanotechnology* **1996**, *7*, 247. (d) Hong, S. H.; Zhu, J.; Mirkin, C. A. *Science* **1999**, *286*, 523. (e) Dagata, J. A. *Science* **1995**, *270*, 1625. (f) Levenson, M. D. *Solid State Technol*. **1995**, *38*, 81. (g) Dunn, P. N. *Solid State Technol*. **1994**, *37*, 49. (h) Menke, E. J.; Thompson, M. A.; Xiang, C.; Yang, L. C.; Penner, R. M. *Nature Mater*. **2006**, *5*, 914.

17 (a) Gou, L.; Murphy, C. J. *Chem. Mater*. **2005**, *17*, 3668. (b) Wiley, B.; Sun, Y.; Xia, Y. *Acc. Chem. Res*. **2007**, *40*, 1067. (c) Choi, J.; Sauer, G.; Nielsch, K.; Wehrspohn, R. B.; Gosele, U. *Chem. Mater*. **2003**, *15*, 776. (d) Xia, Y.; Rogers, J. A.; Paul, K. E.; Whitesides, G. M. *Chem. Rev*. **1999**, *99*, 1823. (e) Yu, Y. –Y.; Chang, S. –S.; Lee, C. –L.; Wang, C. R. C. *J. Phys. Chem. B* **1997**, *101*, 6661.

18 (a) A. Rouxoux, J, Schulz and H. Patin, *Chem. Rev*. **2002**, *102*, 3757. (b) K. R. Williams and G. T. Burstein, *Catal. Today* **1997**, *38*, 401. (c) Xu, C.; Wang, H.; Shen, P. K.; Jiang, S. P. *Adv. Mater*. **2007**, *19*, 4256.

19 (a) Narayanan, R.; El-Sayed, M. A. *Nano Lett*. **2004**, *4*, 1343. (b) Falicov, L. M.; Somorjai, *Proc. Natl. Acad. Sci. USA* **1985**, *82*, 2207. (c) Wieckowski, A.; Savinova, E. R.; Vayenas, C. G. *Catalysis and Electrocatalysis at Nanoparticle Surfaces*; Marcel Dekker, Inc.: New York, 2003. (d) Rolison, D. R. *Science* **2003**, *299*, 1698. (e) M.S. Chen and D.W. Goodman, *Catalysis Today* **2006**, *111*, 22.

20 Leontidis, E.; Kleitou, K.; Kyprianidou, T.; Bekiari, V.; Lianos, P. *Langmuir* **2002**, *18*, 3659.

21 (a) Murphy, C.; Sau, T.; Gole, A.; Orendorff, C. *Mater. Res. Bull*. **2005**, *30*, 349. (b) Sun, Y.; Gates, B.; Mayers, B.; Xia, Y. *Nano Lett*. **2002**, *2*, 165. (c) Sun, Y.; Yin, Y.; Mayers, B. T.; Herricks, T.; Xia, Y. *Chem. Mater*. **2002**, *14*, 4736.

22 Chen, J.; Herricks, T.; Geissler, M.; Xia, Y. *J. Am. Chem. Soc*. **2004**, *126*, 10854.

23 Elechiguerra, J. L.; Reyes-Gasga, J.; Yacaman, M. J. *J. Mater. Chem*. **2006**, *16*, 3906.

24 (a) Hulteen, J. C.; Martin, C. R. *J. Mater. Chem*. **1997**, *7*, 1075. (b) Kline, T. R.; Tian, M.; Wang, J.; Sen, A.; Chan, M. W. H.; Mallouk, T. E. Inorg. Chem. **2006**, *45*, 7555. (c) Luo, Y.; Lee, S. K.; Hofmeister, H.; Steinhart, M.; Gosele, U. *Nano Lett*. **2004**, *4*, 143. (d) Sehayek, T.; Lahav, M.; Popovitz-Biro, R.; Vaskevich, A.; Rubinstein, I. *Chem. Mater*. **2005,** *17*, 3743. (e) Jana, N. R.; Gearheart, L.; Murphy, C. J. *J. Phys. Chem. B* **2001**, *105*, 4065. (f) Yu, Y. Y.; Chang, S. S.; Lee, C. L.; Chris Wang, C. R. *J. Phys. Chem. B* **1997**, *101*, 6661. (g) Zhang, D.; Qi, L.; Ma, J.; Cheng, H. *Chem. Mater.* **2001**, *13*, 2753. (h) Nikoobakht, B.; El-Sayed, M. A. *Chem. Mater.* **2003**, *15*, 1957.

25 (a) Song, Y.; Garcia, R. M.; Dorin, R. M. Wang, H. Qiu, Y.; Coker, E. N.; Steen, W. A.; Miller, J. E.; Shelnutt, J. A. *Nano Lett*. **2007**, *7*, 3650. (b) Sakamoto, Y.; Fukuoka, A.; Higuchi, T.; Shimomura, N.; Inagaki, S.; Ichikawa, M. *J. Phys. Chem. B* **2004,** *108,* 853. (c) Liu, Z.; Sakamoto, Y.; Ohsuna, T.; Hiraga, K.; Terasaki, O.; Ko, C. H.; Shin, H. J.; Ryoo, R. *Angew. Chem. Int. Ed*. **2000**, *39*, 3107. (d) Tie-Ren, G.; Zi-Yu, C.; Yong, P.; Fa-Shen, L. *Chin. Phys*. **2002**, *11*, 1307. (e) Piao, Y.; Lim, H.; Chang, J. Y.; Lee, W. –Y.; Kim, H. *Electrochimica*

Acta **2005**, *50*, 2997. (f) Govindaraj, A.; Satishkumar, B. C.; Manashi, Nath.; Rao, C. N. R. *Chem. Mater*. **2000**, *12*, 202.

26 Xia, Y.; Yang, P.; Sun, Y.; Wu, Y.; Mayers, B.; Gates, B.; Yin, Y.; Kim, F.; Yan, H. *Adv. Mater.* **2003**, *15*, 353.

27 Chen, J.; Herricks, T.; Geissler, M.; Xia, Y. *J. Am. Chem. Soc*. **2004**, *126*, 10854.

28 Rioux, R. M.; Song, H.; Grass, M.; Habas, S.; Niesz, K.; Hoefelmeyer, J. D.; Yang, P.; Somorjai, G. A. *Top. Catal.* **2006**, *39*, 167.

29 Lee, H.; Habas, S. E.; Kweskin, S.; Butcher, D.; Somorjai, G. A.; Yang, P. *Angew. Chem. Int. Ed.* **2006**, *45*, 7824.

30 Fu, X.; Wang, Y.; Wu, N.; Gui, L.; Tang, Y. *J. Mater. Chem*. **2003**, *13*, 1192.

31 Gurlu, O.; Adam, O. A. O.; Zandvliet, H. J. W.; Poelsema, B. *Appl. Phys. Lett*. **2003**, *83*, 4610.

32 (a) Sun, Y.; Mayers, B.; Xia, Y. *Adv. Mater*. **2003**, *15*, 641. (b) Mayers, B.; Jiang, X.; Sunderland, D.; Cattle, B.; Xia, Y. *J. Am. Chem. Soc*. **2003**, *125*, 13364. (c) Luo, Y.; Lee, S. K.; Hofmeister, H.; Steinhart, M.; Gosele, U. *Nano Lett*. **2004**, *4*, 143. (d) Zhao, Y.; Guo, Y. –G.; Zhang, Y. –L.; Jiao, K. *Phys. Chem. Chem. Phys*. **2004**, *6*, 1766. (e) Kijima, T.; Yoshimura, T.; Uota, M.; Ikeda, T.; Fujikawa, D.; Mouri, S.; Uoyama, S. *Angew. Chem. Int. Ed*. **2004**, *43*, 228.

33 (a) Ahmadi, T. S.; Wang, Z. L.; Henglein, A.; El-Sayed, M. A. *Chem. Mater*. **1996**, *8*, 1161. (b) Yu, Y. –T.; Wang, J.; Zhang, J. –H.; Yang, H. –J.; Xu, B. –Q.; Sun, J. –C. *J. Phys. Chem. C* **2007**, *111*, 18563. (c) Zhao, S. –Y.; Chen, S. –H.; Wang, S. –Y.; Li, D. –G.; Ma, H. –Y. *Langmuir* **2002**, *18*, 3315.

34 Song, H.; Kim, F.; Connor, S.; Somorjai, G. A.; Yang, P. *J. Phys. Chem. B* **2005**, *109*, 188.

35 (a) Yamada, M.; Kon, S.; Miyake, M. *Chem. Lett*. **2005**, *34*, 1050.

36 Lee, H.; Habas, S. E.; Kweskin, S.; Butcher, D.; Somorjai, G. A.; Yang, P. *Angew. Chem. Int. Ed*. **2006**, *45*, 7824.

37 Wang, C.; Daimon, H.; Lee, Y.; Kim, J.; Sun, S. *J. Am. Chem. Soc*. **2007**, *129*, 6974.

38 Ren, J.; Tilley, R. D. *J. Am. Chem. Soc*. **2007**, *129*, 3287.

39 (a) Herricks, T.; Chen, J. Y.; Xia, Y. *Nano Lett*. **2004**, *4*, 2367. (b) Teng, X.; Yang, H. *Nano Lett*. **2005**, *5*, 885.

40 Maksimuk, S.; Teng, X.; Yang, H. *Phys. Chem. Chem. Phys*. **2006**, *8*, 4660.

41 Tian, N.; Zhou, Z. –Y.; Sun, S. –G.; Ding, Y.; Wang, Z. L. *Science* **2007**, *316*, 732.

42 Kawasaki, H.; Yonezawa, T.; Watanabe, T.; Arakawa, R. *J. Phys. Chem. C* **2007**, *111*, 16278.

43 Sun, S.; Yang, D.; Villers, D.; Zhang, G.; Sacher, E.; Dodelet, J. –P. *Adv. Mater*. **2008**, *20*, 571.

44 (a) Xu, C.; Wang, H.; Shen, P. K.; Jiang, S. P. *Adv. Mater*. **2007**, *19*, 4256. (b) Kartopu, G.; Habouti, S.; Es-Souni, M. *Mater. Chem. Phys*. **2008**, *107*, 226.

45 Ji, X.; Banks, C. E.; Xi, W.; Wilkins, S. J.; Compton, R. G. *J. Phys. Chem. B* **2006**, *110*, 22306.

46 Xiong,Y.; Cai, H.; Wiley, B. J.; Wang, J.; Kim, M. J.; Xia, Y. *J. Am. Chem. Soc*. **2007**, *129*, 3665.

47 Teng, X.; Han, W. –Q.; Ku, W.; Hucker, M. *Angew. Chem. Int. Ed*. **2008**, *47*, 2055.

48 Steinhart, M.; Jia, Z.; Schaper, A. K.; Wehrspohn, R. B.; Gosele, U.; Wendorff, J. H. *Adv. Mater*. **2003**, *15*, 706.

49 Yu, S.; Welp, U.; Hua, L. Z.; Rydh, A.; Kwok, W. K.; Wang, H. H. *Chem. Mater.* **2005,** *17*, 3445.

50 (a) Haruta, M.; Tsubota, S.; Kobayashi, T.; Kageyama, H.; Genet, M. J.; Delmon, B. *J. Catal*. **1993**, *144*, 175. (b) Kinoshita, K. *J. Electrochem. Soc*. **1990**, *137*, 845. (c) Bockris, J. O'M.; Conway, B. E.; White, R. E. Modern Aspects of Electrochemistry; Plenum Press: New York, 1982. (d) Murkerjee, S. *J. Appl. Electrochem*. **1990**, *20*, 537. (e) Tsunoyama, H.; Sakurai, H.; Tsukuda, T. *Chem.*

Phys. Lett. **2006**, *429*, 528. (f) Overbury, S. H.; Schwartz, V.; Mullins, D. R.; Yan, W.; Dai, S. *J. Catal*. **2006**, *241*, 56. (g) Wilson, O. M.; Knecht, M. R.; Garcia-Martinez, J. C.; Crooks, R. M. *J. Am. Chem. Soc*. **2006**, *128*, 4510. (h) Maillard, F.; Eikerling, M.; Cherstiouk, O. V.; Schreier, S.; Savinova, E.; Stimming, U. *Faraday Discuss.* **2004,** *125***,** 357. (i) Wilson, O. M.; Knecht, M. R.; Garcia-Martinez, J. C.; Crooks, R. M. *J. Am. Chem. Soc.* **2006**, *128*, 4510. (j) Hernandez, C. A.; Gimeno, Y.; Diaz, P.; Vazquez, L.; Gonzalez, S.; Salvarezza, R. C.; Arvia, A. J. *J. Phys. Chem. B* **2004**, *108*, 10785. (k) Ge, J.; Xing, W.; Xue, X.; Liu, C.; Lu, T.; Liao, J. *J. Phys. Chem. C* **2007**, *111*, 17305. (l) Tsuji, Y.; Fujihara, T. *Inorg. Chem*. **2007**, *46*, 1895.

51 Meier, J.; Schiotz, J.; Liu, P.; Norskov, J. K.; Stimming, U. *Chem. Phys. Lett*. **2004**, *390*, 440.

52 (a) Bockris, J. O' M. *J. Serb. Chem. Soc*. **2005**, *70*, 475. (b) Pletcher, D. *J. Appl. Electrochem*. **1984**, *14*, 403.

53 (a) Rotello, V. M. *Nanoparticles: Building Blocks for Nanotechnology*; Springer Science and Business Media, Inc.: New York, 2004. (b) Heiz, U.; Landman, U. *Nanocatalysis*; Springer Science and Business Media, Inc.: New York, 2007.

54 (a) Park, S.; Xie, Y.; Weaver, M. J. *Langmuir* **2002**, *18*, 5792. (b) Chen, M. S.; Goodman, D. W. *Catalysis Today* **2006**, *111*, 22. (c) Han, B. C.; Miranda, C. R.; Ceder, G. *Phys. Rev. B* **2008**, *77*, 075410. (d) Hernandez, J.; Solla-Gullon, J.; Herrero, E. *J. Electroanal. Chem*. **2004**, *574*, 185. (e) Vidal-Iglesias, F. V.; Solla-Gullon, J.; Rodriguez, P.; Herrero, E.; Montiel, V.; Feliu, J. M.; Aldaz, A. *Electrochem. Commun*. **2004**, *6*, 1080. (f) Ge, J.; Xing, W.; Xue, X.; Liu, C.; Lu, T.; Liao, J. *J. Phys. Chem. C* **2007**, *111*, 17305. (g) Liang, H. –P.; Zhang, H. –M.; Hu, J. –S.; Guo, Y. –G.; Wan, L. –J.; Bai, C. –L. *Angew. Chem. Int. Ed*. **2004**, *43*, 1540. (h) Chen, W.; Kim, J.; Sun, S.; Chen, S. *Langmuir* **2007**, *23*, 11303.

55 (a) Somorjai, G. A. *Introduction to Surface Chemistry and Catalysis*; John-Wiley and Sons, Inc.: New York, 1999. (b) Li, Y.; Shi, G. *J. Phys. Chem. B* **2005**, *109,* 23787. (c) Jena, B. K.; Raj, C. R. *J. Phys. Chem. C* **2007**, *111,* 15146.

56 Kinge, S.; Urgeghe, C.; Battisti, A. D.; Bonnemann, H. *Appl. Organometal. Chem.* **2008**, *22*, 49.

57 Zhao, G. –Y.; Xu, C. –L.; Guo, D. –J.; Li, H.; Li, H. –L. *Appl. Surf. Sci.* **2007**, *253*, 3242.

58 Xu, C.; Wang, H.; Shen, P. K.; Jiang, S. P. *Adv. Mater*. **2007**, *19*, 4256.

59 Markovic, N. M.; Gasteiger, H. A.; Ross, P. N., Jr. *J. Phys. Chem.* **1995**, *99*, 3411.

60 Ye, F.; Chen, L.; Li, J.; Li, J. Wang, X. *Electrochem. Commun*. **2008**, *10*, 476.

CHAPTER 2

Porous Alumina Membrane Templates: Fabrication, Growth Mechanism and Characterization

This chapter discusses the fabrication and growth mechanism of porous alumina membrane (PAM) templates along with a brief description of general templated synthesis of nanomaterials. A generic approach to fabricate alumina templates with linear nanopore arrays through a two step anodization process is demonstrated, highlighting the relevance of all key parameters. As pore diameter is linearly proportional to the anodization voltage for a given area, it is easy to fabricate ordered linear nanopore arrays by merely tuning the anodization voltage. More importantly, anodization has been extended to the rational design of hierarchically branched templates such as Y-branched and two generation Y-branched PAM, where uniform Y-junctions are formed with regard to the position of the junction and the diameter of the arms. These templates with nanoporous arrays in linear as well as in branched forms have far-reaching implications in the design of interconnected and controllably branched nanoscale systems for next generation electronic devices.

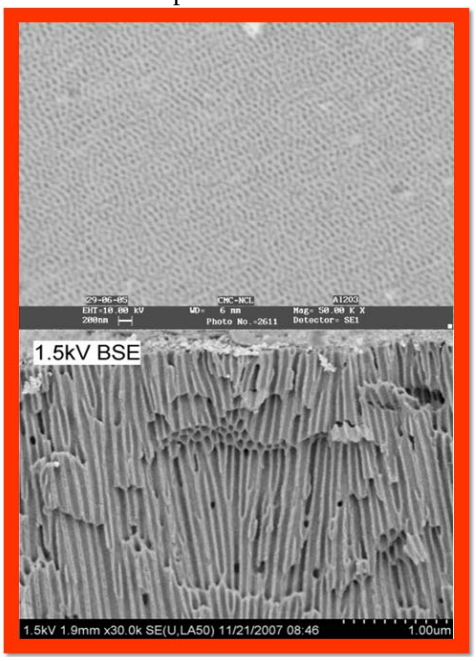

2.1. Introduction

"Templating" essentially involves the replication of one structure into another under structural inversion. For example, the replication of molecular aggregates such as micelles is used as templates for the fabrication of mesoporous silica. Thus a template, in a general sense could be defined as a *structure-directing agent*. Templating is a versatile technique for the formation of nanostructured materials with structural units ranging from nanometers to micrometers.[1] More importantly, size and shape of the resulting structures can be easily tuned by choosing the appropriate template structures/dimensions. The key for a successful template-assisted synthesis is to select a template which ensures the formation of a desired nanostructure that could be easily removed without any damage.

Templates that could be used for solid state synthesis include soft, hard, and complex templates. Soft templates, which can be subsequently removed by heat treatment, are normally surfactant based micelles, reverse micelles and polymers.[2] Additionally, vesicles, ionic liquids, self-assembled colloidal crystals, foams, and air bubbles can also be considered as soft templates. An important advantage of the soft-template method is that it is scalable to bulk quantities of nanostructures, especially when the reduction is carried out in solution. On the other hand, hard template includes inorganic or polymeric materials, typically in the form of porous membrane. The inorganic hard templates (such as alumina membrane, mesoporous silica, ion-track etched mica, and macroporous silicon) can be leached away by using acid or alkali solution whereas, polymeric templates (such as ion track etched polycarbonate and polyester membranes) could be removed by using organic solvents. In the hard-template method, this porous membrane physically constrains the crystal growth.[1(a-p)] The main advantage of using a hard template over a soft one is that it allows unidirectional growth of nanostructures yielding dense arrays of uniform structures aligned on substrates, which are beneficial for their application in device fabrication. Moreover, they cover length scales from a few nanometers over micro to the macro scale. However, since these hard

templates are usually a thin membrane, it is difficult to scale-up to macroscopic quantities of nanowires, although efforts in that direction are underway.

Complex templates, which combine the soft and the hard templates, or two hard templates, or two soft templates of different length scales, have been used to prepare hierarchically bi-modal and tri-modal porous structures with the primary objective of minimizing diffusional resistance and improving the accessibility of various surfaces. For example, bimodal mesoporous–macroporous materials with interconnected pore channels can be prepared by using a surfactant template in combination with a colloidal-crystal template.[2d,3]

Among these templates, hard templates like porous alumina membranes have many favourable characteristics including regular pore distribution, high pore density (10^{11} pores/cm^2) and high aspect ratio. These porous membranes are generally fabricated through a controlled anodization of highly pure aluminium in acidic medium.[4] Interestingly, these cylindrical pores of uniform diameter are arranged in a hexagonal array having little or no tilt with respect to the surface normal, resulting in an isolated and non-connected porous structure. The pore diameter could be tuned from ~ 5 nm to > 100 nm by varying the composition and concentration of the acidic electrolyte, temperature and the voltage of anodization. Also, the thickness of the porous layer is dependent on time, with longer anodization resulting in thicker templates (ranges up to several hundred micrometers). In addition, high chemical, thermal and mechanical stability of these templates allow convenient post-deposition processing, which is useful to release the nanostructures without any extensive damage.

Besides these cylindrical/linear nanopore arrays, Y-branched and hierarchically branched arrays are also obtained through mere tuning of the anodization conditions.[5] The creation of these branched nanopore arrays provides a powerful way to produce interconnected nanostructures. For example, linear alumina templates fabricated through anodization could be extended for the formation of branched arrays. The rationale for creating Y-branched pores in PAM templates includes the reduction of anodizing voltage

by a factor of $1/\sqrt{2}$, which initiates the transformation of a linear pore during the anodization into a symmetrically divided Y.[5c] Based on this rationale, it is possible to generate not just a single Y junction but multiple Y-branching by sequentially reducing the anodization voltage many times, each by a factor of $1/\sqrt{2}$. In general, the anodization voltage to generate 'n' number of pores from a single stem pore could be expressed as $(1/\sqrt{n})\ V_A$, where V_A is the anodizing voltage, and 'n' is the number of branched pores from that stem.

The structure of alumina membrane is described as close-packed array of columnar hexagonal cells which nearly appear like a honeycomb.[4a,6] However, in real situation, the formation of defect free ordered pore arrays is often limited to a domain of few μm only. This is attributed to the non-idealities in the Al sheet such as defects and grain boundaries, where electric field is locally modified which impacts the pore growth direction and balance between neighbouring pores. Therefore the formation of regularly spaced vertical pores is limited to within the boundary of single Al grains. As a result, Masuda et al. have advocated a two-step anodization route and molding process to obtain long-range ordered channel array architecture on the order of millimeter.[4c,d] In the latter case, shallow ordered textures (array of concaves) is made on the Al surface prior to the anodization step by a molding process and as a result, growth of an almost defect free channel array could be achieved throughout the textured area. In a two-step anodization route (which is cost effective compared to that of the previous one), the porous alumina obtained after the first anodization step is removed and subsequently a second anodization is performed. The removal of initial porous film leaves behind an ordered concave textured structure, which facilitates the growth of ordered pore arrays during the second step.

Apart from Al, anodization of Si, Ti and W also forms nanoporous films, and efforts to control their pore dimension similar to that of porous alumina are known, to be successful.[7]

2.2. Growth Mechanism of Al_2O_3 Pore Arrays

The self-organizing nature of the porous alumina is explained by the dynamic nature of the native aluminium oxide.[6b,c,8] Aluminium is a highly reactive element and rapidly forms a thin native oxide upon the exposure to oxygen. When an electric field is applied during the anodization process, two opposing processes occur to rapidly establish a dynamic equilibrium. The first is the electrical breakdown of the oxide layer which is followed by an electrochemically mediated dissolution of the aluminium oxide. Breakdown occurs when an electric field exceeding the dielectric strength of the oxide is applied across the film. When this occurs, Al^{3+} ions under the mask will be injected into the aluminium oxide/electrolyte interface and the O^{2-}/OH^- ions from the electrolyte move to the Al_2O_3/Al interface under the electric field and the aluminium under the broken down aluminium oxide thin film will continue to be anodized to grow a thicker at the Al_2O_3/Al interface. Ultimately, the aluminium oxide layer becomes sufficiently thick and the breakdown–growth cycle stops. A barrier type aluminium oxide is thus formed.[8]

Even though, this barrier oxide layer is stable, they are eroded in the presence of acidic electrolytes used for anodization. In particular, these oxides are isotropically etched by electrolytes such as sulphuric acid, oxalic acid, and phosphoric acid. Electrochemical etching is a field dependent process and also anisotropic in nature, dominating in regions where the field strength is maximum. As the oxide is eroded at the electrolyte/Al_2O_3 interface, it gradually thins to a point wherein the field across the oxide is again sufficient to cause breakdown resulting in additional oxide growth at the Al_2O_3/Al interface. The competition between dissolution of oxide layer at oxide/electrolyte interface and the oxide growth at metal/oxide interface sets up a dynamic equilibrium which is responsible for the porous oxide growth. (A schematic representation of the ion migration at the pore bottom under the applied electric field is shown in figure 2.1.). Here, the loss of Al^{3+} ions to the electrolyte has been found to be an essential prerequisite for the porous oxide growth.[8]

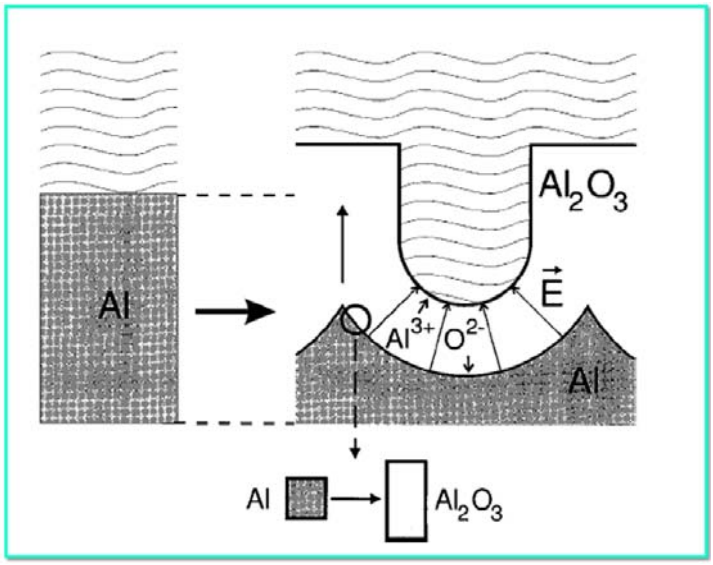

Figure 2.1. A schematic representation of ion migration responsible for the formation of porous structure under applied electric field; pores grow perpendicular to the surface with the migration of oxygen containing ions (O^{2-}/OH^-) from the electrolyte through the oxide layer at the pore bottom and Al^{3+} ions which simultaneously drift through the oxide layer are ejected into the solution at the oxide/electrolyte interface; on the left unoxidized Al metal surface is depicted (wavy pattern denotes the electrolyte). [Adopted from ref. 9a]

The atomic density of aluminium in Al_2O_3 is lower than that of metallic aluminium by a factor of two. As a result, volume expansion of Al_2O_3 will be nearly twice than that of the Al metal developing mechanical stress during oxide formation. This stress is the possible origin of repulsive forces that appear between neighbouring pores.[9] Since the oxidation takes place at the entire pore bottom simultaneously, the material can only expand in the vertical direction, so that the existing pore walls are pushed upwards, ultimately resulting into a parallel and uniformly ordered porous array having a hexagonal arrangement.

2.3. Effect of Anodization Parameters on the Pore Dimension

Since a minor variation in one of the several key variables like anodization voltage, concentration and type of the electrolyte, and temperature can adversely affect the reproducibility of the critical dimensions of the alumina template, it is very important

to systematically investigate the effect of these parameters on porosity. The influence of some of the major parameters is discussed below:

2.3.1. Anodization Voltage (V_A)

The pore diameter (D_p) and inter-pore distance (D_{int}) are linearly proportional to the anodization voltage, in accordance with the theory established by O'Sullivan et al. and the proportionality constant (ζ) is 2.5 nmV^{-1}.[4a,g,6c,8a,10] (A schematic cross-section of the porous alumina is shown in figure 2.2, where the pore diameter, inter-pore distance and barrier layer thickness are clearly seen) This is ascribed to the high current density (diffusion limited current) and strong chemical dissolution enhanced by the electric field.

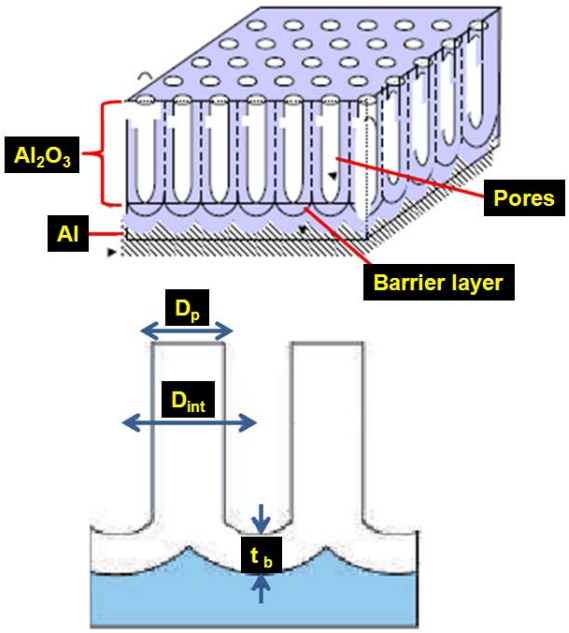

Figure 2.2. Schematic representation of the cross-section of PAM with the barrier layer; D_p = pore diameter, D_{int} = inter-pore distance, t_b = thickness of the barrier layer; hexagonal ordering of cylindrical pore arrays with barrier layer is clearly seen.

2.3.2. Type and Concentration of the Electrolyte

The type and the concentration of the electrolyte for a given anodization potential has to be selected properly to obtain a stable porous structure.[4h,10d,9a,11] The electrolytes

typically used are sulphuric acid, oxalic acid, and phosphoric acid respectively. The optimal voltage depends on the electrolyte used for the anodization (e.g., 25 V for sulphuric acid, 40 V for oxalic acid, and 195 V for phosphoric acid for a given electrode with same inter-electrode distance) perhaps due to the conductivity and pH difference. For example, if aluminium is anodized in sulphuric acid at a high potential, breakdown of the oxide layer often takes place. In addition, the pore diameter is affected strongly by dissolution velocity of alumina which in turn is determined by the pH of the electrolyte. The lower the pH, the lower is the potential threshold for field-enhanced dissolution at the pore tip leading to a smaller size of the pores. Therefore, large pore diameters are formed by using phosphoric acid while smaller pores are obtained by sulphuric acid.[10d]

Change in the electrolyte concentration also has a significant effect on pore diameter. Upon increasing the electrolyte concentration, pore diameter enlarges linearly, although the inter-pore distance does not vary under a given anodization voltage. For example, Du et al. have observed an increase in the pore diameter from 50 nm to 80 nm respectively when the concentration of oxalic acid is increased from 0.3 to 0.5 M at an anodization voltage of 50 V. However, the inter-pore distance remains at 120 nm.

2.3.3. Temperature

During the anodization, temperature should be kept minimum (less than room temperature) to get uniform features and also to prevent complex species from being dissolved in certain electrolytes. A second reason to keep the temperature as low as possible is to avoid a local heating at the bottom of the pores during the course of anodization (specially, in the case of a high potential), to prevent inhomogeneous electric field distribution at the bottom. In fact, cracks and bursts of the oxide film are generated if porous alumina is formed without adequate temperature control.[1j,10d] However, if the temperature is too low (well below 0^{o}C), the growth rate of porous alumina will not be sufficient to facilitate a porous film formation.

Hence by accurately controlling temperature, anodization voltage (current density), type and concentration of the electrolyte, nanoporous structure with well defined pore diameter, inter-pore distance and porosity could be easily fabricated.

In chapter 1, a critical review has been provided on various methods of preparing high aspect ratio nanostructures, demonstrating the importance of porous alumina membrane for the growth of metals like platinum and palladium using electrodeposition. In this chapter, we discuss our efforts to prepare such a porous alumina membrane having linear as well as hierarchically branched nanopore arrays through anodization. These nanoporous structures have been characterized by SEM, XRD, FTIR, BET and Electrochemical Impedance techniques. A few commercial PAM samples from Whatman International Ltd. have also been used to bench mark our membrane structures. Furthermore, contact angle studies of these porous membranes are also carried out to understand the wetting of different solvent into the PAM pore walls. These are valuable for the synthesis of different metallic/semiconducting nanostructures either by electrodeposition or by electro-less deposition after functionalization of the pores by selected organic molecules.

2.4. Experimental Details

2.4.1. Materials

Aluminium sheet GR (99.9 % purity, thickness 0.14 mm) and oxalic acid GR (99.5 %) were purchased from Loba Chemie while, $CuCl_2.2H_2O$ was purchased from Merck. Solvents such as ethanol (99.9 %) and perchloric acid (72 %) were procured from Merck and Rankem chemicals. Dimethyl sulfoxide (99 %), N,N′-dimethyl formamide (99.5 %), methanol (99.8 %), cylohexane (99.5 %) and hexane (95 %) were obtained from Loba Chemie, while toluene (99.5 %) was purchased from Qualigens. All reagents were used without further purification and deionized water (18 MΩ) from milli-Q system was used in all experiments.

2.4.2. Fabrication of Linear PAM

Alumina membranes with linear nanopore arrays were fabricated using a DC power supply (Spectron Model: PLC 3001 DtM) for anodization. First, clean Al foils were degreased in acetone followed by annealing for 5 h at 500 ^{0}C under Ar atmosphere in order to remove the crystal defects and to promote grain growth. Subsequently, the foils were electropolished in a mixture of ethanol and perchloric acid (70:20) at 5 V for 2 min to smoothen the surface morphology and the resultant foils were anodized in 0.25 M oxalic acid at 40 V (current density 5 mA/cm^2) for 4 h at 5 ^{o}C using a Pt wire as the cathode under stirred conditions. However, the order of the pores achieved was often limited to a domain of few μm only and more importantly, the individual domains were separated by wide regions of defects. Hence as per Masuda's suggestion of carrying out a two step anodization for ordered porous structures,[4c] we performed a further second anodization after etching the alumina layer from the first step in a mixture of 1.5 wt % chromic acid and 6 wt % phosphoric acid for about 30 min. Etching of these porous alumina layer produced a patterned aluminium substrate with an ordered array of concave shaped holes which subsequently served as initial sites to form a highly ordered nanoporous array during the second anodization step (which was performed under identical conditions) for 5 h.

A schematic representation of different stages involved during the formation of ordered linear nanopore arrays is shown in Figure 2.3, includes anodization of annealed and electropolished Al sheet to form porous alumina layer, which are however non-uniform. As a result, the porous layer is removed to obtain ordered concave textured structure and subsequently a second step anodization is performed to form ordered linear nanopore arrays. This porous alumina layer was then separated from the underlying aluminium substrate by etching in 1 M $CuCl_2$ solution for 30 min and finally the alumina barrier layer was carefully removed after a brief contact (2 min) with 5 wt % phosphoric acid to obtain a free standing porous alumina membrane.

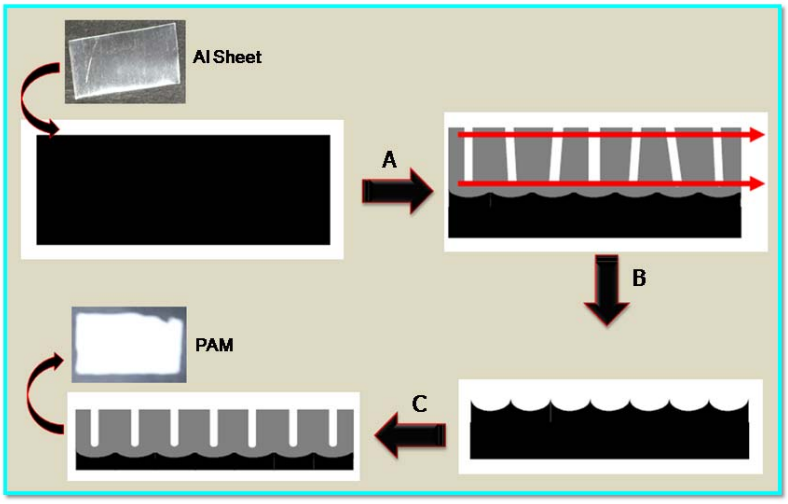

Figure 2.3. Different stages involved in the formation of linear PAM. (A) anodization of annealed and electropolished Al foil at 40 V for 4 h; (B) selective dissolution of the formed porous oxide layer to obtain ordered concave textured structure; (C) second anodization under the same condition for 5 h to obtain highly ordered linear nanopore arrays of alumina; photographs of Al sheet and PAM are also shown.

2.4.3. Fabrication of Y-branched PAM

After the initial anodization to form the straight pore stems (see section 2.4.2 for the fabrication of linear PAM), the voltage was subsequently reduced to 28 V (by a factor of $1/\sqrt{2}$; current density 3.2 mA/cm^2) and finally a third step anodization was performed for 4 h. As a result, nearly all large diameter channels formed at 40 V, get bifurcated into two smaller diameter branches. These Y-branched nanochannels of alumina layer were then separated from the underlying substrate by etching in 1 M $CuCl_2$ or mercurous chloride (aqueous solution) for 30 min and finally the alumina barrier layer was carefully removed after a brief contact (2 min) with 5 wt % phosphoric acid to obtain a free standing alumina membrane.

2.4.4. Fabrication of Two-Generation Y-branched PAM

After the above third step (see section 2.4.3), the anodization voltage was further reduced to 20 V (by a factor of $1/\sqrt{2}$; current density 2.5 mA/cm^2) and continued for 4 h.

As a result of this, a second generation of branched channels was generated from each of the first generation branched channels (formed at 28 V). After the anodization process, a similar procedure (as discussed in section 2.4.3) was followed to obtain free standing PAM.

2.4.5. Structural and Morphological Characterization

2.4.5.1. Scanning Electron Microscopy (SEM)

Dimensions of the nanopore arrays were examined using a scanning electron microscope, Lieca Stereoscan 440 Model. A small piece of the membrane was mounted on a Cu substrate using a carbon tape. For comparative studies, the energy of the electron beam was kept constant while analyzing all the samples. Micrographs were recorded with a 20 kV electrical high tension and 25 pA camera attached on the high-resolution recording unit. Some micrographs were also recorded using a Hitachi S-4800 field emission scanning electron microscope.

2.4.5.2. X-ray Diffraction (XRD)

In order to understand the structure of 'as-prepared' PAM at room temperature and also to elucidate the purity, XRD studies were performed using CuK_α (λ = 1.5405 Å) radiation on a Panalytical XPert Pro diffractometer. Diffraction patterns were collected at a step of 0.02° (2θ) and the background was subtracted with the linear interpolation method.

2.4.5.3. Fourier Transform Infrared Spectroscopy (FTIR)

Detailed information on the different functional groups present in the porous membrane has been investigated using FTIR analysis. Different modes are employed for analysis depending on the nature of the sample and required sensitivity. For example, FTIR measurements were carried out in the diffuse reflectance mode at a resolution of 4 cm^{-1} on a Perkin-Elmer FTIR Spectrum One spectrophotometer.

2.4.5.4. Contact Angle Measurements

Contact angle measurement is a surface sensitive technique, which quantitatively unravels the wetting of a solid by a selected liquid, enabling a simple and effective method to determine the surface tension, and its relation to the structure and composition of a surface. All contact angle measurements were performed on a GBX model (DIGIDROP contact angle instrument) using proprietary Windrop software. The contact angle (θ) was measured using sessile solvent drop method. Prior to the measurements, the membrane was dried at 100 ^{0}C for 1 h and allowed to cool to room temperature. Wetting behavior of PAM was carried out using seven different solvents such as H_2O, dimethyl sulfoxide (DMSO), N,N′-dimethyl formamide (DMF), methanol, toluene, cylohexane and hexane. The measurements were performed after fixing the membrane on the sample holder. Extreme care was taken in monitoring contact angle values within 2 - 3 min to avoid the evaporation effects. At room temperature (27 ^{o}C) and at constant humidity (40-50%), all contact angle measurements showed a standard deviation of ± 2^o. However, since the contact angle depends on the liquid purity, temperature, as well as the statistical errors in the actual reading of the contact angles by different people, average values were taken typically after 5-6 measurements.

2.4.5.5. Determination of Pore Size Distribution

The Brunauer Emmett Teller (BET) method continues to be the most widely used method for the evaluation of surface area, pore volumes and pore size distributions of porous solids from N_2 physisorption isotherm data. The BET equation can be represented as follows:

$$\frac{p}{v(p_0 - p)} = \frac{1}{v_m c} + \frac{c-1}{v_m c}\frac{p}{p_0} \quad \text{..... (2.1)}$$

where, v = volume of N_2 adsorbed by the sample under pressure p, p_0 = saturated vapor pressure at the same temperature, v_m = volume of N_2 adsorbed when the surface is covered with a unimolecular layer, and c = constant for a given adsorbate.

The equation suggests that the plot of $\frac{p}{v(p_0 - p)}$ versus $\frac{p}{p_0}$ should be linear, and from the intercept $\frac{1}{v_m c}$ and slope $\frac{c-1}{v_m c}$, the values of v_m and c can be determined as follows: $v_m = (\text{slope} + \text{intercept})^{-1}$. Thus the specific surface area (S) of a sample can be determined as follows: $S = \frac{N_0 v_m A}{22414 m}$, where N_0 = Avogadro number, m = amount of solid adsorbent, A = cross-section of the gas molecules (16.2 $Å^2$ for N_2), and S is expressed in $cm^2\ g^{-1}$ unit.

Several computational procedures are available for the derivation of pore size distribution of mesoporous samples from physisorption isotherms. Most popular among them is the Barrett-Joyner-Halenda (BJH) model, which is based on speculative emptying of the pores by a stepwise reduction of p/p_0, and allowance being made for the contraction of the multilayer in those pores already emptied by the condensate.

The pore size distribution of PAM was determined by BET method using Quantachrome Autosorb Automated Gas Sorption System with N_2 gas adsorption–desorption measurements at 100°C.

2.4.5.6. Electrochemical Impedance Measurements

Electrochemical Impedance is an important electroanalytical technique based on the measurements of the frequency dependent response of an electrochemical cell after applying a small-amplitude sinusoidal signal under a potentiostatic control. It offers the possibility of obtaining information on important parameters such as ohmic resistance, double layer capacitance, charge transfer kinetics at the electrode/electrolyte interface and also about mass transfer phenomenon. In the present work, electrochemical

impedance studies were performed in 0.1 M KCl containing equal proportions of $K_4[Fe(CN)_6]/K_3[Fe(CN)_6]$ couple (5 mM each) using Autolab PGSTAT30 (ECOCHEMIE) instrument equipped with a frequency response analyzer.

2.5. Results and Discussion

2.5.1. SEM Analysis

Figure 2.4a shows a typical scanning electron micrograph of the "as-prepared" porous alumina membrane (top-view) by the two step anodization process using 40 V, revealing an ordered hexagonally packed nanopores with an average diameter of 65 nm. Indeed, pores are seen over the entire surface of the sample and the distance between two adjacent pores (inter-pore distance) amounts to ca. 100 nm. More specific cross-sectional view of the membrane is shown in figure 2.4b to highlight the periodic linear array with a pore length of ca. 56 μm. Interestingly, a slightly higher anodization voltage (50 V; current density 7 mA/cm^2) as indicated in figure 2.4c reveals the formation of the same hexagonal array, despite with a slightly higher pore diameter (80 nm) and inter-pore distance of 120 nm respectively. Further, the porosity and pore density of PAM film at different anodization voltage could be estimated as follows:

Porosity (*P*), after assuming an ideal hexagonal arrangement of the pores, is given by,[12]

$$P = \frac{2\pi}{\sqrt{3}}(r/D_{\text{int}})^2 \quad \text{..... (2.2)}$$

where, r is the pore radius and D_{int} is the inter-pore distance.

Also, the pore density (ρ, pores/cm^2) is given by,[13]

$$\rho = \frac{2}{\sqrt{3}D_{\text{int}}{}^2} \times 10^{14} \text{ cm}^{-2} \quad \text{..... (2.3)}$$

Accordingly, Table 2.1 summarizes both the porosity and pore density of the PAM film formed at two different voltage, where it could be seen that porosity increases upon increasing the voltage whereas pore density decreases.

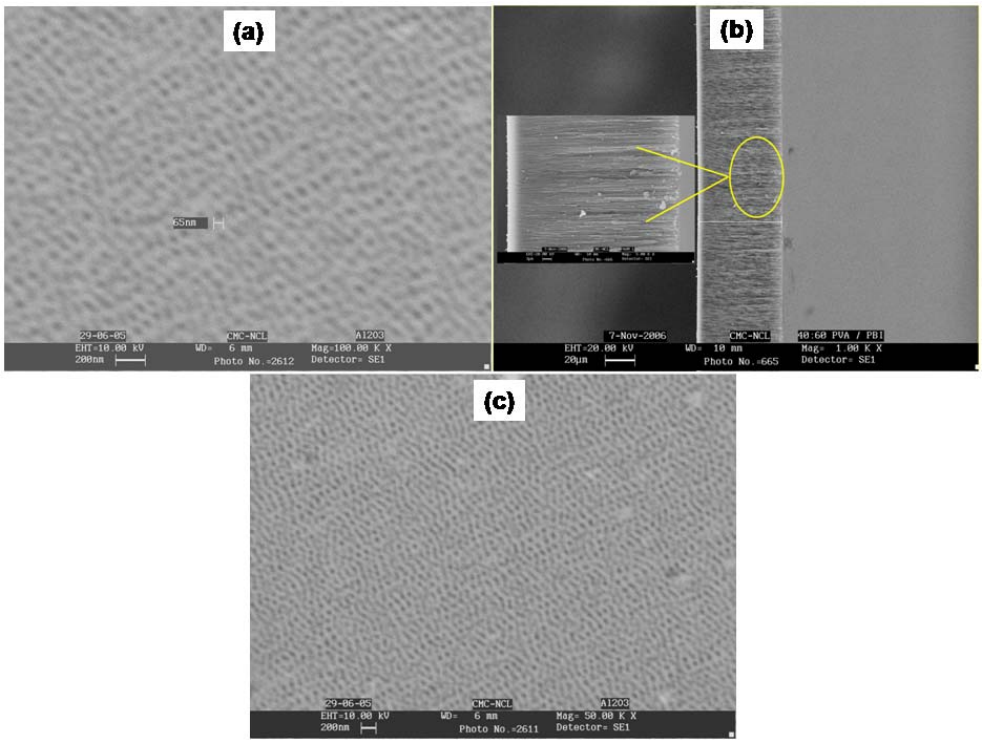

Figure 2.4. SEM images of porous alumina membrane fabricated after a two step anodization in 0.25 M oxalic acid at 5 ^{o}C; (a & b) top and cross-sectional view of porous alumina membrane fabricated at an anodization voltage of 40 V; (c) top view of porous alumina membrane fabricated at 50 V.

Table 2.1. Different structural parameters of PAM fabricated at two different anodization voltages; anodization was performed in 0.25 M oxalic acid at 5 ^{o}C.

	PAM (40 V)	**PAM (50 V)**
Pore Diameter (nm)	65	80
Interpore Distance (nm)	100	120
Porosity (%)	38	40
Pore Density (pores/cm^2)	1.1 x 10^{10}	8 x 10^9

Typical field-emission scanning electron micrographs (FESEM) of alumina membranes with Y-branched nanochannels (cross-sectional view) fabricated via an extended two step anodization are shown in figure 2.5a-c at different magnifications.

More specifically, the images depict Y-branched nanochannels with stems and branches of about 100 and 50 nm diameters respectively, although these parameters could be controlled systematically by varying temperature, anodization time, nature and concentration of the electrolyte. Furthermore, the angle between the two branches is about 10^{o} as shown in the micrograph. The Y-junctions are uniform with regard to both the position of the junction (i.e., orientation) and the diameter of the arms. Similarly, figure 2.6 shows the SEM image of two-generation Y-branched PAM fabricated through an extended three step anodization, where the micrograph shows the first generation and second generation branches. However, it is difficult to mention the diameter of the branches from this low magnification.

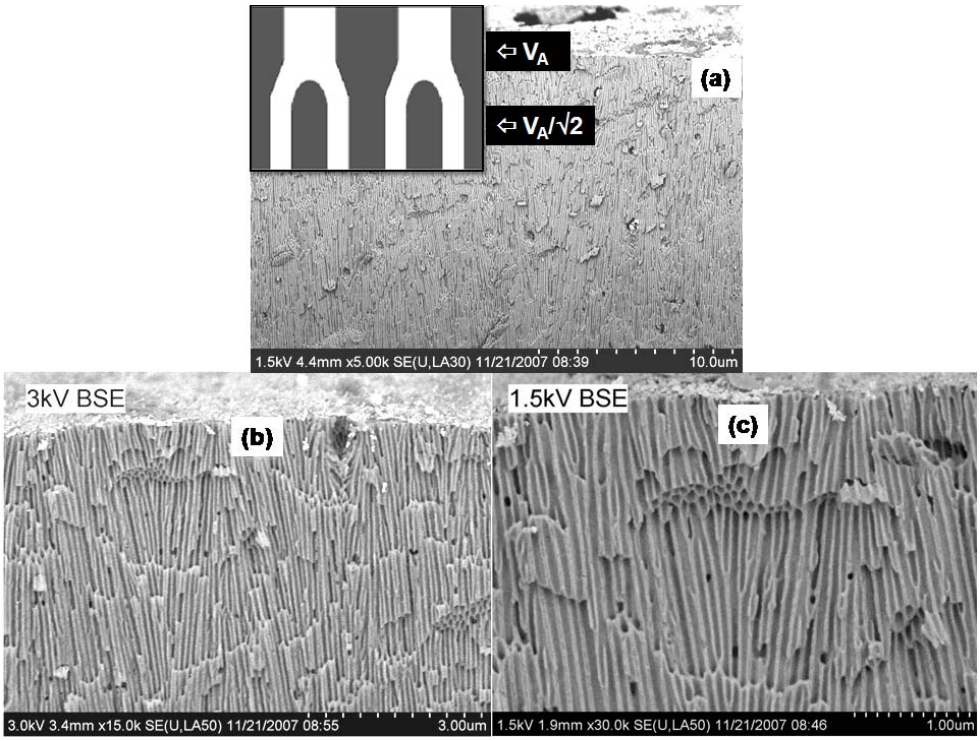

Figure 2.5. FESEM images of Y-branched PAM (cross-sectional view) fabricated via an extended two step anodization; Y-branched nanochannels consist of stems and branches having diameter 100 nm and 50 nm respectively; (a-c) show images at different magnifications; inset shows the schematic view of Y-branch alumina membrane.

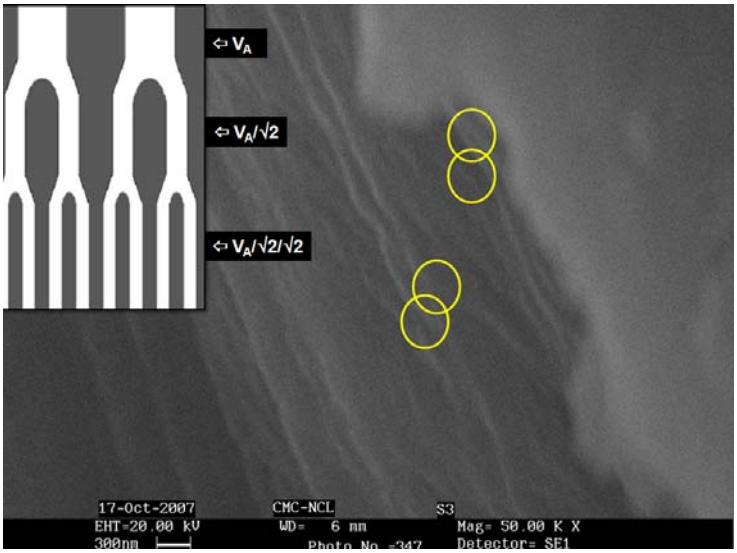

Figure 2.6. SEM image of two-generation Y-branched PAM (cross-sectional view) fabricated through an extended three step anodization; branched nanochannels are marked by circles; schematic view of two-generation Y-branch alumina membrane is shown in the inset.

2.5.2. XRD Analysis

Figure 2.7 reveals the XRD pattern of the free-standing PAM template recorded at room temperature, demonstrating that the 'as-prepared' PAM has an amorphous nature.[14] However, sharps peaks at 2θ values 44.1°, 65.1° and 78.2° respectively are observed corresponding to the (200), (220) and (311) planes of metallic Al [JCPDS 4-787]. This reveals the presence of trace amount of Al debris in the PAM membrane even after the treatment with cupric chloride.

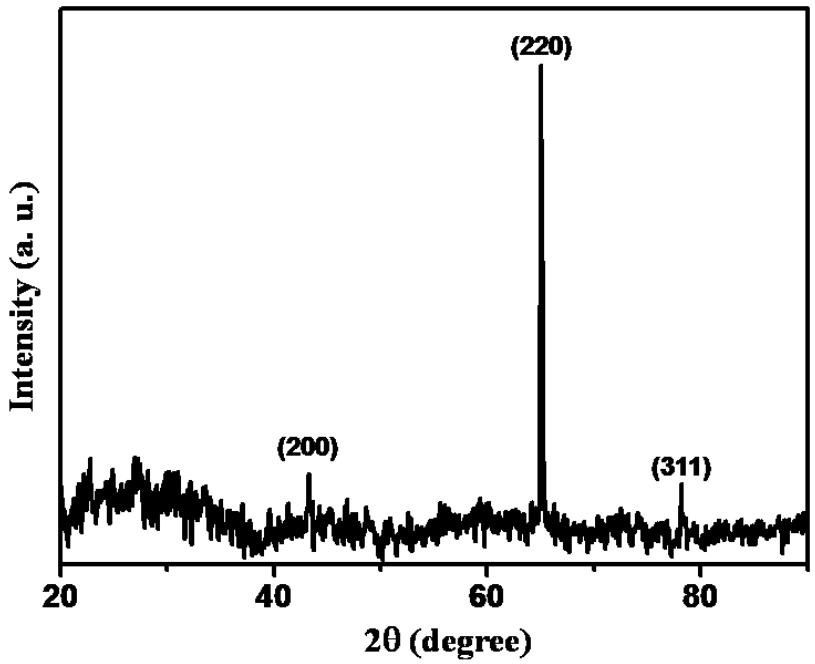

Figure 2.7. XRD spectrum of the free-standing PAM fabricated through a two-step anodization at 40 V in 0.25 M oxalic acid; the pattern reveals amorphous structure of alumina membrane; sharp and intense peaks correspond to the metallic Al.

2.5.3. Wetting Behaviour of Linear PAMs: Results of Contact Angle Measurements

One of the important applications of PAM is in the preparation of high aspect ratio nanostructures through different routes including both electrodeposition and electro-less deposition. However, attempts to fill the pores by natural convection or capillarity effect alone are unsuccessful because of the extremely slow nature of diffusion inside porous structures (Knudsen diffusion).[15] Therefore, it is important to study liquid-solid interactions in order to understand how the interfacial properties affect the influx and outflux of molecules/ions into the pores of the membrane. With this objective, the contact angle studies have been carried out on PAM membranes to understand the wetting behaviour between a liquid and a porous solid surface.

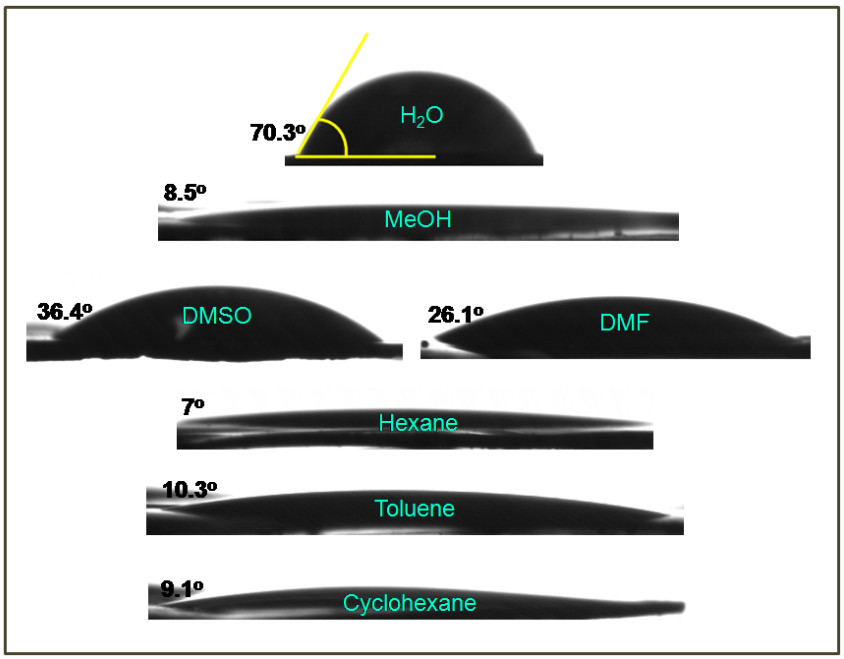

Figure 2.8. Solvent droplet profile obtained with different solvents on free-standing linear PAM at room temperature; prior to the measurements, all membranes were dried at 100 ^{0}C for 1 h and allowed to cool to room temperature.

Figure 2.8 reveals the droplet profile observed with various solvents on PAM (pore diameter 65 nm). A closer look at 'θ' values corresponding to various solvents reveal the following order H_2O > DMSO > DMF > Toluene > Cyclohexane > Methanol > Hexane. A higher 'θ' value is observed for the case of H_2O (70.3 ± 2^o), whereas hexane shows comparatively lower value (7 ± 2^o). Most important properties that affect 'θ' are dielectric constant, dipole moment of the solvent, and surface tension. In the present case, the interaction of membrane with the liquid is through the hydroxyl and oxalate groups (these groups are present on the surface as well as on the pore walls) and hence the wetting of the alumina membrane is partly decided by the density of these groups. The presence of these groups is confirmed by FTIR studies (figure 2.9), where the appearance of peak at 1650 cm^{-1} and 1210 cm^{-1} is attributed to the carbonyl (C=O) and C-O stretching of –COO$^-$ moiety respectively. In addition, peaks at 1410 and 1530 cm^{-1} are assigned to the symmetric and asymmetric stretching of carboxylate ion and apart from

these, a broad band at around 3200 cm^{-1} corresponding to the –OH stretching of hydroxyl group is also observed.[16]

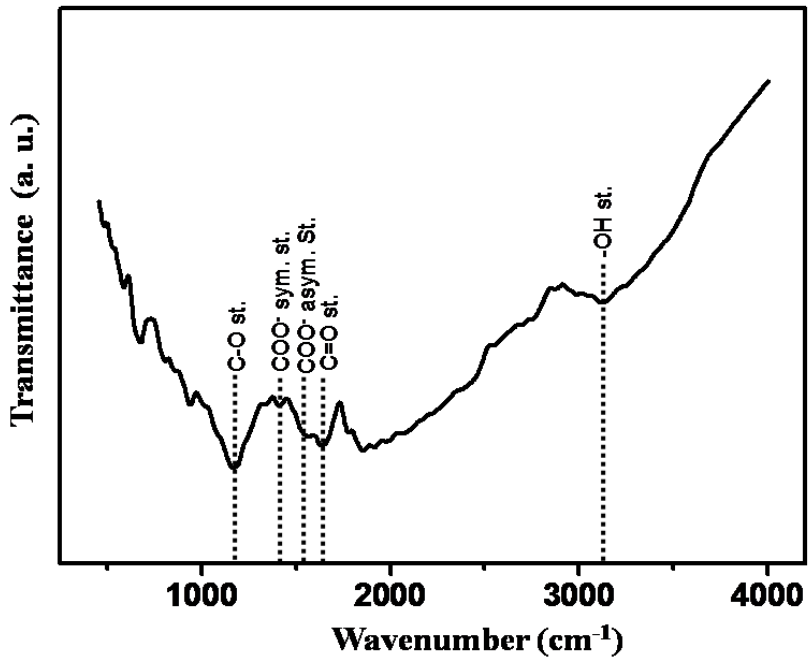

Figure 2.9. DRIFT spectrum of free-standing linear PAM; the stretching frequencies of different functional groups present in the membrane are mentioned.

Even though, water exhibits higher values of dielectric constant (ε) and dipole moment (μ), a higher value of surface tension (γ) is primarily responsible for the poor interaction with the pore walls. In other words, in water the cohesive force ($\gamma_{lv;}$ surface tension at the liquid-vapor interface) is strong enough to overcome the adhesive force ($\gamma_{sl;}$ surface tension at the solid-liquid interface) and as a result prevents it from spreading.[17] In contrast, hexane has comparatively lower surface tension (than that of water) to ensue stronger adhesive force (γ_{sl}) than the cohesive force (γ_{lv}) and as a result, wetting of pore walls occurs. Similarly, wetting behaviour observed with solvents such as DMSO, DMF, methanol, toluene, and cyclohexane as judged by the contact angle values (θ) are in agreement with the corresponding surface tension values.

Similar studies with planar aluminium sheet (with native oxide film) is also carried out and the corresponding droplet profiles with various solvents are shown in figure 2.10. A similar trend as observed in the case of PAM is also obtained for planar alumina sheet although a comparison of the contact angle values on both samples, reveals a slightly higher 'θ' value for the planar alumina (especially in the case of polar solvents). This could be attributed to the hydroxyl and oxalate functional groups present on the surface and pore walls of PAM and also due to the porous structure of the membrane, which in turn increases the surface roughness. Table 2.2 summarizes the contact angle with various solvents (along with surface tension) on both planar and porous alumina. It has been already observed that upon increasing the surface roughness of hydrophilic surfaces, the surface will exhibit enhanced hydrophilicity. All these factors are responsible for the comparatively lower 'θ' for the PAM with respect to planar alumina. However, considering the wetting behaviour of non-polar solvents such as toluene on both surfaces, it is observed that the angle 'θ' is comparatively lower for planar one compared to that on porous membrane. This could be partly attributed to the hydrophilic-hydrophobic interaction on the porous membrane, which leads to a slightly higher angle on porous alumina. However, further studies are desired to pinpoint the exact reason for this behaviour.

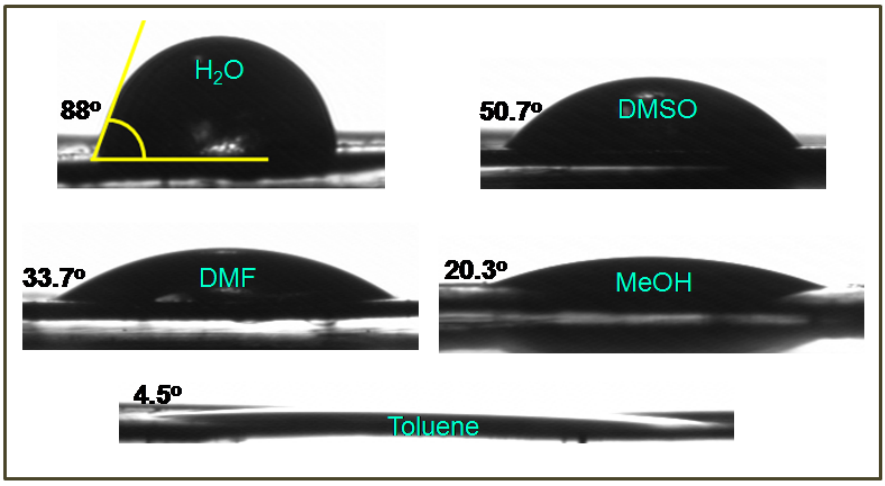

Figure 2.10. Solvent droplet profiles with different solvents on planar alumina at room temperature; the wetting angle 'θ' observed with each solvent is also shown.

Table 2.2. Variation of contact angle 'θ' with different solvents on both porous alumina membrane and planar alumina; surface tension of corresponding solvents are also included.

Solvent	**Contact Angle (θ) (degree)**		**Surface Tension (dynes/cm)**
	PAM	Planar Alumina Sheet	
Water	70.3	88	72.8
DMSO	36.4	50.7	43.54
DMF	26.1	33.7	36.76
Methanol	8.5	20.3	22.55
Toluene	10.3	4.5	28.53
Hexane	7	*	17.91
Cyclohexane	9.1	*	24.98

*Unable to measure

Further, the "critical surface tension" γ_{crit} (a measure of interfacial surface energy) of a material is estimated from the Zisman plot (the cosine of the contact angle (θ) versus the surface tension of various solvents).[18] As the surface tension of the solvent decreases, contact angle also decreases and the extrapolation of this plot to Cosθ = 1 gives the critical surface tension value. Accordingly, figure 2.11a,b shows the Zisman plot of both planar alumina and PAM and corresponding γ_{crit} value is 28.5 and 17.8 dyne/cm respectively. The lower value of γ_{crit} for the PAM with respect to planar alumina is attributed to the increased surface roughness and porosity of the former.

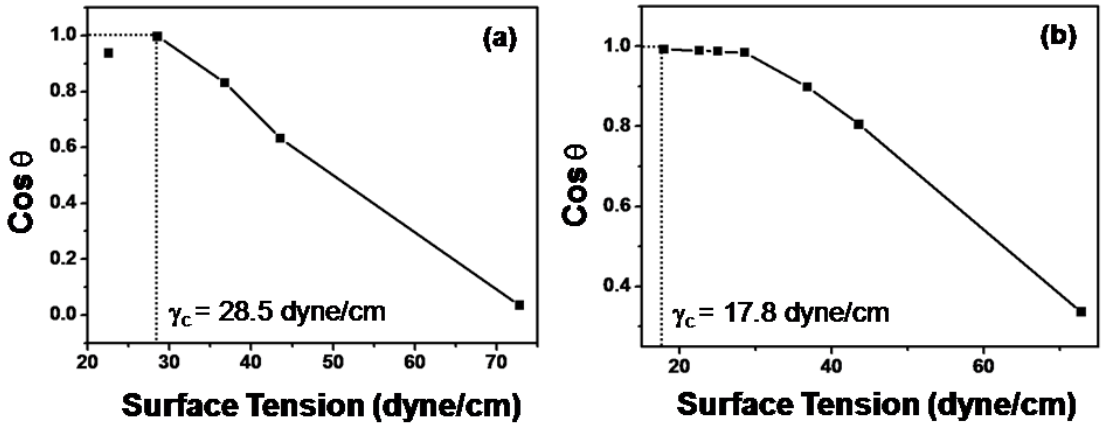

Figure 2.11. Zisman plots for (a) planar alumina sheet and (b) porous alumina membrane; the critical surface tension is obtained after extrapolation of the plot to Cosθ =1.

2.5.4. Determination of Pore Size Distribution from BET Adsorption Isotherm

N_2 adsorption-desorption studies based on BET isotherm are valuable for estimating the surface area and pore size distribution of the porous materials.[19] Accordingly, we have evaluated the pore size distribution of PAM fabricated at an anodization voltage of 40 V. However, the pore size distribution obtained reveals a bimodal distribution with a pore size of 40 and 60 Å respectively, which is an order less than that from SEM analysis (here the pore diameter was estimated based on BJH analysis during desorption process). The reason for this discrepancy is perhaps due to (i) normally, this technique is employed mainly for powder samples and hence getting reliable data for membrane is difficult due to very small surface area, and (ii) between the well-defined cylindrical alumina nanopores, amorphous alumina film is present on the surface which is perhaps more accessible for gases with pore diameters of around 40 and 60 Å thus masking the true nanoporous size distribution.

2.5.5. Electrochemical Impedance Behaviour of PAM

Impedance is a powerful tool to understand the electrochemical behaviour of these porous membranes. Using this technique, the rate of thinning of barrier layer at the bottom of the porous structure has been studied extensively.[20] Moreover, ionic transport

through the porous electrodes, in general have been extensively investigated using impedance.[21] The work of de Levie marks the start of the theory of the impedance of porous electrodes derived from various mathematical models. Two of the most successful models are the cylindrical pore model and the macro homogeneous model. The impedance of the porous electrode under the influence of potential gradient, and concentration gradient and both had been analysed using the cylindrical pore model. However, the cylindrical pore models do not take into account the distribution of pores in the electrode, which is very significant for practical applications of porous electrodes. The macro homogeneous model proves to be a better representation as it takes into consideration the distribution of pores by volume averaging. Using the macro homogeneous model and linear polarization study, Ralph et al. have derived the impedance response of porous electrode under the influence of both the concentration gradient and the potential gradients. Interestingly, using this model they have demonstrated the effect of porosity of these electrodes on the impedance response.

Normally, the impedance response of the porous electrodes in presence of a redox couple, shows two semicircles: the high frequency semicircle is due to charge transfer process and the lower frequency semicircle for diffusion process. With a decrease in porosity of these membranes, both the charge transfer and mass transfer resistance increases. Accordingly, figure 2.12a-c shows the impedance response of Al sheet and alumina membrane with different porosity (38 % and 40 %) in presence of 1:1 mixture of both $K_4[Fe(CN)_6]$ and $K_3[Fe(CN)_6]$ couple in 0.1 M KCl, where with increase in porosity, suggests an increase in the charge transfer resistance (R_{CT}). For example, the R_{CT} value of planar Al sheet is 465 Ω, whereas 485 Ω and 1.6 kΩ are obtained for PAM with 38 % and 40 % porosity respectively. The corresponding enlarged view of the high frequency region is also shown in figure 2.13a-c where the ohmic resistance (R_Ω) of the three samples vary as: PAM (40%) > PAM (38 %) > Al sheet. However, several fluctuations are observed especially at lower frequency region perhaps due to pitting corrosion of Al (in side of the membrane) aggrevated by chloride ions and hence further studies in other electrolyte (e.g., sodium sulphate) are desired to explore this.

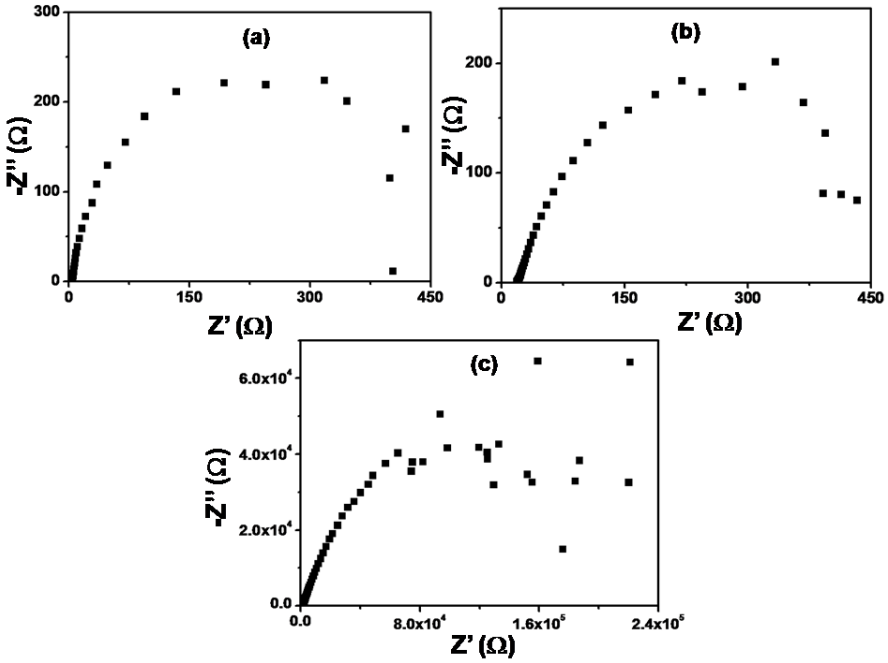

Figure 2.12. Complex plane impedance plots of (a) planar Al sheet; (b and c) PAM with 38 % and 40 % porosity using 10 mV AC signal recorded in the frequency range of 50 kHz to 0.1 Hz.

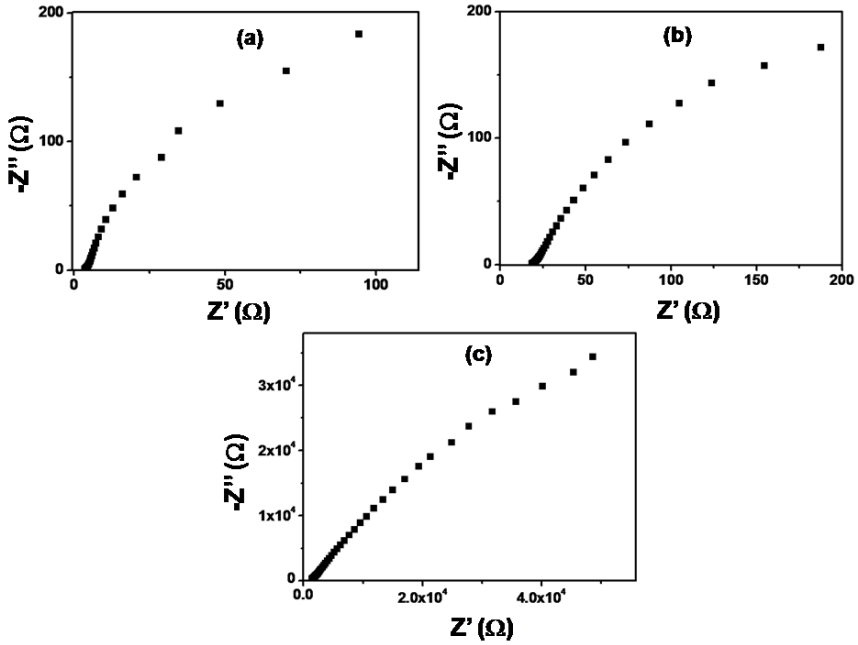

Figure 2.13. Complex plane impedance plots of a) planar Al sheet; (b and c) PAM with 38 % and 40 % porosity; the enlarged view of the high frequency region is shown; variation in R_{Ω} with increase in porosity is clearly seen.

Thus a combination of all the above techniques provides an elegant way to characterize porous alumina membranes which clearly suggests the formation of PAM with well-defined nanopore arrays. Hence, this porous membrane could be effectively utilized for not only as scaffold platform for synthesizing nanostructural array for various material but also could be extended to various other diverse applications such as DNA translocation, size-exclusive filtration, gas separation, and as photonic crystal.

2.6. Conclusions

This chapter discusses various experimental details of the fabrication and growth mechanism of porous alumina template in order to illustrate the critical importance of controlling some of the major factors affecting the nanopore array formation. The methodology for preparing alumina template with linear nanopore arrays having diameter ca. 65 nm and ca. 80 nm through a two step anodization route is described along with extension for the fabrication of hierarchically designed alumina templates including Y-branched as well as two generation Y-branched nanopore channels. The approach developed in this chapter could serve as an efficient and reliable route for the synthesis of high aspect ratio nanostructures such as linear, Y- junction, and multilevel Y-junctions. Considering, the tremendous applications of the junctions nanostructures especially in molecular electronics, we further believe that present route could be extended for other such porous oxides realizing their complete potential. Further, we anticipate that a slight modification of the above template-design strategy could facilitate the fabrication of other potential junction structures such as X, and T.

2.7. References

1 (a) Martin, C. R. *Chem. Mater*. **1996**, *8*, 1739. (b) Hulteen, J. C.; Martin, C. R. *J. Mater. Chem.* **1997**, *7*, 1075. (c) Davis, M. E. *Nature* **2002**, *417*, 813. (d) Schuth, F. *Chem. Mater*. **2001**, *13*, 3184. (e) Kline, T. R.; Tian, M.; Wang, J.; Sen, A.; Chan, M. W. H.; Mallouk, T. E. *Inorg. Chem*. **2006**, *45*, 7555. (f) Hurst, S. J.; Payne, E. K.; Qin, L.; Mirkin, C. A. *Angew. Chem. Int. Ed*. **2006**, *45*, 2672. (g) Preston, C. K.; Moskovits, M. J. *J. Phys. Chem.* **1993**, *97*, 8495. (h) Hernandez-Velez, M. *Thin Solid Films* **2006**, *495*, 51. (i) Nielsch, K.; Muller, F.; Li, A. P.; Gosele, U. *Adv. Mater*. **2000**, *12*, 582. (j) Wade, T. L.; Wegrowe, J. –E. *Eur. Phys. J. Appl. Phys*. **2005**, *29*, 3. (k) Schmid, G. *J. Mater. Chem*. **2002**, *12*, 1231. (l) Luo, Y.; Lee, S. K.; Hofmeister, H.; Steinhart, M., Gosele, U. *Nano Lett*. **2004**, *4*, 143. (m) Martin, C. R. *Science* **1994**, *266*, 1961. (n) Brumlik, C. J.; Martin, C. R. *J. Am. Chem. Soc*. **1991**, *113*, 3174. (o) Schonenberger. C.; Van der Zande, B. M. I.; Fokkink, L. G. J.; Henny, M.; Schmid, C.; Kruger, M.; Bachtold, A.; Huber, R.; Birk, H.; Staufer, U. *J. Phys. Chem. B* **1997**, *101*, 5497. (p) Choi, J.; Sauer, G.; Nielsch, K.; Wehrspohn, R. B.; Gosele, U. *Chem. Mater*. **2003**, *15*, 776. (q) Ramirez, E.; Erades, L.; Philippot, K.; Lecante, P.; Chaudret, B *Adv. Funct. Mater*. **2007**, *17*, 2219. (r) Pileni, M. P. *Nat. Mater.* **2003**, *2*, 145. (s) Song, Y.; Garcia, R. M.; Dorin, R. M.; Wang, H.; Qiu, Y.; Coker, E. N.; Steen, W. A.; Miller, J. E.; Shelnutt, J. A. *Nano Lett*. **2007**, *7*, 3650.

2 (a) Yu, Y. Y.; Chang, S. S.; Lee, C. L.; Chris Wang, C. R. *J. Phys. Chem. B* **1997**, *101*, 6661. (b) Zhang, D.; Qi, L.; Ma, J.; Cheng, H. *Chem. Mater.* **2001**, *13*, 2753. (c) Nikoobakht, B.; El-Sayed, M. A. *Chem. Mater.* **2003**, *15*, 1957. (d) Zhao, G. X. S. *J. Mater. Chem*. **2006**, *16*, 623. (e) Jana, N. R.; Gearheart, L.; Murphy, C. J. *J. Phys. Chem. B* **2001**, *105*, 4065.

3 (a) Yuan, Z. –Y.; Su, B. –L. *J. Mater. Chem*. **2006**, *16*, 663. (b) Jiang, P.; Cizeron, J.; Bertone, J. F.; Colvin, V. L. *J. Am. Chem. Soc*. **1999**, *121*, 7957.

4 (a) Keller, F.; Hunter, M. S.; Robinson, D. L. *J. Electrochem. Soc*. **1953**, *100*, 411. (b) Masuda, H.; Fukuda, K. *Science* **1995**, *268*, 1466. (c) Masuda, H.; Satoh, M. *Jpn. J. Appl. Phys*. **1996**, *35*, L126. (d) Masuda, H.; Yamada, H.; Satoh, M.; Asoh, H. *Appl. Phys. Lett*. **1997**, *71*, 2770. (e) Yuan, J. H.; He, F. Y.; Sun, D. C.; Xia, X. H. *Chem. Mater*. **2004**, *16*, 1841. (f) Thompson, G. E.; Furneaux, R. C.; Wood, G. C.; Richardson, J. A.; Goode, J. S. *Nature* **1978**, *272*, 433. (g) Thompson, G. E.; Wood, G. C. *Nature* **1981**, *290*, 230. (h) Masuda, H.; Hasegwa, F.; Ono, S. *J. Electrochem. Soc*. **1997**, *144*, L127. (i) Lee, W.; Ji, R.; Gosele, U.; Nielsch, K. Nat. Mater. **2006**, 5, 741. (j) Chu, S. –Z.; Wada, K.; Inoue, S.; Isogai, M.; Yasumori, A. *Adv. Mater*. **2005**, *17*, 2115. (k) Wood, G. C.; O'Sullivan, J. P. *Electrochim. Acta* **1970**, *15*, 1865. (l) Li, A. P.; Muller, F.; Birner, A.; Nielsch, K.; Gosele, U. *J. Appl. Phys*. **1998**, *84*, 6023. (j) Li, F.; Zhang, L.; Metzger, R. M. *Chem. Mater*. **1998**, *10*, 2470.

5 (a) Li, J.; Papadopoulos, C.; Xu, J. *Nature* **1999**, *402***,** 253. (b) Papadopoulos, C.; Rakitin, A.; Li, J.; Vedeneev, A. S.; Xu, J. M. *Phys.Rev. Lett.* **2000**, *85***,** 3476. (c) Meng, G.; Jung, Y. J.; Cao, A.; Vajtai, R.; Ajayan, P. M. *PNAS* **2005**, *102*, 7074.

6 (a) Diggle, J. W.; Downie, T. C.; Goulding, C. W. Chem. Rev. **1969**, *69*, 365. (b) Thompson, G. E. *Thin Solid Films* **1997**, *297*, 192. (c) O'Sullivan, J. P.; Wood, G. C. *Proc. R. Soc. London A* **1970**, *317*, 511.

7 (a) Zwilling, V.; Aucouturier, M.; Darque-Ceretti, E. *Electrochim. Acta* **1999**, *45*, 921. (b) Gong, D.; Grimes, C. A.; Varghese, O. K.; Hu, W.; Singh, R. S.; Chen, Z.; Dickey, E. C. *J. Mater. Res*. **2001**, *16*, 3331. (c) Mor, G. K.; Shankar, K.; Paulose, M.; Varghese, O. K.; Grimes, C. A. *Nano Lett*. **2005**, *5*, 191. (d) Tsuchiya, H.; Macak, J. M.; Sieber, I.; Taveira, L.; Ghicov, A.; Sirotna, K.; Schmuki, P. *Electrochem. Commun*. **2005**, *7*, 295.

8 (a) Parkhutik, V. P.; Shershulsky, V. I. J. Phys. D: Appl. Phys. **1992**, *25*, 1258. (b) Uchi, H.; Kanno, T.; Alwitt, R. S. *J. Electrochem. Soc*. **2001**, *148*, B17. (c) Palibroda, E.; Lupsan, A.; Pruneanu, S.; Savas, M. *Thin Solid Films* **1995**, *256*, 101. (d) Siejka, J.; Ortega, C. *J. Electrochem. Soc*. **1977**, *124*, 883. (e) Xu, Y.;

Thompson, G. E.; Wood, G. C. *Trans. Inst. Met. Finish*. **1985**, *63*, 98. (f) Shimizu, K.; Kobayashi, K.; Thompson, G. E.; Wood, G. C. *Philos. Mag. A* **1992**, *66*, 643.

9 (a) Jessensky, O.; Muller, F.; Gosele, U. *Appl. Phys. Lett*. **1998**, *72*, 1173. (b) Jessensky, O.; Muller, F.; Gosele, U. J. Electrochem. Soc. **1998**, *145*, 3735.

10 (a) Furneaux, R. C.; Rigby, W. R.; Davidson, A. P. *Nature* **1989**, *337*, 147. (b) Broughton, J.; Davies, G. A. *J. Membrane Sci*. **1995**, *106*, 89. (c) Bailey, G.; Wood, G. C. *Trans. Inst. Metal*. *Finish*. **1974**, *52*, 187. (d) Zhao, N. -Q.; Jiang, X. -X.; Shi, C.-S.; Li, J. -J.; Zhao, Z. -G.; Du, X. -W. J. Mater. Sci. **2007**, *42*, 3878. (e) Wade, T. L.; Wegrowe, J. –E. *Eur. Phys. J. Appl. Phys.* **2005**, *8*, 3.

11 (a) Shingubara, S.; Okino, O.; Sayama, Y.; Sakaue, H.; Takahagi, T. *Jpn. J.Appl.Phys*. **1997**, *36*, 7791. (b) Li, F.; Zhang, L.; Metzger, R. M. *Chem. Mater*. **1998**, *10*, 2470.

12 Nielsch, K.; Choi, J.; Schwirn, K.; Ralf B. Wehrspohn, R. B.; Gosele, U. *Nano Lett*. **2002**, *2*, 677.

13 Lee, W.; ji, R.; Gosele, U.; Nielsch, K. Nature Mater. **2006**, *5*, 741.

14 Wang, Y. C.; Leu, I. C.; Hon, M. H. *J. Appl. Phys.* **2004**, *95*, 1444.

15 (a) Itoh, N.; Kato, K.; Tsuji, T.; Hongo, M. *J. Membrane Sci*. **1996**, *117*, 189. (b) Berland, B. S.; Gartland, I. P.; Ott, A. W.; George, S. M. *Chem. Mater*. **1998**, *10*, 3941. (c) Lin, Y. S.; Ji, W.; Wang, Y.; Higgins, R. J. *Ind. Eng. Chem. Res*. **1999**, *38*, 2292.

16 (a) Nakamoto, K. *Infrared and Raman spectra of inorganic and coordination compounds*; John Wiley & Sons: USA, 1986.

17 Redon, R.; Vazquez-Olmos, A.; Mata-Zamora, M. E.; Ordonez-Medrano, A.; Rivera-Torres, F.; Saniger, J. M. J. Colloid and Interface Science **2005**, *287*, 664.

18 (a) Zisman, W. A. *J. Chem. Phys*. **1941**, *9*, 534. (b) Ulman, A. *An Introduction to Ultrathin Organic Films: From Langmuir-Blodgett to Self-Assembly*; Academic Press: San Diego, California, 1991. (c) Weiss, P. *Adhesion and Cohesion*; Elsevier Science Publishers: Amsterdam, 1962.

19 Gregg, S.J.; Sing, K. S. W. *Adsorption Surface Area and Porosity*; Academic

Press: London, 1967.

20 (a) Romer, W.; Steinem, C. *Biophys. J*. **2004**, *86*, 955. (b) Drexler, J.; Steinem, C. *J. Phys. Chem. B* **2003**, *107*, 11245.

21 (a) Devan, S.; Subramanian, V. R.; White, R. E. *J. Electrochem. Soc*. **2004**, *151*, A905. (b) Delahay, P.; Tobias, C. T. *Advances in Electrochemistry and Electrochemical Engineering*; Interscience: New York, 1967. (c) Chen, G.; Waraksa, C. C.; Cho, H.; Macdonald, D. D.; Mallouk, T. E. *J. Electrochem. Soc*. **2003**, *150*, E423.

CHAPTER 3

Potential Dependent Morphological Evolution of Platinum Mesostructures: Comparison of their Electrocatalytic Activity for Fuel Cells*

Present chapter demonstrates potential-dependent morphological evolution of platinum mesostructures in the form of multipods, discs and hexagons prepared using a porous alumina membrane (PAM) template potentiostatically at -0.7, -0.5 and -0.3 V, respectively. These structures reveal unique shape-dependent electrocatalytic activity towards formic acid, methanol and ethanol oxidation reactions. A comparison of the electrooxidation kinetics of these structures illustrates that hexagons show better performance towards formic acid and methanol oxidation whereas, for ethanol oxidation, multipods show significantly enhanced activity. Interestingly, the enhancement factor (*R*) for these mesostructures with respect to that of commercial platinized carbon toward formic acid oxidation ranges up to 2000% for hexagons whereas for multipods and discs they are about 700% and 300% respectively. Similarly, for ethanol oxidation, *R* varies up to 600% for multipods while for discs and hexagons these values are 500% and 200% respectively. For methanol oxidation, *R* is about 750% for hexagons and 450% and 350% respectively for multipods and discs. Thus, present results demonstrate the importance of precise control of morphology by electric field and their potential benefits especially for fuel cell applications since designing a better electrocatalyst continues to be an important challenge.

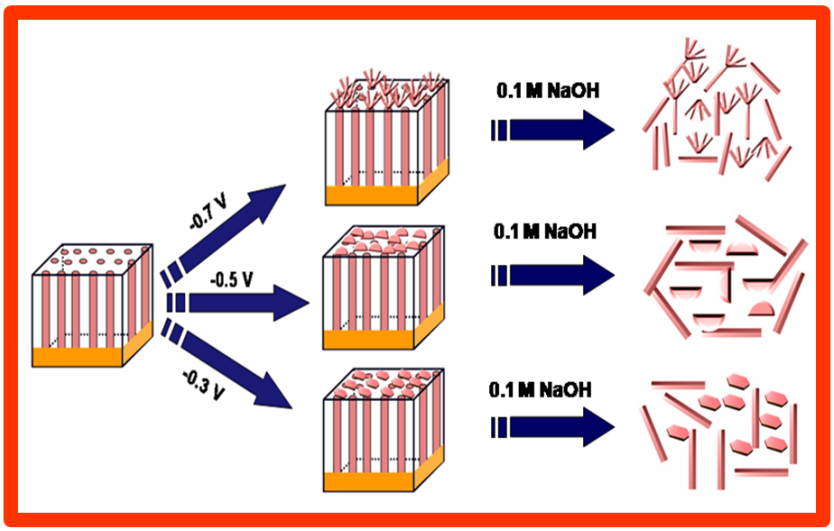

*A part of the work discussed in this chapter has been published in "*Langmuir* **2008**, *24*, 3576".

3.1. Introduction

Materials in mesoscales are known to exhibit a wide range of electrical, optical, and mechanical properties that depend sensitively on both size and shape, and hence their investigation is of fundamental and technological importance.[1-7] As a result, a plethora of research progress has been accomplished in the past few years on the synthesis, characterization, and applications of many metallic and semiconducting mesostructures in various sizes and shapes often with subnanometer resolution.[8-16] Various methods including template synthesis, chemical vapor deposition, and colloidal synthesis using several capping agents\surfactants have been successfully demonstrated to generate many nano to meso level architectures with a remarkable shape control.[17-24] Nevertheless, only limited success has been achieved in synthesizing mesoscale materials with precise morphological control and better shape distribution, despite the use of different types of surfactants. Although the presence of these external agents may alter their intrinsic surface properties, which in turn could hamper some of their technological applications, their presence is essential for long- term stability. For example, certain sensing applications making use of surface enhanced Raman scattering require analyte adsorption to the metallic nanoparticle surface as an essential prerequisite, and consequently the presence of surfactant/capping agents reveals significant interference.[25] In order to obviate this problem, morphological control by electrochemical methods has been identified as a more convenient and reliable approach owing to its sensitivity and ease of handling.[26-28] More significantly, the shape control accomplished by the modulation of an electric field without using any surfactant/capping molecule provides important advantages in terms of both purity of the systems (no surface contamination) and the flexibility to tune many intrinsic properties.

Further, there has been a great deal of interest in studying the shape-dependent catalytic activity of various nanomaterials because both the reactivity and selectivity of these structures in catalytic reactions are dependent on the morphology and therefore on

the crystallographic planes exposed on the surface.[29] For example, El-Sayed's group has recently carried out extensive studies on the shape-dependent catalytic activity of Pt, where tetrahedral Pt is more active than spherical or cubic ones for electron-transfer reaction between hexacyanoferrate(III) ions and thiosulfate ions especially because they contain more catalytically active atoms on the surface.[30] Also, Li et al. have studied the catalytic activity of different shaped silver nanoparticles for the oxidation of styrene[31] to demonstrate that silver nanocubes are more active compared to nanoplates and near-spherical nanoparticles. This is explained on the basis of crystallographic planes, where Ag nanocubes have (100) crystal face as the basal plane whereas, the truncated triangular nanoplates and near spherical nanoparticles predominantly expose their most stable (111) plane. Further, the effect of particle size (ca. 2-9 nm) in methanol, formic acid, and formaldehyde electrooxidation has been explored by Weaver et al. for platinum nanoparticles.[32] These studies clearly indicate that the rate of methanol oxidation decreases for Pt nanoparticle diameters below 4 nm. However, formic acid oxidation exhibits the opposite behaviour while formaldehyde oxidation displays little such sensitivity to size. This size-dependent electrocatalytic activity has been discussed in terms of the availability of Pt terrace sites for the reaction. Although the particle size effect on electrooxidation has been studied, these deal only with spherical particles and hence it is extremely important to carry out similar investigations for various other shapes.

In Chapter 2, we have demonstrated the fabrication of PAM template with linear as well as hierarchically branched nanopore arrays and the control of various factors influencing the pore dimensions. In this chapter, we demonstrate the utility of those linear PAM for the synthesis of different shaped platinum mesostructures through a potentiostatic route followed by a comparison of their electrooxidation activity. To our knowledge, there is no report on the synthesis of different morphology of platinum mesostructures using such a templated electrochemical approach and this mode of confined potentiostatic growth is relevant to the preparation of many other similar mesostructures of Rh, Pd, Ru etc., for their catalytic and other applications. More

interestingly, these differently shaped mesostructures show unique variation in electrocatalytic activity for formic acid, methanol and ethanol oxidations (three important reactions for portable fuel cell applications) in comparison with that of commercial platinized carbon. Analysis of the exchange current density (j_o) using Tafel plot suggests that the hexagons of Pt show better electrocatalytic activity for formic acid oxidation (ca. 3 x 10^{-5} A/cm^2) compared to that of multipods, discs, and commercial platinized carbon (ca. 8 x 10^{-6} A/cm^2) whereas, for ethanol oxidation, multipods show significantly enhanced electrocatalytic activity (ca. 2 x 10^{-6} A/cm^2) compared to that of disc, hexagons, and commercial platinized carbon (ca. 4 x 10^{-7} A/cm^2). Interestingly, for methanol oxidation, hexagons show better performance (ca. 7.76 x 10^{-7} A/cm^2) compared to that of multipods, discs, and commercial platinized carbon (1.02 x 10^{-8} A/cm^2). All these observations are rationalized with the help of a tentative mechanism based on experimental evidences using a combination of both electrochemical and spectroscopic techniques

3.2. Experimental Details

3.2.1. Materials

$H_2PtCl_6.6H_2O$ (99.98%) was purchased from Aldrich chemicals while boric acid (99.5 %) was purchased from Loba Chemie. Solvents like ethanol (99.9 %), methanol (99.5 %) and formic acid (98 %) were purchased from Merck. All reagents were used without further purification and deionized water (18 MΩ) from milli-Q system was used in all experiments.

3.2.2. Preparation of Different Shaped Platinum Mesostructures

Free-standing linear PAM templates fabricated via a two–step anodization (for details see Chapter 2, section 2.4.2) was served as working electrode for templated electrodeposition, after sputtering Au film (200 nm) onto one side of the membrane. (Sputter coating was performed using JEOL JFC-1100E Ion Sputter with a double-pole

horizontal electrode discharge system). Electrodeposition was carried out in an aqueous solution of 5 mM H_2PtCl_6 as the platinum precursor and boric acid, as a buffer (1 mM) at a pH of 2.5. After a pretreatment of the Au film-supported PAM template in ethanol by sonication to drive out trapped air inside the holes, electrodeposition was potentiostatically carried out at -0.3, -0.5, and -0.7 V vs SCE, for 15 min. After electrodeposition, the mesostructures were released from the PAM by dissolving the template in 0.1 M NaOH and then washing several times with deionized water till a neutral pH, followed by a final washing with ethanol. Different structures were subsequently separated from nanorods by centrifugation at 2000 rpm and for each case, almost 90% purity was obtained by this way.

3.2.3. Procedure for the Investigation of Electrocatalytic Activity

In order to investigate the electrocatalytic activity of Pt mesostructures, the working electrode was prepared as follows: 20 wt % Pt mesostructured sample was dispersed well in Vulcan XC -72 carbon (C) using isopropyl alcohol and dropcast to form a thin film on a glassy carbon electrode (ca. 3 mm diameter) using 0.5 wt% Nafion binder and was dried well. A similar procedure was adopted to prepare the electrode of commercial platinized carbon (20 % Pt on Vulcan XC-72 carbon from Arora Matthey Ltd.; diameter = 8 nm) with the same amount.

Cyclic voltammogram (CV) of Pt mesostructures dispersed in Vulcan carbon (Pt/C-mesostructure) was first recorded in 0.5 M H_2SO_4, and the electroactive area (A_{Pt}) was determined from the adsorption/desorption charge of hydrogen measured from CV (ca. 210 $\mu C/cm^2$ for a polycrystalline surface). Further, to measure the electrocatalytic activity of these structures toward formic acid oxidation, the following procedure was adopted: Cyclic voltammogram and transient current-time curve for formic acid oxidation were recorded in a mixture of 0.25 M HCOOH and 0.5 M H_2SO_4 and the response was studied at various potentials ranging from -0.44 V to +0.16 V vs Hg-Hg_2SO_4 at an interval of 0.05 V for a period of 60 s. Further, the current density (j) was obtained after

normalizing the current to A_{Pt}. Before recording the current transients, sufficient care was taken to oxidize any existing adsorbate on the electrode surface so as to obtain a clean surface. Similarly, methanol oxidation was performed in a mixture of 0.5 M CH_3OH and 0.5 M H_2SO_4 whereas, ethanol oxidation was studied in a mixture of 0.1 M C_2H_5OH and 0.1 M $HClO_4$ using a similar procedure. All experiments were also repeated using commercial platinized carbon (Pt/C).

3.2.4. Structural and Morphological Characterization

3.2.4.1. X-ray Diffraction (XRD)

XRD studies were performed in order to understand the crystallinity and also to evaluate the orientation of mesostructures using CuK_α (λ = 1.5405 Å) radiation on a Panalytical XPert Pro diffractometer. Diffraction patterns were collected at a step of 0.02° (2θ) and the background was subtracted with the linear interpolation method. Samples were prepared by making thin films on glass substrates.

3.2.4.2. X-ray Photoelectron Spectroscopy (XPS)

XPS measurements were carried out on a VG MicroTech ESCA 3000 instrument at a pressure of $>1 \times 10^{-9}$ Torr (pass energy of 50 eV, electron takeoff angle 60^o, and overall resolution ~1 eV) using monochromatic Mg Kα (source, $h\nu$ = 1253.6 eV). The core level spectrum of the Pt 4f orbital was recorded with an overall instrumental resolution of ~1 eV and the binding energies (BE) were aligned taking the adventitious carbon BE as 285 eV. The spectra were fitted using a combined polynomial and Shirley type background function.

3.2.4.3. Scanning Electron Microscopy (SEM)

The morphology of platinum mesostructures was examined using a scanning electron microscope and the instrumentation details have already been discussed in Chapter 2,

(section 2.4.5.1). A little amount of sample was dispersed in ethanol and drop-casted on Cu substrate and dried at room temperature.

3.2.4.4. Electrochemical Measurements

All electrochemical experiments were performed on an Autolab PGSTAT30 (Eco chemie) instrument. For electrodeposition, a saturated calomel electrode (SCE) and a Pt foil were used as reference and counter electrodes respectively. For the electrocatalytic study, a glassy carbon electrode modified with mesostructure/C (mesostructure dispersed in Vulcan carbon) was used as the working electrode (section 3.2.3). Also, Hg-Hg_2SO_4 and a platinum foil served as the reference and counter electrodes, respectively.

3.3. Results and Discussion

3.3.1. SEM Analysis

A comparison of the scanning electron micrographs of different shaped Pt mesostructures prepared at various potentials after complete removal of the template is shown in figure 3.1. Interestingly, the image of potentiostatically formed platinum structures at -0.7 V (corresponding to diffusion-limited region in the current-potential curves) shows a distribution of multipods as revealed in figure 3.1a, where the number of arms of each multipod is more than 6, having a common origin with almost the same length (ca. 500 nm). Most of the arms have uniform width (ca. 100 nm), whereas some of the branches are formed by the assembly of nanometer sized rods. It is instructive to compare the present electrochemical route for the formation of Pt multipods with those reported by Yang et al. from organometallic precursors like Pt 2,4-pentanedionate in the presence of a trace amount of Ag acetylacetonate at around 200 ^{o}C.[33] External nucleating agents (Ag salt) has been used here to trigger the formation of platinum multipods of much smaller size, in contrast to our case, where the formation of multipods is achieved exclusively by templated electrodeposition without the assistance of any additive.

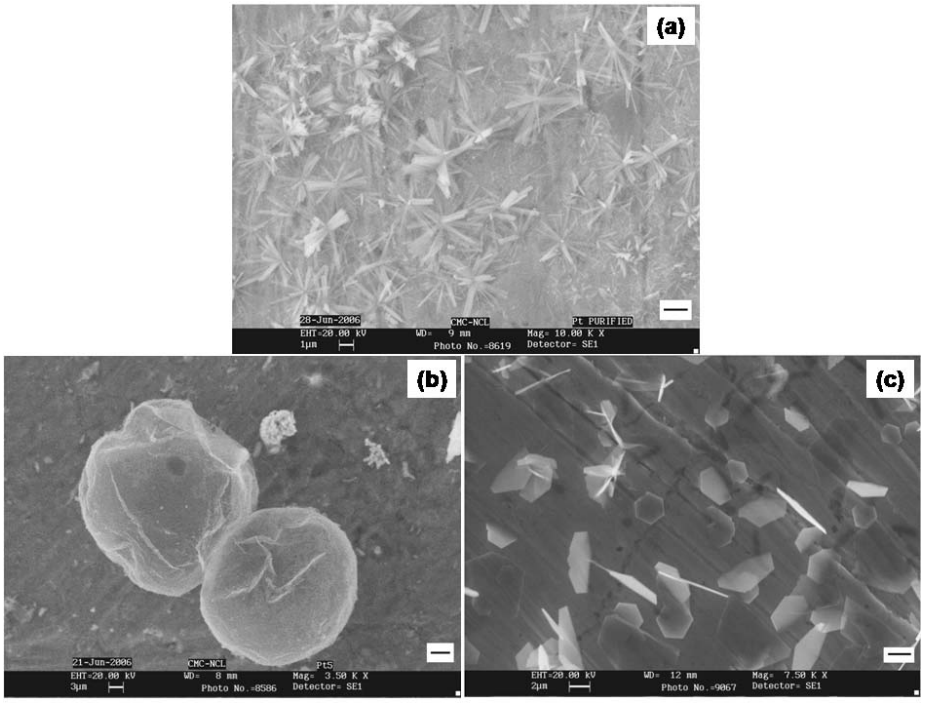

Figure 3.1. (a) - (c) SEM images of platinum mesostructures revealing multipods of platinum prepared potentiostatically at -0.7 V (a), disc shaped structure at -0.5 V (b) and hexagonal structure at -0.3 V (c), after etching the alumina membrane in 0.1 M NaOH; scale bar 1μm.

When templated electrodeposition is carried out at a moderate overpotential (mainly corresponding to the activation polarization region of the current-potential curve) different shapes of Pt structures arise. For example, accurate maintenance of potential at -0.5 V generates disc-shaped mesostructures (diameter ca. 2 μm) as illustrated in figure 3.1b. A close examination of the image, however, reveals that the surface of the disc is not uniform, perhaps because of some involvement of mass transfer effects since the overpotential is about ca. -0.4 V (E_{eq} is -0.1 V). In comparison, electrodeposition at -0.3 V (close to equilibrium potential) predominantly gives hexagons, as shown in figure 3.1c, where the edge length varies from 0.5 μm to 1 μm. In addition to these mesostructures, nanorods of platinum are also obtained, as usually expected from template synthesis. Thus we could observe multipods of Pt at potential regions far away from the equilibrium, hexagonal shaped structures at regions close to equilibrium, and disc-like

structures at intermediate potential regions along with Pt nanorods in all cases, thus illustrating the importance of competition between charge transfer and diffusion. Thus it could be surmised that diffusion limited aggregation favours multipod/fractal formation while kinetic control generates hexagons and discs.

3.3.2. Current –time Transients

In order to understand the nucleation and growth mechanism of such uniquely shaped mesostructures we have analyzed the current transients after polarizing the electrode at various potentials as shown in figure 3.2(a-f). Current-time response is measured after stepping the potential from the equilibrium value to -0.3 (a), -0.5 (c), and -0.7 V (e) respectively. On stepping the potential from the equilibrium value, the current first increases instantaneously to a maximum (I_{max}), followed by a slow exponential decay. Further, a comparison of I_{max} at three different overpotential shows a direct correlation of the magnitude of I_{max} thus establishing a vital link in controlling the morphology of Pt mesostructures during electrodeposition.

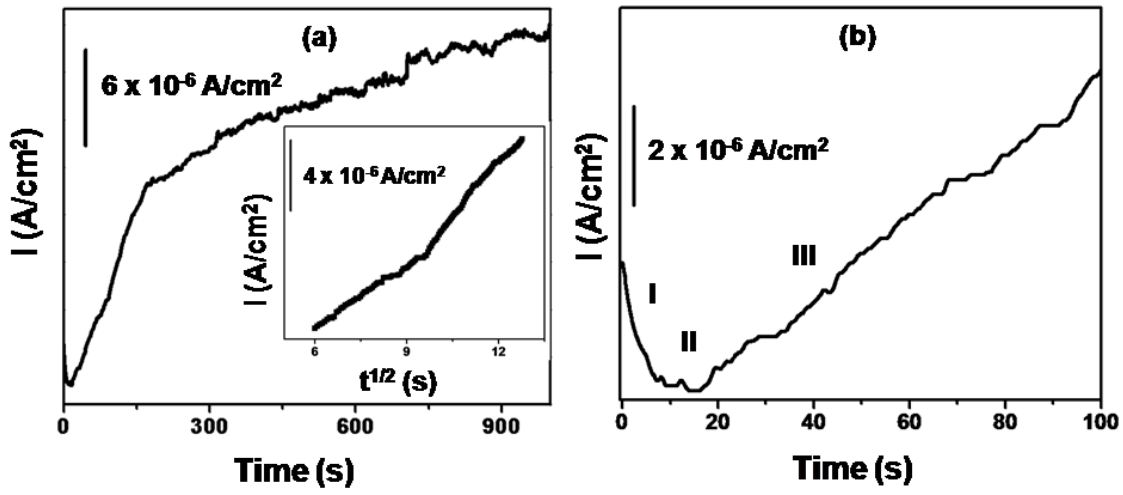

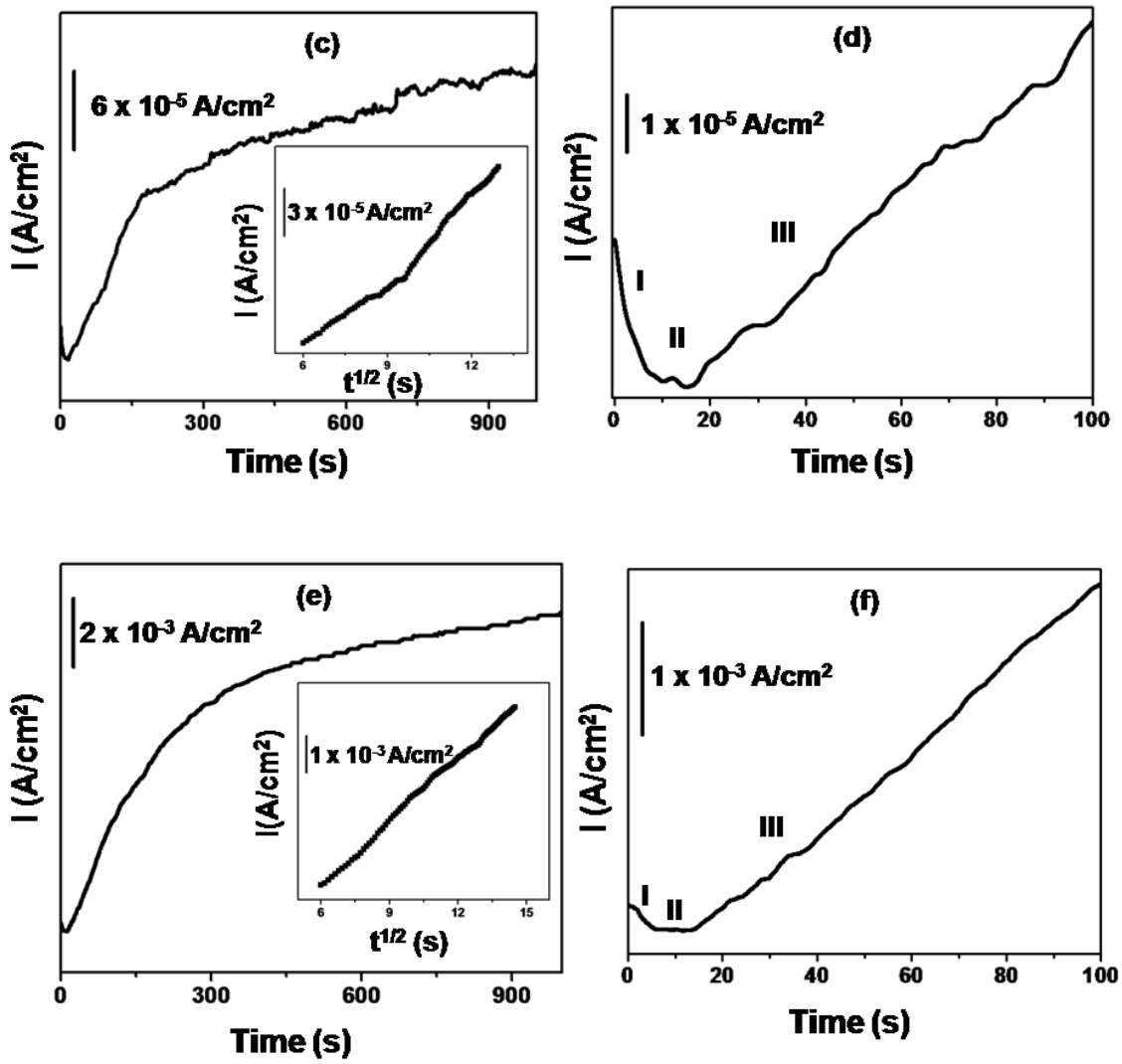

Figure 3.2. Current transients for different potential steps -0.3, -0.5 and –0.7 V revealed in figure (a), (c) and (e) and the inset shows the corresponding I vs $t^{1/2}$ plots; three different zones involved during current transients are clearly shown in (b), (d) and (f) respectively.

For the convenience of analysis, three different zones can be distinguished in all these I-t transients as illustrated in figure (b), (d), and (f). For example, zone 1 reveals an exponential decrease (in few seconds) after an instantaneous rise in current which is

attributed to the effect of double layer charging while zone II corresponds to the deposition of the metal into the pores of the template since the current variation is less prominent. Here, soon after the initial nuclei formation on the bottom of the pore (i.e., on the cathode surface which in our case is gold), the growth proceeds via a two-dimensional nucleation involving a layer-by-layer growth mode.[34]

I-t transients in zone III result from an increase in the deposition area that occurs when the pores are completely filled with the metal and the deposition begins on the surface of the membrane. It is this region which is extremely critical to regulate various shapes depending on the overpotential variation. Finally, almost a steady-state behavior is achieved when the deposition of metal saturates the surface where the limiting current is achieved by the increased overpotential. We have analyzed the rising part of the transient curve (zone III) at three different potentials to check whether the nucleation process occurs by an instantaneous or a progressive mechanism (inset of Figure a, c, and e). The linearity observed using the experimental data for I vs $t^{1/2}$ suggests that an instantaneous nucleation mechanism is valid in all cases.[35] However, there is a slight deviation from linearity, perhaps arising from the presence of pores responsible for changes from ideal Cottrell diffusion (valid mainly for planar surfaces with linear semi-infinite diffusion conditions); shape asymmetry and edge effects could also possibly contribute to this deviation.

3.3.3. XRD Analysis

To understand the crystal structure and preferential growth direction of these mesostructures, powder XRD is very helpful and accordingly figure 3.3 shows a comparison of XRD pattern of Pt/C-hexagons, Pt/C-discs, Pt/C-multipods and Pt/C which reveals the formation of a cubic structure with high crystallinity. All diffraction peaks, (111), (200), and (220) match well with Bragg reflections of the standard and phase-pure face centered cubic (fcc) structure of Pt. Also the XRD pattern reveals no change in the peak position for three different mesostructures as compared to that of Pt multipods

reported by Yang et al. [36] A comparison of the intensity ratio of $I_{(111)}/I_{(200)}$ and $I_{(200)}/I_{(220)}$ reveals that the intensity ratio of the former is higher for hexagons whereas the latter one is higher for multipods *(vide infra).* Apart from the response corresponding to Pt, a broad peak at $2\theta = 25^{o}$ is associated with the (002) planes of Vulcan XC-72 carbon, which is the support.

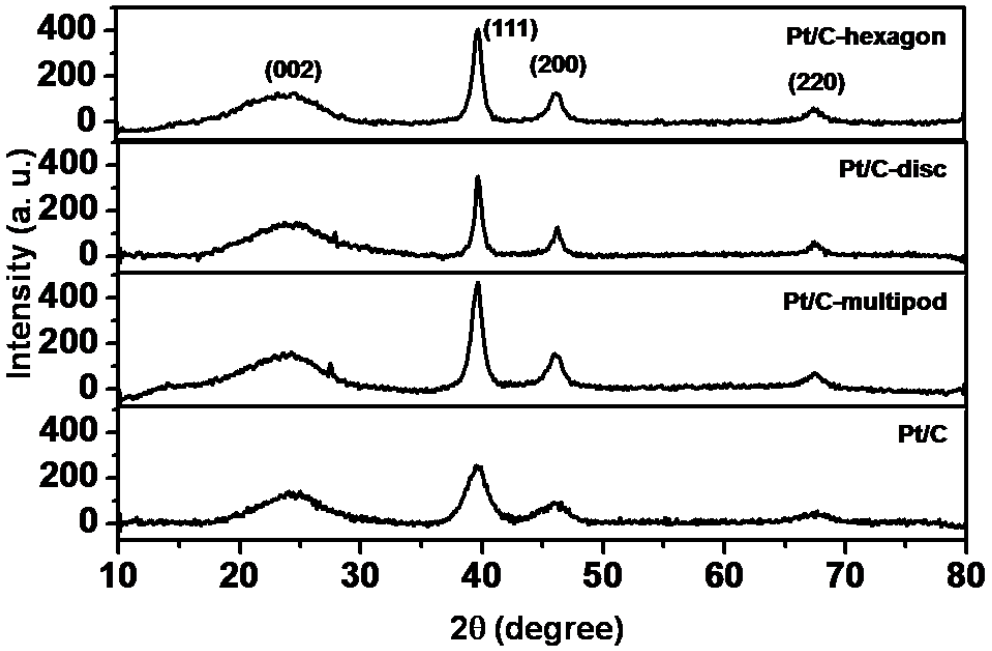

Figure 3.3. A comparison of XRD pattern of different morphology platinum mesostructures dispersed in vulcan carbon; all these diffraction peaks match well with the corresponding peaks of fcc structure of bulk platinum; figure also includes XRD pattern of commercial platinized carbon (Pt/C).

3.3.4. XPS Analysis

Information on the oxidation state of different shaped platinum mesostructures is provided by the XPS analysis, and accordingly a comparison of the XP spectra of Pt-multipods, Pt-disc, and Pt-hexagon is shown in figure 3.4(a-c). Figure (a) shows the Pt 4f region of Pt-multipods, where, deconvolution of the peak reveals two signals at 71.1 eV and 74.3 eV (after carbon correction) corresponding to Pt $4f_{7/2}$ and $4f_{5/2}$ respectively.[37] These values confirm that platinum multipod exists in metallic state with a typical peak to

peak separation of ca. 3 eV, in agreement with that of bulk platinum metal. In addition, XP spectra of Pt-disc and Pt-hexagon (figure b, and c), also reveal similar binding energy values as observed for Pt-multipods, which again supports the existence of Pt(0) oxidation state.

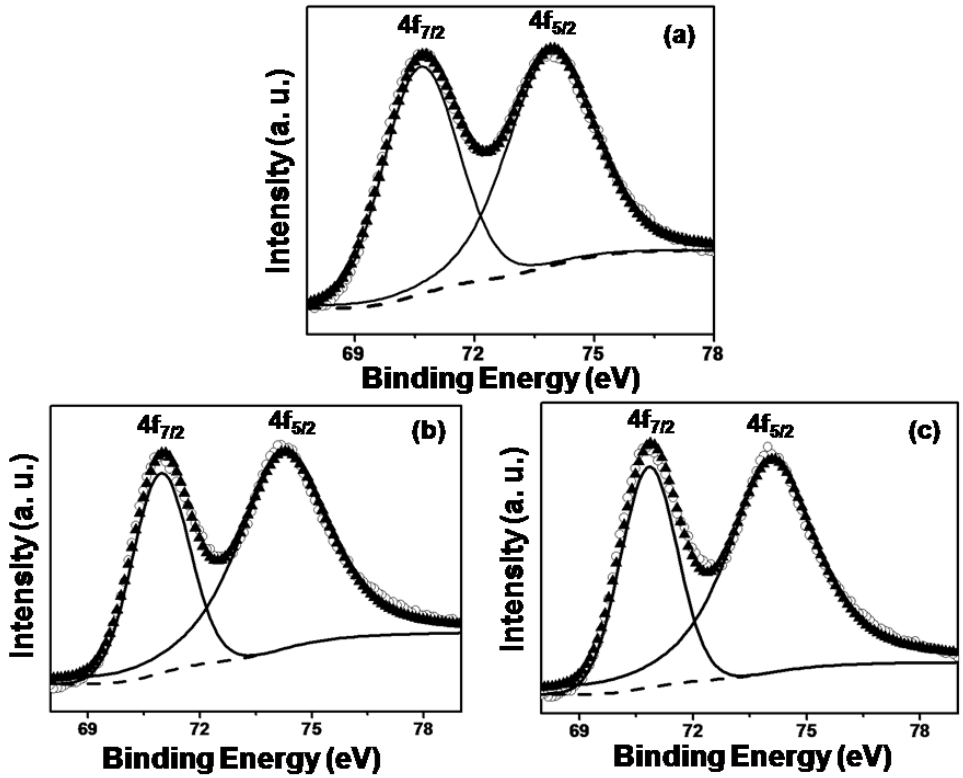

Figure 3.4. X-ray photoelectron spectra of Pt (a) multipod, (b) disc, and (c) hexagon where, Pt 4f core level is deconvoluted using Shirley software; circles represent the raw data while triangles represent the fitted data for the overall signal; dash lines indicate the background, whereas the solid lines represent the deconvoluted individual peaks.

All the above results indicate the importance of electric field modulation through the pores of PAM as a primary reason for the shape variation for these electrodeposited Pt particles after the template removal. This, of course, assumes that template removal by leaching has no effect on the shape of these Pt particles. Accordingly, Scheme 3.I conveniently depicts a comparison of the shape modulation during the potentiostatic

electrodeposition of these structures followed by the release after a complete dissolution of the PAM membrane with sodium hydroxide. Similar shape modulation accomplished by various capping agents in colloidal synthesis suggests that the electric field plays a key role in tuning the shape similar to perhaps the role of concentration of capping agents.[38,39,13] For example, hexagonal shaped mesostructures with the lowest specific surface energy appear at a low overpotential (-0.3 V) whereas multipods with high specific surface energy require high overpotential (-0.7 V) for their formation. Hence, by changing the applied potential of the cathode, it is possible to tune different shapes of electrodeposited mesostructures as illustrated in this case. Observation of these various shapes at different applied potentials is in close agreement with the results of Xiao et al., where different morphological particles at applied potentials close to the equilibrium value and high aspect ratio structures, such as nanowires, nanobrushes, and multipods at high overpotentials, have been obtained on HOPG surfaces.[26]

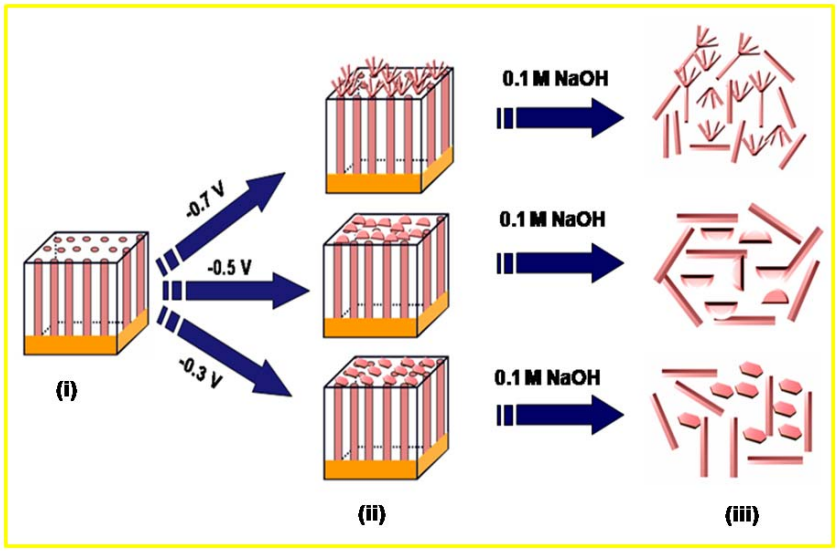

Scheme 3.1. Electric field dependent, morphological evolution of platinum mesostructures using PAM. (i) PAM with one side evaporated with Au film for electrical contact; (ii) formation of hexagonal, disc and multipod structures of Pt over alumina membrane at potentials -0.3 , -0.5 and -0.7 V respectively; (iii) desolution of the membrane in 0.1 M NaOH and the release of different morphology platinum mesostructures along with the nanorods.

3.3.5. Electrocatalytic Activity of Platinum Mesostructures toward Formic acid, Ethanol, and Methanol Oxidation Reactions

While hydrogen as a primary fuel in a polymer electrolyte membrane fuel cell (PEMFC) allows higher energy efficiency to be obtained, its production and storage are expensive since it require either on-site H_2 storage or an onboard reformer to extract H_2 from organic fuels. As a result, extensive research has been launched into the development of direct liquid fuel cells. In liquid fuels, mainly methanol, ethanol, and formic acid are employed, since they are abundant, inexpensive and can be easily handled, stored, transported. Their theoretical mass energy density is also high (for example energy density of methanol and ethanol are 6.1 and 8.0 kWh/kg respectively). However, the electrooxidation kinetics of these organic molecules is very subtle and greatly sensitive to the surface structure leading to a dramatic variation with size, shape and nature of the electrode material. In the following section, we report the results of a comparative study of the electrocatalytic performance of different shaped platinum mesostructures such as multipods, discs and hexagons toward the electrooxidation of formic acid, ethanol, and methanol which, are promising reactions for microfuel cells.

3.3.5.1. Formic Acid Oxidation

The overall reaction involved in the irreversible electrooxidation of formic acid to CO_2 on Pt surface could be written as

$$HCOOH \rightarrow CO_2 + 2H^+ + 2e^- \quad \text{..... (3.1)}$$

$$E^0 = -0.25 \text{ V vs NHE}$$

The electrooxidation of HCOOH to CO_2 on a Pt surface proceeds *via* a dual path mechanism, which involves a reactive intermediate (main path, dehydrogenation) and adsorbed CO as a poisoning species (parallel path, dehydration). The reactive intermediate during the main path is adsorbed formate, which has been confirmed using surface enhanced infrared reflection absorption spectroscopy (SEIRAS).[40]

Figure 3.5 compares cyclic voltammetric response of different shaped platinum mesostructures toward formic acid oxidation at 50 mV/s in a mixture of 0.5 M H_2SO_4 and 0.25 M HCOOH where all samples reveal the characteristic features of formic acid oxidation. Because of the substrate effect (initial effects) variations in the first cycle, we show here only the second cycle, as a representative example although current corresponding to CO oxidation progressively increases with the cycle. The voltammetric response of Pt/C is also shown in figure 3.5. The voltammograms show two peaks during the anodic scan (at -0.07 and 0.72 V for Pt/C-hexagon) while only one peak (-0.15 V for Pt/C-hexagon) is observed during the reverse (cathodic) scan. A slight change in peak position is observed for different electrodes, as obvious from the voltammogram.

It has been widely accepted that formic acid is oxidized to CO_2 via a dual path mechanism, which involves a reactive intermediate (main path, dehydrogenation) and adsorbed CO as the poisoning species (parallel path, dehydration).[41] Hence, all the noticeable current can be attributed to the oxidation of formic acid and/or CO to CO_2. The first anodic peak is due to oxidation of HCOOH to CO_2 on unblocked surface sites[42] whereas the second anodic peak corresponds to the oxidation of adsorbed CO (peak current slightly increases on cycling). During the cathodic sweep, a peak is observed after the partial reduction of irreversibly formed surface oxides, which represents the real catalytic activity of the Pt surface. Interestingly, a close examination of the ratio of area under the first and second anodic peak reveals that charge consumed due to the oxidation of HCOOH to CO_2 is higher compared to that for CO to CO_2, in contrast to the earlier reports.[41] We have calculated this ratio for different shapes of Pt structures, which shows the following order: Pt/C-hexagon > Pt/C-multipod > Pt/C-disc > Pt/C. Hence, it is clear that compared to Pt/C our Pt mesostructures show higher activity for HCOOH oxidation to CO_2 than that to CO, perhaps due to significantly less CO poisoning on Pt mesostructures. In addition, the peak during the cathodic sweep corresponding to the real catalytic activity of the Pt surface almost retraces the first anodic peak as seen from the voltammogram, which clearly confirms less CO adsorption. Interestingly, a comparison of the peak currents of these different electrodes reveal significant change as follows:

Pt/C-hexagon > Pt/C-multipod > Pt/C-disc > Pt/C. (Current has been normalized to the electroactive Pt surface area, A_{Pt}). In addition to the above observed features, a comparison of the voltammetric response of Pt/C and mesostructures/C reveals that the hydrogen adsorption/desorption features of the latter are significantly smaller than that of the former. This is presumed to be due to the blocking of some of the active sites for hydrogen adsorption by carbon or may be due to the poor dispersion of the mesostructures in carbon.

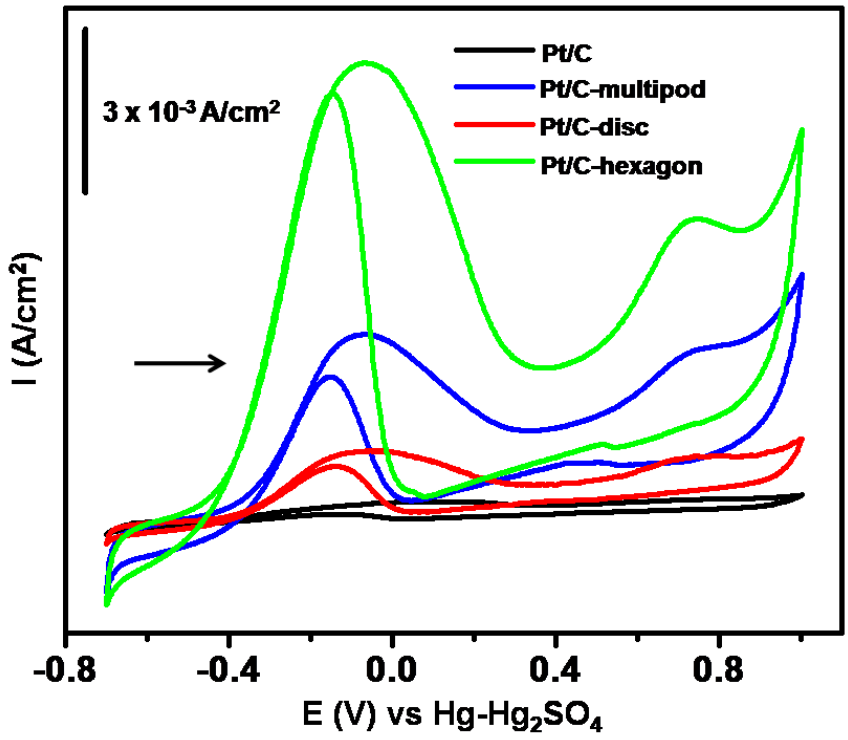

Figure 3.5. Cyclic voltammetric response (2nd cycle data) of Pt/C-multipod, Pt/C-disc, Pt/C-hexagon and Pt/C towards formic acid oxidation at 50 mV/s in a mixture of 0.25 M HCOOH and 0.5 M H_2SO_4 is shown.

Figure 3.6a-d shows the voltammogram of Pt/C-multipod, Pt/C-disc, Pt/C-hexagon, and Pt/C at different scan rates where a shift in peak position with scan rate is observed, as expected for an irreversible charge transfer process. However, the variation

of peak current with scan rate reveals a slight deviation from linearity. This type of non-linearity in the variation of peak current with scan rate was reported by Matsuda et al.[43] for an irreversible systems, and explained in terms of a parameter 'Λ', which is a quantitative measure of reversibility, being effectively the ratio of the kinetics of charge transfer to the mass transfer. For an irreversible reactions, the value of 'Λ' is rather smaller as compared to that of a reversible one.

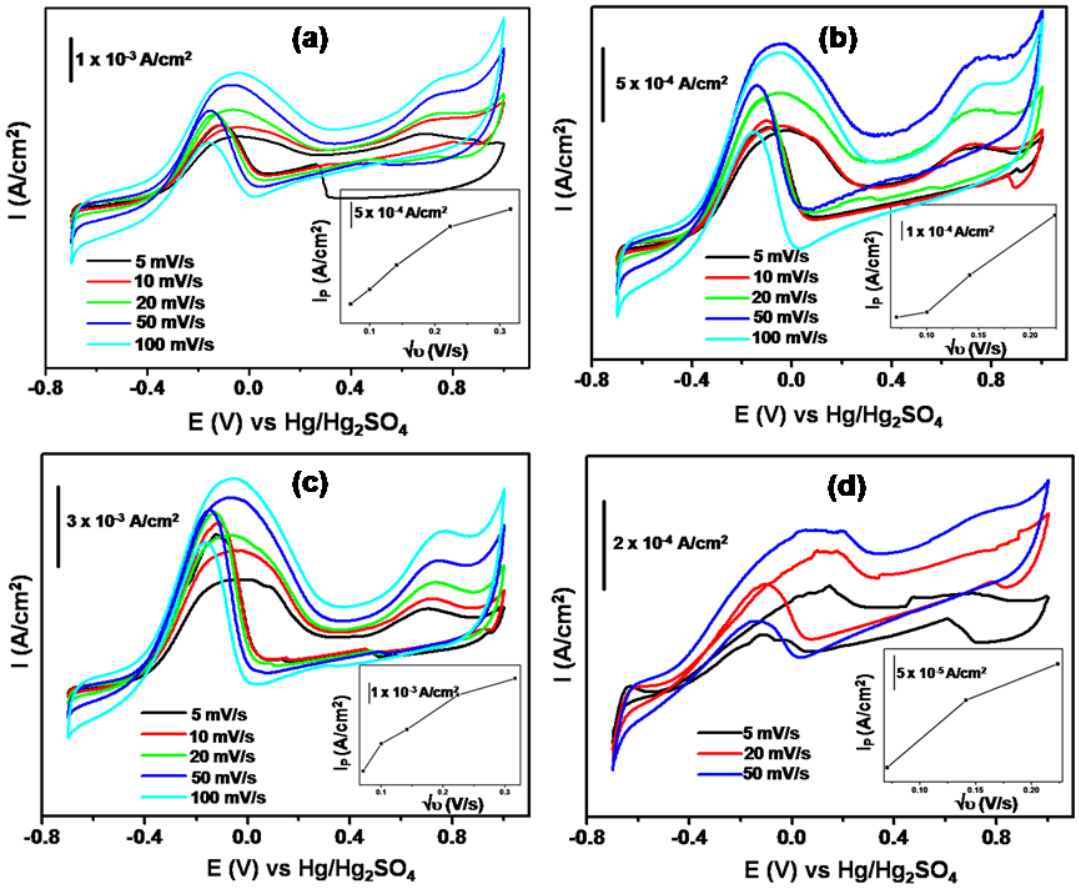

Figure 3.6. Superimposed cyclic voltammetric response of (a) Pt/C-multipod, (b) Pt/C-disc, (c) Pt/C-hexagon and (d) Pt/C toward formic acid oxidation at different scan rates; inset shows the plot of I_p vs $\nu^{1/2}$ of the respective electrodes.

Figure 3.7 shows a comparison of current–time transients of formic acid oxidation at -0.09 V (potential selected from cyclic voltammogram) on the Pt/C, Pt/C-multipod, Pt/C-disc, and Pt/C-hexagon at room temperature after normalizing the current with respect to the electroactive Pt surface area (A_{Pt}). Interestingly, the current density on Pt/C-hexagon is significantly higher compared to that on other structures and the order is as follows: Pt/C-hexagon > Pt/C-multipod > Pt/C-disc > Pt/C. The enhancement factor *R*, which is defined as the ratio of the current density on Pt/C-hexagon versus that acquired on Pt/C, ranges up to 2000% whereas for Pt/C-multipods versus Pt/C it is up to 700% and for Pt/C-disc versus Pt/C the value ranges up to 300% respectively, depending upon the electrode potential. Similar shape dependent studies carried out Wang et al. for tetrahexahedral platinum nanocrystals towards formic acid oxidation reveals only 400% and 310% enhancement respectively for Pt nanospheres and Pt/C catalyst.[44]

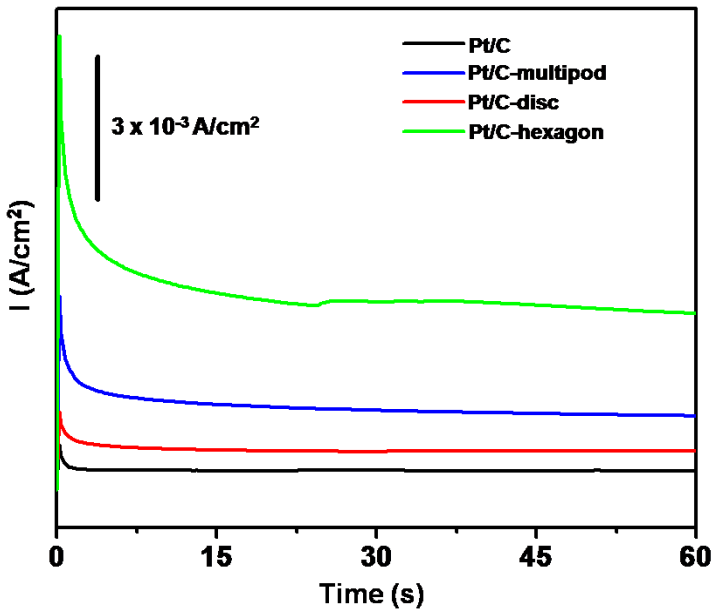

Figure 3.7. A Comparison of the catalytic activity of Pt/C-multipod, Pt/C-disc, Pt/C-hexagon and Pt/C towards formic acid oxidation as revealed in the current-time transients at a potential of -0.09 V for 60 s.

Steady-state current density from the I-t transients (corresponding to various potentials, -0.44 V to +0.16 V) for formic acid oxidation is plotted against each respective potential in figure 3.8 in order to compare their current density (j). A comparison of the j at a given potential (-0.1 V) for different mesostructures of Pt and Pt/C clearly illustrates superior electrocatalytic properties of Pt hexagons. For example, the current density on Pt/C-hexagon, Pt/C-multipod, Pt/C-disc, and Pt/C structures for formic acid oxidation at -0.1 V are 3.62 $x10^{-3}$, 1.35 $x10^{-3}$, 6 x 10^{-4} and 1.9 x 10^{-4} A/cm^2, respectively. In each case, a well-defined volcanic plot is observed, with a maximum near -0.04 V and with decrease in the current density successively at both sides of this potential. The drop in the catalytic performance at lower potentials, may be ascribed to the decrease in the electrochemical driving force that favours the oxidation reaction whereas the deactivation at potentials higher than the platinum oxidation threshold should be attributed to the (bi)sulphate interactions and also due to the oxide formation.[41]

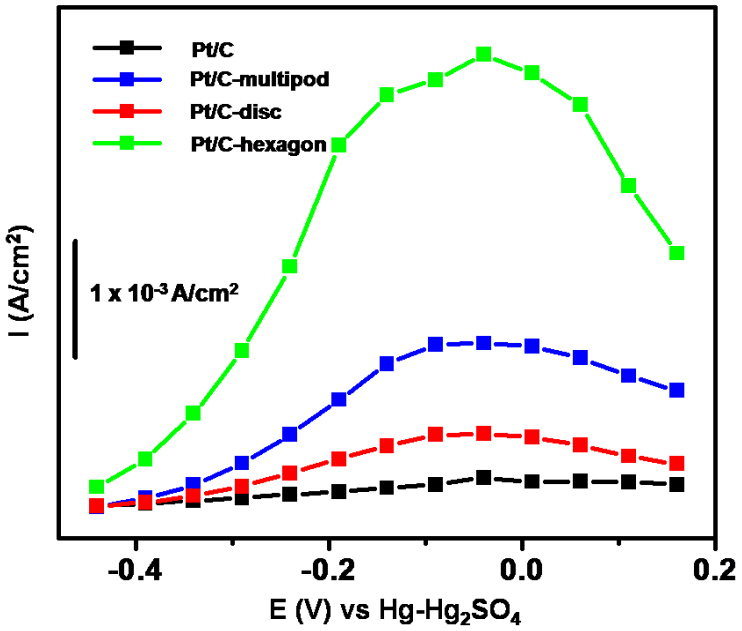

Figure 3.8. Potential-dependent steady state current density of formic acid oxidation on Pt/C-multipod, Pt/C-disc, Pt/C-hexagon and Pt/C, where all the electrodes show maximum activity at -0.04 V.

In order to measure the exchange current density (j_o) towards formic acid oxidation, Tafel polarization studies have been carried out in acid electrolytes using these mesostructures dispersed in C as working electrodes. Accordingly, a plot of log j versus overpotential (η) for three different Pt structures and for Pt/C is shown in figure 3.9a-d, facilitating the estimation of exchange current density from the intercept. Since j_o is a direct measure of the electron-transfer kinetics at the interface at equilibrium conditions a summary of these values in Table 3.1 is very useful to compare the electrocatalytic properties. For example, j_o is slightly higher for the Pt/C-hexagon electrode than that of the Pt/C-multipod, and Pt/C-disc electrodes and Pt/C which could be explained based on the results of other studies.

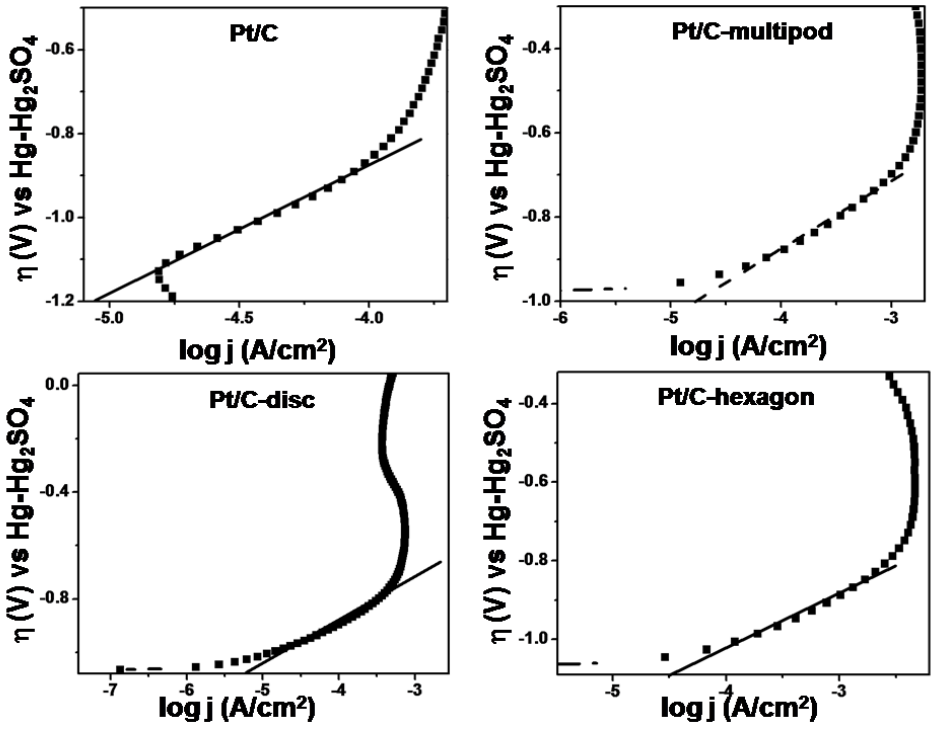

Figure 3.9. A comparison of Tafel Plot for formic acid oxidation on Pt/C-multipod, Pt/C-disc, Pt/C-hexagon and Pt/C under galvanostatic conditions in a mixture of 0.25 M HCOOH and 0.5 M H_2SO_4.

Table 3.1. A summary of exchange current density of Pt/C-multipod, Pt/C-disc, Pt/C-hexagon and Pt/C toward formic acid, ethanol and methanol oxidation estimated from the intercept of Tafel plots based on Figure 3.9.

Electrodes	Exchange Current Density (A/cm^2)		
	Formic acid oxidation	Ethanol oxidation	Methanol oxidation
Pt/C	8×10^{-6}	4×10^{-7}	1.02×10^{-8}
Pt/C-Multipod	1.7×10^{-5}	2×10^{-6}	4.46×10^{-7}
Pt/C-Disc	10×10^{-6}	1×10^{-6}	3.57×10^{-7}
Pt/C-Hexagon	3×10^{-5}	6.3×10^{-7}	7.76×10^{-7}

It is clear that Pt/C-hexagon shows better catalytic activity compared to that of Pt/C-multipod, Pt/C-disc, and Pt/C, for formic acid oxidation. Increase in the rate of electrocatalytic activity has been well studied by means of foreign ad-atoms and anion effects.[45] However, any increase in current density due to the presence of foreign ad-atoms could be neglected in our case since we have not used any foreign ad-atoms. Similarly since the electrocatalytic activity has been studied for all electrodes in the same electrolyte, it is unlikely that the contribution from anion effects is significant. More interestingly, our observation could be correlated with the structural data obtained from XRD results especially because all samples show higher intensity of the (111) crystallographic plane compared to that of the (200) and (220) planes. In addition, the structural effect on formic acid oxidation has been well studied to confirm less CO poisoning on (111) planes. Since for all our samples, (111) plane is highly intense, the oxidation of HCOOH to CO_2 is favored during the positive scan with poor CO adsorption features. Further, in close examination of the intensity ratio of $Pt_{(111)}/Pt_{(200)}$, it is obvious that this ratio varies as follows: Pt/C-hexagon > Pt/C-multipod > Pt/C-disc > Pt/C. Thus,

the Pt/C-hexagon shows higher activity toward formic acid oxidation compared to that of Pt/C-multipod, Pt/C-disc, and Pt/C, respectively. This is in excellent agreement with other reports on the electrocatalytic activity of $Pt_{(hkl)}$ planes for formic acid oxidation where the highest activity during the anodic scan is observed for the (111) plane.[46] Hence, from the above observation, we conclude that one of the possible reasons for varying the reactivity of different shapes of platinum mesostructures is the difference in the intensity ratio of various crystallographic planes present in the sample.

3.3.5.2. Ethanol Oxidation

The overall reaction involved in the electro-oxidation of C_2H_5OH to CO_2 on Pt electrode surface could be written as

$$CH_3CH_2OH + 3H_2O \rightarrow 2CO_2 + 12H^+ + 12e^- \quad \text{..... (3.2)}$$

$E^0 = 0.08$ V vs NHE

Electrooxidation of ethanol to CO_2 is a very complex reaction associated with the cleavage of the C-C bond, which requires higher activation energy than C-H breaking. The reaction is known to proceed via a multistep mechanism, involving a number of adsorbed intermediates and by products resulting from incomplete ethanol oxidation such as adsorbed CO and C-1 and C-2 hydrocarbon residues. Since, the breaking of C-C bond for the total oxidation to CO_2 is a difficult talk, partial oxidization products such as CH_3CHO and CH_3COOH also form along with CO_2. These intermediates and byproducts have been detected using differential electrochemical mass spectrometry (DEMS), infrared spectroscopy, ion chromatography, and liquid chromatography.[47]

Figure 3.10 accordingly, shows the overlayed cyclic voltammetric response of different shaped platinum mesostructures (and also commercial Pt/C for comparison) for ethanol oxidation in a mixture of 0.1 M C_2H_5OH and 0.1 M $HClO_4$ at 20 mV/s. These voltammograms show two peaks during the anodic scan (at 0.17 and 0.70 V respectively for Pt/C-multipods), while one peak (at -0.02 V for Pt/C-multipod) is observed during the cathodic scan. The first anodic peak corresponding to the -OH bond formation on Pt

surface, is presumed to play an important role in ethanol oxidation facilitating the cleavage of the C-C bond thus producing CO_2 via the strongly adsorbed CO intermediate.[48] Also, it is important to point out that not only the strongly adsorbed CO, intermediates with one or two carbon atoms also are formed on Pt surface.[49] Further, the second anodic peak is caused by the formation of CO_2 and other by-products such as acetic acid and acetaldehyde.[49] Interestingly, in the negative-going potential sweep, only one anodic peak appears, which is attributed to renewed oxidation of ethanol. A close examination of these voltammogram reveals a remarkable variation of the peak current for different structures as follows: Pt/C-multipod > Pt/C-disc > Pt/C-hexagon > Pt/C.

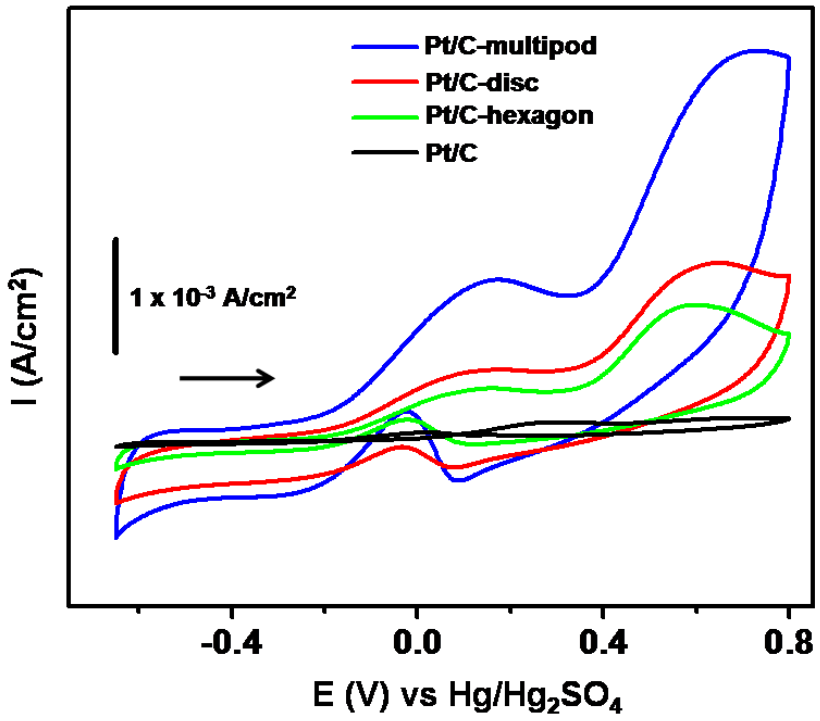

Figure 3.10. Cyclic Voltammetric response (2nd cycle data) of Pt/C-multipod, Pt/C-disc, Pt/C-hexagon and Pt/C towards ethanol oxidation at 20 mV/s in a mixture of 0.1 M C_2H_5OH and 0.1 M $HClO_4$.

Figure 3.11a-d shows the voltammogram of Pt/C-multipod, Pt/C-disc, Pt/C-hexagon, and Pt/C at different scan rates where a shift in peak position suggests an

irreversible charge transfer. As observed for formic acid oxidation, here also the variation of peak current with scan rate reveals a slight deviation from linearity.

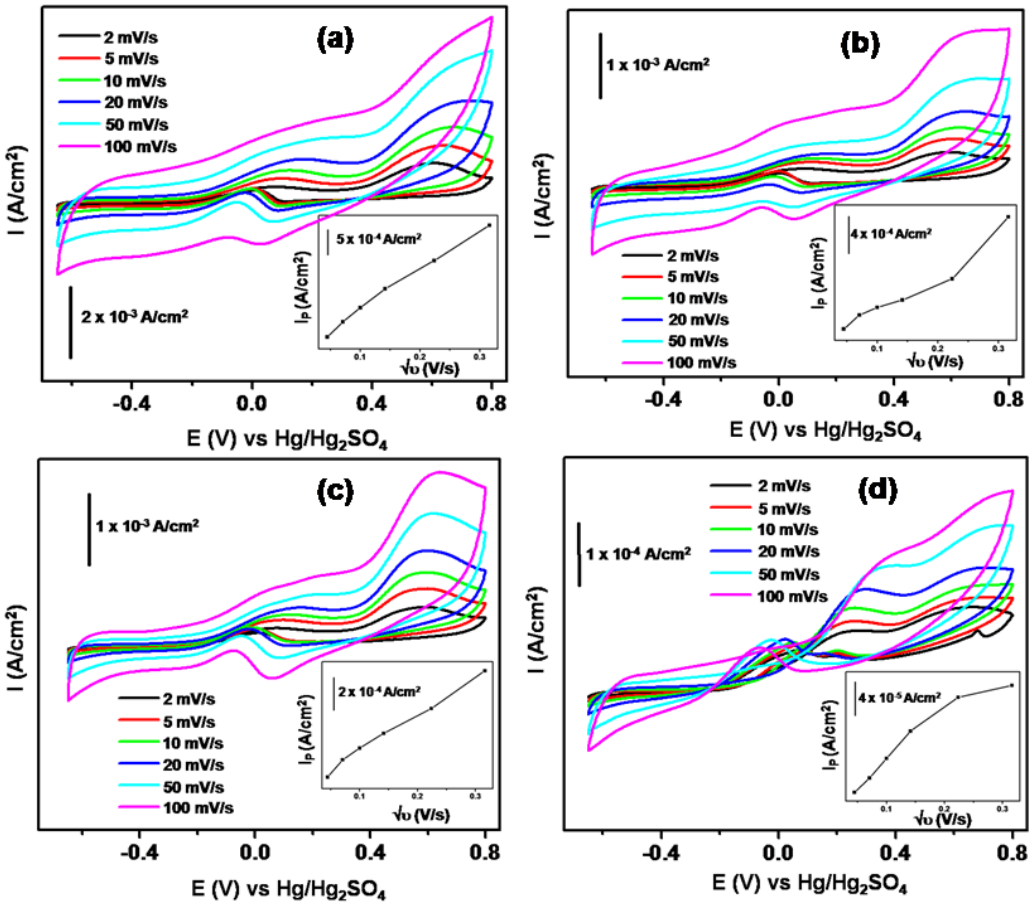

Figure 3.11. Overlayed cyclic voltammetric response of (a) Pt/C-multipod, (b) Pt/C-disc, (c) Pt/C-hexagon and (d) Pt/C toward ethanol oxidation at different scan rates; inset shows the plot of I_p vs $\nu^{1/2}$ of the respective electrodes.

Figure 3.12 shows a comparison of current–time transients of ethanol oxidation at -0.04 V (potential selected from the cyclic voltammogram) on the Pt/C, Pt/C-multipod, Pt/C-disc and Pt/C-hexagon at room temperature. The current density is higher for Pt multipods compared to that for other structures and the activity varies in the following order: Pt/C-multipod > Pt/C-disc > Pt/C-hexagon > Pt/C. This independently confirms the observed trend in the polarization plot. Interestingly, the enhancement factor *R*,

(which is defined as the ratio of the current density measured on a specific shape versus that acquired on Pt/C spherical structures) varies up to 600 % for multipod whereas for Pt/C-disc it is about 500 % and for Pt/C-hexagon versus Pt/C about 200 % respectively, depending on the electrode potential.

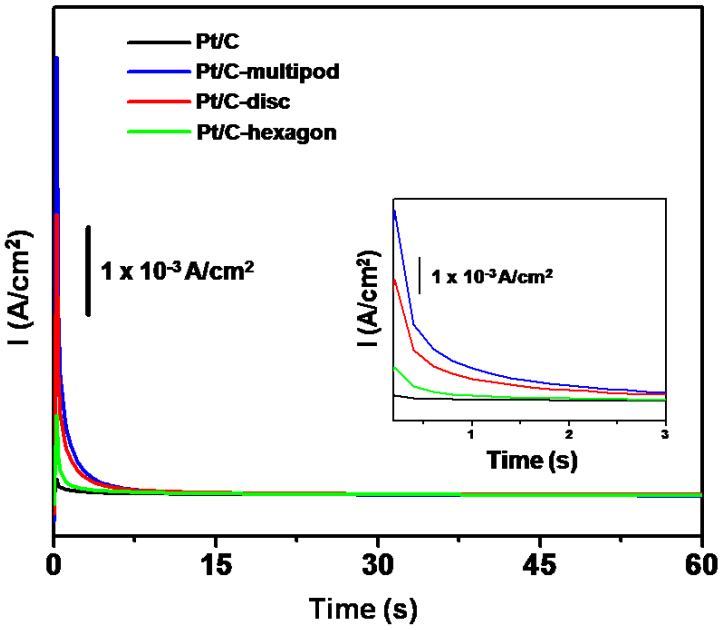

Figure 3.12. Comparison of the current-time transients of Pt/C-multipod, Pt/C-disc, Pt/C-hexagon and Pt/C towards ethanol oxidation at a potential of -0.04 V; inset shows the enlarged view.

A comparison of the steady state current density (obtained from the current transients recorded for 60 s) at different potential is shown in figure 3.13, where we observe that at a given potential, say +0.025 V, the corresponding current density on Pt/C-multipod, Pt/C-disc, Pt/C-hexagon and Pt/C are 2.4 x 10^{-4}, 1.7 x 10^{-4}, 8.33 x 10^{-5} and 3.8 x 10^{-5} A/cm^2 respectively.

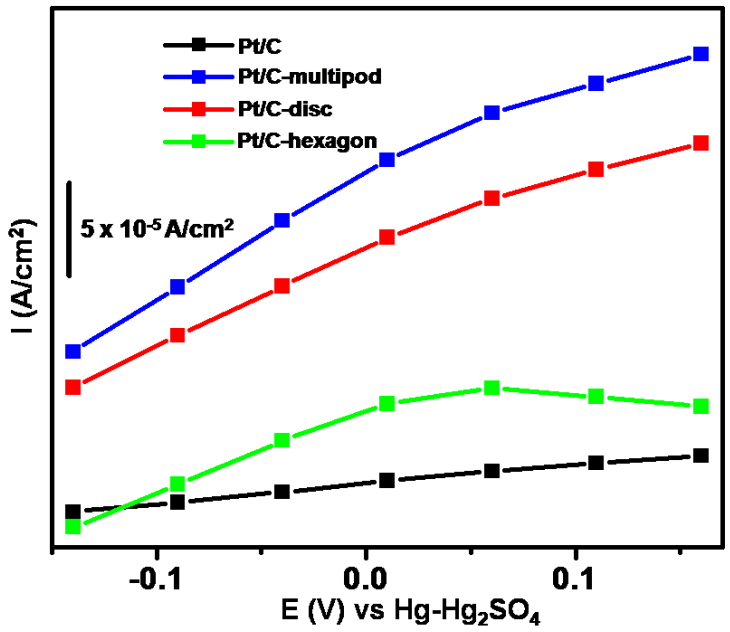

Figure 3.13. Potential-dependent steady state current density for ethanol oxidation on Pt/C-multipod, Pt/C-disc, Pt/C-hexagon, and Pt/C in a mixture of 0.1 M C_2H_5OH and 0.1 M $HClO_4$.

Further, to evaluate j_o corresponding to the ethanol oxidation on these three mesostructures and also on commercial Pt dispersed in C, we have carried out Tafel polarization (figure 3.14 (a-d)), which enables a comparison of the j_o values as summarized in Table (3.1). The value of j_o is higher for the Pt/C-multipod electrode than that of the Pt/C-disc, Pt/C-hexagon, and Pt/C perhaps due to the change in the intrinsic rate constant of this reaction.

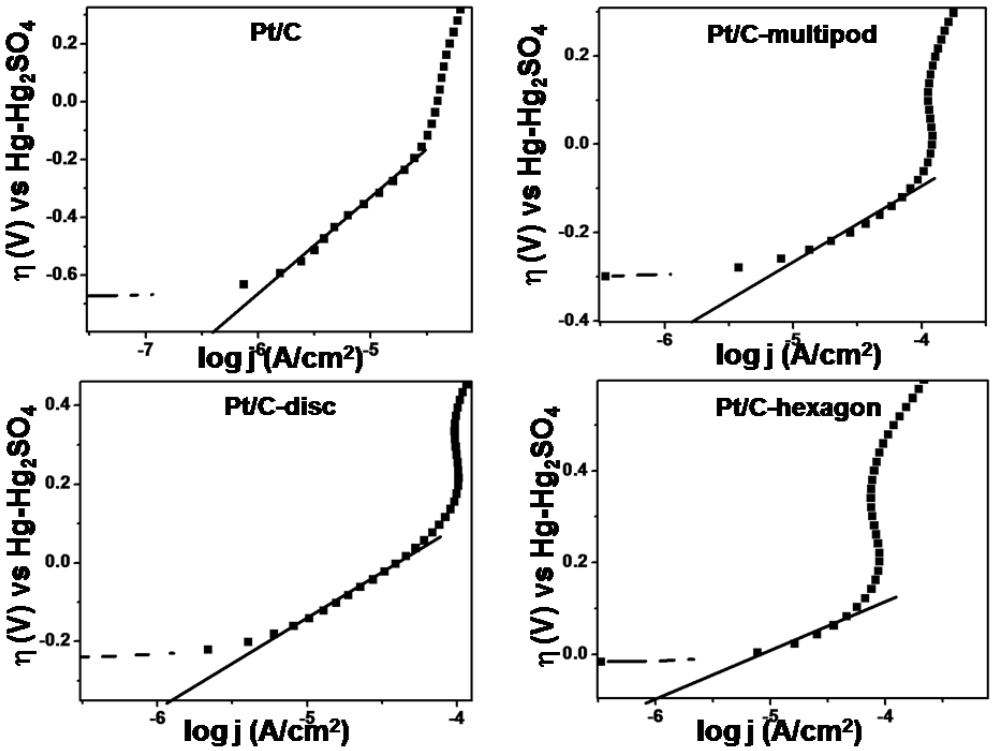

Figure 3.14. Tafel Plots for ethanol oxidation on Pt/C-multipod, Pt/C-disc, Pt/C-hexagon and Pt/C electrodes in a mixture of 0.1 M C_2H_5OH and 0.1 M $HClO_4$.

Thus from the above studies, it is clear that Pt/C-multipod shows better electrocatalytic activity for ethanol oxidation compared to that of Pt/C-disc, Pt/C-hexagon, and Pt/C respectively. Thus present observation could be further explained by the XRD results, using the higher intensity ratio of $Pt_{(200)}/Pt_{(220)}$ for multipods than that for discs, hexagons, and commercial samples. This is in excellent agreement with other reports on the electrocatalytic activity of $Pt_{(hkl)}$ planes for ethanol oxidation, where the activity of different (hkl) planes have been compared for the C-C cleavage involved during the ethanol oxidation and concluded that compared to $Pt_{(111)}$ and $Pt_{(220)}$, $Pt_{(200)}$ shows higher activity, while the $Pt_{(111)}$ shows least activity.[50]

3.3.5.3. Methanol Oxidation

The overall reaction involved in the electrooxidation of CH_3OH to CO_2 on Pt electrode surface could be written as

$$CH_3OH + H_2O \rightarrow CO_2 + 6H^+ + 6e^- \quad \text{..... (3.3)}$$

$E^0 = 0.02$ V vs NHE

Oxidation of methanol has been thoroughly studies for many years, so that the reaction mechanism is now well established. A variety of surface reactions combined with interfacial irreversible electron transfer occur when methanol decomposes on platinum in acidic media via a dual path mechanism that involves non-CO adsorbed intermediates such as $(\dot{C}H_2OH)_{ads}$, $(\dot{C}HOH)_{ads}$, $(\dot{C}HO)_{ads}$ (main path) and adsorbed CO (parallel path). The formation of strongly bound CO_{ad} species and other reactive intermediates have been well established by techniques such as electrochemically modulated infrared reflectance spectroscopy (EMIRS), fourier transform infrared reflectance spectroscopy and liquid or gas chromatography.[51]

In order to explore the shape-dependent electrocatalytic activity of these Pt mesostructures towards methanol oxidation the corresponding cyclic voltammetric response in a mixture of 0.5 M CH_3OH and 0.5 M H_2SO_4 at 20 mV/s is shown in figure 3.15. The voltammetric response corresponding to Pt/C is also included for comparison. The voltammograms show two peaks during the anodic scan (at 0.14 and 0.75 V for Pt/C-hexagon), while one peak (at -0.01 V for Pt/C-hexagon) is observed in the cathodic scan. The first step in the reaction (peak 1) is the adsorption of the methanol molecule, immediately followed by its dissociation into several adsorbed species such as $Pt(CH_2OH)_{ads}$, $Pt(CHOH)_{ads}$, $Pt(CHO)_{ads}$ and $Pt(CO)_{ads}$.[49,52] The second anodic process (peak 2) is caused by the oxidation of these adsorbed species by -OH generated from the dissociation of H_2O molecule. During the cathodic sweep, a peak is observed (peak 3) after partial reduction of irreversibly formed surface oxides, which represents the real catalytic activity of the Pt surface. Further, a close examination of these voltammogram

reveals an interesting variation of the peak current for different structures as follows: Pt/C-hexagon > Pt/C-multipod > Pt/C-disc > Pt/C.

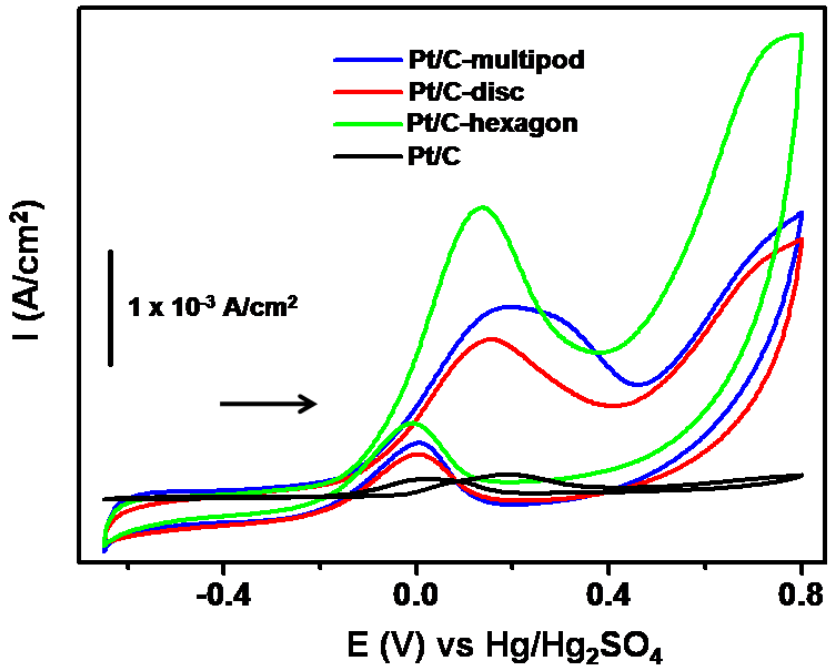

Figure 3.15. Cyclic Voltammetric response (2nd cycle data) of Pt/C-multipod, Pt/C-disc, Pt/C-hexagon and Pt/C towards methanol oxidation at 20 mV/s in a mixture of 0.5 M CH_3OH and 0.5 M H_2SO_4.

A superimposed cyclic voltammogram of Pt/C-multipod, Pt/C-disc, Pt/C-hexagon, and Pt/C at different scan rates is shown in figure 3.16, where a shift in the peak position with scan rate is observed, as expected for an irreversible charge transfer process. As observed for the above two reactions, here also the variation of peak current with scan rate reveals a slight deviation from linearity.

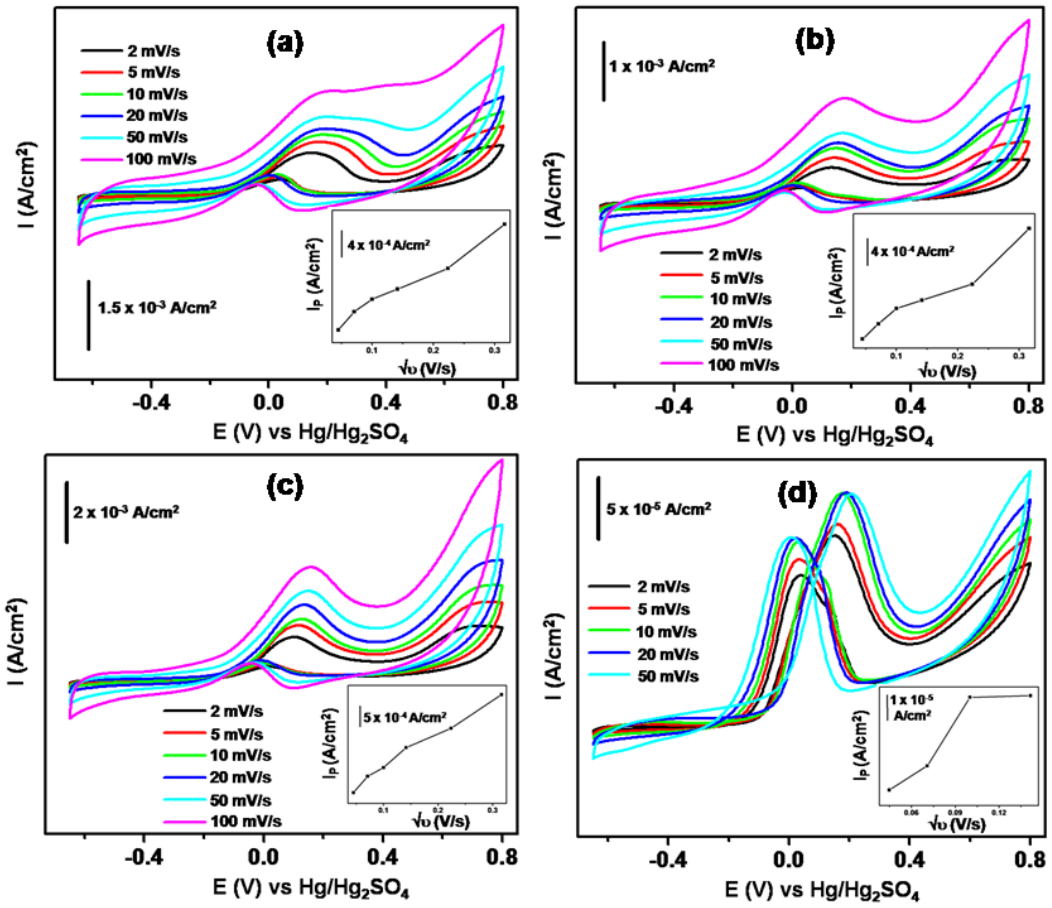

Figure 3.16. Overlayed cyclic voltammetric response of (a) Pt/C-multipod, (b) Pt/C-disc, (c) Pt/C-hexagon and (d) Pt/C toward methanol oxidation at different scan rates; inset shows the plot of I_p vs $\nu^{1/2}$ of the respective electrodes.

Figure 3.17 shows a comparison of the current–time transients of methanol oxidation at -0.09 V (potential selected from cyclic voltammogram) on the Pt/C, Pt/C-multipod, Pt/C-disc, and Pt/C-hexagon at room temperature after normalizing the current with respect to the electroactive Pt surface area (A_{Pt}). Interestingly, the current density on Pt/C-hexagon is significantly higher compared to that on other structures as per the order: Pt/C-hexagon > Pt/C-multipod > Pt/C-disc > Pt/C. The enhancement factor *R*, (which is defined as the ratio of the current density measured on a specific shape versus that

acquired on Pt/C spherical structures) is 750% for hexagons whereas for Pt/C-multipods and discs show 450% and 350% respectively, depending upon the electrode potential.

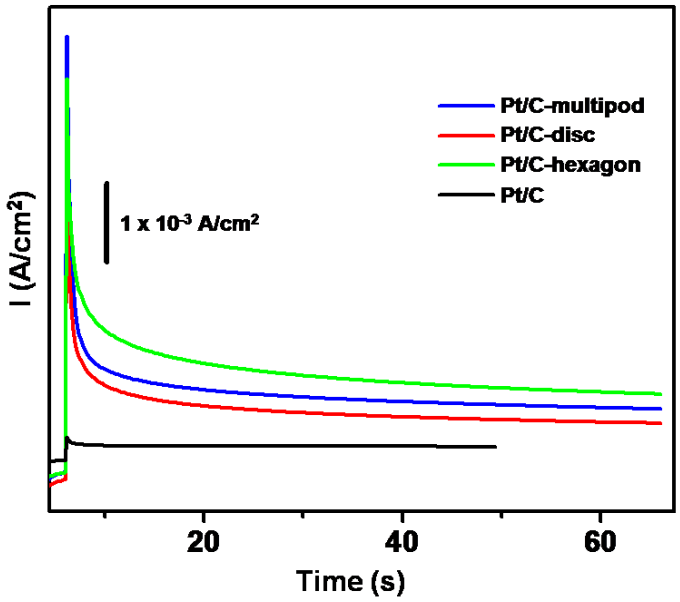

Figure 3.17. Comparison of the catalytic activity of Pt/C-multipod, Pt/C-disc, Pt/C-hexagon and Pt/C towards methanol oxidation in terms of current-time transients at a potential of -0.09 V for 60 s.

Steady-state current density (j) from the I-t transients (for various potentials, -0.2 V to +0.4 V) corresponding to methanol oxidation is plotted against respective potential in figure 3.18 which clearly illustrates superior electrocatalytic properties of Pt hexagons (at +0.1 V) than that of other structures of Pt and Pt/C. For example, the current density on Pt/C-hexagon, Pt/C-multipod, Pt/C-disc, and Pt/C structures for methanol oxidation at +0.1 V are 9 x10^{-4}, 7 x10^{-4}, 5 x 10^{-4} and 1.8 x 10^{-4} A/cm^2, respectively. Moreover, the exchange current density from Tafel polarization (figure 3.19) of these mesostructures dispersed in C toward methanol oxidation is summarized in Table 3.1, which reveals a slightly higher value for the Pt/C-hexagon electrode than that of the Pt/C-multipod, Pt/C-disc, and Pt/C respectively.

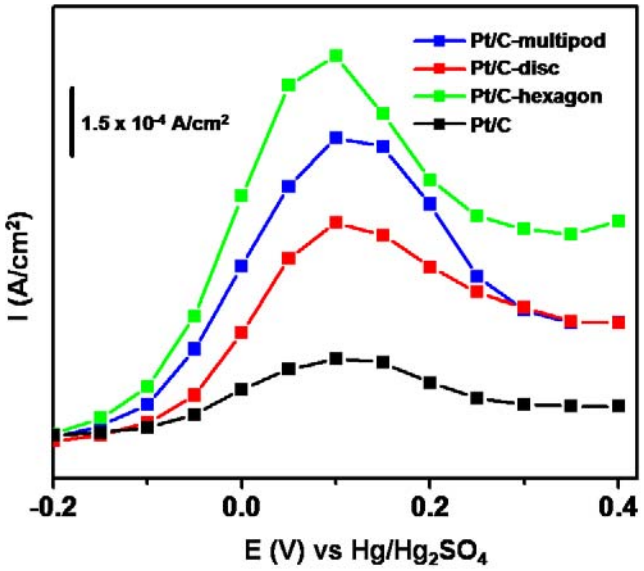

Figure 3.18. Potential-dependent steady state current density of methanol oxidation on Pt/C-multipod, Pt/C-disc, Pt/C-hexagon, and Pt/C.

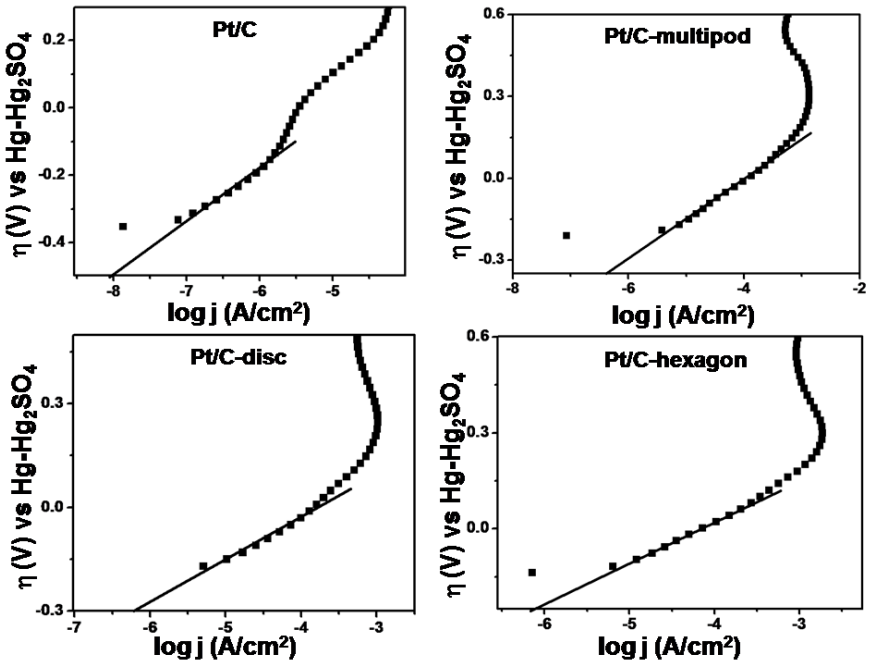

Figure 3.19. Tafel Plots for the methanol oxidation on Pt/C-multipod, Pt/C-disc, Pt/C-hexagon and Pt/C electrodes in 0.5 M CH_3OH and 0.5 M H_2SO_4.

Thus from the above observations, it is clear that Pt/C-hexagons show better electrocatalytic activity compared to that of Pt/C-multipod, Pt/C-disc, and Pt/C for methanol oxidation. Similar to the case of formic acid and ethanol oxidations, the reactivity order could be explained based on the XRD results, where the intensity ratio of $Pt_{(111)}/Pt_{(200)}$, is higher for hexagon than that for multipod, disc, and commercial sample. This is in excellent agreement with other reports on the electrocatalytic activity of $Pt_{(hkl)}$ planes for methanol oxidation, where the activity increases in the sequence, $Pt_{(200)} < Pt_{(220)} < Pt_{(111)}$.[46a,53] This could be attributed to the fact that during methanol oxidation, the adsorbed OH from H_2O molecule acts as the reactant necessary for the oxidation of adsorbed species on the Pt surface. Tripkovic et al. have correlated the onset potential of OH_{ads} and CH_3OH oxidation on different crystallographic planes of Pt and observed that for (111) plane, the initials potentials of OH_{ads} is close to the onset of methanol oxidation compared to that of (220) and (200) planes and as a result, methanol oxidation commences firstly on (111), then on (220) and finally on the (200) plane.[53]

Present approach for the formation of different shapes of platinum mesostructures has many intrinsic benefits over the earlier reported morphological control on planar electrode surfaces[26-28] because, in all these prior cases electric field has been applied on a flat conducting substrate and hence the continuous field gradient existing at the electrode-electrolyte interface (double layer) along with the mass transfer gradients in the diffusion layer is presumably responsible for the morphology. However, if the electric field could be confined in various regions due to the lateral surface heterogeneity rendered by filling the pores of PAM with a metal and the presence of insulating barriers of the electrode surface offers an anisotropic electric field. This anisotropic electric field would be more useful to have a directional control of nucleation and growth and accordingly the use of PAM is expected to cause a discontinuous distribution of electric field at the interface. Also, the findings regarding the electrocatalytic activity of different shaped Pt mesostructures towards both formic acid and ethanol oxidation would be important to fuel cell development work, since the anchoring of different shaped mesostructures on

vulcan carbon can be used to control their electrocatalytic activity. In addition, the present approach is especially important because these structures are generated without the assistance of any surfactants/ capping agents, which could adversely affect the electrocatalytic activity for many reactions. However, since the template is usually a thin membrane, it is difficult to scale-up the nanostructure grown through this hard template method to macroscopic quantities. Moreover, the high cost and limited supply of Pt are still rather prohibitive for full exploitation of fuel cell technology and as a result efforts are concentrated on to replace it with less expensive metals, while retaining the activity at least equal to that of platinum.

3.4. Conclusions

Present chapter demonstrates a unique method for controlling the shape of platinum mesostructures by templated electrodepostion facilitating their potential dependent morphological evolution. Comparison of the electrocatalytic activity for formic acid and methanol oxidation of these structures reveal that the hexagons of platinum is a better electrocatalyst than multipods, disc and commercial platinized carbon, whereas for the ethanol oxidation the activity is higher for multipods compared to that of discs, hexagons and commercial platinized carbon, which is further strengthened by the XRD results. The approach developed in this work could serve as an efficient and reliable way of tuning the morphology (and hence shape-dependent properties) of platinum mesostructures facilitating their potential applications as multifunctional catalysts for many industrial processes, and most interestingly, it plays a central role for energy conversion, particularly in the polymer electrolyte fuel cells. More significantly since this method of shape tuning is very general, we believe that this could be extended to a variety of other metallic and semiconducting nanostructures using hard templates and suitable electrodepostion strategies.

3.5. References

1. Heath, J. R. *Acc. Chem. Res*. **1999**, *32*, 388.

2. Peng, X. G.; Manna, L.; Yang, W.; Wickham, J.; Scher, E.; Kadavanich, A.; Alivisatos, A. P. *Nature* **2000**, *404***,** 59.

3. Lieber, C. M. *Solid State Commun.* **1998**, *107*, 607.

4. Smalley, R. E.; Yakobson, B. I. *Solid State Commun.* **1998**, *107*, 597.

5. Alivisatos, A. P. *Science* **1996**, *271*, 933.

6. Gudiksen, M. S.; Lauhon, L. J.; Wang, J. F.; Smith, D.C.; Lieber, C. M. *Nature* **2002**, *415*, 617.

7. Wong, E. W.; Sheehan, P. E.; Lieber, C. M. *Science* **1997**, *277*, 1971.

8. Lee, D.; Donkers, R. L.; DeSimone, J. M.; Murray, R. W. *J. Am. Chem. Soc.* **2003**, *125*, 1182.

9. Chaki, N. K.; Singh, P.; Dharmadhikari, C. V.; Pillai, V. K. *Langmuir* **2004,** *20,* 10208.

10. Pillai, Z. S.; Kamat, P. V. *J. Phys. Chem. B* **2004,** *108,* 945.

11. Kahn, M. L.; Monge, K.; Colliere, V.; Senocq, F.; Maisonnet, A.; Chaudret, B. *Adv. Funct. Mater.* **2005**, *15*, 458.

12. Burda, C.; Chen, X.; Narayanan, R.; El-Sayed, M. A. *Chem. Rev.* **2005**, *105*, 1025.

13. Peng, X. *Adv. Mater.* **2003**, *15*, 459.

14. Cao, G. *Nanostructures and Nanomaterials: Synthesis, Properties and Applications;* Imperial College London, 2004.

15. Sun. Y.; Xia, Y. *Science* **2002**, *298*, 2176.

16. Murphy, C. J.; Jana, N. R. *Adv. Mater.* **2002***, 14*, 80.

17. Martin, C. R. *Chem. Mater*. **1996**, *8*, 1739.

18. Choi, J.; Sauer, G.; Nielsch, K.; Wehrspohn, R. B.; Gosele, U. *Chem. Mater.* **2003**, *15*, 776.

19. Duan, X. F.; Lieber, C. M. *Adv. Mater.* **2000**, *12*, 298.

20. Manna, L.; Scher, E. C.; Alivisators, A. P. *J. Am. Chem. Soc.* **2000,** *122*, 12700.

21. (a) Rao, A. M.; Jacques, D.; Haddon, R. C.; Zhu, W.; Bower, C.; Jin, S. *Appl. Phys. Lett.* **2000**, *76*, 3813. (b) Ramgir, N. S.; Mulla, I. S.; Pillai, V. K. *J. Phys. Chem. B* **2006**, *110*, 3995.

22. Lifshitz, E.; Bashouti, M.; Kloper,V.; Kigel, A. M.; Eisen, S.; Berger, S. *Nano Lett.* **2003**, *3*, 857.

23. Zhou, G.; Lu, M.; Xiu, Z.; Wang, S.; Zhang, H.; Zhou, Y.; Wang, S. *J. Phys. Chem. B* **2006**, 110, 6543.

24. (a) Wolcott, A.; Kuykendall, T. R.; Chen, W.; Chen, S.; Zhang, J. Z. *J. Phys. Chem. B* **2006**, *110*, 25288. (b) Chen, J.; Herricks, T.; Xia, Y. *Angew. Chem. Int. Ed.* **2005**, *44*, 2589.

25. Kneipp, K.; Kneipp, H.; Itzkan, I..; Dasari, R. R.; Feld, M. S. *Chem. Rev.* **1999**, *99*, 2957.

26. Xiao, Z. –L.; Han, C. Y.; Kwok, W. -K.; Wang, H. -H.; Welp, U.; Wang, J.; Crabtree, G. W. *J. Am. Chem. Soc.* **2004**, *126*, 2316.

27. Murray, B. J.; Li, Q.; Newbweg, J. T.; Menke, E. J.; Hemminger; J. C.; Penner, R. M. *Nano Lett.* **2005**, *5*, 2319.

28. Choi, K. -S.; McFarland, E. W.; Stucky, G. D. *Adv. Mater.* **2003**, *15*, 2018.

29. (a) Narayanan, R.; El-Sayed, M. A. *Nano Lett.* **2004**, *4*, 1343. (b) Falicov, L. M.; Somorjai, G. A. *Proc. Natl. Acad. Sci.* USA **1985**, *82*, 2207.

30. (a) Narayanan, R.; El-Sayed, M. A. *J. Am. Chem. Soc.* **2004**, *126*, 7194. (b) Narayanan, R.; El-Sayed, M. A. *J. Phys. Chem. B* **2003**, *107*, 12416.

31. Xu, R.; Wang, D.; Zhang , J.; Li, Y. *Chem. Asian J.* **2006**, *1*, 888.

32. Park, S.; Xie, Y.; Weaver, M. J. *Langmuir* **2002**, *18*, 5792.

33. Teng, X.; Yang, H. *Nano Lett.* **2005**, *5*, 885.

34. (a) Dou, X.; Zhu, Y.; Huang, X.; Li, L.; Li, G. *J. Phys. Chem. B* **2006**, *110*, 21572. (b) Alvine, K. J.; Shpyrko, O. G.; Pershan, P. S.; Shin, K.; Russel, T. P. *Phys. Rev. Lett.* **2006**, *97*, 175503.

35. Platt, M.; Dryfe, R. A. W. *J. Electroanal. Chem.* **2007**, *599*, 323.

36. Teng, X.; Yang, H. *Nano Lett.* **2005**, *5*, 885.

37. (a) Liu, F.; Lee, J. Y.; Zhou, W. *J. Phys. Chem. B* **2004**, *108*, 17959. (b) Yang, J.; Lee, J. Y.; Deivaraj, T. C.; Too, H. –P. *Langmuir* **2003**, *19*, 10361.

38. Lee, S. M.; Jun, Y. -W.; Cho, S. N.; Cheon, J. *J. Am. Chem. Soc.* **2002**, *124*, 11244.

39. Jun, Y. -W.; Lee, J. -H.; Choi, J. -S.; Cheon, J. *J. Phys. Chem. B* **2005**, *109,* 14795.

40. (a) Mrozek, M. F.; Luo, H.; Weaver, M. J. *Langmuir* **2000**, *16*, 8463. (b) Miki, A.; Ye, S.; Osawa, M. *Chem. Commun*. **2002**, 1500.

41. (a) Kelley, S.C.; Deluga, G. A.; Smyrl, W. H. *Solid-State Lett.* **2000**, *3*, 407. (b) Lu, G.-Q.; Crown, A.; Wieckowski, A. *J. Phys. Chem. B* **1999**, *103*, 9700.

42. Capon, A.; Parsons, R. *J. Electroanal. Chem.* **1973**, *44*, 239.

43. (a) Matsuda, H.; Avabe, Y. *Z. Elektrochem.* **1955**, *59*, 494. (b) Brett, C. M. A.; Brett, A. M. O. Electrochemistry: Principles, Methods, and Applications; Oxford University Press **1993**.

44. Tian, N.; Zhou, Z. -Y.; Sun, S. -G.; Ding, Y.; Wang, Z. L. *Science* **2007**, *316*, 732.

45. (a) Shibata, M.; Furuya, N.; Watanabe, M. *J. Electroanal. Chem.* **1989**, *267*, 163. (b) Oliveira, R. T. S.; Santos, M. C.; Bulhoes, L. O. S.; Pereira, E. C. *J. Electroanal. Chem.* **2004,** *569,* 233. (c) Motoo, S.; Shibata, M. *J. Electroanal. Chem.* **1982**, *139*, 119. (d) Schell, M.; Swamy, B. E. K. *J. Electroanal. Chem.* **2005**, *584,* 157. (e) Swamy, B. E. K.; Schell, M. *J. Phys. Chem. B* **2006**, *110*, 5139.

46. (a) Adzic, R. R.; Tripkovic, A. V.; O'Grady, W. E. *Nature* **1982**, *296*, 137. (b) Tripkovic, A. V.; Popovic, K. D.; Lovic, J. D. *J. Serb. Chem. Soc.* **2003**, *68*, 849.

47. (a) Wang, H.; Jusys, Z.; Behm, R. J. *J. Phys. Chem. B* **2004**, *108*, 19413. (b) Schmiemann, U.; Muller, U.; Baltruschat, H. *Electrochim. Acta* **1994**, *40*, 99. (c) Tarnowski, D. J.; Korzeniewski, C. *J. Phys. Chem. B* **1997**, *101*, 253. (d) Wang, H.; Jusys, Z.; Behm, R. J. *Fuel Cells* **2004**, *4*, 113.

48. (a) Chen, S.; Schell, M. *J. Electroanal. Chem.* **1999**, *478*, 108. (b) Shin, J.; Tornquist, W. J.; Korzeniewski, C.; Hoaglund, C. S. *Surf. Sci.***1996**, *364*, 122.

49. Lemos, S. G.; Oliveira, R. T. S.; Santos, M. C.; Nascente, P. A. P.; Bulhoes, L. O. S.; Pereira, E. C. *J. Power Sources* **2007**, *163*, 695.

50. Xia, X. H.; Liess, H.-D.; Iwasita, T. *J. Electroanal. Chem.* **1997**, *437*, 233.

51. (a) Tripkovic, A. V.; Popovi, K. Dj.; Lovi, J. D.; Jovanovic, V. M.; Kowal, A. *J. Electroanal. Chem.* **2004**, *572*, 119. (b) Lamy, C.; Lima, A.; LeRhum, V.; Delime, F.; Coutanceau, C.; Leger, J. –M. *J. Power Sources* **2002**, *105*, 283.

52. Leger, J. –M. *J. Appl. Electrochem.* **2001**, *31*, 767.

53. Tripkovic, A. V.; Gojkovic, S. LJ.; Popovic, K. DJ.; Lovic, J. D. *J. Serb. Chem. Soc.* **2006**, *71*, 1333.

CHAPTER 4

Template–Assisted Synthesis of Ruthenium Oxide Nanoneedles: Electrical and Electrochemical Properties*

In the present chapter, we demonstrate the unique formation of bundles of RuO_2 nanoneedles (ca. 100 nm diameter) by a template-assisted electrodeposition from aqueous $RuCl_3$ solution under potentiostatic conditions at room temperature. We further explore the application of scanning electrochemical microscopy for mapping the electroactivity of these nanoneedles. Interestingly, cyclic voltammetry in 0.5 M H_2SO_4 shows significantly higher redox- related charging behavior for the RuO_2 nanoneedles compared to that of the commercial sample, which is also supported by the electrochemical impedance data. A comparison of the specific capacitance reveals higher value for nanoneedles (3 F/g instead of 0.4 F/g for the bulk), which has been explained on the basis of enhanced reactivity. More interestingly, electrical transport measurements reveal a transition from metallic to semiconducting behavior especially at low temperature caused possibly by an impurity scattering mechanism. We anticipate that the present simple route for the fabrication of RuO_2 nanostructures will be useful to exploit their potentials in various fields such as electrocatalysis and nanoelectronics.

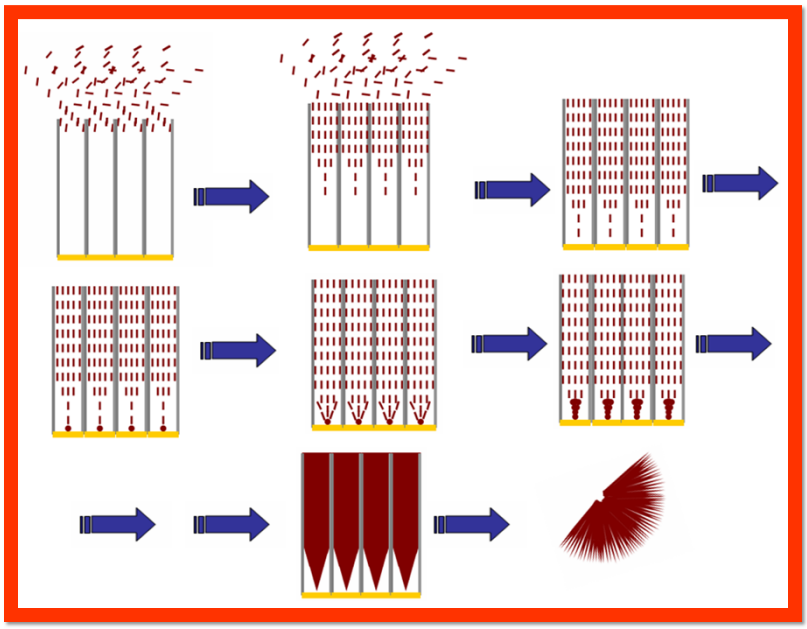

*A part of the work discussed in this chapter has been published in "*J. Phys. Chem. C* **2007**, *111*, 16593".

4.1. Introduction

Ruthenium dioxide (RuO_2) attracts both scientific and technological importance because of a combination of unique characteristics such as high thermal and chemical stability, low resistivity and remarkable redox properties.[1] For example, hydrous RuO_2 has been exploited as a well known electrode for supercapacitors not only due to its excellent specific capacitance but for the long cycle life also.[2] Further, they are of great interest for their applications in a variety of fields such as catalysis and microelectronics. For instance, RuO_2 is the main active component in dimensionally stable anodes (DSA) in the chlor- alkali industry, while many other applications like CO oxidation in sensors, CO_2 reduction in photocatalysis, also use RuO_2, in addition to its well known role in Fisher–Tropsh synthesis.[3] Lastly, in electronics too, these metallic oxides play a significant role, for example as field-emission (FE) cathodes for vacuum microelectronic devices and promising candidates for integrated circuit development.[4] Since, nanomaterials exhibit interesting size and shape dependent properties in the mesoscopic regime[5], it is extremely important to exploit the properties of RuO_2 in these regime in order to realize their full potential for above applications.

Although much attention has been given for the synthesis of one-dimensional nanostructures of several metallic/semiconducting oxides, only a few reports are available on the synthesis of RuO_2 nanostructures to date.[6] For example, Rolison et al. have reported the synthesis of nanowires of RuO_2 inside mesoporous SiO_2 aerogels by cryogenic decomposition of RuO_4.[6a] Similarly, Min et al. have reported a template-assisted synthesis of hollow RuO_2 nanotube array by atomic layer deposition (ALD) using carbon nanotube arrays on porous alumina membrane (PAM) template.[6b] Even though, in both these cases, synthesis of RuO_2 has been achieved by a templated route, the release of pure RuO_2 nanostructures from templates (like mesoporous SiO_2 aerogel and carbon nanotube) is a difficult task. More significantly, the extreme conditions used for the synthesis could change the properties due to altered defect distribution and hence

a room temperature method for making high aspect ratio RuO_2 structures should be interesting due to its enormous application potential.

Although, many attempts have been made to explore some of the unique properties of these materials at the bulk level, only few reports are available on the size and shape dependent properties of nanostructured RuO_2.[8] Accordingly, here we describe a simple approach based on PAM template to synthesize RuO_2 nanoneedles by the direct current electrodeposition inside alumina membranes. Various advantages have been realized through template-assisted electrochemical deposition (using hard templates like PAM and ion-track etched membrane) for the formation of one dimensional nanostructures, which include low operating temperature, environmental friendliness, less time, better control over shape/size, and easy removal of template compared to other available methods.[7]

In Chapter 3, we observed how alumina templates could be utilized to synthesize various shaped platinum mesostructures by mere tuning of applied potential whereas in the present chapter we focus on the synthesis of one-dimensional RuO_2 nanostructures using the same template. We also investigate some of the important properties of these materials mainly the electrical conductivity and specific capacitance to understand their efficiency at the nano level along with the formation of RuO_2 nanoneedles. Further, we describe a method to study the electrochemical activity of RuO_2 nanoneedles using the feedback mode of scanning electrochemical microscopy (SECM). SECM is a "chemical microscope" that has a response based on faradaic current changes at the scanning tip and the sample.[9] This is useful in obtaining topographic and chemical information about a wide range of sample surfaces, including polymers and biological materials. In the feedback mode, with appropriate choice of mediator or substrate potential or both, it is possible to image variations in turnover activity otherwise called reaction-rate imaging. Recently, H^+/H_2 couple has been used as a mediator in SECM to study the H_2 oxidation activity of PEMFC anode catalysts.[9e,9f] Using this mode, we attempt to reveal the electrochemical behavior of RuO_2 nanoneedles, by holding the tip and substrate at different potentials. More importantly, we also explore the applicability of this technique

for imaging these nanostructures, which allows direct mapping of electroactivity of the materials compared to other optical and electronic surface characterization techniques. These nanoneedles are further characterized by scanning electron microscopy (SEM), x-ray photoelectron spectroscopy (XPS), x-ray diffraction (XRD) and thermogravimetric analysis (TGA).

4.2. Experimental Details

4.2.1. Materials

$RuCl_3.xH_2O$ (99.98%) and anhydrous RuO_2 (99.9 %) were purchased from Aldrich chemicals while boric acid (99.5 %) was purchased from Loba Chemie. All reagents were used without further purification and deionized water (18 MΩ) from milli-Q system was used in all experiments.

4.2.2. Preparation of RuO_2 Nanoneedles through Template-Assisted Electrodeposition

Free-standing linear-PAM template fabricated via a two–step anodization route (for details see Chapter 2, section 2.4.2) was served as working electrode for templated electrodeposition, after evaporating Au film (200 nm) onto one side of the membrane. Electrodeposition was carried out using the above working electrode in an aqueous solution of $RuCl_3$ (5 mM) as the ruthenium oxide precursor and boric acid (1 mM), as a buffer at a pH of 3.5. After a pretreatment of the Au film supported linear-PAM template in ethanol by sonication to drive out trapped air inside the holes, electrodeposition was carried out at a potential of 1.6 V Vs SCE (saturated calomel electrode), for 30 min. After electrodeposition, the structures were released from the PAM by dissolving the template in 0.1 M NaOH and then washing several times with deionized water till neutral pH, followed by a final washing with ethanol to yield almost 95 % pure structures.

Similarly, we have also carried out electrodeposition at slightly lower potential (+1 V), while keeping the same concentration of $RuCl_3$ and boric acid, 5 mM and 1 mM

respectively. Further, in order to understand the effect of concentration of Ru precursor, we have performed electrodeposition also at higher concentration of $RuCl_3$ and boric acid (0.05 M $RuCl_3$ and 0.01 M H_3BO_3).

4.2.3. Structural and Morphological Characterization

4.2.3.1. X-ray Diffraction (XRD)

XRD studies were performed in order to understand the sample crystallinity and also to evaluate the crystallite size using CuK_α (λ = 1.5405 Å) radiation on a Rigaku Miniflex diffractometer. Diffraction patterns were collected at a step of 0.02° (2θ) and the background was subtracted with the linear interpolation method. Samples were prepared by making thin films on glass substrates.

4.2.3.2. Thermogravimetric Analysis (TGA)

Both the thermal stability and purity of the sample could be easily traced out by using TGA measurements. TG analysis was carried out on a Perkin-Elmer TGA 7 Thermal Analyzer by heating about 3 mg of RuO_2 sample from 50^{o}C to 900^{o}C at a rate of 10 °C/min in Nitrogen.

4.2.3.3. Four-Probe Electrical Conductivity

Electrical conductivity measurement was performed using 1 cm^2 thin film of "purified RuO_2 nanoneedle" sample using a KEITHLY 220 Programmable current source and another KEITHLY 181 Nanovoltmeter coupled with an OXFORD Intelligent temperature controller ITC-4. A thin film of sample was made by drop-coating on a glass slide after making a good dispersion in ethanol and the conductivity was measured at various temperatures using four point electrical measurements. Similar procedure was followed to measure the electrical conductivity of commercial anhydrous RuO_2.

4.2.3.4. Electrochemical measurements

All electrochemical studies were performed on an Autolab PGSTAT30 (Eco chemie) instrument. For electrodeposition, SCE and a Pt foil were used as reference and counter electrodes respectively. Further, for capacitance measurements of RuO_2 nanoneedles, the working electrode was prepared by drop casting 0.4 mg of RuO_2 sample (dispersed in isopropyl alcohol) on a glassy carbon electrode (ca. 3 mm diameter) using 0.5 wt% teflon binder; similar procedure was adopted to prepare the electrode of commercial anhydrous RuO_2 (Aldrich, 99.9 %) and same amount of sample was used to prepare the electrode in both cases. A Pt foil and a $Hg\text{-}Hg_2SO_4$ electrode served as the counter and reference electrodes respectively and the voltammogram was recorded in 0.5 M H_2SO_4.

A CHI 900B SECM (CH instruments) was employed for SECM experiments, using a platinum disc (d = 1.5 mm) as the substrate-working electrode, a 10 μm Pt tip as probe electrode, Ag/AgCl as a reference electrode and a Pt wire as the counter electrode at room temperature in a 1.5 ml Teflon holder cell having 0.5 M H_2SO_4. The substrate and the tip/probe electrode was polished using 0.05 μm alumina powder.

Other characterization details like SEM and XPS have already been described in Chapter 2, section 2.4.5.1 and Chapter 3, section 3.2.4.2 respectively.

4.3. Results and Discussion

4.3.1. SEM Analysis

Representative scanning electron micrographs of RuO_2 nanoneedles prepared using alumina template at a potential of 1.6 V are shown in figure 4.1a and 4.1b (low and high magnification micrographs) respectively, revealing a typical diameter of ca. 100 nm and length of few microns for these interesting structures. Often the tip of such nanostructures acquires significantly smaller diameters (ca. 50 nm) compared to that of the base. These images reveal a uniform and smooth surface, suggesting that the wall of the PAM template is also likely to be flat. However, the diameter of the RuO_2

nanoneedles is found to be larger compared to that of the original pore (pore diameter of PAM used here is ca. 80 nm; for details see Chapter 2, section 2.5.1), which is supposed to be due to the widening during the chemical etching stage in H_3PO_4 solution. Further, the micrograph reveals congregated nanoneedles, which might have been formed during the dissolution of the membrane in NaOH as normally observed during the template assisted growth.[10] Since, we have neither used any stabilizing agents nor any surfactants to prevent congregation of these structures during the dissolution of the alumina membrane, it is quite possible that they will come closer to form bundles or congregated nanoneedles after releasing from the template pores. Nevertheless, the micrograph shows some broken nanorods occasionally having very small aspect ratio, which might have been formed during the isolation process.

Further, SEM image of RuO_2 nanoneedles formed at +1 V is shown in figure 4.1c, where the diameter of the nanoneedle is ca. 100 nm and the length in few microns. Even though, electrodeposition at + 1 V also gives RuO_2 nanoneedles with almost same diameter, the percentage yield of these nanoneedles is relatively low compared to that formed at 1.6 V. This could be due to the lower electric field for the electrodeposition, which could in principle limit the filling of majority of the pores. Since, diffusion of ions through the pores is very slow, increasing the field leads to enhanced driving force for the metal ions to diffuse inside the porous structure. Similarly, we have also increased the concentration of $RuCl_3$ precursor (0.05 M) and a closer look at the electron micrograph (figure 4.1d) reveals that both the aspect ratio and yield of the nanostructures are comparatively very low. A plausible reason for the above observation is that, due to the higher concentration of Ru^{3+} ions, majority of the pores are blocked, which in turn prevents diffusion of metal ions inside the structure.

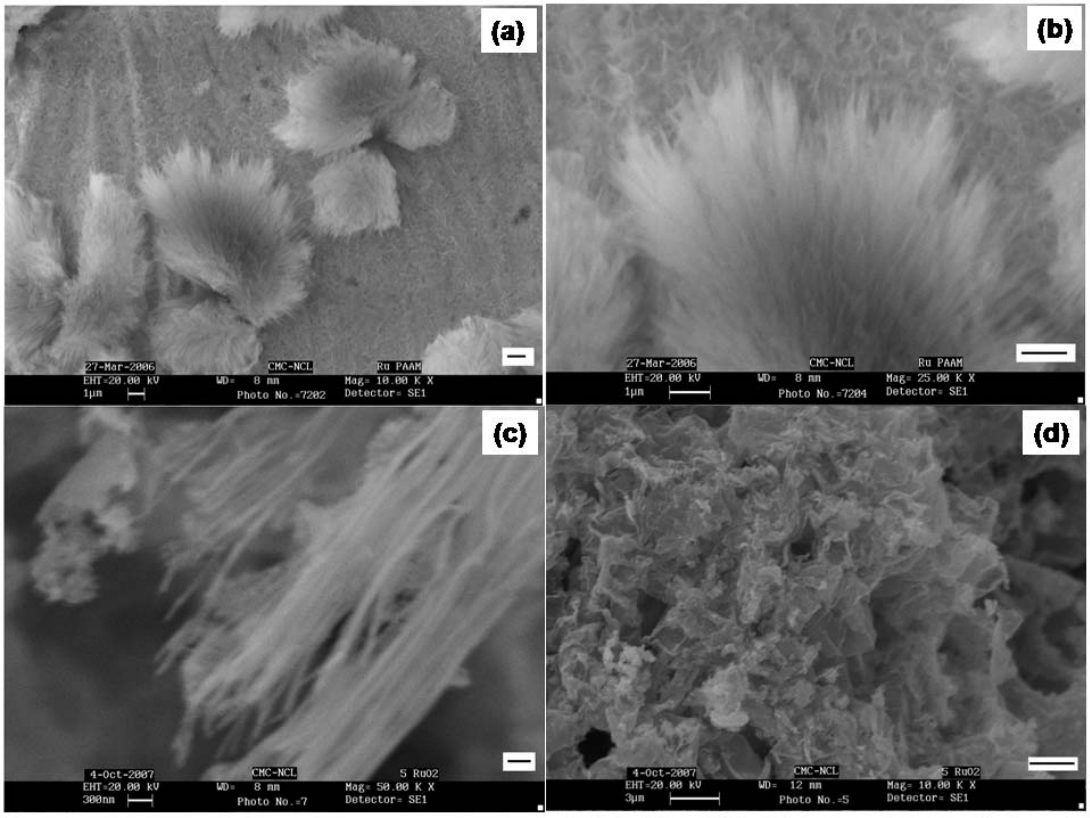

Figure 4.1. SEM images of RuO_2 nanoneedles prepared by potentiostatic method using PAM as the template; (a & b) nanostructures prepared at +1.6 V; micrograph reveals bundles of RuO_2 nanoneedles, where the diameter of the each nanoneedle is ca. 100 nm; (c) RuO_2 nanoneedles formed at +1 V; (d) RuO_2 nanoneedles prepared using a higher concentration of metal precursor (0.05 M); scale bar 1 μm, 1 μm, 300 nm and 3 μm.

Scheme 4.1 depicts a tentative mechanism for the formation of RuO_2 nanoneedles. Diffusion of Ru^{3+} ions towards the pores of alumina membrane under different velocity and field gradients (from edges to middle of the pore) is believed to be responsible for the unusual morphology. We presume that the ions present in the mid layer of the solution reach the Au deposited surface of the PAM relatively at a faster rate, whereas the ions in the remaining layers diffuse at relatively slow rates to facilitate growth ultimately giving rise to unique needle morphology with diameter of the tip smaller than the base dimension. On etching the membrane in NaOH solution, these structures release from the inner part of the pores together, giving rise to congregated RuO_2 nanoneedles.

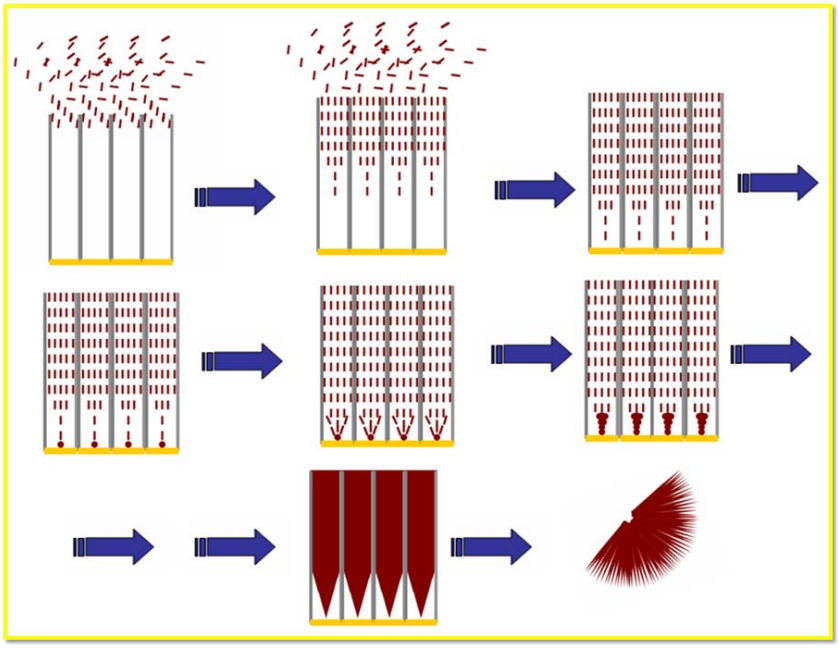

Scheme 4.1. A tentative mechanism of formation of RuO_2 nanoneedles; scheme depicts diffusion of Ru^{3+} ions towards the pores of alumina membrane under different velocity and field gradients (from edges to middle of the pore) facilitating the formation of needle like morphology. Finally, on etching the membrane in NaOH solution, these structures get released from the inner part of the pores together, giving rise to congregated RuO_2 nanoneedles.

4.3.2. XPS Analysis

Analysis of the oxidation state of both Ru and oxygen is particularly important to understand the chemical composition of the nanoneedles and accordingly, the XP spectrum of the Ru 3d level is shown in figure 4.2a, where deconvolution (using Shirley software) reveals two peaks at 285 eV and 280.7 eV corresponding to Ru $3d_{3/2}$ and $3d_{5/2}$ respectively. Here the peak corresponding to Ru $3d_{3/2}$ has not been considered on account of the serious interference by C 1s, whereas the faint peak corresponding to Ru $3d_{5/2}$ at 280.7 eV could be attributed to Ru(IV) oxide. Also an additional peak is observed at 283 eV, which could be assigned to Ru(VI), as reported by Zeng et al.[11] Similarly, deconvolution of the O1s spectrum of the sample shows a peak at 529.4 and 531.5 eV

(figure 4.2b) respectively attributed to the oxygen in Ru(IV) oxides and adsorbed oxygen. Apart from these two peaks, an additional signal is observed at ca. 530.5 eV assigned to the O 1s state in RuO_3. Also the binding energy values of Ru(IV), Ru(VI) and O 1s states are surmised in Table 4.1 for comparison. Hence, from the XPS analysis it could be concluded that the nanoneedles formed is primarily RuO_2 along with a trace amount of RuO_3. Further we have calculated the ratio of RuO_2 to RuO_3 as ~ 2:1 using the following equation, where the area of the respective peaks was estimated from the peaks deconvoluted using Shirley software.

$$RuO_2/RuO_3 = Area\ of\ RuO_2/Area\ of\ RuO_3 \times \sigma_{RuO_3}/\sigma_{RuO_2} \times \sqrt{K.E\ of\ RuO_2/K.E\ of\ RuO_3} \quad \text{..... (4.1)}$$

where, σ is the sensitivity factor and K.E is the kinetic energy of the ejected electron.

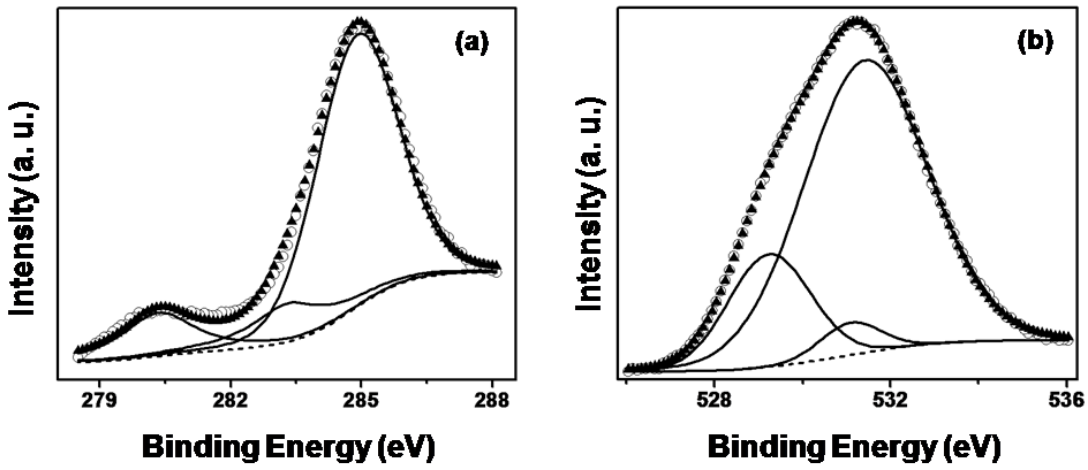

Figure 4.2. XP spectra of Ru 3d (a) and O1s level (b) of RuO_2 nanoneedles; circles represent the raw data while triangles represent the fitted data for the overall signal; dash lines indicate the background, whereas the solid lines represent the deconvoluted individual peaks.

Table 4.1. Binding energies of Ru $3d_{5/2}$ and O 1s electrons of Ru-Oxygen systems.

Sample	Binding Energy (eV)	
	Ru $3d_{5/2}$	O 1s
RuO_2	280.7	529.4
RuO_3	283	530.5

4.3.3. XRD Analysis

To understand both the crystal structure and crystallite size of these nanoneedles, we have performed powder XRD studies of "as-prepared" RuO_2 nanoneedles and after heating to 160 ^oC. Accordingly, figure 4.3 shows XRD pattern of nanoneedle soon after the preparation (a) and after heating to 160 ^oC (b), where only two peaks at 2θ values ca. 28.3^o and ca. 35^o related to (110) and (101) planes respectively are observed for 'as prepared' RuO_2 sample (figure 4.3a). In this case, the remaining peaks are suppressed, which is presumed to be due to the presence of bound water on the surface of RuO_2 nanostructures. In contrast, the annealed sample (figure 4.3b) reveals well defined peaks centered around 2θ values of ca. 28.3^0, 35^0, 55^0 and 67^0 corresponding to the (110), (101), (211) and (310) reflections ascribable to the rutile type anhydrous RuO_2 structure, which is consistent with the reported values.[12] Hence, the XRD pattern reveals that the RuO_2 nanoneedle is polycrystalline with no preferred orientation, which is considered as one of the major drawbacks for nanostructures fabricated by a template-assisted electrodeposition.[13] Further, we have calculated the crystallite size using Scherrer formula applied for (110) plane, which shows ca. 10.2 nm and ca. 12.8 nm for as prepared and annealed RuO_2 samples respectively. Considering the (101) plane of both the samples, slight broadening is obvious for the annealed RuO_2 sample although this peak has not been considered for the calculation due to a large contribution from noise.

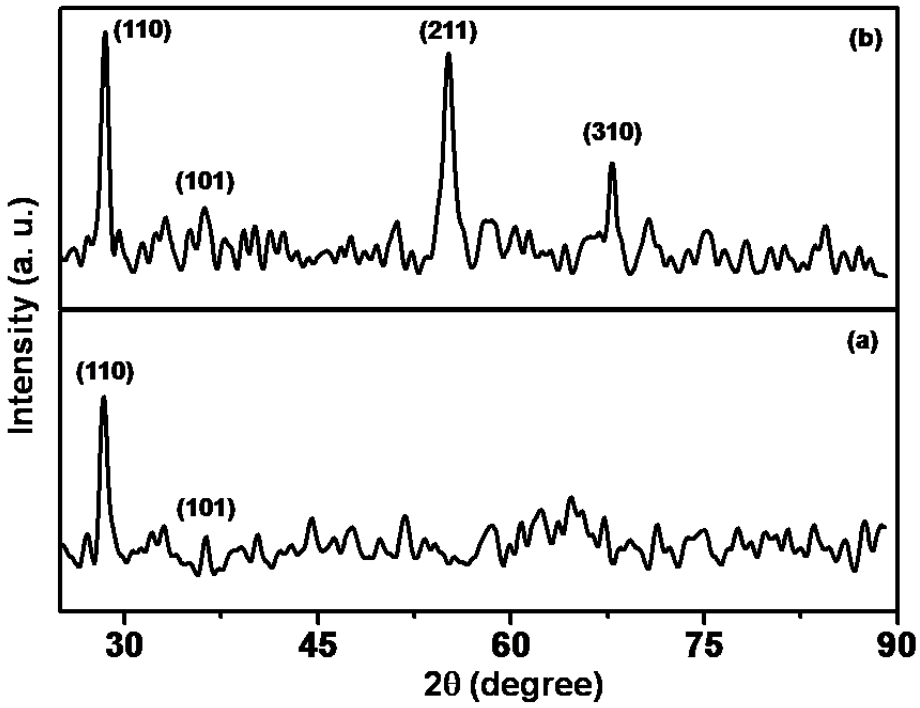

Figure 4.3. XRD pattern of RuO_2 nanoneedles; (a) as-prepared sample (b) sample heated at 160^oC. All peaks are assigned to the rutile phase of RuO_2.

4.3.4. TG Analysis

To understand the thermal stability of RuO_2 nanoneedles compared to that of commercial RuO_2 samples, we have carried out thermogravimetric analysis under flowing N_2. Accordingly, figure 4.4 shows the TGA curves obtained for RuO_2 nanoneedle as well as for the commercial RuO_2 sample. Interestingly, RuO_2 nanoneedle sample loses ca. 18 wt % till 200 ^oC, presumably from the desorption of volatile solvents and adsorbed water (figure 4.4b). A further weight loss at around 325 ^oC may indicate the formation of Ru^{3+} and loss of oxygen from the material.[14] Similarly, the thermogram of commercial sample also shows a two-step weight loss (figure 4.4a) with the inflection points at ca. 160 ^oC (ca. 9 wt% loss) attributed to the desorption of adsorbed water and at ca. 520 ^oC (ca. 4 wt% loss), due to the formation of Ru^{3+} and loss of oxygen respectively as mentioned above. Comparison of the thermogram of both samples indicates that the

inflection point due to the formation of Ru^{3+} and loss of oxygen is fundamentally different for both. Here the nanoneedle shows decomposition at around 325 ^{o}C whereas the commercial one shows decomposition at a higher temperature (ca. 520 ^{o}C), which indicates lower thermal stability (quantum size effect along with large surface area of tips compared to that for bulk) of Ru(IV) oxide nanoneedle. This reduction in decomposition temperature is also due to the presence of RuO_3, which could transform fast to the Ru^{3+} state. Apart from the weight loss (total 22 wt%) at these inflection points, no loss is observed for the RuO_2 nanoneedle sample, which in turn reveals the purity of the sample.

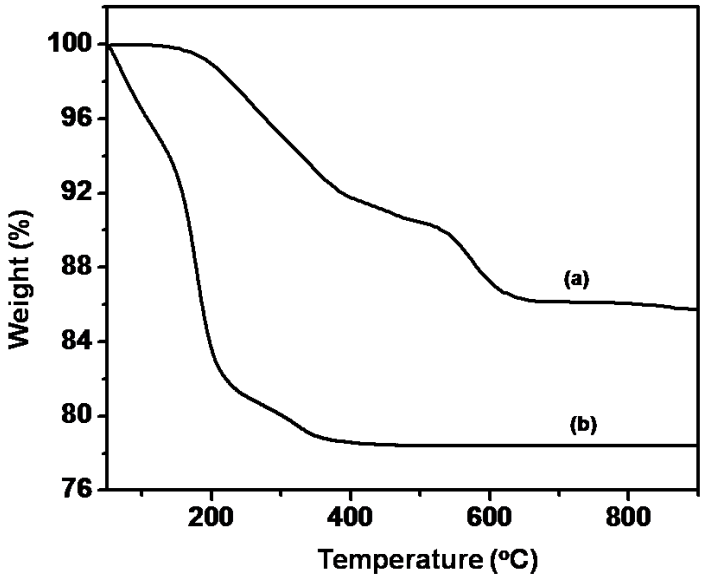

Figure 4.4. TGA curve of (a) commercial anhydrous RuO_2; (b) RuO_2 nanoneedles performed in N_2 atmosphere at heating rate of 10^{o}C/min.

4.3.5. Electrochemical Measurements

In order to demonstrate the redox related charging behavior of RuO_2 nanoneedles, we show (figure 4.5) cyclic voltammetric response of blank platinum ultra-microelectrode tip, RuO_2 nanoneedle modified Pt substrate electrode and bare Pt substrate electrode in 0.5 M H_2SO_4 at 100 mV/s. A steady- state current is obtained for the ultra-microelectrode (figure 4.5a) at potentials more negative than -0.6 V, indicating diffusion

controlled current corresponding to proton reduction ($2H^+ + 2e \rightarrow H_2$). This is in aggreement with the previous studies of the voltammetry of hydrogen evolution in aqueous solutions on platinum microelectrodes.[15] Similarly, figure 4.5b shows the CV response of the RuO_2 nanoneedle modified substrate electrode, where the substrate is a Pt disc electrode coated partially with RuO_2 nanoneedles (nanoneedle was dispersed in ethanol and drop casted using micro-pipette on the substrate). The voltammogram shows a peak at –0.2 V corresponding to hydrogen oxidation by the Pt substrate, whereas the redox peaks at ca. +0.5 V and ca. +0.6 V vs Ag/AgCl are observed, which correspond to insertion and deinsertion of H^+ ions respectively by the RuO_2 sample.[16] For comparison, the voltammogram for the blank substrate electrode is also shown in figure 4.5c, which reveals the normal response expected for bare Pt electrode in acidic medium.[17]

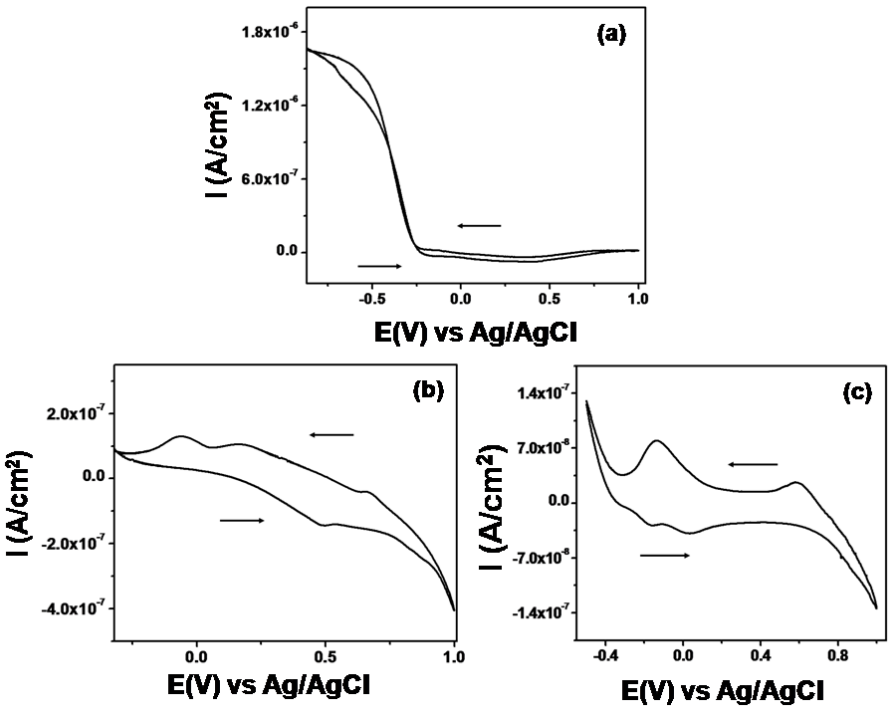

Figure 4.5. Cyclic voltammetric response of (a) Pt microelectrode tip (10 μm) (b) RuO_2 nanoneedle modified Pt disc substrate electrode and (c) Bare Pt disc substrate electrode recorded at 100 mV/s in 0.5 M H_2SO_4.

4.3.5.1. SECM Measurements

The SECM probe approach experiment can be used for reaction-rate imaging for heterogeneous electron transfer on substrates by recording tip current, i_T versus d (the approach curve). Accordingly, to understand the H_2 oxidation activity on blank and RuO_2 nanoneedle modified Pt substrate electrode, approach curves were performed by setting the potential of the Pt microelectrode tip at -0.7 V, where diffusion-controlled H_2 evolution occurs at the tip and then moving the tip towards the substrate held at +0.6 V. Figure 4.6 shows the probe approach curves for blank as well as for RuO_2 modified Pt substrate electrodes by fixing the tip and substrate at different potentials. Interestingly, approach curves obtained on keeping the tip at -0.7 V and the substrate at +0.6 V, show a decrease in i_T as the tip approaches the blank substrate (negative feedback) whereas for the RuO_2 modified substrate electrode, i_T shows an increase in current on approaching the substrate (positive feedback) as illustrated in figure 4.6a and 4.6b respectively. The reason for this observation is as follows: at +0.6 V, for the RuO_2 modified substrate electrode, i_T increases due to the enhanced H^+ desorption activity of the RuO_2 nanoneedles, whereas a negative feedback current at the same bias for the blank substrate indicates the onset of Pt oxide formation and the activity of Pt substrate toward H_2 oxidation decreases dramatically.

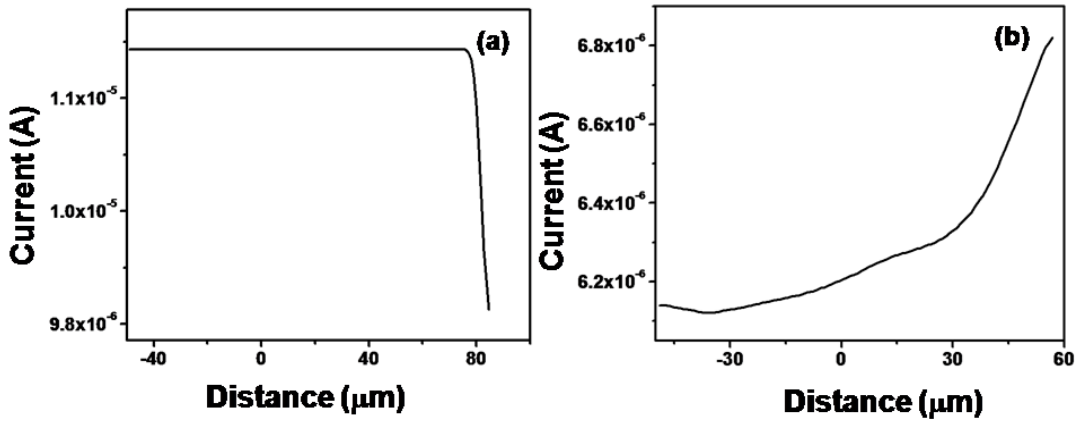

Figure 4.6. SECM approach curves obtained on (a) blank Pt substrate electrode; (b) RuO_2 nanoneedle modified substrate electrode; here the potential of the Pt microelectrode tip and substrate electrode were held at -0.7 V and +0.6 V respectively.

Further, for mapping the electroactivity of these nanoneedles we have also imaged by keeping the tip at 5 μm away from the substrate (the distance was found via a probe approach experiment), while scanning the same in x-y plane. At first, we have imaged by fixing the tip at -0.7 V and bare substrate at +0.6 V respectively, where the images reveal inactive substrate, since i_T is negligibly low, suggesting relative sluggishness of Pt electrode for hydrogen oxidation due to the commencement of oxide formation (figure 4.7a). Interestingly, SECM image after modifying the Pt substrate with RuO_2 nanoneedles reveals higher current for a particular area of the substrate electrode where RuO_2 nanoneedles are present, whereas the regions where the Pt surface is exposed, the image shows highly inactive area (figure 4.7 b), although both the tip and substrate electrodes are maintained at -0.7 V and +0.6 V respectively. This remarkable enhancement in i_T could be attributed to the increased rate of hydrogen desorption by the RuO_2 nanoneedles following the spatial current distribution. However, a clear image of nanoneedles is not observed due to comparatively larger probe diameter (10 μm). Even though the platinum surface becomes inactive towards hydrogen oxidation at more positive bias, the RuO_2 nanoneedles on the platinum substrate electrode becomes active by releasing the adsorbed H^+ ions and produces an enhancement in the i_T (a cartoon

picture of the RuO_2 nanoneedle modified Pt disc substrate electrode is shown in figure 4.7c). The observed active region at positive bias (figure 4.7b) could be assigned due to the hydrogen deinsertion activity of RuO_2 nanoneedles with profound implications on the mechanism of supercapacitor electrodes.

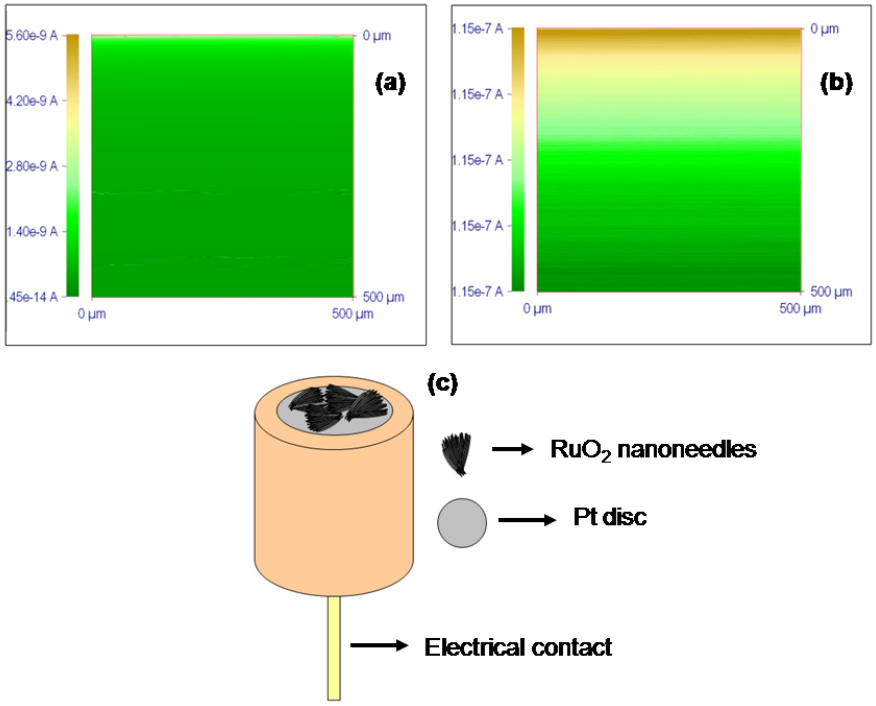

Figure 4.7. SECM images of (a) bare Pt substrate electrode, (b) Pt substrate electrode after partially modifying with RuO_2 nanoneedles; the potential of the Pt microelectrode tip and substrate electrode are held at -0.7 V and +0.6 V respectively; (c) electrode surface, which depicts RuO_2 nanoneedle deposited on Pt disc substrate electrode.

4.3.5.2. Cyclic Voltammetry and Impedance Measurements

In order to understand the charge storage efficiency of these nanoneedles compared to that of bulk RuO_2 samples, we have performed cyclic voltammetric and impedance measurements. A typical voltammetric response of RuO_2 nanoneedles at a scan rate of 10 mV/s in 0.5 M H_2SO_4 is shown in Figure 4.8b. The voltammogram includes double layer charging, the redox related charging at ca. 0.3 V and 0.2 V vs Hg-Hg_2SO_4 respectively, attributed to the electrosorption of ions on the surface of the oxide

and also proton diffusion into defect sites, interstitial sites and/or grain boundaries below ca. -0.1 V vs Hg-Hg_2SO_4 as reported earlier.[16] Figure 4.9 depicts the voltammogram of nanoneedles at various scan rates, where the capacitance shows a minor increase with scan rate (inset of figure 4.9). However for planar electrodes, capacitance ideally (especially in the absence of adsorption induced capacitance or pseudocapacitance) should be independent with scan rate, where the anodic and cathodic processes are symmetrical.[17,18] The observed minor increase in capacitance with scan rate could be explained as follows: three possible processes could occur at the interface, including electrical double layer charging, redox related charging, and proton diffusion into defect sites, interstitial sites and/or grain boundaries. These reactions especially redox related charging, and proton diffusion can affect the symmetrical nature of anodic and cathodic processes, resulting in a slight deviation from the behavior observed for planar electrodes. Further, we have compared the voltammetric response of RuO_2 nanoneedles with that of commercial RuO_2 (figure 4.8a), where it is clearly seen that the contribution from redox-related charging and other two processes are significantly higher for nanoneedles compared to that of commercial sample. The voltammetric response of commercial sample is also shown separately in the inset of figure 4.8 for clarity. The larger contribution from these redox-related charging, is attributed to the presence of RuO_2 nanoneedles in congregated form, which in turn facilitates ionic transport through inter-needles. Consequently, a higher specific capacitance is observed for the nanoneedles (3 F/g) compared to that of the commercial ones (ca. 0.4 F/g), although the same amount of sample was used for both the electrodes. More interestingly, the value of specific capacitance obtained in our case for the nanoneedles is very much higher compared to the reported value for anhydrous RuO_2, (0.75 F/g), even though this itself is lower to what is known for hydrous RuO_2.[8a]

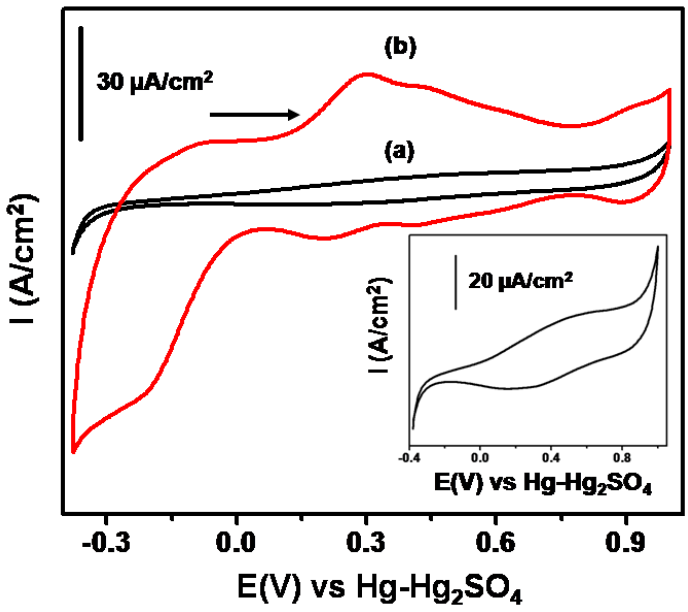

Figure 4.8. Cyclic voltammetric response of (a) commercial anhydrous RuO_2 (b) RuO_2 nanoneedles in 0.5 M H_2SO_4 at 10 mV/s; voltammetric response of commercial RuO_2 sample is also shown in the inset for comparison.

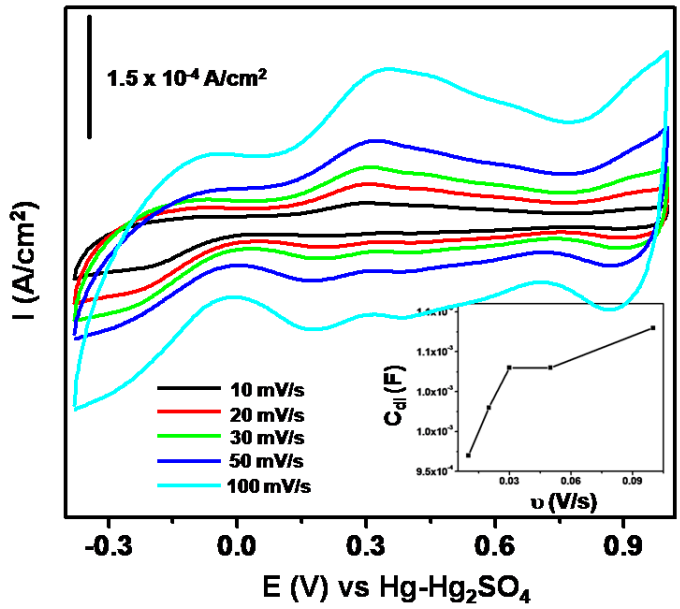

Figure 4.9. Overlayed cyclic voltammetric response of RuO_2 nanoneedles at different scan rates recorded in 0.5 M H_2SO_4; inset shows the variation of capacitance with scan rate.

Electrochemical impedance technique has also been employed in order to compare the behavior of both bulk RuO_2 and RuO_2 nanoneedles. Accordingly, figure 4.10 shows typical Nyquist plot (Z(Im) vs Z(Re)) for the RuO_2 nanoneedles and the commercial RuO_2 respectively, in 0.5 M H_2SO_4 in the frequency range of 10 kHz to 0.01 Hz. The charge transfer process at the electrode- electrolyte interface is determined by the region represented by a semicircle at higher frequencies, whereas the straight line inclined at an angle of around 45^o to the real axis represents the diffusion- controlled electrode kinetics in the lower frequency region. The frequency at which there is a deviation from the semicircle is the knee frequency, which reflects the maximum frequency at which capacitive behavior is dominant. Comparison of the Nyquist plot of RuO_2 bulk and RuO_2 nanoneedles shows significant differences. For example, the high-frequency part of RuO_2 nanoneedle (left inset of figure 4.10) and bulk RuO_2 (right inset of figure 4.10) is fitted with a semicircle using the CNLS (complex nonlinear least-square fitting) method with the help of a simple Randles circuit. Analysis of the charge transfer resistance (R_{CT}) indicates significantly lower value for the nanoneedles compared to that of commercial one, which is in agreement with the larger contribution from the redox related charges as observed from the cyclic voltammograms of the nanoneedles. The calculated specific capacitance for both nanoneedles and commercial RuO_2 are 125 mF/g and 6 mF/g respectively. Further, using the R_{CT} value, the exchange current (i_o) can be obtained using the following equation:

$$i_o = RT / nFR_{CT} \quad \text{..... (4.2)}$$

Where R is the gas constant T is temperature (298 K), n is the number of electrons involved in the reaction (n=1) and F is the Faraday constant. Accordingly, the value of exchange current density, j_o (i_o/A, where 'A' is the electrode area) calculated for RuO_2 nanoneedle and bulk RuO_2 samples are 7.33 mA/cm^2 and 0.2 mA/cm^2 respectively.

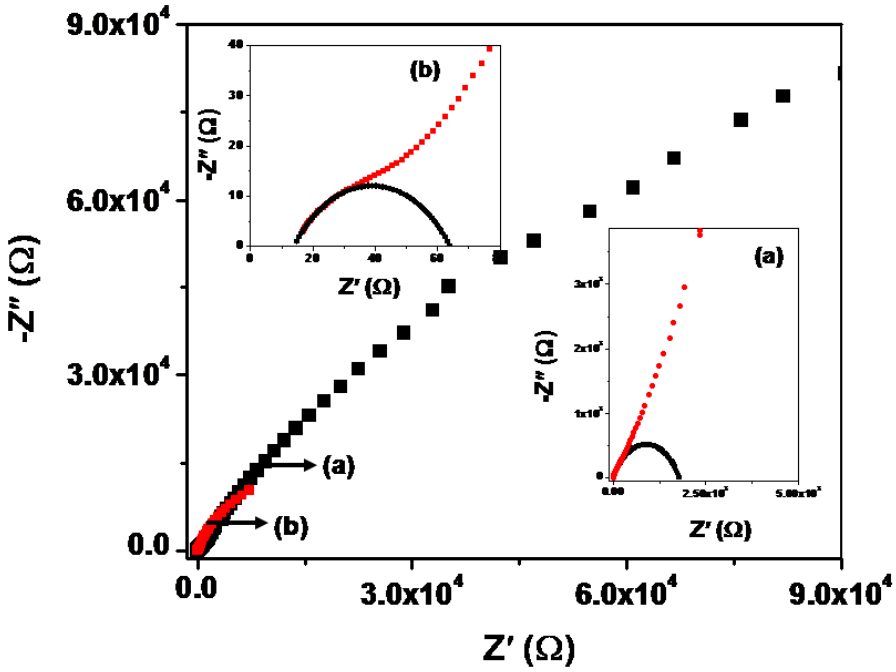

Figure 4.10. Overlayed impedance plot of (a) commercial anhydrous RuO_2 and (b) RuO_2 nanoneedles using 10 mV AC signal recorded in the frequency range of 10 kHz to 0.01 Hz; left and right insets show enlarged high frequency region for both.

4.3.6. Electrical Conductivity Measurements

RuO_2 being an excellent catalyst for a variety of industrial reactions and processes (like hydrogen storage), it would be of great interest to examine the electron transport properties of these congregated nanoneedles. Accordingly, electrical conductivity was measured from 80 K to 250 K using a standard DC four-point probe method under Ar atmosphere. Accordingly, figure 4.11a shows logarithmic variation of DC conductivity as a function of reciprocal of absolute temperature for the RuO_2 nanoneedles (RuO_2 nanoneedles after the complete dissolution of the alumina membrane template). The reproducibility has been verified by repeating the experiment more than three times under identical conditions. (The ohmic nature of the contact has been confirmed by carrying out I-V measurements at different temperatures as shown in the inset of figure 4.11a). Interestingly, on lowering the temperature, the conductivity, which remains constant up

to 125 K, shows a sharp increase up to 90 K followed by a considerable decrease. Increase in conductivity from 125 K to 90 K symbolizing a mere suppression of phonon scattering, which is predominant at high temperature and consequently at 90 K, conductivity shows a transition from metallic to semiconducting behavior due to the increased contribution from other scattering phenomena like impurity-scattering.[19] The latter effect is of practical significance since it allows the estimation of sample purity by conductivity measurement at low temperatures as it reveals the occurrence of impurity scattering/ non-stotiometric scattering. Since we have performed electrodeposition at sufficiently high potential, the formation of higher valent oxides of Ru such as RuO_2 and RuO_3 cannot be neglected[20] and hence we conclude that along with RuO_2, trace amount of RuO_3 is also present inside the nanoneedle. In addition, XPS studies show the presence of RuO_3 along with the RuO_2, which gives rise to impurity scattering and perhaps to decreased mobility. Hence, the conductivity decreases dramatically and shows a transition from metallic to semiconducting nature. On the other hand, the initial temperature-independent conductance could be presumed to be due to the combined effect of conduction 'along' and 'across' the ensemble of nanoneedles. In our case, since nanoneedles are assembled, electrical conduction can occur through the needle (intra-needle) as well as between the needles (inter-needle). Conductivity through the nanoneedle decreases with increase in temperature (since RuO_2 is metallic[21]) whereas conductivity between the nanoneedles increases with increase in temperature, assuming that the contact resistance between the nanoneedles decreases with increase in temperature. Also, for comparison, electrical conductivity plot of bulk RuO_2 sample is shown in figure 4.11b, which reveals metallic nature.

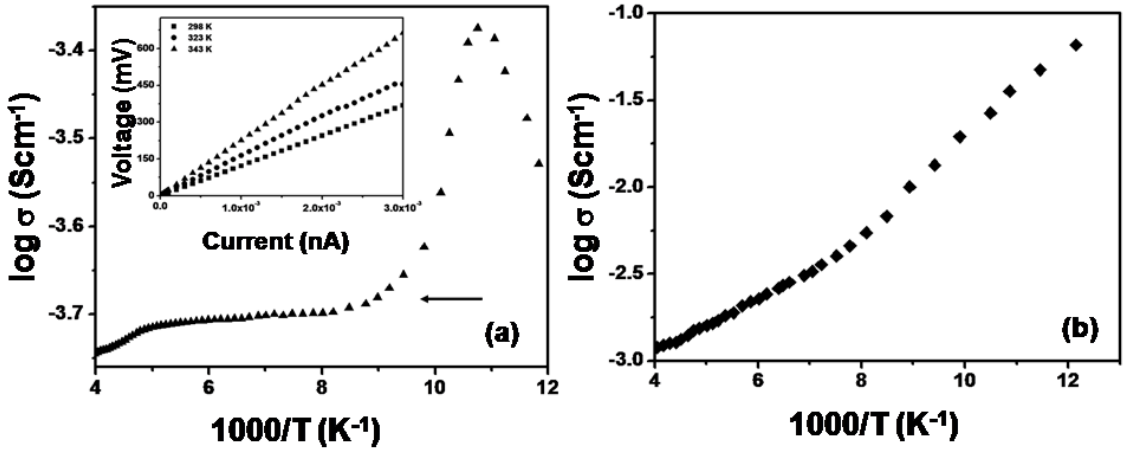

Figure 4.11. Temperature dependence of electrical conductivity in the range of 80 K to 250 K of (a) RuO_2 nanoneedles and (b) commercial anhydrous RuO_2 sample; inset of (a) shows I-V response of nanoneedles measured at different temperatures.

4.4. Conclusions

A simple route has been demonstrated for the formation of highly selective RuO_2 nanoneedles, which uses PAM template for electrodeposition. Further, the applicability of SECM technique for mapping the electroactivity of these nanostructures has been explored, which could be achieved by tuning the substrate potential. Interestingly, a comparison of the specific capacitance of these nanoneedles shows higher value compared to that of the bulk material. Electrical conductivity measurement of these RuO_2 nanoneedles show a transition from metallic to semiconducting behavior at 90 K suggesting the dominant role of impurity scattering over phonon scattering. Further, the redox related charging features have been studied using the feedback mode of SECM, which could be effectively achieved by tuning the substrate potential. The above findings will potentially benefits their applications in various areas including the designing of electrochemical supercapacitors.

4.5. References

1. (a) Campbell, P. F.; Ortner, M. H.; Anderson, C. *J. Anal. Chem*. **1961**, *33*, 58. (b) Vadimsky, R. G.; Frankenthal R. P.; Thompson, D. E. *J. Electrochem. Soc*. **1979**, *126*, 2017. (c) Goodenough, J. B. *Prog. Solid State Chem*. **1971**, *5*, 145. (d) Kim, Y. *Appl. Phys. Lett.* **1997**, *70*, 209. (e) Rolison, D. R.; Dunn, B. *J. Mater. Chem.* **2001**, *11*, 963. (f) Chang K. H.; Hu, C. C. *Appl. Phys. Lett*. 2006, **88**, 193102. (g) Zheng, J. P.; Jow, T. R. *J. Electrochem. Soc*. **1995**, *142*, L6.

2. (a) Trasatti, S.; Buzzanca, G. *J. Electroanal. Chem.* **1971**, *29*, A1 (b) Zheng, J. P.; Cygan P. J.; Jow, T. R. *J. Electrochem. Soc.* **1995**, *142*, 2699. (c) Jow, T. R.; Zheng, J. P. *J. Electrochem. Soc.* **1998**, *145*, 49.

3. (a) Trasatti, S. *Electrochim. Acta*. **1991**, *36*, 225. (b) Over, H.; Kim, Y. D.; Seitsonen, A. P.; Wendt, S.; Lundgren, E.; Schmid, M.; Varga, P.; Morgante, A.; Ertl, G. *Science* **2000**, *287*, 1474. (c) Popic, J. P.; Avramov-Ivic, M. L.; Vukovic, N. B. *J. Electroanal. Chem*. **1997**, *421*, 105. (d) Ryan, J. V.; Berry, A. D.; Anderson, M. L.; Long, J. W.; Merzbacher, C. I. *Nature (London)*, **2000**, *406*, 169. (e) Kameda, K.; Haruna, S.; Imanaka, T.; Kawamoto, K. *J. Chem. Soc., Chem. Comm*. **1990**, 1467.

4. (a) Hsieh, C. S.; Tsai, D. S.; Chen R. S.; Huang, Y. S. *Appl. Phys. Lett*. **2004**, 85, 3860. (b) Hsieh, C. S.; Wang, G.; Tsai, D. S.; Chen, R. S.; Huang, Y. S.; *Nanotechnology* **2005**, *16*, 1885. (c) Cheng, C. L.; Chen, Y. F.; Chen, R. S.; Huang, Y. S. *Appl. Phys. Lett.* **2005**, *86***,** 103104. (d) Krusin-Elbaum, L.; Wittmer, M. *J. Electrochem. Soc*. **1988**, *135*, 2610.

5.(a) Fernandez- Garcia, M.; Martinez-Arias, A.; Hanson, J. C.; Rodrignez, J. A. *Chem. Rev*. **2004**, *104*, 4063. (b) Burda, C.; Chen, X.; Narayanan, R.; El-Sayed, M. A. *Chem. Rev*. **2005**, *105*, 1025. (c) Heath, J. R. *Acc. Chem. Res*. **1999**, 32, 388. (d) Alivisatos, A. P. *Science* **1996**, *271*, 933. (e) Gudiksen, M. S.; Lauhon, L. J.; Wang, J. F.; Smith, D.C.; Lieber, C. M. *Nature* **2002**, *415*, 617.

6. (a) Ryan, J. V.; Berry, A. D.; Anderson, M. L.; Long, J. W.; Stroud, R. M.; Cepak, V. M.; Browning, V. M.; Rolison, D. R.; Merzbacher, C. I. *Nature* **2000**, *406*, 169. (b) Min, Y. -S.; Bae, E. J.; Jeong, K. S.; Cho, Y. J.; Lee, J. –H.; Choi, W. B.; Park, G. –S. *Adv.*

Mater. **2003**, *15*, 1019. (c) Wang, G.; Hsieh, C.-S.; Tsai, D.-S.; Chen, R.-S.; Huang, Y.-S. *J. Mater. Chem.* **2004**, *14*, 3503.

7. (a) Masuda, H.; Yamada, H.; Satoh, M.; Asoh, H.; Nakao, M.; Tamamura, T. *Appl. Phys. Lett.* **1997**, *71*, 2770. (b) Masuda, H.; Hasegwa, F.; Ono, S. *J. Electrochem.Soc.* **1997**, *144*, L127. (c) Li, A. P.; Muller, F.; Birner, A.; Nielsch, K.; Gosele, U. *J. Appl. Phys.* **1998**, *84*, 6023. (d) Jessensky, O.; Muller, F.; Gosele, U. *Appl. Phys. Lett.* **1998**, *72*, 1173.

8. (a) Long, J. W.; Swider, K. E.; Merzbacher, C. I.; Rolison, D. R. *Langmuir* **1999**, *15*, 780. (b) Chen, C. C.; Chen, R. S.; Tsai, T. Y.; Huang, Y. S.; Tsai, D. S.; Tiong, K. K. *J. Phys. Condend. Mater.* **2004**, *16*, 8475.

9. (a) Bard, A. J.; Fan, F.-R. F.; Pierce, D. T.; Unwin, P. R.; Wipf, D. O.; Zhou, F. *Science* **1991**, *254*, 68. (b) Bard, A. J.; Fan, F. -R. F.; Kwak, J.; Lev, O. *Anal. Chem.* **1989**, *61*, 132. (c) Fan, F.-R. F.; Bard, A. J. *PNAS* **1999**, *96*, 14222. (d) Lee, S.; Zhang, Y.; White, H. S. *Anal. Chem.* **2004**, *76*, 6108. (e) Zhou, J.; Zu, Y.; Bard, A. J. *J. Electroanal. Chem.* **2000**, *491*, 22. (f) Jambunathan, K.; Shah, B. C.; Hudson, J. L.; Hillier, A. C. *J. Electroanal. Chem.* **2001**, *500*, 279

10. (a) Hulteen, J. C.; Martin, C. R. *J. Mater. Chem.* **1997**, *7*, 1075. (b) Jin, C. G.; Jiang, G. W.; Liu, W. F.; Cai, W. L.; Yao, L. Z.; Li, X. G. *J. Mater. Chem.* **2003**, *13*, 1743. (c) Wang, X. W.; Fei, G. T.; Xu, X. J.; Jin, Z.; Zhang, L. D. *J. Phys. Chem. B* **2005**, *109*, 24326.

11. Ji, L.; Lin, J.; Zeng, H. C. *Chem. Mater*. **2001**, *13*, 2403.

12. Hones, P.; Levy, F.; Gerfin, T.; Gratzel, M. *Chem. Vap. Deposition*. **2000**, *6*, 193.

13. Xia, Y.; Yang, P.; Sun, Y.; Wu, Y.; Mayers, B.; Gates, B.; Yin, Y.; Kim, F.; Yan, H. *Adv. Mater*. **2003**, *15*, 353.

14. McKeown, D. A.; Hagans, P. L.; Carette, L. P. L.; Russel, A. E.; Swider, K. E.; Rolison, D. R. *J. Phys. Chem. B* **1999**, *103*, 4825.

15. Zoski, C. G. *J. Phys. Chem. B* **2003**, *107*, 6401.

16. Sugimoto, W.; Iwata, H.; Yokoshima, K.; Murakami, Y.; Takasu, Y. *J. Phys. Chem. B* **2005**, *109*, 7330.

17. Bard, A. J.; Faulkner, L. R. *Electrochemical Methods: Fundamentals and Applications*; Wiley: New York, 2001.

18. Huang, Q.; Wang, X.; Li, J. *Electrochim. Acta* **2006**, *52*, 1758.

19. (a) Datta, S. *Electronic transport in mesoscopic systems*; Cambridge University Press, 1995. (b) Shimakawa, M.; Maki, H.; Nishihara, H.; Hayashi, K. *Mat. Res. Bull*. **1997**, *32*, 689. (c) Nakazawa, H.; Ito, Y.; Matsumoto, E.; Adachi, K.; Aoki, N.; Ochiai, Y. *J. Appl. Phys*. **2006**, *100*, 093706.

20. Kim, H.; De Moraes, R.; Tremiliosi-Filho, G.; Haasch, R.; Wieckowski, A. *Surf. Sci. Lett.* **2001**, *474*, L203.

21. (a) Butler, S. R.; Gillson, J. L. *Mat. Res. Bull.* **1971**, *6*, 81. (b) Glassford, K. M.; Chelikowsky, J. R. *Phys. Rev. B.* **1994**, *49*, 7107. (c) Ryden, W. D.; Lawson, A. W.; Sartain, C. C. *Phys. Rev. B*. **1970**, *1*, 1494.

CHAPTER 5

Y-junction Nanostructures of Platinum and Palladium Using Hierarchically Designed Alumina Templates*

The utility of hierarchically designed alumina templates for the shape-selective preparation of platinum Y-junction nanostructures through electrodeposition is demonstrated in this chapter. Although these Y-junctions have typical diameters of the stem and branches as 100 nm and 50 nm respectively, it is indeed, possible to tune both these parameters by controlling the template design strategies. This chapter also describes our efforts using similarly designed alumina templates for the formation of Y-junction nanostructure of palladium possessing stem and branches having diameter 200 and 110 nm, respectively through a chemical vapour deposition. When the electrocatalytic performance of Pt Y-nanostructures is compared with that of commercial platinized carbon, towards formic acid oxidation, these junctions exhibit enhanced activity (up to 270 %), whereas for methanol and ethanol oxidation, the enhancement is up to 680 % and 180 % respectively. With respect to Pt nanowires, however, these Y-junctions show 200 % enhancement for formic acid oxidation while 400 % and 130 % are seen for methanol and ethanol oxidations respectively. In the end of this chapter we also demonstrate the usefulness of Pd Y-junctions as an alternative catalyst to Pt for formic acid oxidation where, about 1000 % better relative activity is seen. Apart from the obvious applications in developing electrocatalytic anodes for micro-fuel cells, these Y-junction nanostructures have several other promising applications such as interconnects in many molecular scale electronic devices like single electron transistors, resonant tunnelling diodes, and molecular rectifiers.

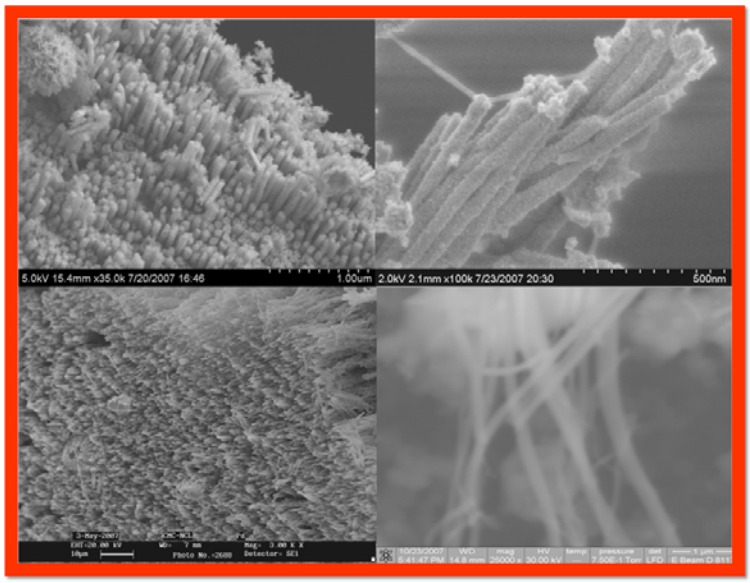

*A part of the work discussed in this chapter has been published in "*Chem. Mater*. **2008**, *20*, 601".

5.1. Introduction

Recently, much effort has been directed towards the fabrication of shape selective nanostructures because of their exquisite size and shape dependent properties and also their technological relevance in diverse areas such as catalysis, photochemistry, chemical sensors and optoelectronics.[1] These nanostructures are generally synthesized in many forms including highly monodispersed spherical nanoparticles on one hand, to several anisotropic nanostructures such as wires/rods, tubes and ribbons.[2] It is generally accepted that the morphology of a nanostructure could be remarkably tuned during the synthesis by controlling pertinent parameters such as temperature, nature of surfactant, metal ion to capping molecule ratio, and the concentration of other additives in order to control the physical and chemical properties of these materials.[3] As a result, various methods have been developed to generate many of these nano level architectures with relatively good shape control.[4] Among these, the template-assisted route has been one of the widely investigated and exploited approaches, because it provides several distinct advantages over other approaches. More importantly, it offers a convenient route to control precisely the dimension of the nanostructures and these structures can be released easily from the support.[5] Templates that can be used include soft (such as micelles) as well as hard (such as porous polymeric or ceramic membranes) templates.[6] In particular, hard templates, like porous alumina membranes (PAM) have been extensively used due to many desirable characteristics, including tunable pore dimensions and lengths, good mechanical and thermal stability, and well developed fabrication methods.[7] Even though, processing inside these type of porous templates is ideal to produce uniform morphologies, this route has been accomplished to date successfully, only for linear structures.

Interestingly, the fabrication of three terminal morphology like Y-junctions has drawn widespread attention considering their technological importance in advanced molecular-scale electronic devices and prospective applications in catalysis.[8] For

example, electron transport across multi-terminal junctions like Y, T, and X nanostructures is non-linear revealing interesting rectifying behavior at room temperature which, could be used for many efficient nanoelectronic devices.[9] For example, Papadopoulos et al. have investigated the electron transport behavior of carbon nanotube Y-junctions to demonstrate intrinsic non-linear transport facilitating rectifying behavior at room temperature.[8a] However, the fabrication of these junctions is difficult using conventional methods because these linear structures cannot be controllably altered along their length. Although, much effort has been devoted to the fabrication of junction type nanostructures, the main attention, to date, has been focused mainly on Y-junctions of carbon nanotubes. For example, Rao et al. and others have synthesized Y-junctions of carbon nanotubes by a chemical vapor deposition route using a suitable metal catalyst, which facilitates the nucleation of junctions/branches.[8f,10] However, no metallic Y junction has been reported for metals such as Pt and Pd despite their theoretical and practical importance.

In chapter four, we have discussed the potentiostatic synthesis of nanoneedles of RuO_2 using linear PAM to indicate their unique electron transport behaviour. In comparison, here we demonstrate the utility of hierarchically designed PAM templates for the fabrication of Y-shaped platinum nanostructures through a similar electrodeposition route. Platinum has been selected because of its outstanding role as multifunctional catalysts in many industrial applications, particularly in fuel cells.[11] Apart form this, the fabrication of Y-branched nanostructures of other catalytically active metals such as palladium is also discussed by extending a similar template-assisted approach, although chemical vapour deposition is used instead of electrodeposition. The utility of these structures for the electrocatalytic activity towards methanol, ethanol, and formic acid oxidations has been demonstrated which could be of immense relevance to portable fuel cell technology, since designing a better electrocatalysts continues to pose daunting challenges.

5.2. Experimental Details

5.2.1. Materials

$H_2PtCl_6.6H_2O$ (99.98%) and $PdCl_2$ (99 %) were purchased from Aldrich chemicals while boric acid (99.5 %) was purchased from Loba Chemie. Solvents like ethanol (99.9 %), methanol (99.5 %) and formic acid (98 %) were purchased from Merck. All reagents were used without further purification and deionized water (18 MΩ) from milli-Q system was used in all experiments.

5.2.2. Preparation of Y-junction Platinum Nanostructures

A free-standing Y-PAM template, fabricated via an extended two–step anodization route (for details see Chapter II, section 2.4.3) was used as the working electrode for electrodeposition, after evaporating Au film (200 nm) on one side of the membrane. Electrodeposition was carried out using this working electrode in an aqueous solution of 5 mM H_2PtCl_6 and boric acid as a buffer (1 mM) at a pH of 2.5.[12] After a pretreatment of the Au film supported PAM template in ethanol by sonication to drive out trapped air inside the holes, the membrane was kept at 80 ^oC in a mixture of H_2PtCl_6 (5 mM) and boric acid (1 mM) for 30 min and subsequently electrodeposition was carried out at a potential of -0.7 V vs SCE, for 15 min. In addition, electrodeposition was carried out at 60 ^oC and also without any prior heat treatment. Finally, the nanostructures were released from the PAM by dissolving the template in 0.1 M NaOH and then washing several times with deionized water till a neutral pH, followed by a final washing with ethanol to yield almost 80 % of pure structures. A schematic representation of different stages involved during the formation of Pt Y-junction is shown in scheme 5.1, which includes evaporation of Au film on one side of the free standing Y-PAM and followed by electrodeposition of Pt.

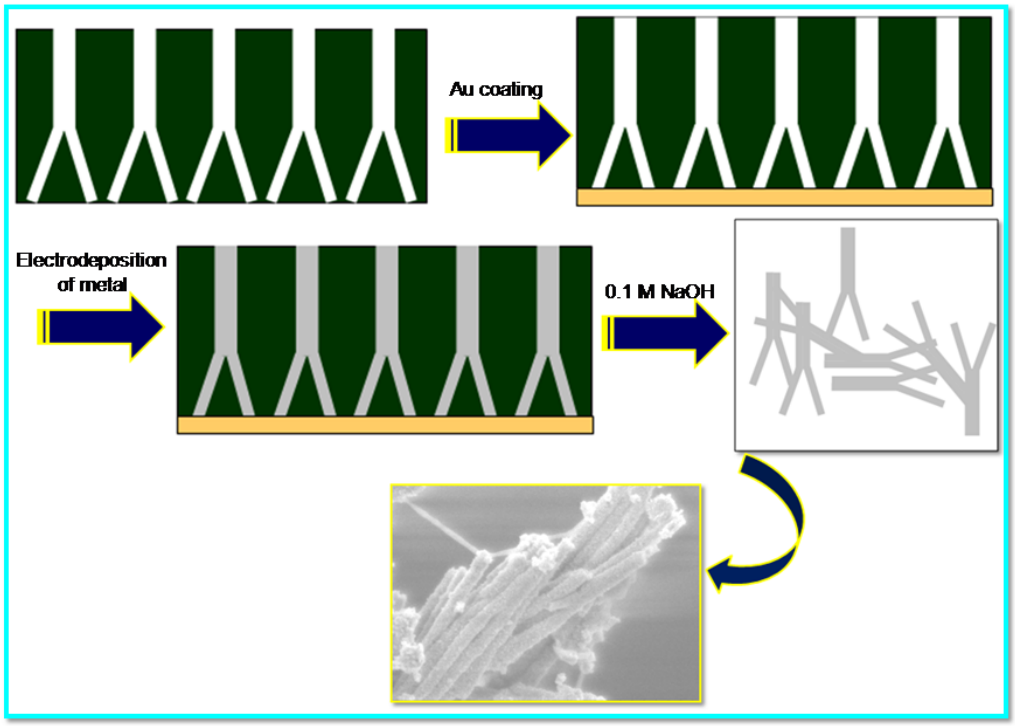

Scheme 5.1. Different steps involved in the preparation of Pt Y-junction nanostructure through an electrodeposition route; coating of Au film on one side of the free-standing Y-PAM by sputtering; electrodeposition of Pt using a mixture of aqueous H_2PtCl_6 and boric acid; etching of alumina membrane in NaOH to release Y-junction nanostructures.

5.2.3. Preparation of Platinum Nanowires

A free-standing linear PAM template fabricated via a two–step anodization route (for details see Chapter II, section 2.4.2) was used as working electrode, after evaporating Au film (200 nm) onto one side of the membrane for electrical contact. Similar electrodeposition procedure as discussed above was adopted for the formation of Pt nanowires.

5.2.4. Preparation of Y-junction Palladium Nanostructures

Monolayer protected gold nanoclusters, AuMPCs (capped by tridecylamine, prepared via a modified Brust synthesis route; diameter ca. 6 nm) was vacuum (10^{-3} torr) filtered through the Y-branched alumina membrane, in order to deposit the nanoparticles

at the bottom of these membrane. These nanoparticles could act as catalysts for the growth of Y-junction Pd inside the membrane. After filtration, the membrane was washed thoroughly in dichloromethane to remove particles adhered on the external surface of the membrane. An indigenously fabricated CVD set-up capable of attaining 1000^{o}C comprising a single zone furnace was used for the synthesis of Pd Y-junction nanostructures. CVD set-up for the deposition of Pd inside the Y-PAM is shown in figure 5.1. It consists of a tubular furnace, in which the above membrane was placed (face down) on the top of the alumina boat containing 25 mg of $PdCl_2$ at the centre of the furnace. The reaction was carried out at 850 ^{0}C under N_2 atmosphere for 4 h. After the reaction, the temperature of the furnace was cooled to room temperature with uninterrupted N_2 flow. Subsequently, the membrane was dissolved in 0.1 M NaOH and the sample was washed several times with deionized water till neutral pH, followed by a final washing with ethanol to yield almost 90 % pure structures. A cartoon, representing different stages involved during the formation of Pd Y-junction nanostructure is shown in scheme 5.2, where incorporation of AuMPCs at the pore bottom and subsequent deposition of Pd inside the branched alumina membrane are shown.

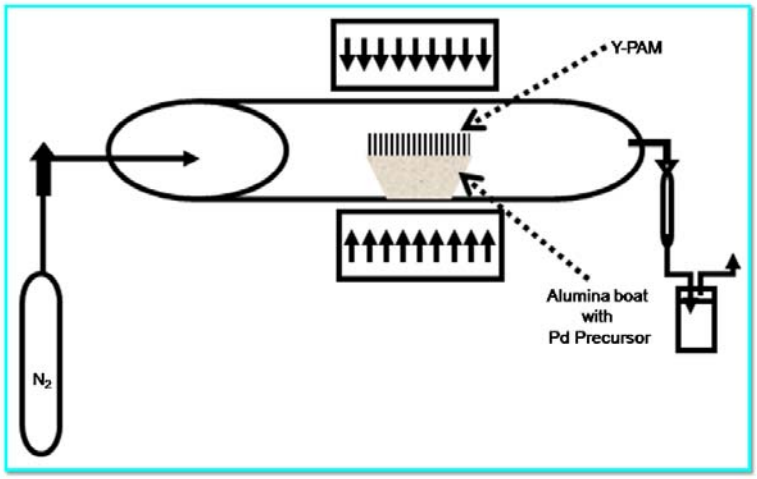

Figure 5.1. CVD set-up used for the deposition of palladium inside the Y-PAM; reaction was performed at 850^{o}C for 4h under N_2 atmosphere; various components including single zone furnace, carrier gas and precursors are shown.

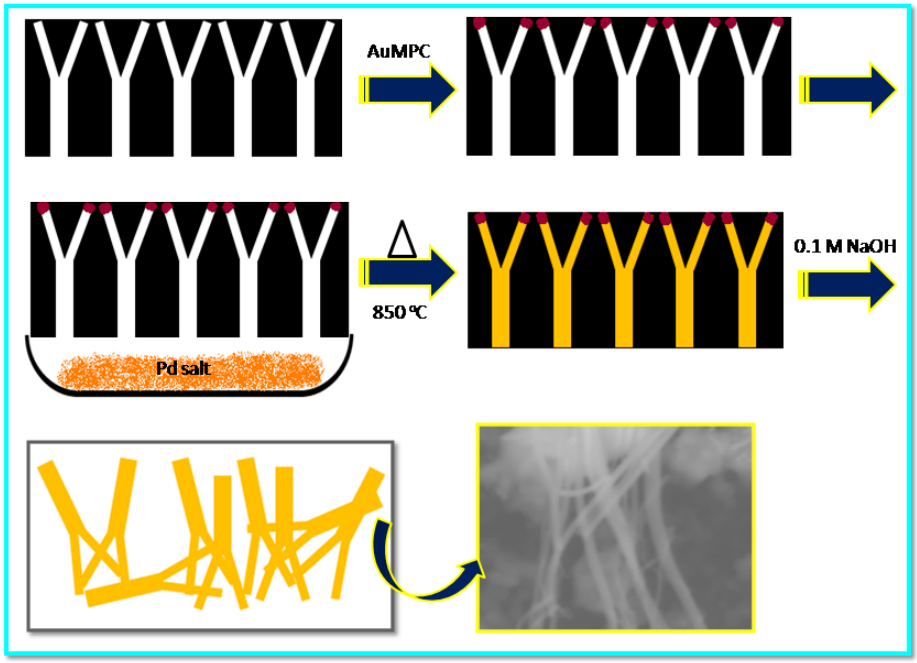

Scheme 5.2 Different steps involved in the preparation of Pd Y-junction nanostructure through chemical vapour deposition; deposition of AuMPCs at the bottom of the porous membrane was followed by Pd deposition through CVD at 850 ^{o}C under N_2 atmosphere; finally the structures were released after dissolving the membrane in NaOH.

5.2.5. Investigation of electrocatalytic activity

To investigate the electrocatalytic activity of Pt Y-junction nanostructures, the working electrode was prepared by dispersing 20 wt % Pt Y- nanostructures in Vulcan XC -72 carbon (C) using isopropyl alcohol followed by drop casting to form a thin film on a glassy carbon electrode (ca. 3 mm diameter) using 0.5 wt% Teflon binder. A similar procedure was adopted to prepare the electrode of Pt nanowires, Pd Y-junctions and commercial platinized carbon (20 % Pt on Vulcan XC-72 carbon from Arora Matthey Limited; diameter 8 nm) always using identical amounts.

Cyclic voltammogram (CV) of Pt Y-junction nanostructure was first recorded in 0.5 M H_2SO_4, and the electroactive area (A_{Pt}) was determined from the adsorption/desorption charge of hydrogen atoms from this (ca. 210 μC/cm^2 for a

polycrystalline surface).[13] Cyclic voltammogram and transient current-time curve for formic acid oxidation were recorded in a mixture of 0.25 M HCOOH and 0.5 M H_2SO_4 at various potentials ranging from -0.44 V to +0.16 V Vs Hg-Hg_2SO_4 at an interval of 0.05 V. Further, the current density (j) was obtained after normalizing the current to A_{Pt}. Before recording the current transients, sufficient care was taken to oxidize any adsorbate on the electrode surface so as to obtain a clean surface. Similarly, the electrocatalytic activity of Pt Y-junctions towards ethanol oxidation was studied in a mixture of 0.1 M CH_3CH_2OH and 0.1 M $HClO_4$, whereas the mixture of 0.5 M H_2SO_4 and 0.5 CH_3OH was used for methanol oxidation, following similar procedures. All experiments were repeated using commercial platinized carbon and nanowires of Platinum.

For Pd Y-junctions, cyclic voltammogram was first recorded in 0.5 M H_2SO_4, and the electroactive area (A_{Pd}) was determined from the charge required for the reduction of palladium oxide monolayer (i.e., 405 $\mu C/cm^2$).[14] Further, to measure the electrocatalytic activity of these structures towards formic acid oxidation, polarization experiment was performed in a mixture of 0.25 M HCOOH and 0.5 M H_2SO_4 using a similar procedure as discussed above.

5.2.6. Structural and Morphological Characterization

5.2.6.1. SEM and EDX

The morphology of the Y-junction nanostructures was characterized using three scanning electron microscopes, Lieca Stereoscan 440 Model, Hitachi S-4800 field emission scanning electron microscope and FEI Quanta 200 3D microscope equipped with tungsten filament. Energy dispersive point spectra were measured at 10 keV using an Oxford INCA x-sight energy dispersive X-ray microanalysis system connected with the Hitachi S-4800. For these, a little amount of sample was dispersed in ethanol and dropcast on Cu substrate and dried at room temperature.

5.2.6.2. TEM

TEM images were recorded on a JEOL model 1200 EX instrument operated at an accelerating voltage of 120 kV after placing a drop of the dispersed solution onto a carbon-coated Cu grid (3 nm thick, deposited on a commercial copper grid for electron microscope), which was dried in air and loaded into the electron microscopic chamber.

5.2.6.3. Electrochemical Measurements

All electrochemical experiments were performed on an Autolab PGSTAT30 (Eco chemie) instrument at room temperature. For electrodeposition, Au film supported linear PAM/Y-PAM was used as the working electrode whereas saturated calomel electrode (SCE) and two Pt foils were used as reference and counter electrodes respectively. Electrocatalytic study was performed using a glassy carbon (GC) electrode modified with nanostructure/C (nanostructure dispersed in Vulcan carbon) as explained in details in section 5.2.5. Also, a Hg-Hg_2SO_4 and a platinum foil were used as the reference and counter electrodes, respectively.

5.2.6.4. Conducting Atomic Force Microscopy

Platinum nanowires and Y-junctions were characterized by using conducting AFM-built around Burleigh Metris-2000 AFM head. Prior to the measurements, Si (111) wafer was dipped for 30 s in hydrofluoric acid in order to remove the oxide layer. The conducting force sensing probe was connected to the virtual ground of the preamplifier. The sample was isolated from ground and connected to a bias voltage. n-type silicon cantilever (from nanosensors) of resistivity 0.01-0.02 Ωcm and spring constant of 40-50 Nm^{-1} was used after depositing platinum (thickness 10 nm) on the n-type Si cantilever to avoid oxidation of the tip. After dispersing the sample in chloroform, a drop was added onto the silicon wafer for measurements.

Other characterization details like XRD and XPS have already been described in Chapter 2, section 2.4.5.2 and Chapter 3, section 3.2.4.2 respectively.

5.3. Results and Discussion

5.3.1. SEM Analysis

A typical field-emission scanning electron micrograph (FESEM), (top view) of the Pt Y-junction (before dissolving the membrane) prepared using the above mentioned hierarchically designed alumina template is shown in figure 5.2a, revealing that almost all the pores are effectively filled with Pt. Similar FESEM images after dissolving the membrane in 0.1 M NaOH, however, in figure 5.2b-d, depict uniform Y-junctions with well defined branches and stems having diameter ca. 100 and 50 nm respectively, closely in agreement with those of the Y-branched alumina nanochannels. In addition, the angle between the branches is ca. 12^{o}, slightly higher compared to that of the template, perhaps due to the tendency of the structure to release the strain involved at the junction after the dissolution of the membrane. Also, figure 5.2e shows image of some broken Y-junction nanostructures, presumably formed during the purification. In addition the energy dispersive x-ray analysis (EDX) spectrum (Figure 5.2f) confirms the complete removal of Al from the sample (Si peak seen in the spectrum, could be from the substrate).

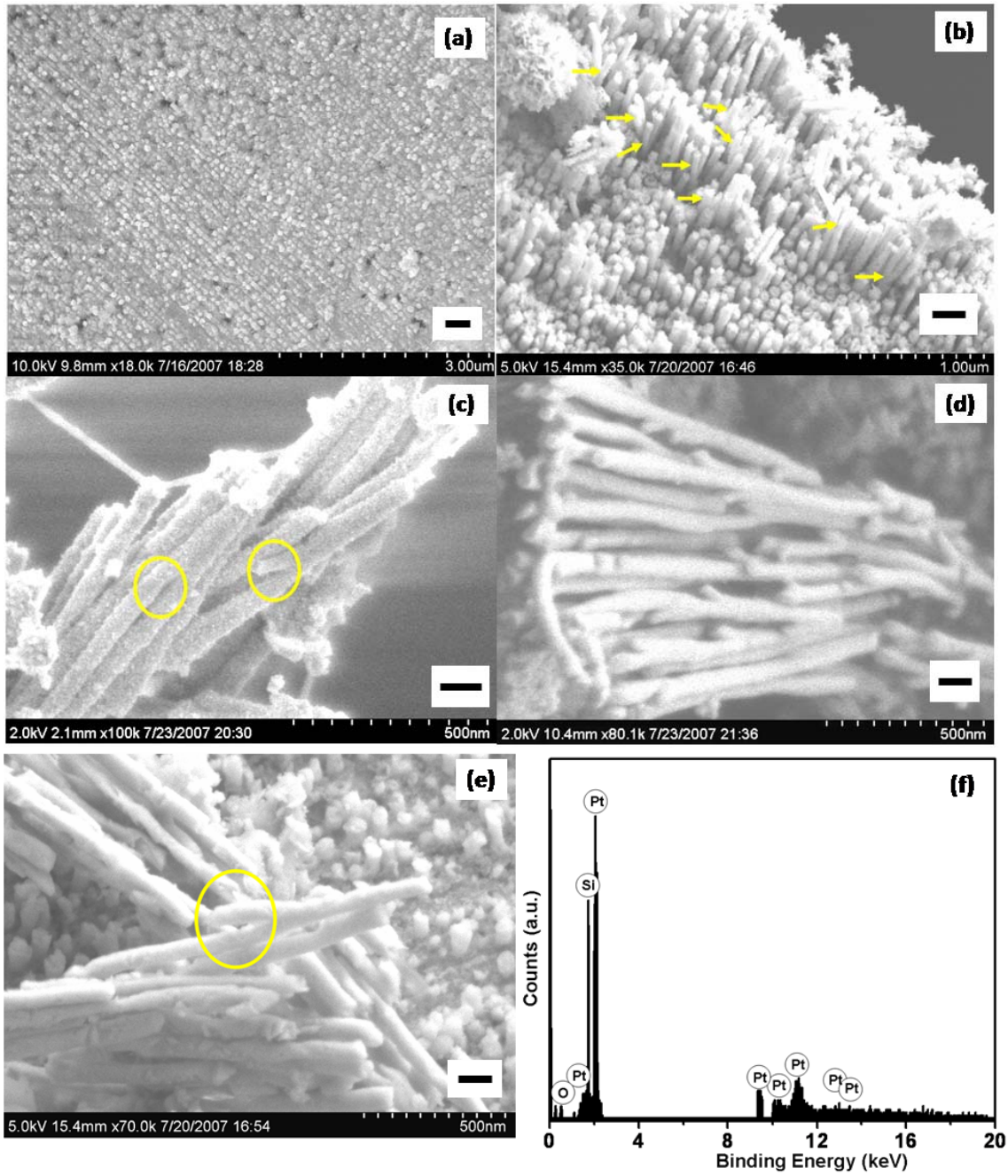

Figure 5.2. FESEM images of Pt-Y junction nanostructures (a) before dissolving the membrane (top view; scale bar 300 nm); (b-d) after etching the alumina template in 0.1 M NaOH, where the diameter of the stem and branches are ca. 100 and 50 nm respectively (scale bar 200 nm, 100 nm and 100 nm); (e) some broken Y-junction nanostructures (scale bar 100 nm); (f) shows the EDX spectrum taken from the Pt Y-junction nanostructure.

Since these Y-junction nanostructures are obtained only after maintaining the electrolyte above a critical temperature (80 ^{o}C) for 30 min, it is important to understand systematically the influence of temperature on controlling the dimensional features of Y-junctions. Interestingly, at room temperature and also at 60 ^{o}C, scanning electron micrographs (SEM) reveal only tiny nanorods of Pt and low aspect ratio Y-junction with poor yield respectively, (as shown in figure 5.3a,b) and hence it is absolutely essential to maintain higher temperature like 80 ^{o}C to form Y-junctions. This is because the nanoporous structure of the template, due to its slow diffusion, (Knudsen diffusion) hinders the deposition rate, which in turn prevents uniformity and quality of the structure at low temperature.[15] At higher temperatures, the mass-transfer resistance is reduced by decreasing the Nernst diffusion layer thickness, which facilitates the Y-junction formation. In contrast, reports are available on the utilization of ultrasonication during template-assisted electrodeposition to improve the mass-transfer resistance.[16]

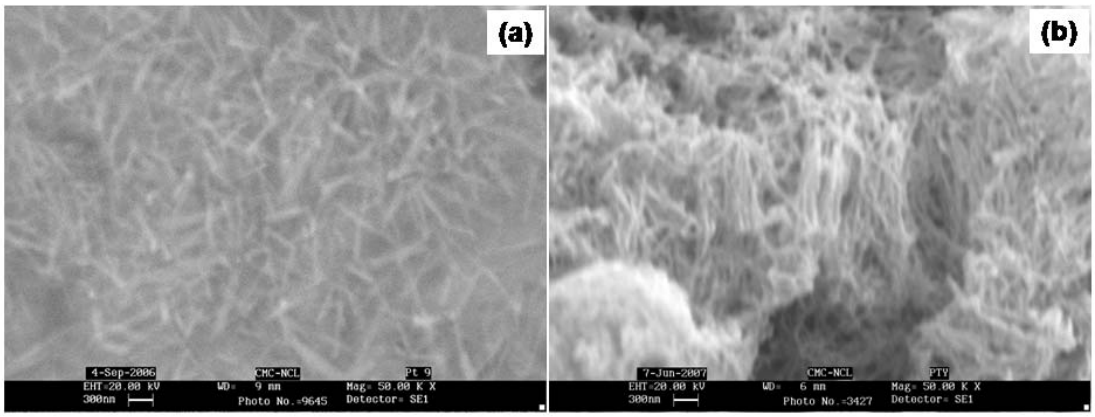

Figure 5.3. SEM images of Pt nanostructure after dissolving the alumina membrane (a) Pt nanorods at room temperature; (b) low aspect ratio Pt Y-junction nanostructure at 60^{o}C.

Similarly FESEM image of Pt nanowires prepared through the same electrodeposition route, but using linear PAM is shown in figure 5.4 after releasing the structures form alumina template, where the nanowires are perfectly aligned possessing a uniform diameter of ca. 80 nm.

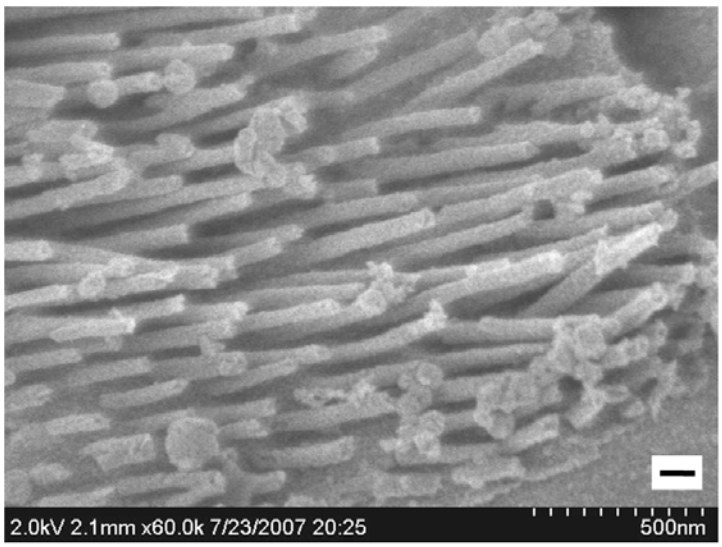

Figure 5.4. FESEM image of Pt nanowires after dissolving the alumina membrane in 0.1 M NaOH; the nanowires were prepared through an electrodeposition route after maintaining the electrolyte bath at 80^{o}C; scale bar 100 nm.

Similarly, SEM images of Pd Y-junction nanostructures (after dissolving the membrane in 0.1 M NaOH) prepared using hierarchically designed alumina templates through a CVD route, are shown in figure 5.5. In contrast to electrodeposition route followed for Pt Y-junction nanostructure, CVD procedure is adopted basically due to the two reasons: (1) prior to electrodeposition, the membrane needs to be maintained at a particular temperature for efficient filling of the porous structure, and (2) relatively higher yield is obtained through CVD with respect to electrodeposition route. Here, figure 5.5a reveals an array of Pd Y-junctions, whereas individual Y-junctions are clearly shown in figure 5.5b revealing uniform and well defined branches and stems having a diameter of ca. 110 and 200 nm respectively. A close examination reveals that diameter of both the stem and branches are slightly higher compared to that of the template, presumed to be due to the expansion of the Y-branched nanochannels during the synthesis of the Pd Y-junction nanostructure at higher temperature. Furthermore, the angle between the branches is ca. 20^{o}, slightly higher compared to that of the template, perhaps due to the tendency of the structure to release the strain involved at the junction

after the dissolution of the membrane. This larger angle may also be due to the significantly higher reaction temperature (850^{o}C).

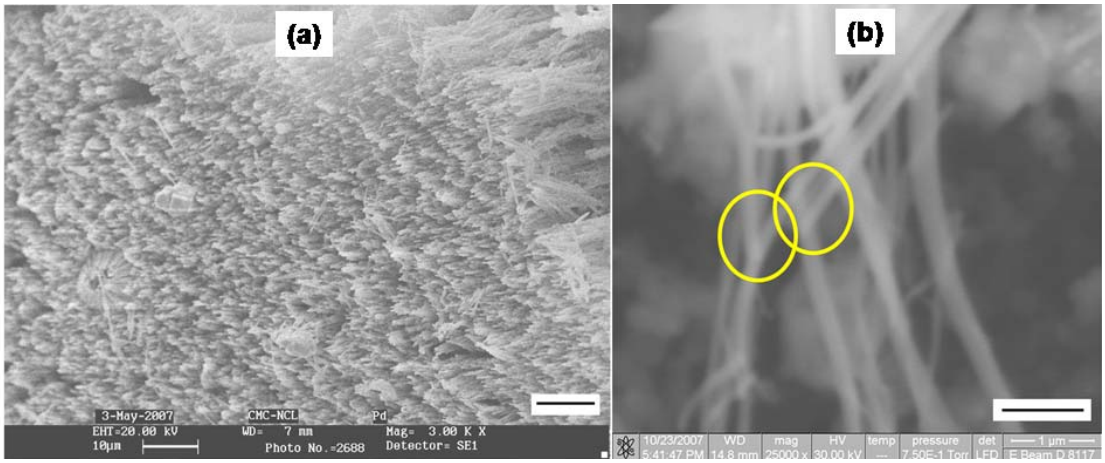

Figure 5.5. SEM images of Y-branched Pd Y-junction nanostructure after dissolving the alumina membrane in 0.1 M NaOH, where (a) reveals an array of Y-junction palladium while individual Pd Y-junctions are clearly seen in (b); scale bar 10 µm and 1 µm, respectively.

5.3.2 TEM Analysis

Figure 5.6a shows the bright field transmission electron micrograph (TEM) of such a Y-junction nanostructure, after removing the structures from the template revealing the stem and branches having a diameter in complete agreement with the SEM results. Figure 5.6b shows the selected area electron diffraction (SAED) taken from a single Y-junction, where the diffractogram demonstrates that the structure is polycrystalline with (111), (200), and (220) preferred planes, corresponding to the face centered cubic (fcc) structure of Pt.[17]

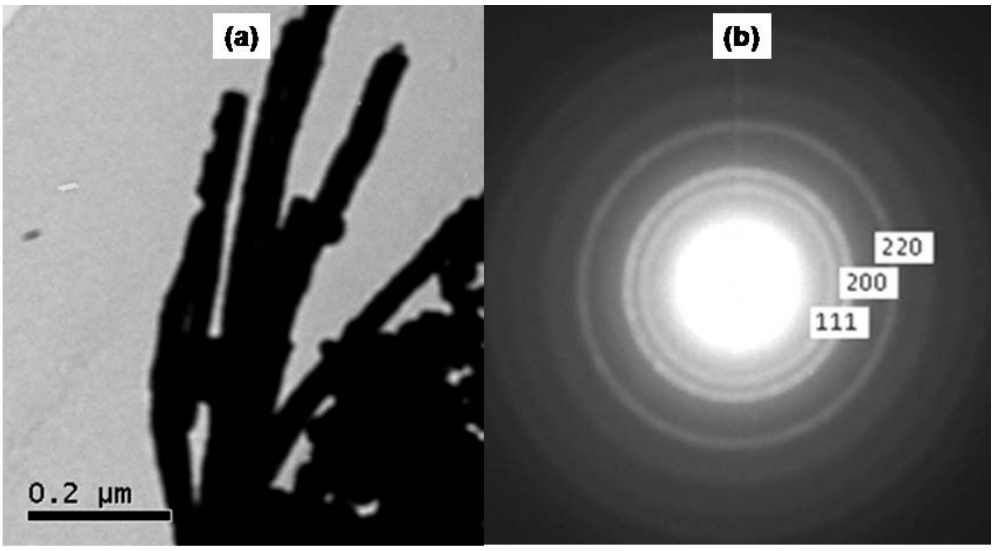

Figure 5.6. (a) TEM image of Y-junction platinum nanostructures after etching the alumina membrane, where the diameters of the stem and branches are consistent with the SEM images; the SAED pattern (b) taken from a single Y-junction revealing polycrystalline nature.

5.3.3. XRD Analysis

Information on the crystal structure and the crystallite size of these Y-junction nanostructures is also provided by powder XRD. Accordingly, figure 5.7a shows the XRD pattern of Pt-Y which reveals the formation of a cubic structure with high crystallinity. All diffraction peaks, (111), (200), and (220) match well with Bragg reflections of the standard and phase-pure face centered cubic (fcc) structure of Pt. Further, the crystallite size calculated using the Scherrer formula is ca. 9.2 nm, considering the (111) reflection. Also the XRD pattern reveals no change in the peak position for Pt-Y as compared to that of XRD pattern of Pt nanowires prepared using anodic alumina membrane.[18] Apart from the response corresponding to Pt, a broad peak at $2\theta = 25^{o}$ associated with the (002) planes of Vulcan XC-72 carbon, is also seen due to the support.

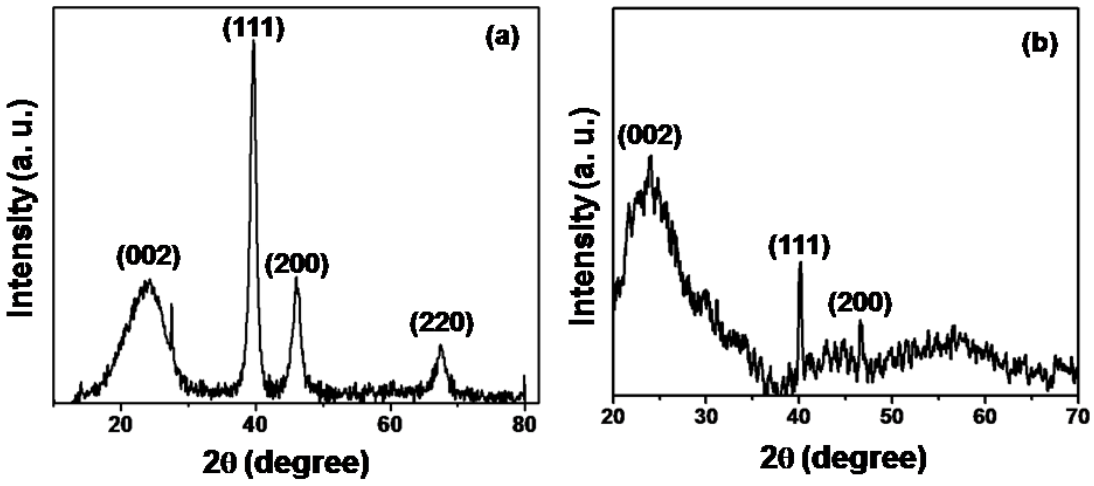

Figure 5.7. Powder XRD pattern of (a) Pt Y-junction (b) Pd Y-junction dispersed in vulcan carbon; all these diffraction peaks match well with the corresponding peaks for the standard fcc structure of bulk Pt and Pd respectively; the spectrum also reveals a broad peak corresponding to the (002) planes of vulcan carbon.

Similarly, figure 5.7b shows the XRD pattern of Pd-Y/C which reveals the formation of a cubic structure with high crystallinity. All diffraction peaks for (111), (200) planes match well with Bragg reflections of the standard and phase pure face centered cubic (fcc) structure of Pd. Besides the response corresponding to Pd, a broad peak at $2\theta = 25^{o}$ is associated with the (002) planes of vulcan XC-72 carbon due to the support. Also the XRD pattern reveals no change in the peak position for Pd-Y as compared to that of Pd nanowires prepared using, anodic alumina membrane.[19] The crystallite size of these Y-junction nanostructures calculated using the Scherrer formula is ca.15.8 nm, considering the reflection from (111) plane. Thus XRD results are in excellent agreement with the results obtained from TEM analysis.

5.3.4. XPS Analysis

Since XPS analysis provides valuable information on the oxidation state of these Y-junctions, XP spectra of both Pt-Y and Pd-Y junction structures are shown in figure 5.8a and b respectively. Figure 5.8a shows the Pt 4f region where, deconvolution reveals two

peaks at 71.08 eV and 74.3 eV (after carbon correction) corresponding to Pt $4f_{7/2}$ and $4f_{5/2}$ respectively.[20] These values confirm that Y-junctions are metallic with a typical peak to peak separation of ca. 3.2 eV, which is in excellent agreement with the bulk platinum metal. Similarly, XP spectrum of Pd Y-junctions shown in figure 5.8b reveals four peaks corresponding to Pd $3d_{3/2}$ and $3d_{5/2}$, where peaks at 337.6 and 335.5 eV could be attributed to the Pd(0) state, with a peak to peak separation of 2.1 eV. In addition, the remaining two peaks at 343.4 and 340.7 eV could be assigned to $3d_{3/2}$ and $3d_{5/2}$ levels of Pd(II), representing perhaps un-reacted $PdCl_2$.[21]

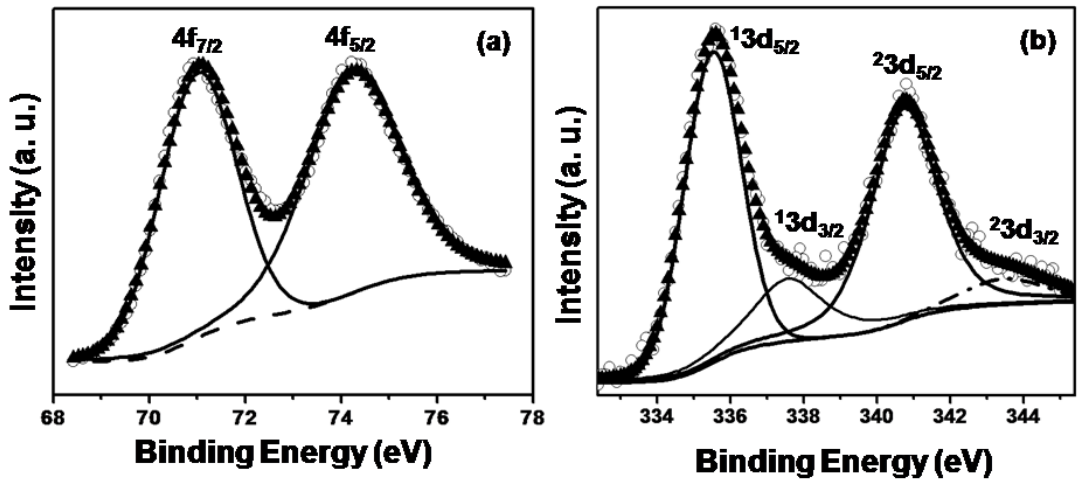

Figure 5.8 X-ray photoelectron spectra of (a) Pt Y-junction showing Pt 4f core level; (b) Pd Y-junction showing 3d core level (here, Pd(0) and Pd(II) states are distinguished by superscripts 1 and 2 respectively) where, core levels are deconvoluted using Shirley software; the circles represent the raw data while triangles represent the fitted data for the overall signal; dash lines indicate the background, whereas the solid lines represent the deconvoluted individual peaks.

5.3.5. Electrocatalytic Performance of Pt Y-junctions, Nanowires and Commercial Platinized Carbon

5.3.5.1. Formic Acid Oxidation

Cyclic voltammetric response of Pt-Y/C and Pt-NW/C towards formic acid oxidation at 50 mV/s in a mixture of 0.5 M H_2SO_4 and 0.25 M HCOOH are shown in figure 5.9, where both samples reveal the characteristic features of formic acid oxidation.

The voltammetric response of Pt/C is also shown in figure 5.9 where two peaks are clear during the anodic scan (at -0.07 V and +0.7 V for Pt-Y/C) while only one peak (-0.12 V for Pt-Y/C) is observed during the reverse (cathodic) scan. A considerable shift in peak position is observed for different electrodes, as obvious from the voltammogram. The first anodic peak is due to the oxidation of HCOOH to CO_2 on surface sites that remain unblocked by CO, whereas the second anodic peak corresponds to the oxidation of surface adsorbed CO. During the cathodic sweep, a peak is observed after the partial reduction of irreversibly formed surface oxides, which represents the real catalytic activity of the Pt surface. [Reaction mechanism and different pathway involved during the formic acid oxidation has already been discussed in chapter III, section 3.3.5.1] Furthermore, a closer look at the voltammogram reveals a substantial enhancement in peak current corresponding to Y-junction compared to that of other samples. (In all the cases oxidation current has been normalized to electroactive Pt surface area (A_{Pt}) so that the current density (j) can be directly used to compare the catalytic activity of all samples).

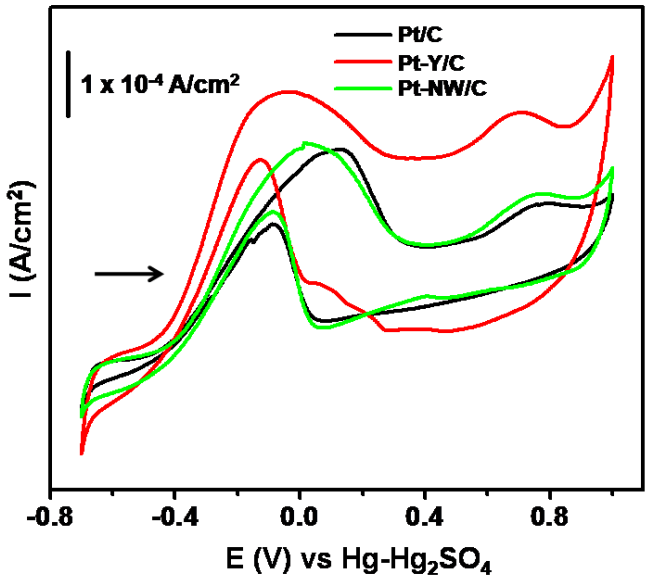

Figure 5.9. Cyclic voltammetric response (2nd cycle data) of Pt-Y/C, Pt-NW/C and Pt/C toward formic acid oxidation in a mixture of 0.25 M HCOOH and 0.5 M H_2SO_4 at 50 mV/s.

Figure 5.10 shows a comparison of transient current density of formic acid oxidation at -0.24 V (potential selected from the cyclic voltammogram, Figure 5.9) on Pt/C (commercial platinized carbon), Pt-Y/C (Y-junction Pt nanostructure in vulcan XC -72 carbon) and Pt-NW/C (Pt nanowires in vulcan XC -72 carbon) samples. Interestingly, the oxidation current density on Pt-Y/C is significantly higher compared to that on both Pt-NW/C and Pt/C and the enhancement factor *R*, (which is defined as the ratio of the current density measured on Pt-Y/C versus that acquired on Pt-NW/C or Pt/C) increases up to 270 % for Pt/C and up to 200 % for Pt-NW/C sample respectively, depending upon the electrode potential. Further, from the steady state I-V plot (where the steady state current density is obtained from the current transients recorded for 60 s for various potentials, -0.44 to +0.16 V), shown in figure 5.11, we observe that at a given current density, the corresponding potential on Pt-Y/C is much lower than that for Pt-NW/C and Pt/C. Further, the value is shifted negatively by ca. 90 mV at a current density of 9.5×10^{-5} A/cm^2 with respect to that of Pt/C, whereas the shift is ca. 40 mV as compared with Pt-NW/C. Recently Wang et al. have seen for tetrahexahedral platinum nanocrystals that at a given oxidation current density, these tetrahexahedra show a negative shift in potential by 60 mV compared to that on Pt/C catalyst towards formic acid oxidation, which is indeed significantly lower compared to that of Pt-Y nanostructures.[22] This shows that formic acid oxidation is thermodynamically more feasible on Pt Y-junctions compared to that on highly faceted structure such as tertrahexahedra.

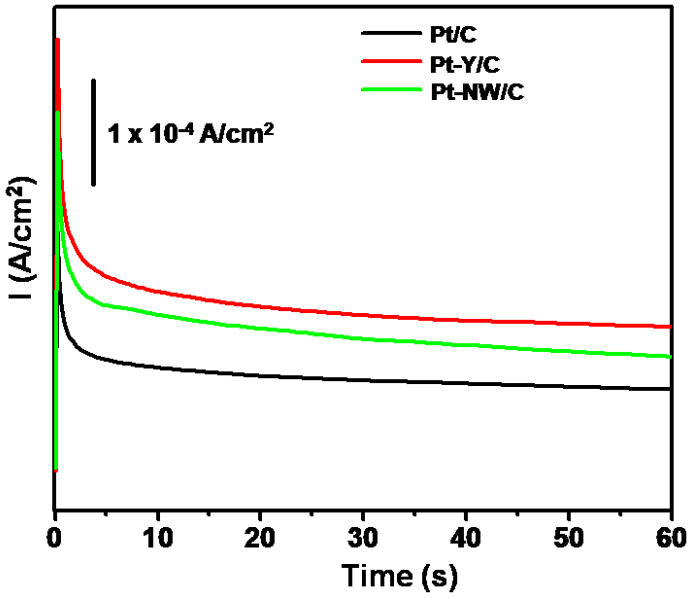

Figure 5.10. Transient current density curves of Pt-Y/C, Pt-NW/C and Pt/C toward formic acid oxidation at -0.24 V for 60 s.

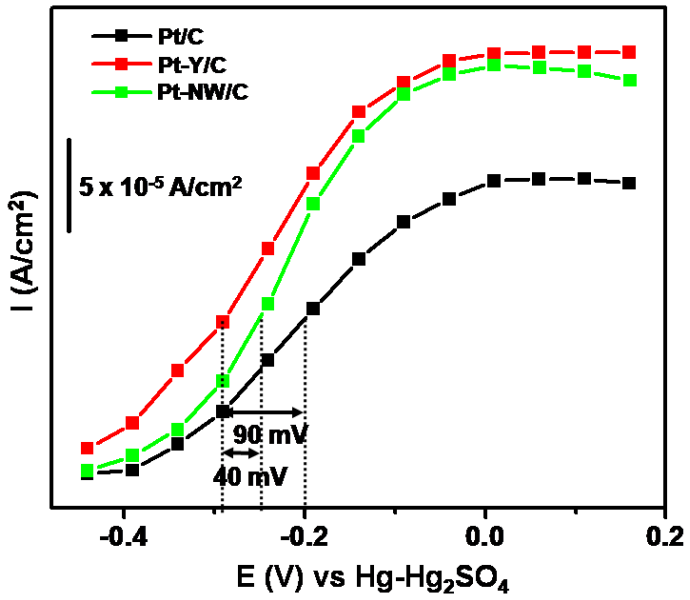

Figure 5.11. Potential-dependent steady state current density curves of Pt-Y/C, Pt-NW/C and Pt/C toward formic acid oxidation; the corresponding shift in the potential at a particular current density is also shown.

In addition, the value of exchange current density (j_o) of these structures toward formic acid oxidation is calculated from the Tafel polarization studies as summarized in Table 5.1. The value of j_o is slightly higher for Pt-Y/C than that of Pt-NW/C and Pt/C respectively highlighting the change in the intrinsic rate constant.

Table 5.1. Exchange current density values of Pt-Y/C, Pt-NW/C and Pt/C toward formic acid, methanol and ethanol oxidation; these values are obtained from the Tafel plots of the respective electrodes.

Electrodes	Exchange Current Density (A/cm^2)		
	Formic acid oxidation	Ethanol oxidation	Methanol oxidation
Pt-Y/C	1.7×10^{-7}	5.7×10^{-7}	1×10^{-6}
Pt-NW/C	7.2×10^{-8}	1.9×10^{-7}	6.7×10^{-7}
Pt/C	1.8×10^{-8}	2×10^{-9}	8×10^{-9}

5.3.5.2. Methanol Oxidation

Similar studies have also been explored for methanol oxidation and accordingly cyclic voltammetric response of Pt-Y/C, Pt-NW/C, and Pt/C in a mixture of 0.5 M CH_3OH and 0.5 M H_2SO_4 at 20 mV/s are shown in figure 5.12. The voltammogram shows two peaks during the anodic scan (at 0.13 and 0.73 V for Pt-Y/C), while one peak (at -0.01 V for Pt-Y/C) is observed during the reverse (cathodic) scan. The first step in the reaction (peak 1) is the adsorption of the methanol molecule, immediately followed by its dissociation into several adsorbed species such as $Pt(CH_2OH)_{ads}$, $Pt(CHOH)_{ads}$, $Pt(CHO)_{ads}$ and $Pt(CO)_{ads}$. The second anodic process (peak 2) is caused by the oxidation of these adsorbed species by OH generated from the dissociation of H_2O molecule. During the cathodic sweep, a peak is observed (peak 3) after partial reduction of irreversibly formed surface oxides, which represents the real catalytic activity of the Pt

surface. [Details of the reaction mechanism have already been discussed in chapter III, section 3.3.5.3]. Similarly, as observed for formic acid oxidation, in the present case also, a considerable change in both the peak position and peak current are observed for all the three electrodes, as obvious from the voltammogram.

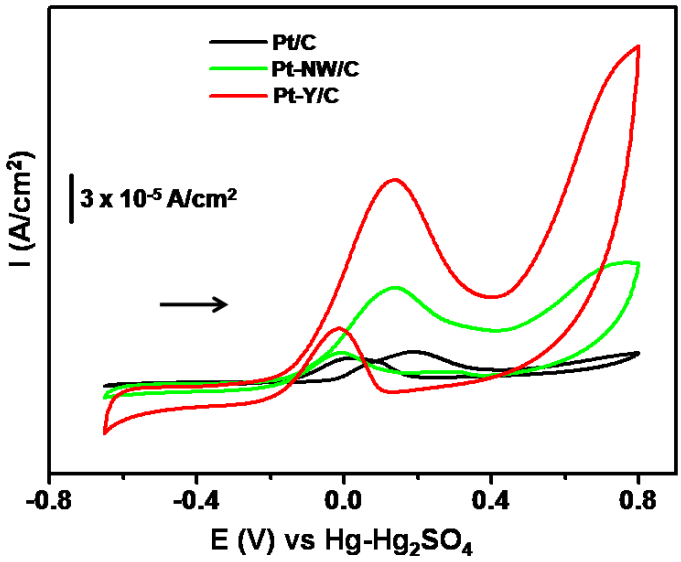

Figure 5.12. Cyclic voltammetric response (2nd cycle data) of Pt-Y/C, Pt-NW/C and Pt/C towards methanol oxidation in a mixture of 0.1 M CH_3OH and 0.5 M H_2SO_4 at 20 mV/s.

Figure 5.13 shows a comparison of current–time transients of methanol oxidation at +0.1 V (potential selected from cyclic voltammogram, Figure 5.12) on the Pt/C, Pt-Y/C, and Pt-NW/C. Interestingly, the current density on Pt-Y/C is significantly higher compared to that on Pt-NW/C and Pt/C. The enhancement factor *R*, (which is defined as the ratio of the current density measured on Pt-Y/C versus that acquired on Pt-NW/C or Pt/C,) varies up to 680 % for Pt/C whereas up to 400 % for Pt-NW/C depending upon the electrode potential.

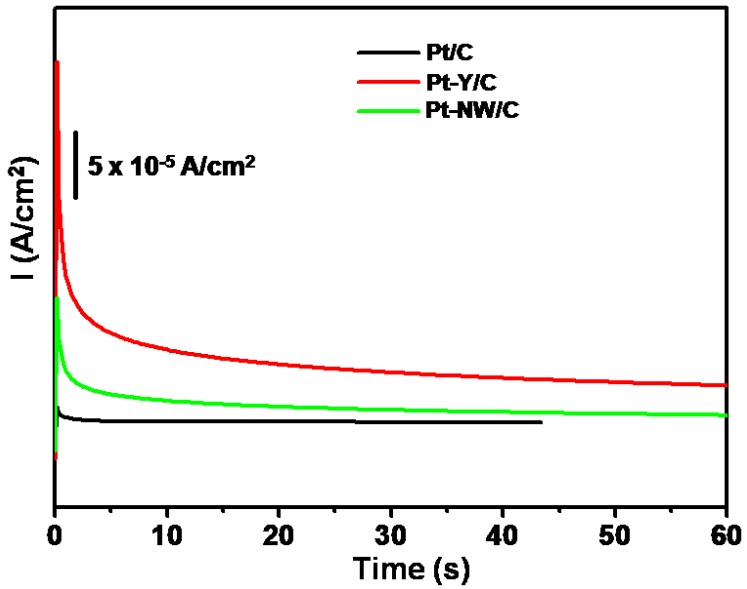

Figure 5.13. Transient current density curves of Pt-Y/C, Pt-NW/C and Pt/C toward methanol oxidation at + 0.1 V for 60 s.

Steady-state current density obtained from the I-t transients (at various potentials, -0.2 V to +0.4 V) is plotted against respective potential as shown in figure 5.14. Interestingly, it is observed that at a given current density, the corresponding potential on Pt-Y/C is much lower than that for Pt-NW/C and Pt/C. Further, the value is shifted negatively by ca. 90 mV at a current density of 1.6 X 10^{-5} A/cm^2 with respect to that of Pt/C, whereas the shift is ca. 50 mV as compared with Pt-NW/C. Furthermore, the value of j_o of these structures as calculated from the Tafel polarization studies is summarized in Table 5.1, where as observed for formic acid oxidation, a slightly higher value is observed for Pt-Y/C than that of Pt-NW/C and Pt/C respectively.

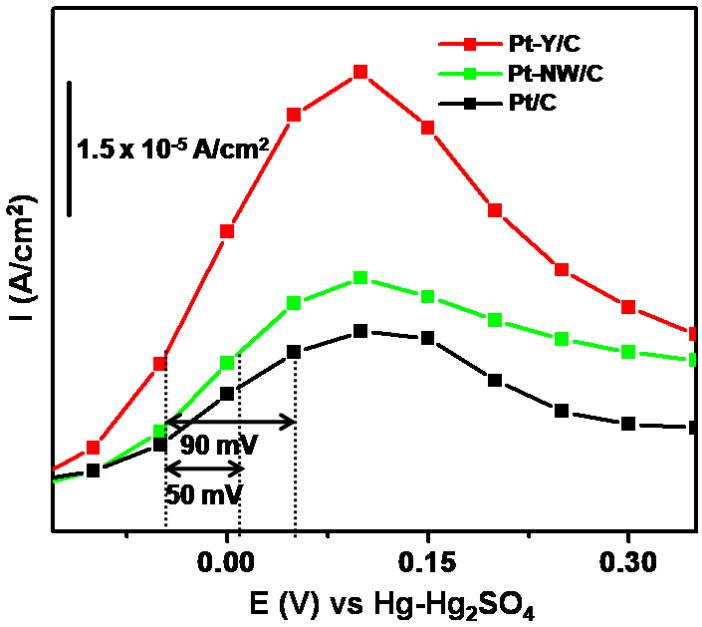

Figure 5.14. Potential-dependent steady state current density curves of Pt-Y/C, Pt-NW/C and Pt/C toward methanol oxidation; corresponding shift in the potential at a particular current density is also shown.

5.3.5.3. Ethanol Oxidation

Similar shape-dependent activity is also investigated for ethanol oxidation and the corresponding voltammetric response in a mixture of 0.1 M C_2H_5OH and 0.1 M $HClO_4$ at 50 mV/s is presented in figure 5.15 for comparison. The voltammograms show two peaks during the anodic scan (at +0.11 V and 0.61 V for Pt-Y/C), while one peak (at -0.05 V for Pt-Y/C) is observed in the cathodic scan where the first anodic peak corresponds to the -OH bond formation to the Pt surface, which plays an important role in ethanol oxidation. Further, the second anodic peak is caused by the formation of CO_2 and other by-products such as acetic acid and acetaldehyde. In the negative-going potential sweep only one peak appears and this is attributed to renewed oxidation of ethanol. [Details of the reaction mechanism have already been discussed in chapter III, section 3.3.5.2]. Similarly, as in the case of above two oxidation reactions, here also the respective voltammograms reveal a considerable change in both the peak position and peak current with shape.

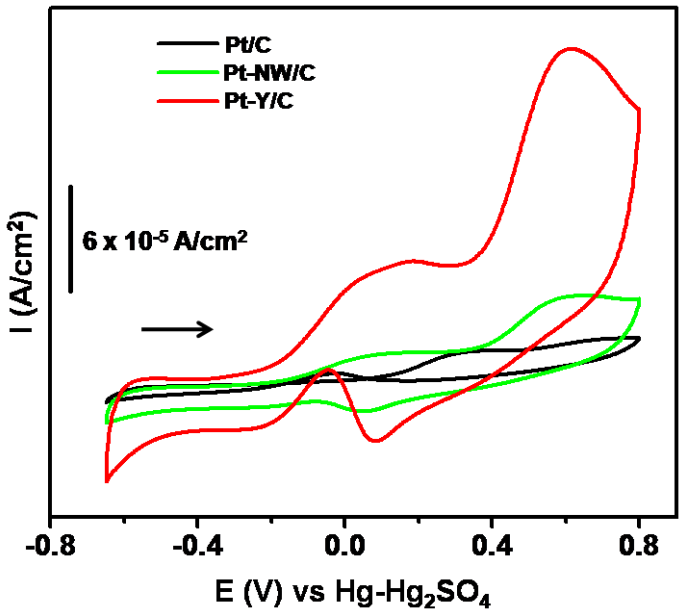

Figure 5.15. Cyclic voltammetric response (2nd cycle data) of Pt-Y/C, Pt-NW/C and Pt/C towards ethanol oxidation in a mixture of 0.1 M CH_3CH_2OH and 0.1 M $HClO_4$ at 50 mV/s.

Furthermore, the transient current density response of the three samples (Pt-Y/C, Pt-NW/C and Pt/C) at -0.04 V is shown in figure 5.16 for comparison. Interestingly, the enhancement factor of Pt-Y/C with respect to Pt-NW/C or Pt/C increases up to 180 % for Pt/C sample, whereas the factor varies up to 130 % for Pt-NW/C. Also from the potential-dependent current density curve (figure 5.17), it is obvious that the potential on Pt-Y/C is shifted negatively by 70 mV as compared to that of Pt/C, while 20 mV shift with respect to that of Pt-NW/C occurs at the same current density of 5.5 x $\mu A/cm^2$. Moreover, as observed for the above two reactions, the value of j_o of these structures (Table 5.1) is slightly higher for Pt-Y/C than that of Pt-NW/C and Pt/C respectively.

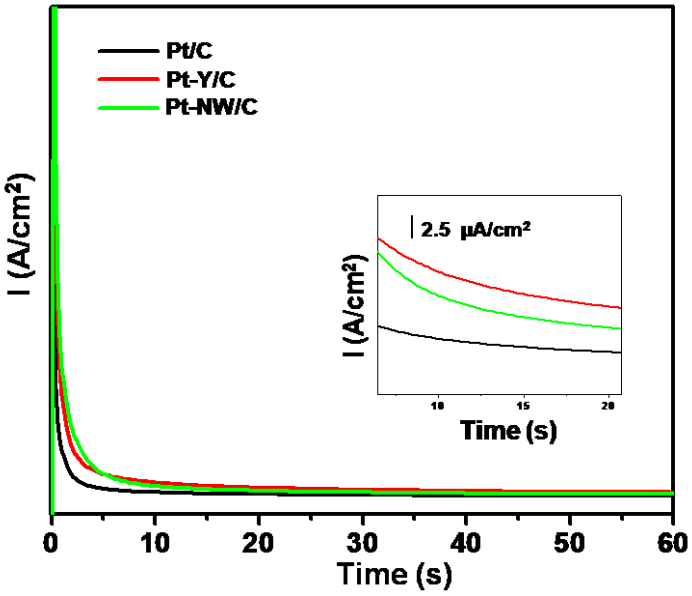

Figure 5.16. Transient current density curves of Pt-Y/C, Pt-NW/C and Pt/C toward ethanol oxidation at -0.04 V for 60 s; inset shows the enlarged view.

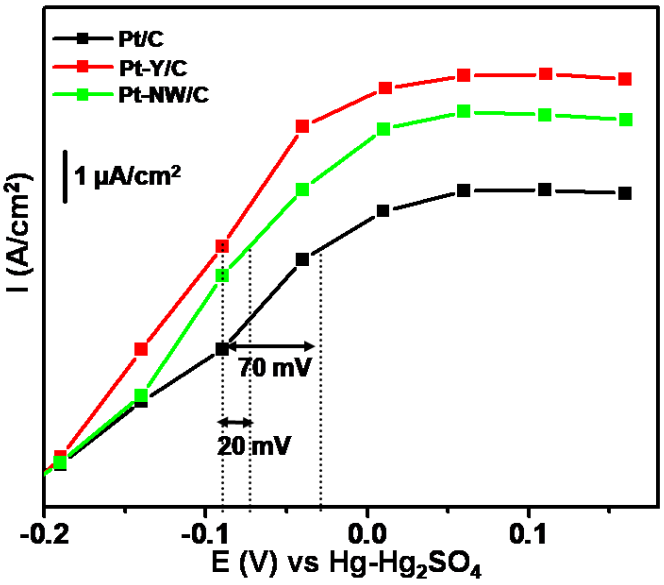

Figure 5.17. Potential-dependent steady state current density curves of Pt-Y/C, Pt-NW/C and Pt/C toward ethanol oxidation; the corresponding shift in the potential at a particular current density is also shown.

Hence, form the above three electrooxidation reactions, it could be concluded that Pt-Y nanostructures exhibit enhanced catalytic activity per unit surface area for the oxidation of formic acid, methanol, and ethanol compared to that of Pt nanowires and commercial platinized carbon. This could be perhaps due to the high density of active sites on the surface of Y-junction Pt (large surface area is expected for these high aspect ratio nanostructures), and in addition it is presumed that the branched regions also enhance the activity due to large field gradient. This is clearly obvious on comparison of the performance of both Y-junctions and linear structures (nanowires) of Pt.

5.3.6. Electrocatalytic Performance of Pt Y-junction and Pd Y-junction Nanostructures toward Formic Acid Oxidation: A Comparative Study

From the above studies, especially on the electrocatalytic performance of Pt Y-junction nanostructures toward formic acid oxidation, it is obvious that Pt suffer from a major drawback such as poisoning by CO-like intermediate species. In order to obviate this problem, we have selected palladium as an alternative catalyst because it is known that this facilitates formic acid oxidation through a direct CO_2 pathway without the formation of poisonous CO intermediate and more importantly due to their relatively low cost.[23] Accordingly, we have compared the electrocatalytic efficiency of these palladium Y-junction nanostructures with that of platinum Y-junctions. Figure 5.18 shows the cyclic voltammetric response of both Pd-Y/C and Pt-Y/C towards formic acid oxidation at 50 mV/s in a mixture of 0.5 M H_2SO_4 and 0.25 M HCOOH. As discussed earlier, the voltammogram corresponding to the Pt-Y/C shows two peaks during the anodic scan (at -0.025 V and 0.73 V), while only one peak (-0.12 V) is observed during the reverse (cathodic) scan. The first anodic peak is due to oxidation of HCOOH to CO_2 on surface sites that remain unblocked by CO, whereas the second anodic peak (shown by dotted arrow) corresponds to the oxidation of surface adsorbed CO (*vide supra)*. Nevertheless, the voltammetric response corresponding to Pd-Y/C shows only one peak during the anodic scan (0.03 V) in contrast to the two peaks observed for Pt-Y/C. This could be attributed to the presence of palladium promoting the formic acid oxidation through a

dehydrogenation pathway wherein the reaction proceeds without any poisonous CO intermediate.[24] Hence, in the case of Pd-Y/C no peak corresponding to the oxidation of CO is observed, whereas for Pt-Y/C due to the build-up of CO (since oxidation proceeds through a dual pathway, *vide supra*) on the electrode surface, a peak corresponding to the CO oxidation is observed. Further, the build-up of CO on the Pt electrode surface in turn decreases the availability of active sites for formic acid oxidation. Also, a comparison of the peak current density on both electrodes reveals a higher value for the Pd-Y/C than that for Pt-Y/C. Another factor which contributes to the enhanced performance of Pd-Y/C towards formic acid oxidation is the presence of Pd (II) species (confirmed from XPS studies, *vide supra*), which could also facilitate a direct CO_2 pathway without the formation of a poisonous CO intermediate.[23b,c,25]

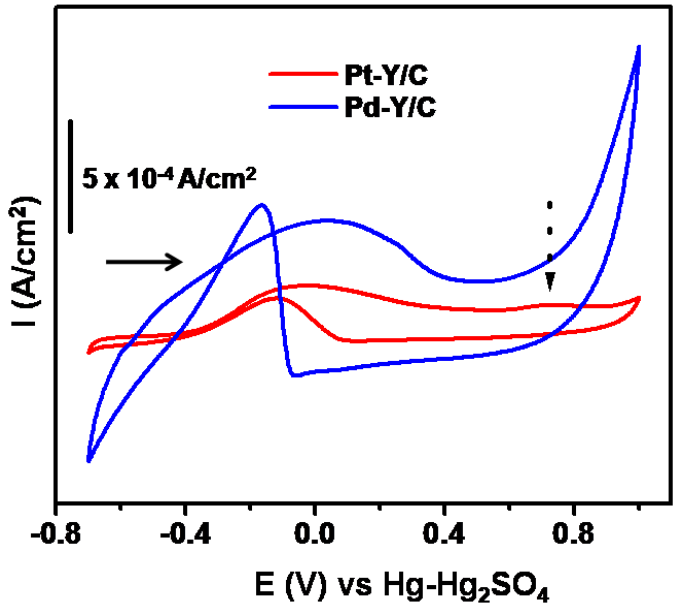

Figure 5.18. Superimposed cyclic voltammetric response of Pd-Y/C and Pt-Y/C toward formic acid oxidation in a mixture of 0.25 M HCOOH and 0.5 M H_2SO_4 at 50 mV/s.

Figure 5.19 shows a comparison of the transient current density of formic acid oxidation at -0.09 V (potential selected from cyclic voltammogram) on the Pd-Y/C and Pt-Y/C at room temperature. Interestingly, the oxidation current density on Pd-Y/C is

significantly higher compared to that on Pt-Y/C and the enhancement factor R (which is defined as the ratio of the current density measured on Pd-Y/C versus that acquired on Pt-Y/C) varies up to 1000 % depending upon the electrode potential.

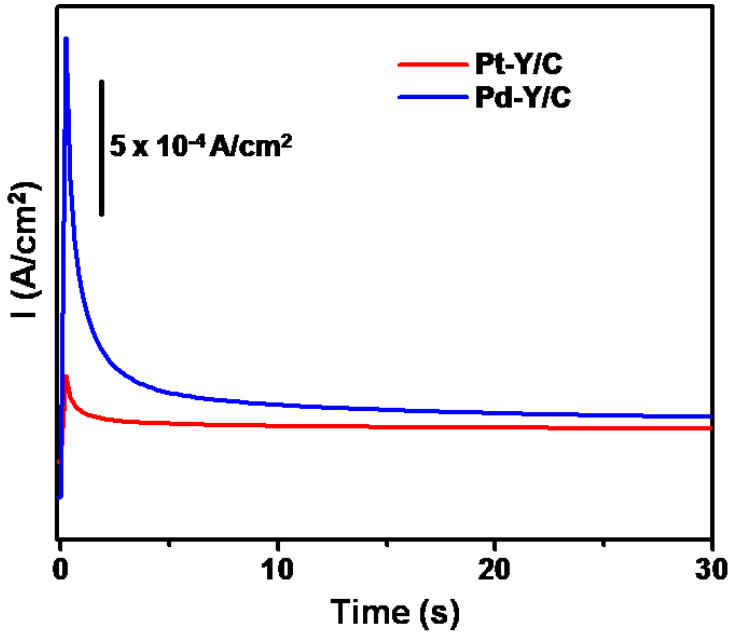

Figure 5.19. Transient current density curves of Pd-Y/C and Pt-Y/C toward formic acid oxidation at -0.09 V.

The steady state current density from the I-t transients (for various potentials, in the range of -0.44 V to + 0.36 V) corresponding to formic acid oxidation is plotted against each respective potential in figure 5.20, which clearly illustrates the superior electrocatalytic performance of Pd-Y/C compared to that of Pt-Y/C. For example, the value of current density (j) on Pd-Y/C and Pt-Y/C for formic acid oxidation at -0.04 V are 1.5 x 10^{-4} and 1.1 x 10^{-4} A/cm^2 respectively.

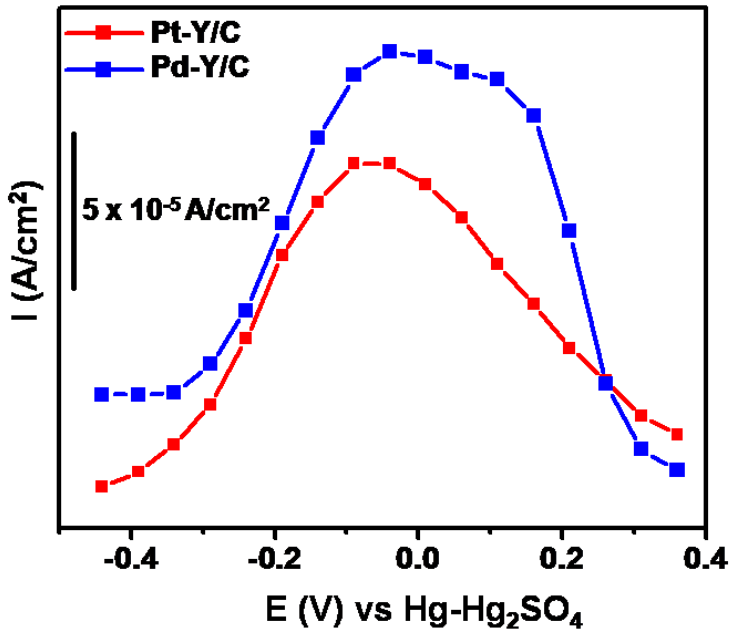

Figure 5.20. Potential-dependent steady state current density plot of Pd-Y/C and Pt-Y/C samples towards formic acid oxidation; comparison of the current density reveals higher value for the Pd-Y/C compared to that of Pt-Y/C.

In order to estimate relative values of exchange current density, (which helps to compare electrocatalytic behaviour) j_o towards formic acid oxidation on these nanostructures dispersed in Vulcan carbon, Tafel polarization offers several advantages. The value of j_o obtained is considerably higher for the Pd-Y/C (3 x 10^{-6} A/cm^2) than that of the Pt-Y/C electrodes (6.3 x 10^{-7} A/cm^2) respectively, which further supports the above results. A cartoon representation showing the formic acid oxidation pathway on both Pt Y-junction and Pd Y-junction nanostructures is shown in scheme 5.3, where it is obvious that formic acid oxidation on platinum electrodes proceed either through CO or directly to CO_2. In contrast, the reaction proceeds directly to CO_2 without any poisonous intermediate on palladium, which is relevant for fuel cell applications.

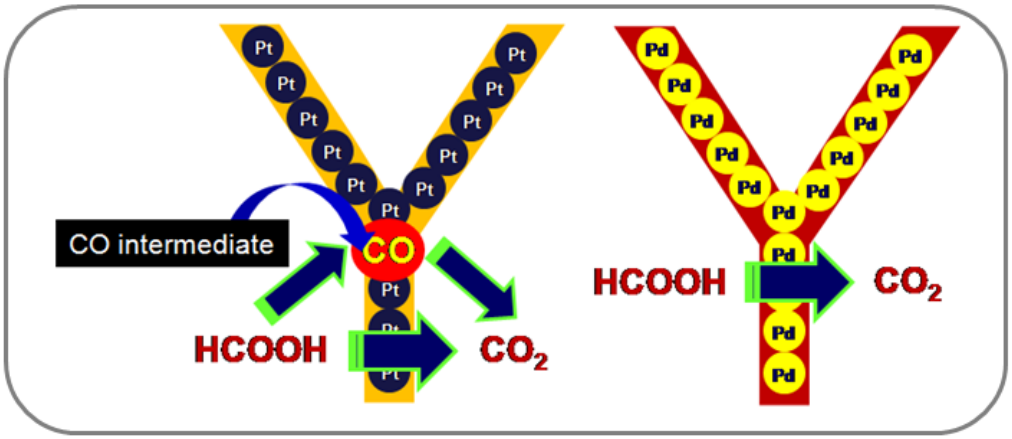

Scheme 5.3. A cartoon representing different formic acid oxidation pathways on Pt Y-junction and Pd Y-junction electrodes; the oxidation reaction proceeds through a poisonous CO intermediate on Pt Y-junctions in contrast to that on palladium Y-junctions.

5.3.7. Electronic Transport in Y- junction Pt Nanostructures

In order to explain the enhanced electrocatalytic performance of Pt Y-junction nanostructures compared to that of nanowires the electron transport behaviour of these Y-junctions has been explored using conducting AFM (conducting AFM rather than STM has been used primarily because of the availability). Accordingly, figure 5.21a shows the I-V profile after positioning the tip on the junction as well as on the individual arms of the Y-junction, where an increase in current is almost linear for positive bias while non-linear response is observed for negative bias. In contrast, the I-V profile corresponding to the Pt nanowires (figure 5.21c) reveals almost linear behaviour at both positive and negative bias. All measurements have been repeated after keeping the tip at different positions and these locations are indicated clearly in Fig. 5.21b,d where the contact mode AFM image of the both Pt Y-junctions and Pt nanowires are shown. However, more detailed studies are essential to pinpoint the exact reason for the non-linear behaviour of these Y-junctions, with respect to their fascinating electronic structure.

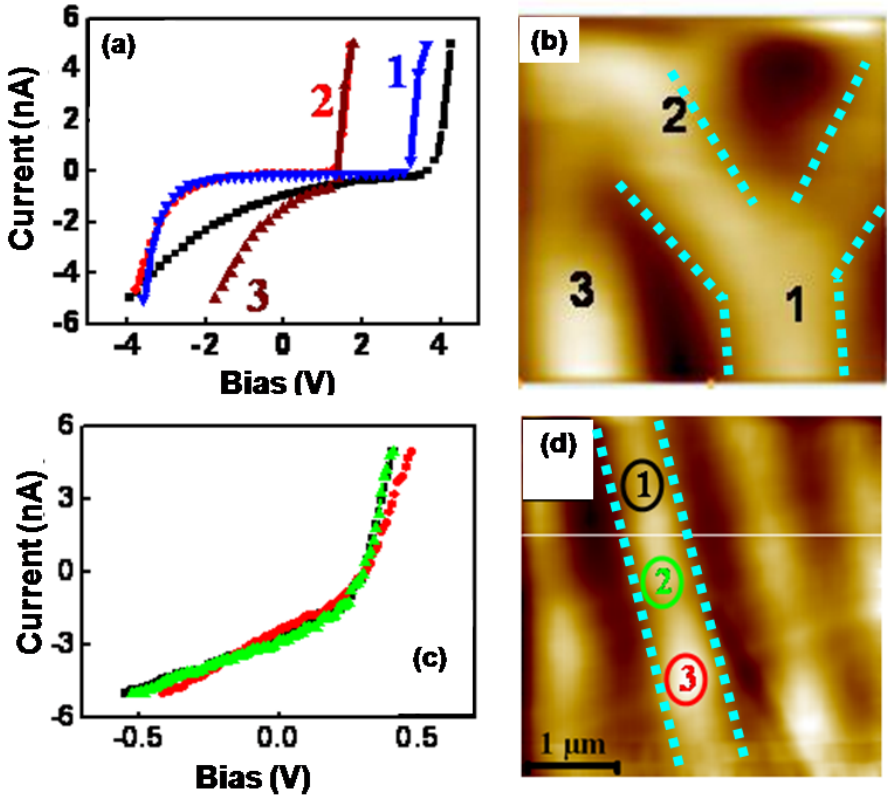

Figure 5.21. (a) I-V profile of Pt Y-junctions taken at different points marked by 1, 2 and 3, where the position of these points are shown in contact AFM image (b); (c) I-V profile of Pt nanowires obtained after positioning the tip at different positions on the nanowires and the positions are marked on the AFM image shown in (d); for clarity both the Y-junctions and nanowires are marked by dotted lines in the micrograph.

5.4. Conclusions

In summary, the use of hierarchically designed porous alumina membrane template is described in this chapter facilitating the fabrication of Y-junction nanostructures of Pt and Pd. These metallic Y-junctions are uniform with regard to the position of the junction and the diameter of the stem and arms. More importantly, a comparison of the electrooxidation activity of Y-junction nanostructures of platinum with that of nanowires and commercial platinized carbon reveals enhanced performance of the junction structures, which are relevant for designing new electrocatalysts for microfuel cells. These structures exhibit enhanced electrocatalytic activity for the oxidation of

formic acid (up to 270 %), methanol (up to 680 %) and ethanol (up to 180 %) compared to that of Pt/C, whereas with respect to Pt-NW/C the enhancement is up to 200 % for formic acid, up to 400 % and 130 % for methanol and ethanol oxidation respectively. Moreover, the potential on Y-junction platinum is shifted negatively by ca. 90 mV as compared with Pt/C whereas the shift is ca. 40 mV with respect to Pt-NW/C at the same current density for the case of formic acid oxidation. Similarly, for methanol oxidation the shift is 90 and 50 mV with respect to Pt/C and Pt-NW/C whereas in the case of ethanol oxidation, the Y-junction nanostructure shows a negative shift of 70 and 20 mV with respect to Pt/C and Pt-NW/C respectively.

We have also explored the utility of Y-junction nanostructures of palladium as an alternative catalyst with respect to platinum for formic acid oxidation reaction, where the former reveals a better performance compared to that of the latter, attributed to the direct oxidation pathway on Pd electrode and hence negligible CO poisoning. The present method of fabrication of Y-junction nanostructures using hierarchical alumina templates could be extended to other metallic/semiconducting systems, facilitating more opportunities for hierarchical designs in nanoelectronics.

5.5. References

1 (a) Hirai, H.; Wakabayashi, H.; Komiyama, M. *Chem. Lett.* **1983**, 1047. (b) Brugger, P. A.; Cuendet, P.; Gratzel, M. *J. Am. Chem. Soc.* **1981**, *103*, 2923. (c) Thomas, J. M. *Pure Appl. Chem.* **1988**, *60*, 1517. (d) Schon, G.; Simon, U. *Colloid Polym. Sci.* **1995**, *273*, 202.

2 (a) Turkevich, J. *Discuss. Faraday Soc.* **1951**, *11*, 55. (b) Finke, R. G. *In Metal Nanoparticles: Synthesis, Characterization, and Applications*; Feldheim, D. L.; Foss, C. A.; Jr., Eds.; Marcel Dekker: New York, **2002**, 17. (c) Schwartzberg, A. M.; Olson, T. Y.; Talley, C. E.; Zhang, J. Z. *J. Phys. Chem. B* **2006**, *110*, 19935; (d) Sau, T. K.; Murphy, C. J. *J. Am. Chem. Soc.* **2004**, *126*, 8648. (e) Widegren, J. A.; Aiken, J. D.; Ozkar, S.; Finke, R. G. *Chem. Mater.* **2001**, *13*, 312. (f) Zhao, Y.; Guo, Y.-G.; Zhang, Y.-L.; Jiao, K. *Phys. Chem. Chem. Phys.* **2004**, *6*, 1766. (g) Melosh, N. A.; Doukai, A.; Diana, F.; Gerardot, B.; Badolato, A.; Petroff, P. M.; Heath, J. R. *Science* **2003**, *300*, 112. (h) Xiao, Z. –L.; Han, C. Y.; Kwok, W. –K.; Wang, H. –H.; Welp, U.; Wang, J.; Crabtree, G. W. *J. Am. Chem. Soc.* **2004**, *126*, 2316. (i) Shirai, M.; Igeta, K.; Arai, M. *Chem. Commun.* **2000**, 623.

3 (a) Lifshitz, E.; Bashouti, M.; Kloper, V.; Kigel, A.; Eisen, M. S.; Berger S. *Nano Lett.* **2003,** *3*, 857. (b) Zhou, G.; Lu, M.; Xiu, Z.; Wang, S.; Zhang, H.; Zhou, Y.; Wang, S. *J. Phys. Chem. B* **2006,** *110*, 6543. (c) Chen, J.; Herricks, T.; Xia, Y. *Angew. Chem. Int. Ed.* **2005,** *44*, 2589.

4 (a) Martin, C. R. *Chem. Mater*. **1996**, *8*, 1739. (b) Yang, C. –M.; Weidenthaler, C.; Spliethoff, B.; Mayanna, M.; Schuth, F. *Chem. Mater.* **2005**, *17*, 355. (c) Duan, X. F.; Lieber, C. M. *Adv.Mater.* **2000**, *12*, 298. (d) Manna, L.; Scher, E. C.; Alivisators, A. P. *J. Am. Chem. Soc.* **2000,** *122*, 12700. (e) Lifshitz, E.; Bashouti, M.; Kloper,V.; Kigel, A. M.; Eisen, S.; Berger, S. *Nano Lett.* **2003**, *3*, 857. (f) Zhou, G.; Lu, M.; Xiu, Z.; Wang, S.; Zhang, H.; Zhou, Y.; Wang, S. *J. Phys. Chem. B* **2006**, 110, 6543. (g) Chen, J.; Herricks, T.; Xia, Y. *Angew. Chem. Int. Ed.* **2005**, *44*, 2589.

5 (a) Hulteen, J. C.; Martin, C. R. *J. Mater. Chem.* **1997**, *7*, 1075. (b) Ou, F. S.; Shaijumon, M. M.; Ci, L.; Benicewicz, D.; Vajtai, R.; Ajayan, P. M. *Appl. Phys. Lett.* **2006**, *89*, 243122.

6 Zhang, D.; Qi, L.; Yang, J.; Ma, J.; Cheng, H.; Huang, L. *Chem. Mater.* **2004**, *16*, 872.

7 Masuda, H.; Hasegwa, F.; Ono, S. *J. Electrochem.Soc.* **1997**, *144*, L127. (b) Li, A. P.; Muller, F.; Birner, A.; Nielsch, K.; Gosele, U. *J. Appl. Phys.* **1998**, *84*, 6023. (c) Jessensky, O.; Muller, F.; Gosele, U. *Appl. Phys. Lett.* **1998**, *72*, 1173.

8 (a) Papadopoulos, C.; Rakitin, A.; Li, J.; Vedeneev, A. S.; Xu, J. M. *Phys. Rev. Lett.* **2000**, *85*, 3476. (b) Tian, Y.; Meng, G.; Biswas, S. K.; Ajayan, P. M.; Sun, S.; Zhang, L. *Appl. Phys. Lett.* **2004**, *85*, 967. (c) Zach, M. P.; Ng, K. H.; Penner, R.M. *Science* **2000**, *290*, 2120. (d) Bandaru, P. R.; Daraio, C.; Jin, S.; Rao, A. M. *Nat. Mater*. **2005**, *4*, 663. (e) Andriotis, A. N.; Menon, M. *Appl. Phys. Lett*. **2006**, *89*, 132116. (f) AuBuchon, J. F.; Chen, L. – H.; Daraio, C.; Jin, S. *Nano Lett*. **2006**, *6*, 324. (g) Sau, T. K.; Murphy, C. J. *J. Am. Chem. Soc*. **2004**, *126*, 8648. (h) Xiao, Z. –L.; Han, C. Y.; Kwok, W. –K.; Wang, H. –H.; Welp, U.; Wang, J.; Crabtree, G. W. *J. Am. Chem. Soc.* **2004**, *126*, 2316. (i) Chu, Y.; Hu, J.; Yang, W.; Wang, C.; Zhang, J. Z. *J. Phys. Chem. B* **2006**, *110*, 3135.

9 (a) Biro, L. P.; Ehlich, R.; Osvath, Z.; Koos, A.; Horvath, Z. E.; Gyulai, J.; Nagy, J. B. *Diamond Relat. Mater*. **2002**, *11*, 1081. (b) Andriotis, A.; Menon, M.; Srivastava, D.; Chernozatonski, L. *Phys. Rev. B* **2002**, *65*, 165416. (c) Grimm, D.; Muniz, R. B.; Latge, A. *Phys. Rev. B* **2003**, *68*, 194307. (d) Xu, H. Q *Appl. Phys. Lett*. **2001**, *78*, 2064. (e) Shorubalko, I.; Xu, H. Q.; Maximov, I.; Omling, P.; Samuelson, L.; Seifert, W. *Appl. Phys. Lett*. **2001**, *79*, 1384.

10 (a) Satishkumar, B. C.; Thomas, P. J.; Govindaraj, A.; Rao, C. N. R. *Appl. Phys. Lett*. **2001**, *77*, 2530. (b) Gothard, N.; Daraio, C.; Gaillard, J.; Zidan, R.; Jin, S.; Rao, A. M. *Nano lett*. **2004**, *4*, 213. (c) Wei, D.; Cao, L.; Fu, L.; Li, X.; Wang, Y.; Liu, Y. *Adv. Mater*. **2007**, *19*, 386.

11 (a) Rouxoux, A.; Schulz, J.; Patin, H. *Chem. Rev*. **2002**, *102*, 3757. (b) Williams,

K. R.; Burstein, G. T. *Catal. Today* **1997**, *38*, 401.

12 (a) Lowenheim, F. A. *Modern Electroplating*; John Wiley and Sons Inc.: New York, 1963. (b) Ling-Bin, K.; Mei, L.; Meng-Ke, L.; Xin-Yong, G.; Hu-Lin, L. *Chin. Phys. Lett*. **2003**, *20*, 763.

13 Schmidt, T.J.; Gasteiger, H.A.; Stab, G.D.; Urban, P.M.; Kolb, D.M.; Behm, R.J. *J. Electrochem. Soc*. **1998**, *145*, 2354.

14 Pattabiraman, R. *Appl. Catal. A* **1997**, *153*, 9.

15 Itoh, N.; Kato, K.; Tsuji, T.; Hongo, M. *J. Membrane Sci*. **1996**, *117*, 189. (b) Berland, B. S.; Gartland, I. P.; Ott, A. W.; George, S. M. *Chem. Mater*. **1998**, *10*, 3941. (c) Lin, Y. S.; Ji, W.; Wang, Y.; Higgins, R. J. *Ind. Eng. Chem. Res*. **1999**, *38*, 2292.

16 Singh, K. V.; Martinez-Morales, A. A.; Andavan, G. T. S.; Bozhilov, K. N.; Ozkan, M. *Chem. Mater*. **2007**, *19*, 2446.

17 Yee, C.; Scotti, M.; Ulman, A.; White, H.; Rafailovich, M.; Sokolov, J. *Langmuir* **1999**, *15*, 4314.

18 Piao, Y.; Lim, H.; Young Chang, J.; Lee, W.-Y.; Kim, H. *Electrochim. Acta* **2005**, *50*, 2997.

19 Kim, K.; Kim, M.; Cho, S. M. *Mater. Chem. Phys*. **2006**, *96*, 278.

20 (a) Liu, F.; Lee, J. Y.; Zhou, W. *J. Phys. Chem. B* **2004**, *108*, 17959. (b) Yang, J.; Lee, J. Y.; Deivaraj, T. C.; Too, H. –P. *Langmuir* **2003**, *19*, 10361.

21 Lengke, M. F.; Fleet, M. E.; Southam, G. *Langmuir* **2007,** *23*, 8982.

22 Tian, N.; Zhou, Z. -Y.; Sun, S. -G.; Ding, Y.; Wang, Z. L. *Science* **2007**, *316*, 732.

23 (a) Xu, C.; Wang, H.; Shen, P. K.; Jiang, S. P. *Adv. Mater*. **2007**, *19*, 4256. (b) Selvaraj, V.; Alagar, M.; Kumar, K. S. *Appl. Catal. B: Environ*. **2007**, *75*, 129. (c) Bauer, J. C.; Chen, X.; Liu, Q.; Phan, T. –H.; Schaak, R. E. *J. Mater. Chem.* **2008**, *18*, 275. (d) Hoshi, N.; Nakamura, M.; Kida, K. *Electrochem. Comm*. **2007**, *9*, 279. (e) Lu, G. –Q.; Crown, A.; Wieckowski, A. *J. Phys. Chem. B* **1999**, *103*, 9700.

24 Kelley, S.C.; Deluga, G. A.; Smyrl, W. H. *Solid-State Lett*. **2000**, *3*, 407.

25 Pavese, A. G.; Solis, V. M.; Glordano, M. C. *Electrochim. Acta* **1987**, *32*, 1213.

CHAPTER 6

Synthesis of Rh@Au Core-Shell Nanorods Using Porous Alumina Membranes

This chapter demonstrates preliminary attempts to synthesize Rh@Au core-shell nanorods using porous alumina membrane templates. High resolution TEM studies reveal the formation of core-shell nanorods where the core and shell regions are made up of Rh and Au respectively. In addition, the overall diameter of these nanorods is ca. 100 nm with a core diameter of 70 ± 5 nm while the shell thickness is 20 ± 5 nm respectively. These Rh@Au core-shell nanorods are promising as multifunctional catalysts for a variety of reactions such as hydrogenation of unsaturated organic compounds, electrooxidation of carbon monoxide and alcohols and for light induced H_2 generation from water.

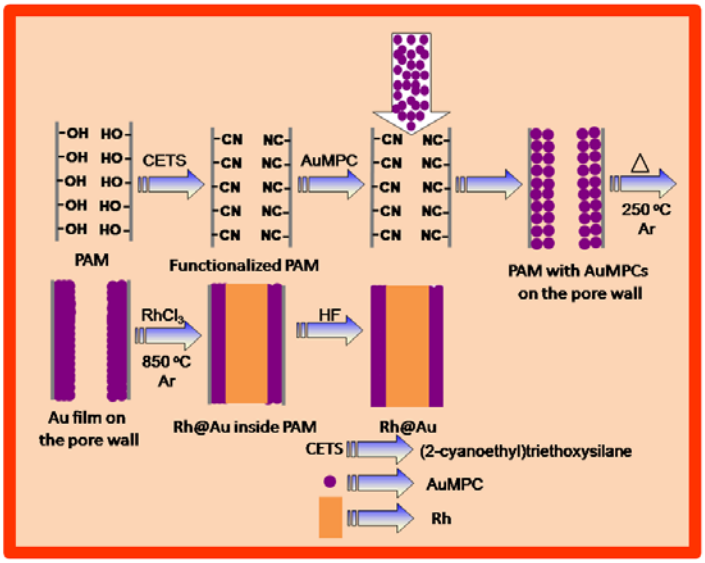

6.1. Introduction

Recently, core-shell nanostructures have received considerable attention due to their improved and sometimes unique physical and chemical properties over their single-component counterparts.[1] A significant change in their properties could be realized by controlling the chemical composition and the relative thickness of the core and shell. For example, Au@Ag core shell nanorods exhibit much sharper, stronger, and shorter-wave length surface plasmon absorption than that of gold nanorods.[2] As a result, these nanostructures have tremendous applications spanning many disciplines including catalysis, magnetism, sensors, and nanoelectronics.[3] However, the ability to fabricate these core-shell structures with uniform thickness and controllable composition is really a daunting task. In addition, during the encapsulation, the core nanostructure should withstand the process of shell formation avoiding inter-diffusion. Hence, the development of a generalized method for the synthesis of metallic core-shell nanorods remains a major challenge.

In order to overcome this challenge and to realize the potential benefits of these core-shell structures, several routes have been developed, which include laser ablation, chemical vapour deposition, electrophoretic or electrochemical deposition, carbothermal reduction, and sol-gel process.[4] Though these routes are successful to some extend, a majority of them yield spherical structures that also with very poor yield. In this context, reports on the synthesis of core-shell nanorods of different metals are sparse in comparison with that of oxides.[5,2] For example, Zamborini et al. have demonstrated the synthesis of Au@Pd core shell nanorods through a galvanic displacement route, where Ag shell deposited on Au nanorods is replaced with Pd by galvanic exchange.[5a] However, these core shell nanorods have non-uniform surface with many pits and cracks.

Nanostructures of gold and rhodium have tremendous application potential in many areas although their effective impact is especially in catalysis with respect to size and shape dependent selectivity and turn over number.[6] As a result, different morphologies of Au and Rh including spherical particles, nanocubes, nanotriangles, nanorods/nanowires,

nanotubes, etc have been synthesized successfully for their effective use as highly selective heterogenous catalysts.[7] However, no efforts have been made till date to couple these two metals so as to form core-shell structures. Hence, in order to fill this lacuna, we demonstrate the synthesis of Rh@Au core-shell nanostructures using porous alumina membrane (PAM) in the present chapter. In the previous chapter, we have seen the utility of alumina membrane but hierarchically branched for the synthesis of Y-junction nanostructures of Pt and Pd, whereas here these membranes with linear nanpore arrays are employed for the synthesis of core-shell structure. More specifically, these core-shell structures have been prepared using the PAM derivatized by a molecular anchor followed by the decoration of Au nanoparticles on the pore walls via filtration and deposition of Rh inside the pore through chemical vapour deposition. The synthesis of core-shell structures using these PAM templates is well suited because it provides an excellent support for the formation of core-shell nanostructures with controllable thickness of core as well as shells.

6.2. Experimental Details

6.2.1. Materials

$RhCl_3.xH_2O$ (99.98%) and $HAuCl_4.3H_2O$ (99.9%) were purchased from Aldrich chemicals while trisodium citrate (99 %) was purchased from Qualigens. (2-cyanoethyl) triethoxysilane (97 %) was procured from Lancaster. Porous alumina membrane with an average pore diameter of 100 nm was purchased from Whatman International Ltd., Kent, UK.[*] All reagents were used without further purification and deionized water (18 MΩ) from milli-Q system was used in all experiments.

[*]Similar nanoporous membranes are also available from SPI Supplies, West Chester, PA, USA and BioAmerica Inc, Homestead, FL, USA.

6.2.2. Decoration of AuMPCs on the Pore Walls of PAM

5 mM (2-cyanoethyl)triethoxysilane in isopropyl alcohol was brought to reflux and subsequently alumina membranes were added to the above solution and refluxing was continued for 15 min. After cooling to room temperature, these membranes were rinsed with isopropyl alcohol and blown dry with a jet of nitrogen. Citrate capped Au nanoparticles with an average diameter of ca. 8 nm (AuMPCs) synthesized by Frens method[8] was passed 4-5 times through the alumina membrane by vacuum (10^{-3} torr) impregnation in order to deposit AuMPCs on the pore walls in a special set-up as shown in figure 6.1. These membranes were then washed with de-ionized water to remove excess of AuMPCs physically adhered on the surface of the membrane, followed by drying under a stream of nitrogen.

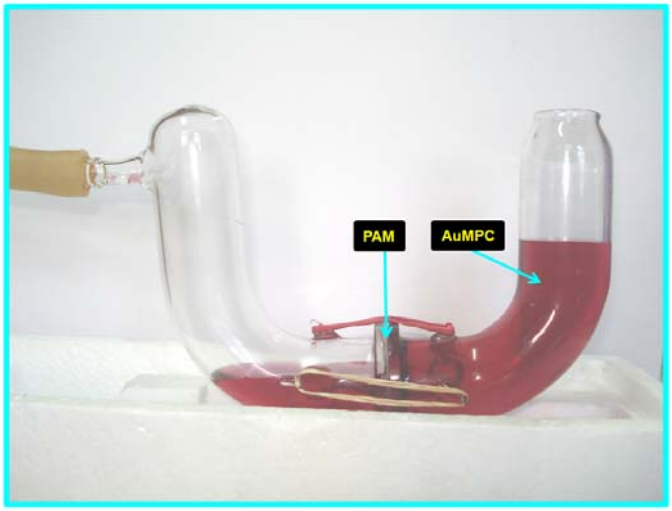

Figure 6.1. Set-up used for depositing the AuMPCs on the pore walls of the alumina membrane by vacuum impregnation; aqueous solution of AuMPC is filtered through the alumina membrane placed in the middle of the set-up (shown by an arrow).

6.2.3. Deposition of Rh Inside the AuMPC Decorated PAM

Soon after the above step, the membranes were heated at 250^{o}C under Ar atmosphere for 2 h to form a uniform coating of Au on the pore walls. Subsequently, Rh was deposited inside the pore walls through a CVD route. (Details of the CVD set-up have already been

mentioned in chapter 5, section 5.2.4). Above membranes were placed (face down) on top of an alumina boat containing 25 mg of $RhCl_3$ at the centre of the tubular furnace. The reaction was carried out at 850 ^{0}C under Ar atmosphere for 4 h followed by cooling to room temperature. Subsequently, the membranes were dissolved in 40 % HF and washed several times with deionized water till neutral pH, followed by a final washing with ethanol to yield almost pure structures. A cartoon representing different stages involved during the formation of Rh@Au core-shell is shown in scheme 6.1, where the decoration of AuMPCs on the cyanoethylsiloxane functionalized pore walls and subsequent deposition of Rh inside the porous structure are shown.

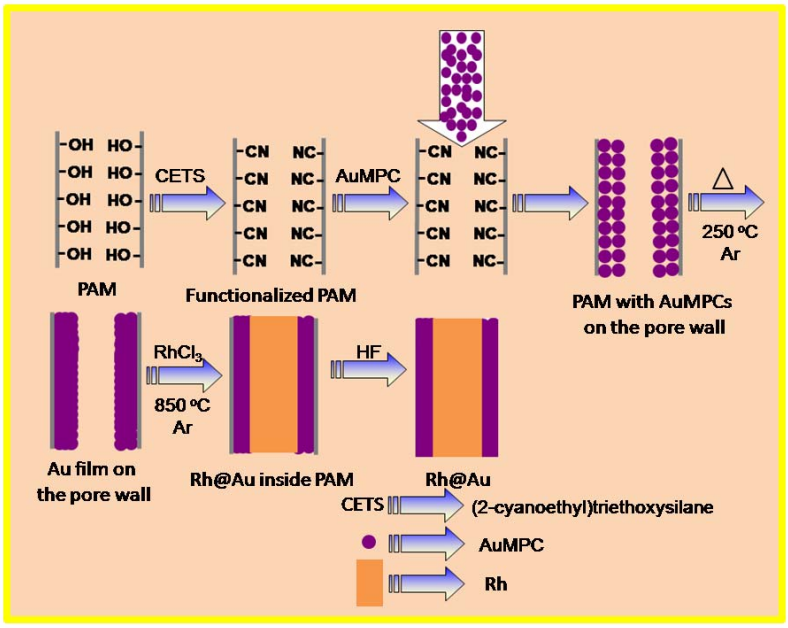

Scheme 6.1. A cartoon representing different steps involved during the formation of Rh@Au core-shell nanorods; functionalization of PAM containing hydroxyl groups with (2-cyanoethyl)triethoxysilane (CETS) to obtain cyanoethylsiloxane functionalized PAM with –CN terminal groups; decoration of the pore walls with monolayer protected gold nanoclusters (AuMPCs) through vacuum impregnation and followed by heating at 250 ^{o}C in Ar to form Au film on the pore walls; deposition of Rh inside the Au decorated PAM through CVD by treating the membrane with Rh precursor at 850 ^{o}C in Ar; finally removal of alumina membrane in HF to release the structures.

6.2.4. Structural and Morphological Characterization

6.2.4.1. High-Resolution Transmission Electron Microscopy (HRTEM)

High resolution images of Rh@Au core-shell nanorods were obtained from a FEI, Tecnai F30G^2, 300 kV HRTEM with FE gun with a resolution of 0.14 nm. The samples were prepared by placing a drop of the dispersed solution onto a carbon-coated Cu grid (3-nm thick, deposited on a commercial copper grid for electron microscope), dried in air and loaded into the electron microscope chamber.

6.2.4.2. UV-Visible Spectroscopy

Solid state UV-visible analysis (in diffuse reflectance mode) was performed using a Shimadzu UV-2101 PC spectrometer equipped with a diffuse reflectance attachment, with $BaSO_4$ as the reference.

The details of characterization techniques like SEM, XRD and FTIR have already been described in Chapter 2, (section 2.4.5.1, section 2.4.5.2 and section 2.4.5.3 respectively) while similar details regarding XPS have been given in Chapter 3 (section 3.2.4.2).

6.3. Results and Discussion

6.3.1. FTIR Analysis

In order to verify the functionalization of PAM with cyanoethylsiloxane, we have performed FTIR studies and accordingly figure 6.2a reveals the FTIR spectrum of PAM after treatment with (2-cyanoethyl)triethoxysilane. The appearance of peaks at 1100 cm^{-1} and 850 cm^{-1} corresponding to Si-O and Si-C stretching respectively confirms the silanization of porous membrane.[9] In addition, a small peak attributed to the terminal cyano moiety is also observed at 2280 cm^{-1}. Similarly, the decoration of silanized pore walls with citrate capped gold nanoparticles is also confirmed by the FTIR spectrum as

shown in figure 6.2b. Here, the decrease in the stretching frequency corresponding to cyano group (2100 cm^{-1}) reveals the attachment of AuMPC on the silanized pore walls through the cyano moiety.[9b] Further, the appearance of peaks at 1644 cm^{-1} and 1200 cm^{-1} is attributed to the carbonyl (C=O) and C-O stretching of $–COO^-$ moiety of citrate monolayer respectively on Au surface. In addition to these, peaks are also observed at 1472 and 1594 cm^{-1} assigned to the symmetric and asymmetric stretching of carboxylate ion of citrate monolayer. Apart from these, a broad band at around 3200 cm^{-1} corresponding to the –OH stretching of hydroxyl group is also seen, which perhaps originates either from the adsorbed moisture or from the hydroxyl functional groups of PAM.

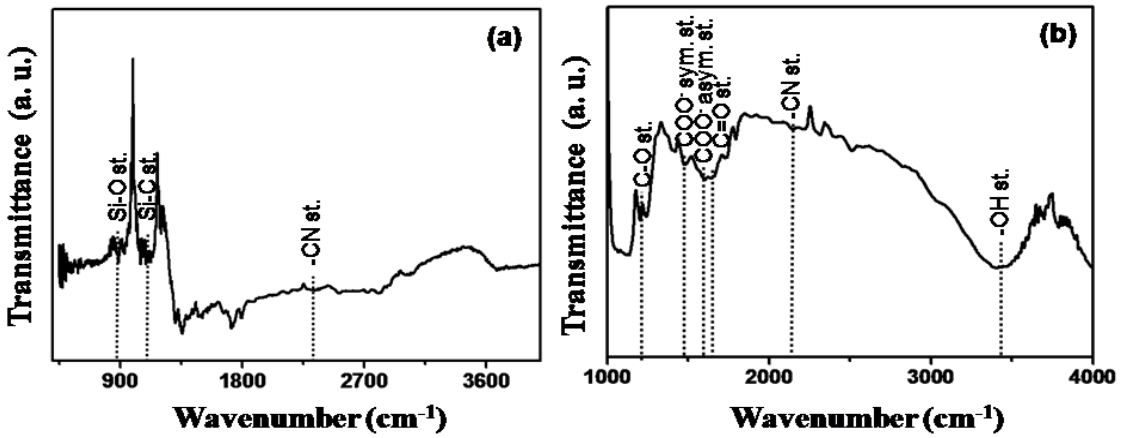

Figure 6.2. FTIR spectrum of (a) cyanoethylsiloxane functionalized PAM; (b) AuMPC decorated on cyanoethylsiloxane functionalized PAM; the characteristic stretching frequencies of different functional groups are indicated in the spectrum.

6.3.2. UV-visible Analysis

Figure 6.3a-c shows a comparison of the UV-visible absorption spectra of pristine PAM, PAM-AuMPC (AuMPC decorated on the pore walls of PAM) and PAM-Rh@Au (PAM with Rh@Au core-shell nanorods), where no peaks are observed for pristine PAM and PAM-Rh@Au. In contrast, AuMPC decorated PAM (figure 6.3b) reveals a characteristic peak at around 520 nm, which arises due to the surface Plasmon resonance (SPR) of gold nanoparticles.[10] Although SPR is a characteristic of nanoscale Au particle

surfaces, since these AuMPCs are confined on the pore walls, the collective excitations are restricted to some extend to cause the absorption peak not well resolved as normally observed for AuMPCs in solution.

The optical properties of core-shell particles and rods are especially important for many plasmonic applications.[11] For e.g., the Surface Plasmon from the shells are extremely sensitive and many novel chemical and biological sensors are demonstrated based on this innovative concept. Independent control of the core and shell dimensions offers a valuable opportunity to systematically control the Plasmon resonance frequency from visible region into the infrared giving rise to potential applications in plasmonics.

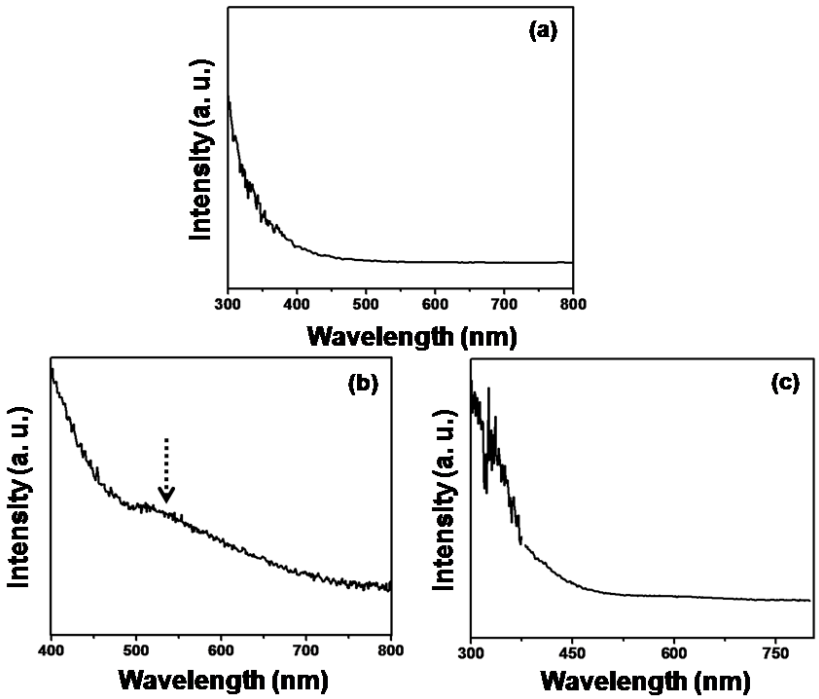

Figure 6.3. Solid-state UV-visible absorption spectrum of (a) pristine PAM; (b) PAM-AuMPC and PAM-Rh@Au; PAM-AuMPC shows surface plasmon absorption at around 520 nm (shown by an arrow).

6.3.3. XRD Analysis

Figure 6.4 shows the XRD pattern of Rh@Au core-shell nanorods before dissolving the membrane. From the 2θ values corresponding to various peaks, it is clear that the core-shell nanorods are made up of Au and Rh. The diffraction peaks

corresponding to (111) and (200) planes of both Au and Rh (marked separately in the XRD pattern) match well with Bragg reflections of the standard and phase-pure fcc structure of Au and Rh respectively. The remaining intense peaks (unmarked) originates from the alumina template, which indicate that alumina becomes crystalline (since the reaction has been performed at 850^{o}C) and hence the peaks could be indexed to boehmite phase, γ-AlOOH.[12]

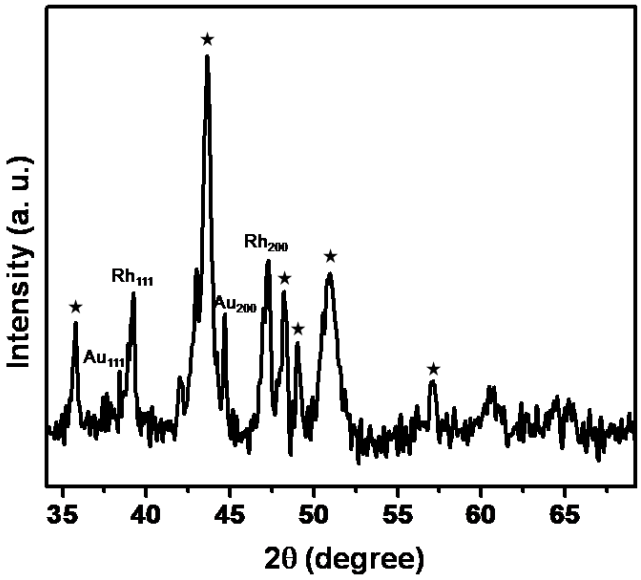

Figure 6.4. XRD pattern of Rh@Au core-shell nanorods before dissolving the alumina template; diffraction peaks corresponding to (111) and (200) planes of both Au and Rh are marked separately; all these diffraction peaks match well with the corresponding peaks for the standard fcc structure of bulk Au and Rh respectively; the spectrum also reveals intense peaks (marked by star shaped symbols) corresponding to the boehmite phase of alumina.

6.3.4. SEM and HRTEM Analysis

Figure 6.5a,b shows the SEM image of the core-shell nanorods synthesized using alumina membrane although the formation of core-shell structure is not clear due to low resolution. Accordingly, the HRTEM images of core-shell nanorods taken from different regions are shown in figure 6.6a-c, which reveal a distinct variation in contrast between the darker core and the lighter shell, verifying the formation of core-shell morphology. The difference in morphology especially at the rod end can also be clearly evident. These

nanorods are formed with an overall diameter of ca. 100 nm with a core diameter of 70 ± 5 nm while the shell thickness is 20 ± 5 nm respectively. Due to the blocking of some of the pores, core-shells are not observed in a few regions instead only hollow structures of Au are seen, as indicated by an arrow in figure 6.6c.

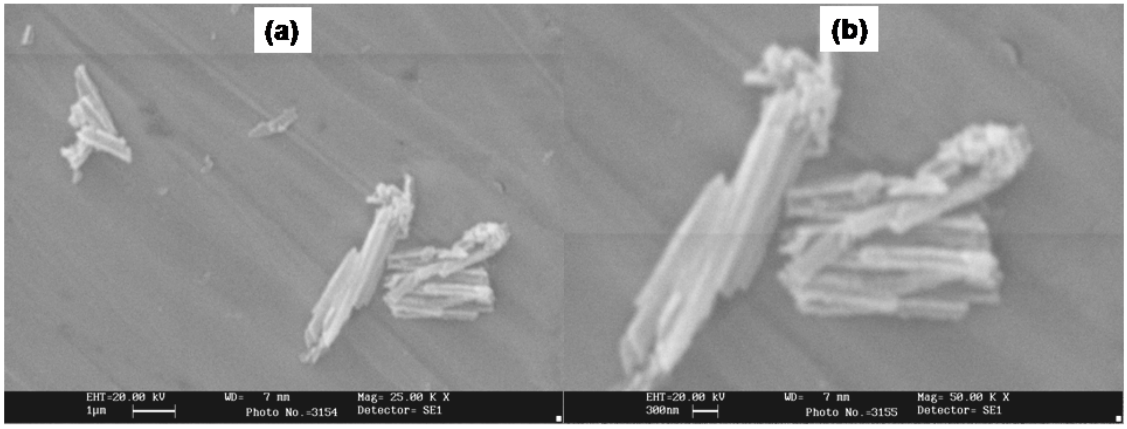

Figure 6.5. SEM images of Rh@Au core-shell nanorods synthesized using porous alumina template; images taken at different magnifications are shown in figure (a) and (b).

Figure 6.7a shows the HRTEM image of the shell with an inter-planar spacing (d spacing) of ca. 0.235 nm, which agrees well with the spacing of the (111) plane of Au (JCPDS 4-784). This is confirmed by the fast Fourier transform (FFT) analysis as shown in the inset, where the pattern corresponding to only one set of diffraction spots corresponding to i.e., (111) plane. In addition, HRTEM image taken from another region of shell is also shown in figure 6.7b, where the FFT analysis gives two sets of diffraction spots corresponding to (111) and (200) planes of Au. Similarly, the core gives ca. 0.219 nm inter-planar spacing in agreement with the lattice spacing of the (111) plane of Rh (JCPDS 5-685) as shown in figure 6.7c, which is again confirmed by the FFT analysis. The FFT pattern corresponding to (111) diffraction spot is shown in the inset.

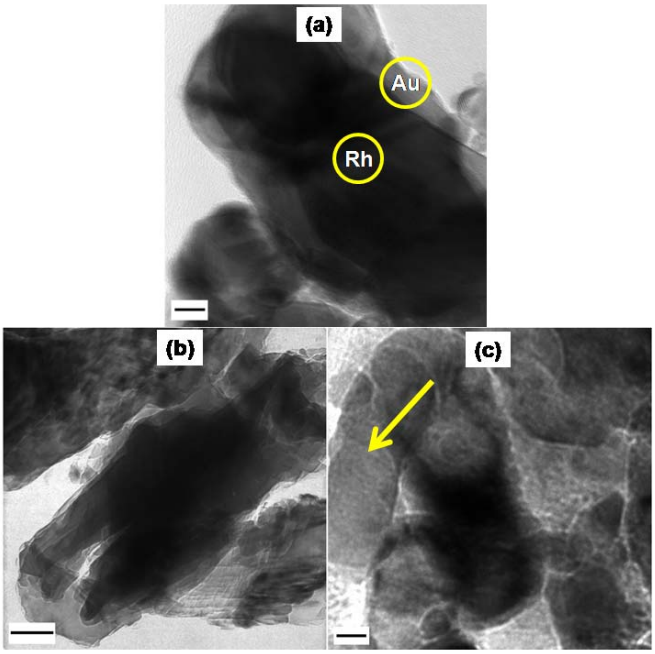

Figure 6.6. HRTEM images of Rh@Au core-shell nanorods synthesized using porous alumina template; Images taken from different regions are shown; along with core-shell nanorods, hollow structure of gold is also observed as marked by an arrow in (c); scale bar 20 nm.

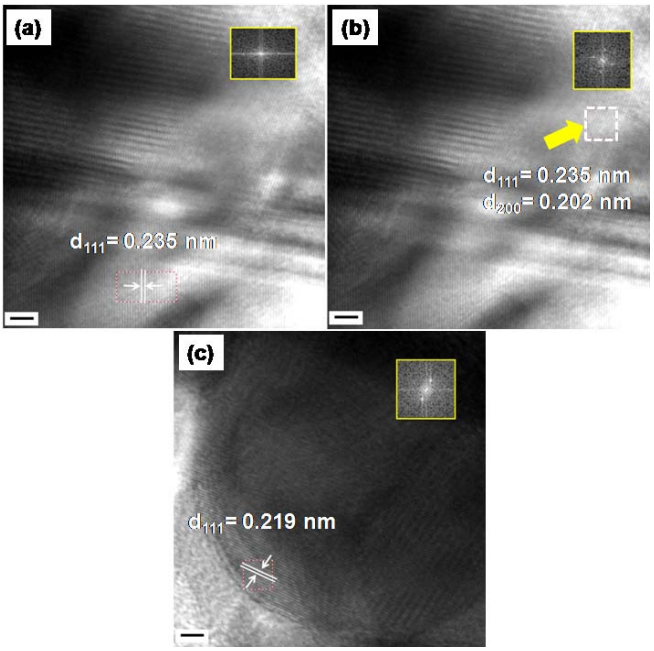

Figure 6.7. HRTEM images focused separately on (a & b) shell (c) core; the micrograph also reveals the interplanar spacing corresponding to the shell and core; the insets are the corresponding fast Fourier transform patterns; scale bar 2 nm.

One of the major limitations of the present study is relatively small aspect ratio of the core-shell structures and also non-uniform shell thickness as revealed by the HRTEM studies. As a result, further studies are needed to understand some of the key synthetic parameters which facilitates the formation of these core-shell structures with uniformity in both core and shell dimensions and also with high aspect ratio. More importantly, it is also essential to explore the optical properties of our nanostructures by tuning both the core and shell dimensions.

6.4. Conclusions

This chapter demonstrates our preliminary attempts for the templated synthesis of Rh@Au core-shell nanorods using porous alumina membrane. These structures consist of core and shell regions made of different metals such as Rh and Au respectively, confirmed by HRTEM results. Moreover, the overall diameter of these nanorods is ca. 100 nm with a core diameter of 70 ± 5 nm while the shell thickness is 20 ± 5 nm respectively. However, these parameters could be easily tuned by varying the template dimension as well as by changing the deposition time or concentration of each metal. The present synthesis provides a rational approach to the design of novel core-shell nanomaterials which could be extended easily to other metallic/semiconducting materials.

6.5. References

1 (a) Martin, B. R.; Dermody, D. J.; Reiss, B. D.; Fang, M.; Lyon, L. A.; Natan, M. J.; Mallouk, T. E. *Adv. Mater*. **1999**, *11*, 1021. (b) Huang, C. –C.; Yang, Z.; Chang, H. –T. *Langmuir* **2004**, *20*, 6089. (c) Dabbousi, B. O.; Rodriguez-Viejo, J.; Mikulec, F. V.; Heine, J. R.; Mattoussi, H.; Ober, R.; Jensen, K. F.; Bawendi, M. G. *J. Phys. Chem. B* **1997**, *101*, 9463. (d) Yoffe, A. D. *Adv. Phys*. **2001**, *50*, 1.

2 Ah, C. S.; Hong, S. D.; Jang, D. –J. *J. Phys. Chem. B* **2001**, *105*, 7871.

3 (a) Caruso, F. *Adv. Mater*. **2001**, *13*, 11. (b) Van Bommel, K. J. C.; Friggeri, A.; Shinkai, S. *Angew. Chem. Int. Ed*. **2003**, *42*, 3027. (c) Lauhon, L. J.; Gudiksen, M. S.; Wang, C. L.; Lieber, C. M. *Nature* **2002**, *420*, 57. (d) Gao, M.; Dai, L.; Wallace, G. G. *Synth. Met*. **2003**, *137*, 1393. (e) Zhou, S.; Varughese, B.; Eichhorn, B.; Jackson, G.; Mcllwrath, K. *Angew. Chem*. **2005**, *117*, 4615.

4 (a) Suenaga, K.; Colliex, C.; Demoncy, N.; Loiseau, A.; Pascard, H.; Willaime, F. *Science* **1997**, *278*, 653. (b) Morales, A. M.; Lieber, C. M. Science 1998, 279, 208. (b) Shi, W. S.; Peng, H. Y.; Xu, L.; Wang, N.; Tang, Y. H. H.; Lee, S. T. *Adv. Mater*. **2000**, *12*, 1927. (c) Zhang, Y.; Suenaga, K.; Colliex, C.; Iijima, S. *Science* **1998**, *281*, 973. (d) Goldberger, J.; He, R. R.; Zhang, Y. F.; Lee, S. K.; Yan, H. Q.; Choi, H. J.; Yang, P. D. *Nature* **2003**, *422*, 601. (e) Zhang, H. F.; Wang, C. M.; Wang, L. S. *Nano Lett*. **2002**, *2*, 941. (f) Zhan, J. H.; Bando, Y.; Hu, J. Q.; Li, Y. B.; Golberg, D. *Chem. Mater*. **2004**, *16*, 5158. (g) Hu, J. Q.; Bando, Y.; Zhan, J. H.; Golberg, D. *Appl. Phys. Lett*. **2004**, *85*, 2932. (h) Hsu, Y. J.; Lu, S. Y. *Chem. Commun*. **2004**, 2102. (i) Ku, J. R.; Vidu, R.; Talroze, R.; Storeve, P. *J. Am. Chem. Soc*. **2004**, *126*, 15022. (j) Zhu, Y. C. Bando, Y.; Uemura, Y. *Chem. Commun*. **2003**, 836. (k) Yin, Y.; Lu, Y.; Sun, Y.; Xia, Y. *Nano Lett*. **2002**, 2, 427.

5 (a) Slawinski, G. W.; Zamborini, F. P. *Langmuir* **2007**, *23*, 10357. (b) Xiang, Y.; Wu, X.; Liu, D.; Jiang, X.; Chu, W.; Li, Z.; Ma, Y.; Zhou, W.; Xie, S. Nano Lett. 2006, 6, 2290. (c) Yoo, S. –H.; Park, S. *Adv. Mater*. **2007**, *19*, 1612. (d) Si, S.; Li,

C.; Wang, X.; Peng, Q.; Li, Y. *Sens. Actuators* **2006**, *119*, 52. (e) Takahashi, K.; Wang, Y.; Cao, G. *J. Phys. Chem. B* **2005**, *109*, 48. (f) Zhang, H. –F.; Wang, C. –M.; Wang, L. –S. *Nano Lett*. **2002**, *2*, 941. (g) Guo, Y. –G.; Wan, L. –J.; Bai, C. –L. *J. Phys. Chem. B* **2003**, *107*, 5441. (h) Hu, J. Q.; Li, Q.; Meng, X. M.; Lee, C. S.; Lee, S. T. *Chem. Mater*. **2003**, *15*, 305.

6 (a) Tsunoyama, H.; Sakurai, H.; Tsukuda, T. *Chem. Phys. Lett*. **2006**, *429*, 528. (b) Overbury, S. H.; Schwartz, V.; Mullins, D. R.; Yan, W.; Dai, S. *J. Catal*. **2006**, *241*, 56. (c) Chen, M. S.; Goodman, D. W. *Science* **2004**, *306*, 252. (d) Sculz, J.; Roucoux, A.; Patin, H. *Chem. Eur. J.* **2000**, *6*, 618. (e) Yoon, B.; Wai, C. M. *J. Am. Chem. Soc*. **2005**, *127*, 17174. (f) Miao, S.; Liu, Z.; Zhang, Z.; Han, B.; Miao, Z.; Ding, K.; An, G. *J. Phys. Chem. B* **2007**, *111*, 2185.

7 (a) Daniel, M. –C.; Astruc, D. *Chem. Rev*. **2004**, *104*, 293. (b) Lahav, M.; Sehayek, T.; Vaskevich, A.; Rubinstein, I. *Angew. Chem. Int. Ed*. **2003**, *42*, 5576. (c) Sharma, J.; Vijayamohanan, K. P. *J. Colloid Interface Sci.* **2006**, *298*, 679. (d) Nikoobakht, B.; El-Sayed, M. A. *Chem. Mater*. **2003**, *15*, 1957. (e) Yu, Y. –Y.; Chang, S. –S.; Lee, C. –L.; Wang, C. R. C. *J. Phys. Chem. B* **1997**, *101*, 6661. (f) Jana, N. R.; Gearheart, L.; Murphy, C. J. *J. Phys. Chem. B* **2001**, *105*, 4065. (g) Sun, Y.; Xia, Y. *Science* **2002**, *298*, 2176. (h) Hoefelmeyer, J. D.; Niesz, K.; Somojai, G. A.; Tilley, T. D. *Nano Lett*. **2005**, *5*, 435. (i) Harada, M.; Abe, D.; Kimura, Y. *J. Colloid Interface Sci*. **2005**, *292*, 113. (j) Li, M.; Mayer, T. S.; Sioss, J. A.; Keating, C. D.; Bhiladvala, R. B. *Nano Lett*. **2007**, *7*, 3281.

8 Frens, G. *Nature: Phys. Sci*. **1973**, *241*, 20.

9 (a) Pretsch, E.; Buhlmann, P.; Affolter, C. *Structure Determination of Organic Compounds*; Springer-Verlag: Berlin, 2000. (b) Beltramo, G. L.; Shubina, T. E.; Mitchell, S. J.; Koper, M. T. M. *J. Electroanal. Chem*. **2004**, *563*, 111.

10 (a) Klabunde, K. J. *Nanoscale Materials in Chemistry*; John Wiley and Sons, Inc.: New York, 2001. (b) Kelly, K. L.; Coronado, E.; Zhao, L. L.; Schatz, G. C. *J. Phys.Chem. B* **2003**, *107*, 668. (c) Daniel, M. C.; Astruc, D. *Chem. Rev*. **2004**, *104*, 293. (d) Cheng, S.; Wei, Y.; Feng, Q.; Qiu, K. –Y.; Pang, J. –B.; Jansen, S.

A.; Yin, R.; Ong, K. *Chem. Mater*. **2003**, *15*, 1560.

11 (a) Oldenburg, S. J.; Averitt, R. D.; Westcott, S. L.; Halas, N. J. *Chem. Phys. Lett.* **1998**, *288*, 243. (b) Jackson, J. B.; Halas, N. J.; *J. Phys. Chem. B* **2001**, *105*, 2743. (c) Oldenburg, S. J.; Jackson, J. B.; Westcott, S. L.; Halas, N. J. *Appl. Phys. Lett.* **1999**, *111*, 2897. (d) Loo, C.; Lin, A.; Hirsch, L. R.; Lee, M.; Barton, J.; Halas, N. J.; West, J.; Drezek, R. *Technol. Cancer Res. Treat.* **2004**, *3*, 33. (e) Hirsch, L. R.; Jackson, J. B.; Lee, A.; Halas, N. J.; West, J. L. *Anal. Chem.* **2003**, *75*, 2377. (f) Jackson, J. B.; Halas, N. J. *PNAS* **2004**, *101*, 17930.

12 Wang, Y. C.; Leu, I. C. Hon, M. H. *J. Appl. Phys*. **2004**, *95*, 1444.

CHAPTER 7

Conclusions and Future Prospects

Major highlights of the work are summarized in the present chapter, outlining the potential utility of linear as well as hierarchically branched porous alumina templates for the formation of uniform and well-aligned high aspect ratio metallic nanostructures of Pt, Pd and RuO_2. Several advantages of template-assisted approach over other available routes along with some of their limitations are also demonstrated. Moreover, the prospective applications of such high aspect ratio nanostructures formed in the absence of surface passivating agents especially in fuel cell electrocatalysis are also reviewed. Related promising developments and daunting challenges in the broad area are also discussed to extend the applications of these fascinating metallic nanomaterials in view of their fundamental and technological interest by physicists, chemists, biologists and engineers. Finally, some of the future prospects and precautions for processing these nanomaterials are also explained within the broad perspective of nanotechnology and its societal impact.

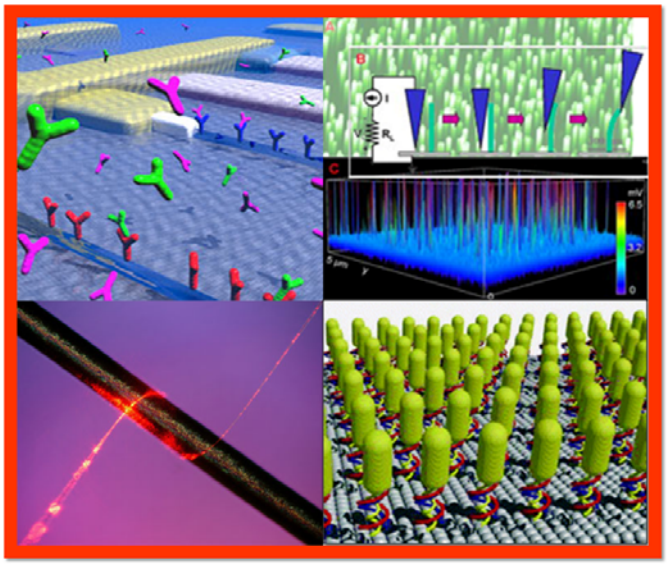

Preparation and characterization of one dimensional nanomaterials have emerged as a major theme in contemporary nanotechnology due to its immense application possibilities. These are the smallest dimensional structures that can be used for efficient transport of electrons/phonons and optical excitations, and are thus expected to be critical to the function and integration of nanoscale devices. Their unique and outstanding physical and chemical properties which could be controlled remarkably by tuning their morphology, have captured amazing attention (even from general public). However, the ultimate potential of these nanostructures is strongly dependent upon the ability to precisely control their morphology (which include size, shape and dimensionality), composition, crystal structure and phase purity. Despite immense knowledge in this area, the synthesis of these nanostructures with high selectivity and their applications are still in an early stage of development. A number of challenges such as difficulty of precisely controlling the aspect ratio, lack of selectivity and uniformity in size distribution, difficulties of scale-up and cost effectiveness remain to be addressed before these materials will find viable applications. In this regard, a thorough understanding of the growth mechanism is a key step towards achieving selective growth of nanostructures, which is of particular significance both for the creation of new materials as well as for the fabrication of devices using these structures.

Various methods including the template-assisted approach, electrochemical route and reduction using several capping molecule/surfactants have been demonstrated to generate these nanostructures as discussed in Chapter 1. Nevertheless, only limited progress has been achieved in synthesizing these materials with precise morphological control and better shape distribution, that too often in the presence of different types of capping molecule/surfactants and in some cases foreign species. Although these external agents are essential for the shape-selective evolution of nanostructures, their presence could drastically hamper their potential benefits. Accordingly, through the present investigation we demonstrate the potential utility of hard templates such as porous alumina membrane (PAM) to synthesize metallic high aspect ratio and other non-

spherical nanostructures. These porous templates, including both linear and branched types are fabricated through an anodization route as discussed in Chapter 2.

PAM templates are beneficial for shape controlled synthesis of not only high aspect nanostructures but also other non-spherical shapes without the assistance of any capping molecule/surfactants or any other foreign species. However, till date these templates have been accomplished successfully only for high aspect ratio structures and no reports are available on the synthesis of non-spherical nanostructures. As a consequence, we have successfully utilized these porous templates for the synthesis of nanorods as well as other non-spherical shapes such as multipods, discs and hexagons of platinum as illustrated in Chapter 3. One of the important characteristics of these structures is their unique electrocatalytic performance which depends highly on their shape/structure. Accordingly, we have compared the electrocatalytic performance of different shapes of platinum towards reactions such as formic acid, methanol, and ethanol oxidation, which are relevant for fuel cell technology. Further, we have extended this template-assisted strategy for the synthesis of bundles of RuO_2 nanoneedles through a potentiostatic route as mentioned in Chapter 4. More importantly, electrical transport measurement reveals a transition from metallic to semiconducting behavior especially at low temperature, in contrast to that of bulk commercial RuO_2. The application of scanning electrochemical microscopy for mapping the electroactivity of these nanoneedles has also been explored in the end.

Synthesis of Y, T and other junction type nanostructures are potentially promising for the development of molecular-scale electronic devices. However, this is difficult to achieve using conventional methods because the linear structures cannot be controllably altered along its length. Consequently, Y-junctions of carbon nanotubes have been recently fabricated successfully through different routes such as template-assisted route and chemical vapour deposition using a suitable catalyst. However, only a limited progress has been made on the synthesis of metallic Y-junctions due to the lack of flexibility in controlling the rigid structures. Accordingly, in Chapter 5 we demonstrate the utility of Y-branched alumina nanochannels for the formation of platinum Y-junction

nanostructures through electrodeposition. These structures reveal enhanced electrocatalytic activity for the oxidation of formic acid, methanol and ethanol compared to that of commercial platinized carbon and Pt nanowires.

In addition to the Y-junction nanostructures of platinum, we also discuss the formation of Pd Y-junction using the Y-branched alumina nanochannels through chemical vapour deposition (Chapter 5). Palladium has been selected as an alternative catalyst for platinum because it is known to facilitate formic acid oxidation through a direct CO_2 pathway without the formation of CO intermediate. Consequently, we have compared the electrocatalytic performance of Pd Y-junction in relation to that of Pt Y-junction nanostructure in order to demonstrate enhanced performance of the former towards formic acid oxidation.

Nanostructures of gold and rhodium have tremendous application potential in many areas although their effective impact is especially in catalysis with respect to size and shape-dependent selectivity. As a result, different morphologies of Au and Rh including spherical particles, nanocubes, nanotriangles, nanorods/nanowires, nanotubes, etc., have been synthesized successfully for their effective use as highly selective heterogenous catalysts. However, no efforts have been made to couple these two metals so as to form core-shell structures. Hence, in order to fill this lacuna, we demonstrate a preliminary attempt to the synthesis of Rh@Au core-shell nanorods using PAM in Chapter 6. These Rh@Au core-shell nanorods are promising as multifunctional catalysts for a variety of reactions such as hydrogenation of unsaturated organic compounds, electrooxidation of carbon monoxide and alcohols and for light-induced generation of H_2 from water.

Thus main results of this thesis unravel few issues related to the synthesis and applications of high aspect ratio metallic nanostructures. In the entire thesis, we have focused mainly on platinum, palladium and ruthenium oxide because of their outstanding role as multifunctional catalysts in many applications, particularly in fuel cells. We have explored the uniqueness of template-assisted approach for the synthesis of these

nanostructures without the assistance of surfactants/capping molecule and foreign species, which is beneficial from their application point of view. More importantly, we have demonstrated how the properties unique to nanostructures vary with morphology by considering their application in electrocatalysis.

Thus the major accomplishments of the present investigations could be summarized as follows-

- ❖ Fabrication of both linear and hierarchically branched porous alumina membranes through anodization route.
- ❖ Precise control of different shapes of platinum mesostructures such as multipods, discs, and hexagons by mere tuning of the electric field using alumina templates.
- ❖ Shape-dependent electrocatalytic performance of platinum nanostructures for many oxidation reactions of interest to fuel cells.
- ❖ Synthesis of Y-junction nanostructures of platinum and palladium using hierarchically designed porous alumina template.
- ❖ Enhanced electrocatalytic performance of Pd Y-junction nanostructures for formic acid oxidation compared to that of Pt Y-junctions.
- ❖ Preparation of RuO_2 nanoneedles using porous alumina template and their transition from metallic to semiconducting behavior at low temperature.
- ❖ Synthesis of Rh@Au core-shell nanorods using templated approach.

However, there are a number of unsolved issues that remain to be urgently addressed before these materials could be exploited commercially. Even though, template-assisted approach allows a precise control of morphology without the aid of any surfactants/capping molecule, the nanostructures synthesized through reduction often proceeds through the mediation of these external species, which retards their reactivity. For example, in electrocatalysis, better performance of a catalyst requires the absence of surface passivating agents normally used during the synthesis often via the chemical reduction route. More importantly, the nanostructures which are used as catalysts should

have high uniformity in size and shape distribution to precisely quantify the catalytic influence. As a result, much more efforts are essential to resolve these issues before realizing the complete potential of these nanostructures. In addition, several existing gaps in our understanding need to be filled by important investigations focusing on structure property correlations. For example, to envisage the electronic application of these metallic linear as well as junction morphologies, understanding several fundamental and fascinating issues about the electronic properties such as the coherence of extended states, difficulty of having individually addressable electronic contacts, the role of finite size and symmetry breaking, and new phenomena at low energies is essential.

Furthermore, there are several daunting tasks like addressing the environmental concern and societal impact of these materials since very little is known about these materials especially how they behave inside living organisms. Based on previous studies on asbestos and chrysolite, we expect many of these nanostructures to be perhaps environmentally hazardous. Researchers dealing with these types of nanostructures should take great caution while handing these structures. In this regard, a systematic, but rigorous evaluation on how these nanostructures will impact our environment and health is urgently needed!

Our novel approach based on template-assisted route for the shape selective synthesis of nanostructures and its processing offers an unprecedented opportunity to obviate many limitations of currently employed materials, opening new possibilities of manipulating the properties and stability to give enhanced performance. However, several limitations need to be kept in mind before these results could commercially be exploited.

- ❖ Since the template is usually a thin membrane, it is difficult to scale-up the nanostructure and grow through this route to macroscopic quantities, although efforts in that direction are underway.
- ❖ The nanostructures synthesized through this template are often polycrystalline.

- ❖ Low mechanical stability and tendency to coalesce upon release from the template.
- ❖ The exact reason behind the metallic to semiconducting transition observed in the case of RuO_2 nanoneedles at low temperature has not been explored. This could have been possible by carrying out the measurement by varying the aspect ratio of nanoneedles and also experimental procedure.
- ❖ More details on both the preparation and characterization the core-shell rods are needed to prove their potential applications
- ❖ Recycling potential of these nanostructured electrocatalyst has not been pursued, which is important for exploiting their utility in practical applications.

Since, some of these disadvantages restrict the full potential of commercial applications of these structures, further work is desired to alleviate these problems. Despite these limitations, the present approach offers enough scope to design different shaped nanostructures through a simple route with better reproducibility. In addition to the shape-dependent electrocatalysis, the present approach is also believed to pave the way to understand several shape-dependent fundamental phenomena of these nanomaterials. More significantly since this method of shape tuning is very general, we believe that apart from linear and Y-junctions this could be extended to the synthesis of other potential multi-terminal junctions such as T and X of a variety of metallic and semiconducting nanostructures, and it is further hoped that more studies would contribute significantly in the years to come.

List of Publications

1. *Comparative Study of the Shape Dependent Electrocatalytic Activity of Platinum Multipods, Discs, and Hexagons: Applications for Fuel Cells*: **Mahima Subhramannia**, Ramaiyan Kannan, and Vijayamohanan K. Pillai; *Langmuir* **2008**, *24*, 3576.

2. *Synthesis of Platinum Y-Junction Nanostructures using Hierarchically Designed Alumina Templates and their Enhanced Electrocatalytic Activity for Fuel Cells Applications*: **Mahima Subhramannia**, Kannan Ramaiyan, Indulekha Komath, Mohammed Aslam, and Vijayamohanan K. Pillai; *Chem. Mater.* **2008,** *20*, 601.

3. *High-Purity Synthesis of Scrolled Mats of Multi-walled Carbon Nanotubes using Temperature Modulation*: Bhalchandra A. Kakade, Hatem Allouche, **Mahima Subhramannia**, Bhaskar R. Sathe, and Vijayamohanan K Pillai; *Carbon* **2008,** *46*, 567**.**

4. *Y-junction Nanostructures of Palladium using Hierarchically Designed Alumina Templates: Enhanced Electrocatalytic Properties for Fuel Cell Reactions*: **Mahima Subhramannia**, Kannan Ramaiyan, Mohammed Aslam, and and Vijayamohanan K. Pillai; Communicated to *J. Phys. Chem. C*.

5. *Shape-Dependent Electrocatalytic Activity of Platinum Nanostructures*: **Mahima Subhramannia**, and Vijayamohanan K. Pillai; *J. Mater. Chem*. Feature Article (Under Preparation).

6. Synthesis of Rh@Au Core-Shell Nanorods using Porous Alumina Membranes: **Mahima Subhramannia**, and Vijayamohanan K. Pillai; (Under Preparation).

7. *Template-Assisted Synthesis of Ruthenium Oxide Nanoneedles: Electrical and Electrochemical Properties*: **Mahima Subhramannia**, Beena K. Balan, Bhaskar R. Sathe, Imtiaz S. Mulla, and Vijayamohanan K. Pillai; *J. Phys. Chem. C* **2007**, *111*, 16593.

8. *Role of Polyfunctional Organic Molecules in the Synthesis and Assembly of Metal Nanoparticles*: Jadab Sharma, Bhalchandra Kakade, Nirmalya Chaki, **Mahima Subhramannia**, Vijayamohanan K. Pillai; *J. Nanosci. Nanotechnol.* **2007**, *7*, 2139.

9. *Electrochemical organization of monolayer protected gold nanoclusters on single-walled carbon nanotubes: Significantly enhanced double layer capacitance*: **Mahima Subhramannia**, Nirmalya Chaki, Jadab Sharma, Bhalchandra Kakade, Renu Pasricha, Apparao M. Rao, and Vijayamohanan Pillai; *J. Nanosci. Nanotechnol.* **2006,** *6*, 1387.

10. *Solvent-assisted one-pot synthesis and self-assembly of 4-aminothiophenol-capped gold nanoparticles*: Jadab Sharma, **Mahima Subhramannia**, Bhalchandra Kakade, Renu Pasricha, A. B. Mandale, and Vijayamohanan Pillai; *J. Phys. Chem. B* **2004**, *108*, 13280.

11. *Tuning the Aspect Ratio of Silver Nanostructures: The Effect of Solvent Mole Fraction and 4-aminothiophenol Concentration*: Jadab Sharma, Nirmalya K. Chaki, **Mahima Subhramannia**, Rajesh G. Gonnade, Imtiaz S. Mulla, and Vijayamohanan K. Pillai; *J. Mater. Chem*. **2004**, *14*, 970.

12. *Highly resolved quantized double-layer charging of relatively larger dodecanethiol-passivated gold quantum dots*: Chaki, N. K., Bhalchandra Kakade, Jadab Sharma, **Mahima Subhramannia**, Vijayamohanan Pillai, and Santosh Haram; *J. Appl. Phys.* **2004**, *96*, 5032.

13. Light-Induced Modulation of Self-Assembly on Spiropyran-Capped Gold nanoparticles: A Potential System for the Controlled Release of Amino Acid Derivatives: Binil I. Ipe, **Mahima Subhramannia**, and George K. Thomas; *J. Am. Chem. Soc.* (Communication) **2003,** *125*, 7174.

Erratum